

Non-Assembly Additive Manufacturing of Medical Devices

Lussenburg, K.M.

DOI

[10.4233/uuid:d46d5f09-9a3b-4887-a4b5-17690920cb1d](https://doi.org/10.4233/uuid:d46d5f09-9a3b-4887-a4b5-17690920cb1d)

Publication date

2024

Document Version

Final published version

Citation (APA)

Lussenburg, K. M. (2024). *Non-Assembly Additive Manufacturing of Medical Devices*. [Dissertation (TU Delft), Delft University of Technology]. <https://doi.org/10.4233/uuid:d46d5f09-9a3b-4887-a4b5-17690920cb1d>

Important note

To cite this publication, please use the final published version (if applicable). Please check the document version above.

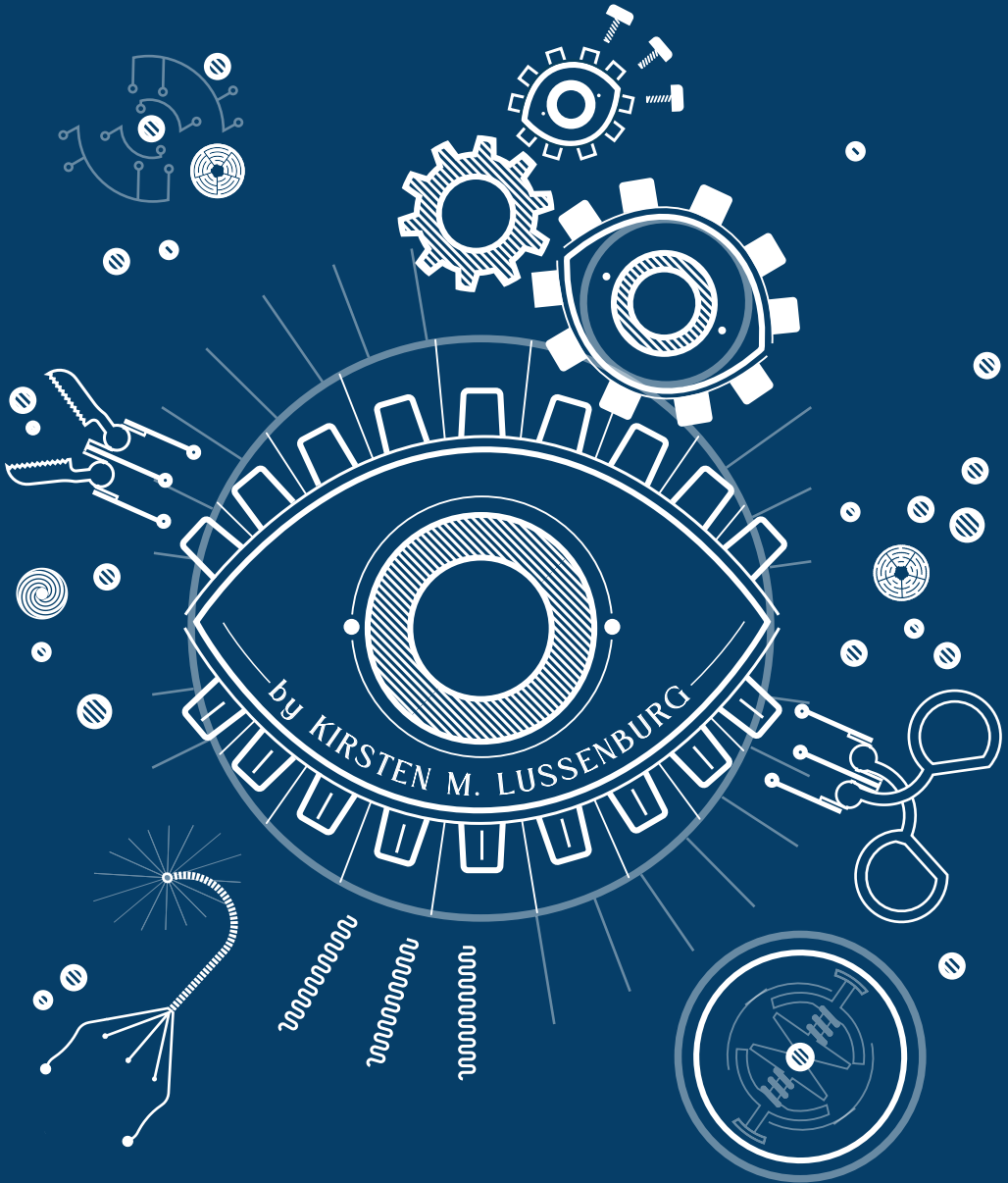
Copyright

Other than for strictly personal use, it is not permitted to download, forward or distribute the text or part of it, without the consent of the author(s) and/or copyright holder(s), unless the work is under an open content license such as Creative Commons.

Takedown policy

Please contact us and provide details if you believe this document breaches copyrights. We will remove access to the work immediately and investigate your claim.

NON-ASSEMBLY
ADDITIVE MANUFACTURING
of
MEDICAL DEVICES



NON-ASSEMBLY ADDITIVE MANUFACTURING OF MEDICAL DEVICES

Proefschrift

ter verkrijging van de graad van doctor
aan de Technische Universiteit Delft,
op gezag van de Rector Magnificus Prof. dr. ir. T.H.J.J. van der Hagen;
voorzitter van het College voor Promoties,
in het openbaar te verdedigen op
dinsdag 30 april 2024 om 12:30 uur

door

Kirsten Marie-Anne LUSSENBURG

Master of Science in Integrated Product Design,
Technische Universiteit Delft, Nederland
geboren te Utrecht, Nederland.

Dit proefschrift is goedgekeurd door de promotoren.

Samenstelling promotiecommissie bestaat uit:

Rector magnificus	voorzitter
Prof. dr. ir. P. Breedveld	Technische Universiteit Delft, promotor
Dr. ir. A. Sakes	Technische Universiteit Delft, copromotor

Onafhankelijke leden:	
Prof. dr. A.A. Zadpoor	Technische Universiteit Delft
Prof. dr. J. Dankelman	Technische Universiteit Delft
Dr. E. Vander Poorten	Katholieke Universiteit Leuven
Prof. dr. C.C.L. Wang	The University of Manchester
Dr. D. Vasilic	Erasmus Medisch Centrum



This project has received funding from the Interreg 2 Seas programme 2014-2020 co-funded by the European Regional Development Fund under subsidy contract No. 2S04-014.

Research data supporting the findings described in this thesis are available at:
DOI 10.4121/55a825d7-79e6-43a8-82a3-83588a23f596.

Printed by: Gildeprint
Cover designed by: K.M. Lussenburg

Copyright © 2024 by K.M. Lussenburg
ISBN: 978-94-6496-092-1

An electronic version of this dissertation is available at <http://repository.tudelft.nl/>

TABLE OF CONTENTS

SUMMARY	IX
SAMENVATTING	XIII
1. INTRODUCTION.....	1
1.1 Background	2
1.2 Additive manufacturing	3
1.2.1 Technology	3
1.2.2 Non-assembly manufacturing.....	3
1.3 Medical devices	5
1.3.1 The rise of minimally invasive surgery.....	5
1.3.2 Additive manufacturing of medical devices	6
1.4 Goal of this thesis	7
1.5 Thesis Outline	8
PART 1. ON DESIGNING WITH 3D PRINTING	
2. A REVIEW ON 3D PRINTED NON-ASSEMBLY MECHANISMS	15
2.1 Introduction	16
2.2 Literature search method	17
2.3 Classification	18
2.4 Geometry-based mechanisms	18
2.4.1 Multi-body	18
2.4.2 Mono-body.....	24
2.5 Material-based mechanisms	27
2.5.1 Mono-material.....	28
2.5.2 Multi-material.....	30
2.6 Pattern-based mechanisms	32
2.7 Self-assembly	33
2.8 Discussion	34
2.8.1 Design solutions for non-assembly mechanisms.....	34
2.8.2 Advantages and disadvantages of non-assembly mechanisms	36
2.8.3 Future directions	37
2.9 Conclusion	38

3. A REVIEW ON 3D PRINTED SPRINGS	47
3.1 Introduction	48
3.2 Search method	49
3.2.1 Scientific data	49
3.2.2 Non-scientific data	49
3.2.3 Exclusion criteria	50
3.2.4 Search results	51
3.3 Types of 3D printed springs	52
3.3.1 Planar designs	52
3.3.2 Spatial designs	56
3.3.3 Spring type distribution	58
3.4 Manufacturing 3D printed springs	59
3.4.1 3D print technologies	59
3.4.2 Materials	59
3.4.3 Settings	60
3.5 Advantages of 3D printed springs	62
3.6 Discussion and conclusion	64
4. A STUDY ON POLISHING COMPLEX 3D PRINTED PARTS	75
4.1 Introduction	76
4.2 Materials and methods	78
4.2.1 Process	78
4.2.2 Analysis	79
4.3 Results and Discussion	81
4.3.1 Surface effects	81
4.3.2 Feature effects	83
4.3.3 Limitations and recommendations	86
4.4 Conclusion	86
 PART 2. DESIGNING TOWARDS NON-ASSEMBLY 3D PRINTING	
5. HIGH-PRECISION 3D PRINTING: MINIATURE TROCAR	93
5.1 Introduction	94
5.1.1 Trocar design	94
5.1.2 Stereolithography	95
5.1.3 Challenges	96
5.2 Initial design	96
5.2.1 Initial design and method	96
5.2.2 Initial design results	99

5.2.3	Initial design discussion	100
5.3	Design optimization	101
5.3.1	Optimized design and method.....	101
5.3.2	Optimized design results	103
5.4	Eye phantom insertion	105
5.4.1	Insertion test method	105
5.4.2	Insertion test results.....	105
5.5	Discussion	106
5.5.1	Process and method	106
5.5.2	3D printed trocar	107
5.6	Conclusion	108
6.	MINIMAL ASSEMBLY 3D PRINTING: STEERABLE GRASPER	115
6.1	Introduction	116
6.1.1	State of the art.....	116
6.1.2	Challenges in minimally invasive surgery	116
6.1.3	Additive manufacturing for surgical devices	117
6.1.4	Objective and requirements	118
6.2	3D-GriP design	119
6.2.1	Gripper design	119
6.2.2	Steerable segment design	120
6.2.3	Handgrip ergonomics	121
6.2.4	Steering control	121
6.2.5	Gripper control.....	122
6.2.6	Prototype fabrication and assembly	123
6.3	Experimental methods and Results	124
6.3.1	Bending angle measurements.....	124
6.3.2	Steering force test.....	126
6.3.3	Grasping force test.....	128
6.4	Discussion	129
6.4.1	Production and customization	129
6.4.2	Performance and improvements.....	131
6.4.3	Limitations and future studies	132
6.5	Conclusion	133
7.	SMALL SCALE 3D PRINTING: STEERABLE LIGHT PIPE	137
7.1	Introduction	138
7.2	Materials and methods	138

7.3 Testing and evaluation	140
7.4 Results and discussion	140
8. MULTI-MATERIAL 3D PRINTING: RECIPROCATING VITRECTOME	143
8.1 Introduction	144
8.2 Design and fabrication	145
8.2.1 Specifications	145
8.2.2 Driving mechanism	146
8.2.3 3D print technology	148
8.2.4 Non-assembly vitrectome design	149
8.3 Experimental evaluation	151
8.3.1 Diaphragm requirements	151
8.3.2 Prototype design and production.....	151
8.3.3 Experimental design and procedure	152
8.3.4 Digital material diaphragms	153
8.3.5 Spring reinforced diaphragms	156
8.4 Discussion	158
8.4.1 Production	158
8.4.2 Performance	160
8.4.3 Limitations of the tests	162
8.4.4 Future design directions	162
8.5 Conclusion	163
9. NON-ASSEMBLY 3D PRINTING: STEERABLE METAL GRASPER	167
9.1 Introduction	168
9.1.1 Additive manufacturing	168
9.1.2 Steerable surgical instruments.....	169
9.2 Materials and methods	169
9.2.1 Instrument requirements.....	169
9.2.2 SLM design guidelines	170
9.2.3 Low friction joint design.....	171
9.2.4 3D printing of flexures	172
9.2.5 Test parts	173
9.2.6 Production	174
9.2.7 Characterization.....	175
9.3 Results	176
9.3.1 Flexures	176
9.3.2 Rolling joints.....	179

9.4 Instrument design and manufacture	181
9.4.1 Joint configuration and actuation	181
9.4.2 3D printed prototypes	182
9.5 Evaluation and discussion	184
9.5.1 Flexures and joints	184
9.5.2 Instrument design improvements	185
9.5.3 Design process	186
9.6 Conclusion	187
9.7 References	187
10. DISCUSSION	193
10.1 Main findings	194
10.2 Limitations of the research	196
10.3 Design for non-assembly	197
10.3.1 Smart assembly	197
10.3.2 3D printer-driven design	198
10.4 Future outlook	199
10.4.1 Technological developments and materials	199
10.4.2 Towards clinical use	200
10.4.3 Future of non-assembly medical devices	201
ACKNOWLEDGEMENTS	207
CURRICULUM VITAE	209
LIST OF PUBLICATIONS	210

SUMMARY

Additive manufacturing, or 3D printing, offers a new paradigm for the way functional products are designed, manufactured, and assembled. Its additive nature provides the ability to create complex-shaped parts, without an increase in production time or costs, which would be difficult to produce with conventional manufacturing. In addition, integration of different functions and materials allows for the production of completely functional assemblies or mechanisms that can be produced in a single production step, known as non-assembly additive manufacturing. These mechanisms are functional immediately after 3D printing, without requiring additional assembly steps. Non-assembly mechanisms have some advantages over traditional assembly-based mechanisms, as they reduce the processing time and costs, and allow for an increase in complexity.

In the medical field, non-assembly designs enable the creation of increasingly complex devices that can facilitate a wide range of complex operations. In conventional medical device manufacturing, intricate components are typically produced separately and then assembled, a process that introduces complexities, costs, and potential points of failure. Non-assembly additive manufacturing addresses these challenges by allowing the creation of complex medical structures, such as surgical instruments, prosthetics, and patient-specific implants, in a seamless and continuous manner. For the production of complex medical devices with miniature- and micro-sized components, for which conventional assembly processes can be long and time-consuming, non-assembly manufacturing can shorten the total manufacturing time, reduce costs, and eliminate the need for specialized knowledge and tools for the assembly and fine-tuning of the device. This efficiency is particularly crucial in the medical field, where timely access to customized and precise solutions can significantly impact patient outcomes.

Non-assembly additive manufacturing also has the potential to drive innovation in medical device design. Designers and engineers can explore new possibilities, pushing the boundaries of what is achievable in terms of functionality, customization, and patient-specific adaptations. Therefore, the main purpose of the research described in this thesis, is to explore the possible contributions of non-assembly additive manufacturing to the production of complex medical devices. This thesis is divided into two parts: state-of-the-art of current 3D printed non-assembly mechanisms and their challenges (Chapter 2 - 4); and exploring design opportunities of additive manufacturing for non-assembly by means of the design of novel medical devices (Chapters 5 - 9).

In Part 1, Chapter 2 reviews the state-of-the-art of non-assembly mechanisms by means of a systematic literature review. Categorized by production considerations, the review discusses challenges and opportunities for various types of mechanisms. This review aims to provide a comprehensive overview of best-practice examples that can be used

as inspiration for further development of innovative non-assembly mechanisms. It highlights the potential applications in healthcare and aerospace engineering and stresses the importance of tools and methodologies to navigate the expansive design space provided by additive manufacturing. One of the challenges that was identified for non-assembly additive manufacturing is that standard components, which ordinarily can be bought off-the-shelf, need to be redesigned to work with the constraints of the additive manufacturing technology and materials. Therefore, Chapter 3 reviews the state-of-the-art for 3D printed springs, examining both scientific and hobbyist contributions. The springs were categorized into planar and spatial designs, and their design, 3D print technology, materials, and settings were analysed. Scientifically derived springs focus more on spatial designs, while hobbyist creations are diverse and creative, with an inclination towards planar designs. The chapter provides a comprehensive overview of the possibilities and best practices for functional 3D printed springs, serving as a resource for future research and inspiration.

Another challenge identified in Chapter 2, is that the interconnected structure of non-assembly mechanisms offers little room for post-processing operations. Therefore, Chapter 4 examines the challenges of poor surface finish in metal additive manufacturing on a complex-shaped part. Focusing on centrifugal disk finishing, this Chapter illustrates a method to visualize the impact of surface finishing techniques on geometric features. Through a case study, the research offers specific design guidelines for metal 3D printed parts subjected to centrifugal disk finishing. The proposed visualization method can be considered a tool for gaining insights into the influence of various polishing methods and aiding in the design process.

Part 2 presents several designs of non-assembly 3D printed medical devices. Chapter 5 focuses on Stereolithography as an emerging additive manufacturing technology for miniature medical applications, specifically addressing challenges in creating sub-millimeter features for a miniature trocar used in ophthalmic surgery. The research was performed in two stages: in the first stage the effect of different materials and print settings on the current design of the parts of the trocar was investigated, identifying issues related to hollow features and proposing strategies to overcome them, and in the second stage these findings were used to optimize the design and production process. The optimized trocar design demonstrates the potential of overcoming production limitations by leveraging the geometrical complexity of additive manufacturing, in order to create miniature features using SLA in various contexts.

Chapter 6 introduces a fully 3D-printed, minimum assembly steerable instrument for laparoscopic surgery. The design, named 3D-GriP, has a pistol-grip handle with a compliant end-effector actuated by cables, allowing omnidirectional steering, and consists of only five separate 3D printed parts, by making use of compliant joints and snap-fit connectors which simplify assembly. The use of additive manufacturing allows for personalization of the handle to each surgeon's needs, aiming to increase the user's comfort during use. Chapter 7 presents the design of an ultraslender steerable light pipe, named Acci, for

use in eye surgery. Printed using Stereolithography, the entire handle and end-effector can be produced in a single production step, with the exclusion of the optical fiber that is inserted afterwards and functions as actuation cable as well. This Chapter demonstrates the potential of additive manufacturing for a non-assembly instrument as part sizes approach the maximum resolution of the additive manufacturing method.

Chapter 8 explores the design of a non-assembly vitrectome mechanism for eye surgery using multi-material PolyJet printing, with strict requirements for its performance. A pneumatically actuated dual diaphragm mechanism was proposed to generate the linear motion required for this mechanism, showing promise in terms of displacement and force, although viscoelastic properties of the printing materials influenced the performance of the mechanism. To negate some of the limitations of the PolyJet technology, such as the need for support material, “smart assembly” solutions were introduced, allowing the design to be produced more efficiently.

Chapter 9 investigates the potential of designing a non-assembly steerable surgical instrument using Selective Laser Melting. Low-friction rolling joints with grid-based lattice structures as flexures were explored for the design. The resulting steerable surgical instrument, with no need for surface finishing, highlights the possibilities of additive manufacturing in creating functional medical products with high shape complexity and no assembly, conjured by means of a 3D printer-driven design process.

This thesis demonstrates that non-assembly additive manufacturing can contribute to a new generation of medical devices, leveraging the inherent design freedom of additive manufacturing to enhance functionalities without assembly constraints. Additive manufacturing opens opportunities for the creation of surgeon- and patient-specific devices, allowing on-demand production without the need for extensive manufacturing and assembly facilities, thereby facilitating localized manufacturing.

SAMENVATTING

Additieve productie, ook bekend als 3D-printen, biedt een nieuw paradigma voor de manier waarop functionele producten voor medische toepassingen worden ontworpen, vervaardigd en geassembleerd. De additieve aard biedt de mogelijkheid om complex gevormde onderdelen te creëren zonder toename van de productietijd of kosten, iets wat moeilijk te realiseren is met conventionele productiemethoden. Bovendien maakt de integratie van verschillende functies en materialen het mogelijk volledig functionele assemblages of mechanismen te produceren die in één enkele productiestap kunnen worden vervaardigd, bekend als montageloze additieve productie. Deze mechanismen zijn direct functioneel na het 3D-printen, zonder dat aanvullende montageschappen nodig zijn. Montageloze mechanismen hebben enkele voordelen ten opzichte van traditioneel geassembleerde mechanismen, omdat ze de verwerkingstijd en -kosten verminderen en het mogelijk maken de complexiteit te vergroten.

In het medische veld maken montageloze ontwerpen het mogelijk om steeds complexere apparaten te creëren die een breed scala aan ingewikkelde operaties kunnen vereenvoudigen. In de conventionele productie van medische apparaten worden complexe componenten doorgaans afzonderlijk geproduceerd en vervolgens geassembleerd, een proces dat complexiteit, kosten en potentiële faalpunten introduceert. Montageloze additieve productie vermindert deze uitdagingen door het mogelijk te maken complexe medische structuren te creëren op een naadloze en continue manier, zoals bijvoorbeeld chirurgische instrumenten, prothesen en op maat gemaakte implantaten. Voor de productie van complexe medische apparaten met miniatuur- en micro-onderdelen, waar conventionele assemblageprocessen lang en tijdrovend kunnen zijn, kan montageloze productie de totale productietijd verkorten, kosten verminderen en de noodzaak voor gespecialiseerde kennis en gereedschappen voor de montage en fijn-afstemming van het apparaat elimineren. Deze efficiëntie is met name cruciaal in het medische veld, waar tijdige toegang tot op maat gemaakte en nauwkeurige oplossingen de patiëntresultaten aanzienlijk kan beïnvloeden.

Montageloze additieve productie heeft ook het potentieel om innovatie in het ontwerp van medische apparaten te stimuleren. Ontwerpers kunnen nieuwe mogelijkheden verkennen door de grenzen van wat haalbaar is op het gebied van functionaliteit, maatwerk en patiënt-specifieke aanpassingen te verleggen. Daarom is het hoofddoel van het onderzoek beschreven in dit proefschrift om de mogelijke bijdragen van montageloze additieve productie aan de productie van complexe medische apparaten te verkennen. Dit proefschrift is verdeeld in twee delen: de huidige stand van zaken op het gebied van 3D-geprinte mechanismen en het verkennen van de beperkingen van additieve productie technologie (hoofdstuk 2-4); en het exploreren van ontwerpkanalen die additieve productie biedt door middel van het ontwerpen van nieuwe medische apparaten (hoofdstukken 5-9).

In Deel 1 geeft Hoofdstuk 2 een overzicht van de stand van zaken op het gebied van montage-loze mechanismen door middel van een systematische literatuurstudie. Gecategoriseerd naar overwegingen omtrent de productie bespreekt de studie uitdagingen en kansen voor verschillende soorten mechanismen. Deze studie beoogt een uitgebreid overzicht te bieden van de beste praktijkvoorbeelden die als inspiratie kunnen dienen voor verdere ontwikkeling van innovatieve montage-loze mechanismen. Het belicht de potentiële toepassingen in de gezondheidszorg en de ruimtevaarttechniek en benadrukt het belang van hulpmiddelen en methodologieën om de uitgebreide ontwerpruimte van additieve productie te navigeren. Eén van de uitdagingen die werden geïdentificeerd voor montage-loze additieve productie is dat standaardcomponenten, die normaal gesproken kant-en-klaar kunnen worden gekocht, opnieuw moeten worden ontworpen om te werken met de beperkingen van de 3D-printtechnologie en materialen. Daarom bekijkt Hoofdstuk 3 de stand van zaken voor 3D-geprinte veren, waarbij zowel wetenschappelijke als hobbybijdragen worden onderzocht. De veren werden gecategoriseerd in vlakke en ruimtelijke ontwerpen, en hun ontwerp, 3D-printtechnologie, materialen en instellingen werden geanalyseerd. De wetenschappelijk bijgedragen veren richten zich meer op ruimtelijke ontwerpen, terwijl hobby-creaties divers en creatief zijn, met een neiging naar vlakke ontwerpen. Het hoofdstuk biedt een uitgebreid overzicht van de mogelijkheden en beste praktijkvoorbeelden voor functionele 3D-geprinte veren, als een bron voor toekomstig onderzoek en inspiratie.

Een andere uitdaging die werd geïdentificeerd in Hoofdstuk 2, is dat de onderling verbonden structuur van montage-loze mechanismen weinig ruimte biedt voor nabewerking. Daarom onderzoekt Hoofdstuk 4 de uitdagingen van een slechte oppervlaktafwerking bij metalen additieve productie op een complex gevormd onderdeel. Met de focus op centrifugaal schijfpolijsten illustreert dit hoofdstuk een methode om de impact van oppervlaktafwerkingsmethoden op geometrische vormkenmerken te visualiseren. Door middel van een case study biedt het onderzoek specifieke ontwerprichtlijnen voor metalen 3D-geprinte onderdelen die bewerkt moeten worden met centrifugaal schijfpolijsten. De voorgestelde visualisatiemethode kan worden gebruikt om inzicht te krijgen in de invloed van verschillende polijstmethoden en om als ondersteuning bij het ontwerpproces.

Deel 2 presenteert verschillende ontwerpen van 3D-geprinte montage-loze medische apparaten. Hoofdstuk 5 richt zich op stereolithografie als een opkomende 3D-printtechnologie voor miniatuur medische toepassingen en behandelt specifiek uitdagingen bij het creëren van sub-millimeter vormkenmerken voor een miniatuur trocar gebruikt in oogheelkundige chirurgie. Het onderzoek werd uitgevoerd in twee fasen: in de eerste fase werd het effect van verschillende materialen en printinstellingen op het huidige ontwerp van de delen van de trocar onderzocht, waarbij problemen met holle vormkenmerken werden geïdentificeerd en strategieën werden voorgesteld om deze te overwinnen, en in de tweede fase werden deze bevindingen gebruikt om het ontwerp- en productieproces te optimaliseren. Het geoptimaliseerde trocar-ontwerp toont het potentieel om productie-

eperkingen te overwinnen door gebruik te maken van de geometrische complexiteit van additieve productie, om zo miniatuurvormkenmerken te creëren met behulp van stereolithografie in verschillende contexten.

Hoofdstuk 6 introduceert een volledig 3D-geprint, minimaal-montage stuurbaar instrument voor laparoscopische chirurgie. Het ontwerp, genaamd 3D-GriP, heeft een pistoolhandgreep met een flexibele eindgrijper aangedreven door kabels, waardoor omnidirectioneel sturen mogelijk is, en bestaat uit slechts vijf afzonderlijke 3D-geprinte onderdelen, door gebruik te maken van flexibele gewrichten en snap-fit connectoren die de montage vereenvoudigen. Het gebruik van additieve productie maakt personalisatie van de handgreep mogelijk naar de behoeften van elke chirurg, met als doel het comfort tijdens gebruik te vergroten. Vergelijkbaar, Hoofdstuk 7 presenteert het ontwerp van een ultraslank stuurbaar lichtpijpje, genaamd Acci, voor gebruik in oogheekkundige chirurgie. Het hele handvat met eindgrijper kan in één productiestap worden geproduceerd met stereolithografie, met uitzondering van de optische vezel die naderhand wordt ingebracht en tevens fungeert als activeringskabel. Dit Hoofdstuk laat de mogelijkheden zien van het gebruik van additieve productie voor een montageloos miniatuurinstrument wanneer op de grenzen van de maximale resolutie wordt ontworpen.

Hoofdstuk 8 verkent het ontwerp van een montageloos vitrectoommechanisme voor oogchirurgie met behulp van multimateriaal PolyJet-printen, waarbij strikte eisen verbonden zijn aan het functioneren van het mechanisme. Een pneumatisch aangedreven dubbel diafragma-mechanisme werd voorgesteld om de benodigde lineaire beweging te genereren, welke veelbelovend bleek op het gebied van verplaatsing en kracht, hoewel de visco-elastische eigenschappen van de printmaterialen de prestaties van het mechanisme beïnvloedden. Om enkele van de inherente beperkingen van de PolyJet-technologie te compenseren, zoals de noodzaak van ondersteuningsmateriaal, werden “slimme montage” oplossingen geïntroduceerd, waardoor het ontwerp efficiënter kon worden geproduceerd.

Hoofdstuk 9 onderzoekt de mogelijkheid om een volledig montageloos stuurbaar chirurgisch instrument te ontwerpen met behulp van Selective Laser Melting, zonder de noodzaak van oppervlakteafwerking. Wrijvingsarme rollende gewrichten met rastervormige latwerkstructuren als flexuren werden onderzocht voor het ontwerp. Het resulterende stuurbare chirurgisch instrument belicht de mogelijkheden van additieve productie bij het creëren van functionele medische producten met een hoge vormcomplexiteit en zonder montage, tot stand gekomen door middel van een door de 3D-printer aangedreven ontwerpproces.

Dit proefschrift toont aan dat montageloze additieve productie kan bijdragen aan een nieuwe generatie medische apparaten, waarbij de inherente ontwerpvrijheid van additieve productie wordt benut voor het verbeteren van de functionaliteit zonder montagebeperkingen. Additieve productie creëert mogelijkheden voor op maat gemaakte apparaten voor chirurgen en patiënten, waardoor productie op aanvraag mogelijk is zonder uitgebreide productie- en assemblagefaciliteiten, en opent daarmee deuren voor lokale productie.

1

INTRODUCTION

1.1 BACKGROUND

For as long as humans have been around, we have felt the need to create tools to improve the quality of our lives. Starting from simple tools made in the Stone Age that made it easier to acquire basic necessities, technological progress over millions of years has enabled us to make increasingly complex products that affect every aspect of our lives. One of the main contributors to making complex products is the ability to assemble them from a collection of individually fabricated parts. From early humans that figured out how to attach a stone axe head to a wooden stick, to airplanes that consist of literally thousands of parts. Assembly of products enables us to combine different types of materials and different production techniques, allowing optimization of each part according to its function.

Until recently, assembly was only accomplished by hand, with some help from hand tools [1]. Well into the nineteenth century, skilled laborers had to make on-the-spot adjustments to parts in order to assemble them [1]. The invention of the automated assembly line by Henry Ford led to the age of mass production by increasing the accuracy and repeatability of fabrication machinery [1], [2]. At first, automatic assembly lines were developed to assemble simple products in a fast and efficient way. Later, in the 1970s, robotic assembly gained traction, with the goal of replacing certain human tasks with robots, a development that is still progressing to this day. Such high-tech assembly methods rely on economies of scale to be economically feasible, which means they are only available for mass-produced products.

As products become more complex, their individual parts tend to become smaller. For instance, a smartphone consists of components with sizes ranging from macro-scale to nano-scale (Figure 1.1). Each of these size ranges requires the use of different materials and assembly techniques to produce and place the components the right way [3]. Particularly assembly of very small components on the micro- and millimetre scale remains challenging, since traditional production methods have difficulty achieving the necessary

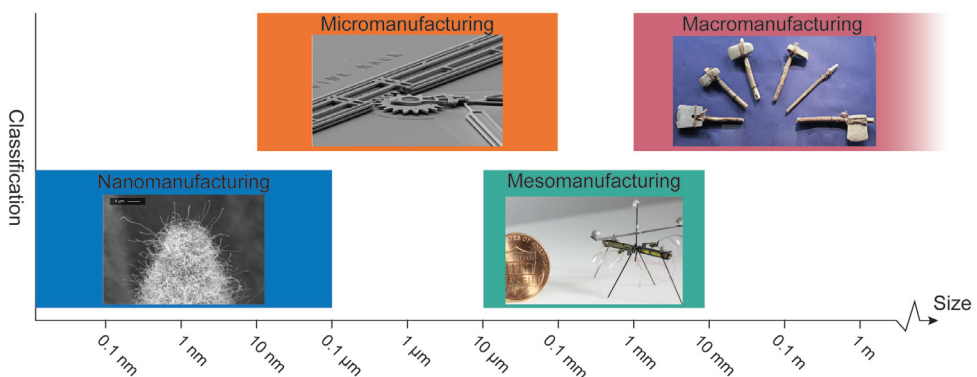


Figure 1.1: Classification of manufacturing scales with example technologies. Nanomanufacturing: detail of the tip of an electrospay emitter covered in carbon nanotubes [11]. Micromanufacturing: meshed gear teeth of a drive gear and a linear rack used in MEMS [12]. Mesomanufacturing: an insect-sized robot capable of flight, ground, and water surface locomotion [13]. Macromanufacturing: stone axes as manufactured by early humans [public domain].

precision and tolerances at this size range [4]–[6]. For miniaturized products with high required precision, manual assembly still prevails [6]. However, manual assembly methods are time-consuming, costly, and susceptible to human error. A solution could be to reduce or eliminate the necessary assembly steps for micro-devices through a higher level of integration between components. To achieve this, it is necessary to consider integration of components, production, and material choices in the early stages of the design process [5], [6]. This requires a change in the way of thinking, using new design principles and solutions, such as origami and folding approaches [7], ‘pop-up’ mechanisms [8], compliant mechanisms [9], and self-assembling machines [10], as well as new production technologies, such as Additive Manufacturing (AM).

1.2 ADDITIVE MANUFACTURING

1.2.1 Technology

Conventional manufacturing methods are often subtractive in nature, which means that they rely on material to be removed in order to fabricate a part. In contrast, AM or 3D printing are processes that build objects directly from a Computer Aided Design (CAD) model in a layer wise fashion, adding material only where needed [14]. This results in less waste and increased design freedom compared to conventional manufacturing methods. A large variety of AM technologies exist, with more being developed every day. The American Society for Testing and Materials (ASTM) [15] recognizes seven different groups of AM technologies: 1) binder jetting, 2) direct energy deposition, 3) material extrusion, 4) material jetting, 5) powder bed fusion, 6) sheet lamination, and 7) vat photo-polymerization. These technologies differ based on the nature of their input materials, for instance in liquid-, powder-, or filament form, and the manner in which they fuse or solidify the material, for instance by means of photopolymerization or thermal energy. The working principles of four common AM techniques: material extrusion, vat photo-polymerization, powder bed fusion, and material jetting, are illustrated in Figure 1.2. AM enables the creation of complex, customized products with reduced resource consumption. However, some limitations of AM include the limited choice of materials, poor surface finish, anisotropic material properties, and specific design constraints, such as the need to use support material.

1.2.2 Non-assembly manufacturing

The additive nature of AM brings many advantages in the way we can design and manufacture products, such as the ability to create complex-shaped parts, without an increase in production time or costs. This potential for complexity offers opportunities for the production of mechanical assemblies on a micro-scale. By integrating multiple, separate parts into one complex-shaped part, the number of components can be reduced, which is known as “part consolidation” [16]–[18]. The goal of part consolidation is to integrate as many functions as possible into one part, and thereby reducing the need to assemble

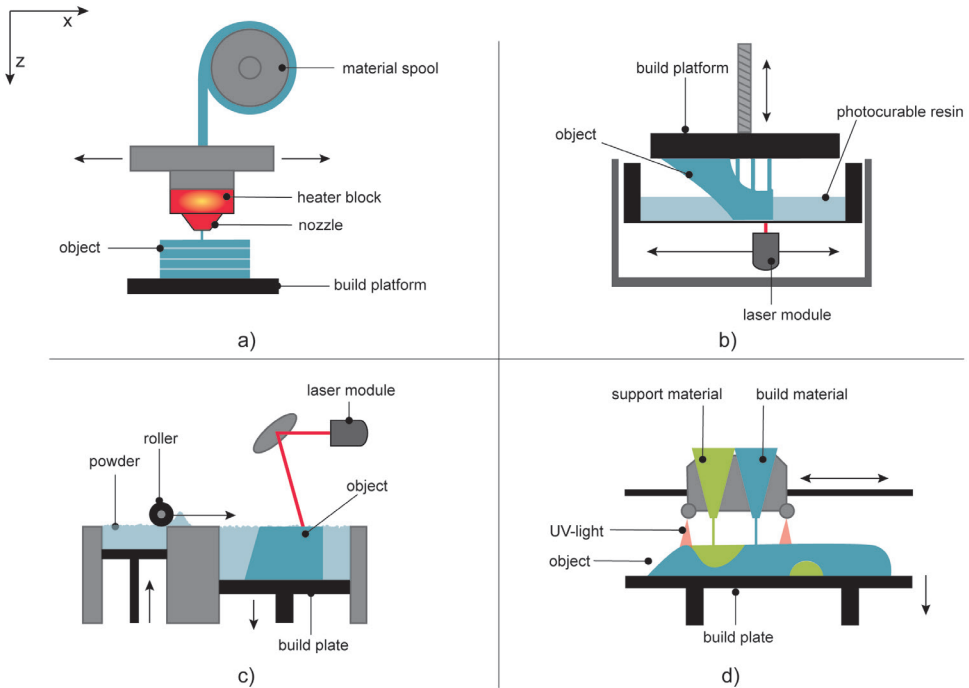


Figure 1.2: Working principle of four commonly used AM technologies. a) In material extrusion, a solid thermoplastic in the form of a thin filament is fed through a heated nozzle to deposit the melted plastic onto a build plate. b) In vat photo-polymerization, a liquid photurable resin is cured by means of a UV-laser. c) In powder bed fusion, a metal or plastic powder is sintered by means of a laser. d) In material jetting, one or more liquid photurable materials are deposited in droplets on the build plate and cured with UV-light.

multiple parts [14]. Further integration of different functions and materials allows for the production of completely functional assemblies or mechanisms that can be produced in a single production step, known as non-assembly manufacturing (Figure 1.3) [19], [20]. These mechanisms are functional immediately after 3D printing, without requiring additional assembly steps, although some post-processing may still be required.

Although the concept of non-assembly manufacturing has received renewed attention with the advent of AM, examples of non-assembly mechanisms were already produced in ancient China, in the form of puzzle balls meticulously carved by hand out of a solid block of ivory (Figure 1.4a). Naturally, these took incredible effort and time to produce. AM makes it possible to produce similar structures in a fraction of the time (Figure 1.4b). Non-assembly AM has been explored in for instance rigid-body joints [21]-[23] and rigid-body mechanisms [24], [25]. There are multiple advantages to non-assembly manufacturing for the production of complex mechanisms with micro- and miniature-sized components. Since there is a reduction in necessary post-processing operations, the total manufacturing time can be shortened, which in turn reduces costs. In addition, non-assembly AM reduces the need for specialized knowledge and tools for the assembly and fine-tuning of the mechanism, as well as reduces potential points of failure during manu-

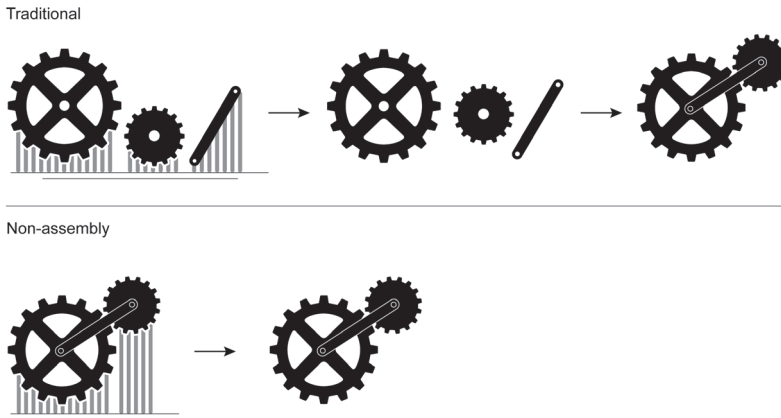


Figure 1.3: Difference between traditional additive manufacturing, where it is necessary to produce and assemble individual parts, and non-assembly additive manufacturing, where the entire mechanism is printed in a single production step. The separate parts are shown in black, while the grey bars represent the support material.

al assembly. Therefore, non-assembly AM has the potential to streamline the production process of micro-mechanisms.

1.3 MEDICAL DEVICES

1.3.1 The rise of minimally invasive surgery

The first surgical procedures performed on the human body were practiced as early as 3000 BC and consisted of cutting holes in the skull to treat medical or ‘mystical’ conditions. The primitive tools used for this practice were of a very simple design, as evidenced by bronze archaeological findings [26]. Since then, a lot has changed in the field of surgery and medical devices. Nowadays, invasive surgical procedures are prevented whenever possible, instead Minimally Invasive Surgery (MIS) is performed. In MIS, only one to three small incisions are created in the body that act as entry ports for slender rigid surgical instruments. Usually, temporary ports called trocars are placed in the small incisions to facilitate the insertion of instruments and seal the body cavity. The advantages of MIS are a reduced risk of complications during surgery, such as infections or haemorrhaging, less pain and scar tissue for the patient, and a decrease in hospitalization time [27], [28]. However, these advantages come at the cost of reduced vision and mobility for the surgeon, leading to longer operative times [29], [30]. In contrast to open surgery, where the surgeon has direct vision and access to the operation area, in MIS, the surgeon’s performance is hindered by indirect visualization and limited operational space to maneuver the instruments. The rigid, slender instruments, in combination with the small incision size, severely reduce the dexterity of the surgeon due to the loss of wrist articulation and limits the number of Degrees Of Freedom (DOF) of the instrument. Additionally, the sur-

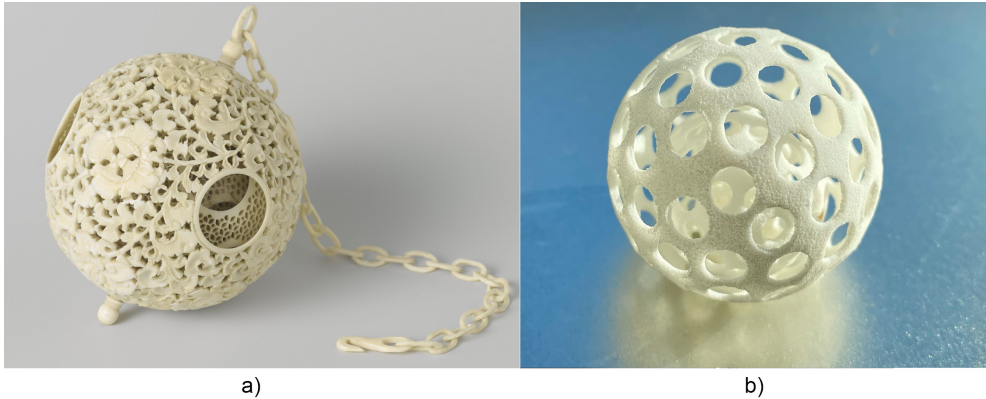


Figure 1.4: Examples of non-assembly manufacturing. a) Ancient Chinese puzzle ball carved from a single block of ivory [image courtesy of Rijksmuseum (Amsterdam, The Netherlands)]. b) A similar structure of concentric balls 3D printed in a single production step.

geon has to cope with the fulcrum effect; the inversion of the handle movements at the end-effector, which is caused by the trocar that acts as a pivot point.

Solutions have been proposed to overcome the limitations of MIS by enhancing the dexterity and functionality of instruments, using for instance wrist-like mechanisms and integrated sensors [31], [32]. This results in progressively intricate MIS instruments, consisting of many small parts and mechanisms, with enhanced functionality for surgeons to work more efficiently. The complexity in design translates to complexity in production and assembly of these instruments, rendering it unfeasible to produce them on a larger scale or for reasonable costs. Currently, small, complex parts hinder instruments from being miniaturized [33]. Appropriate instrument sizes for MIS vary between different surgical areas, in laparoscopic surgery diameters range from 5 to 10 mm (Figure 1.5a), while in ophthalmic surgery current instrument diameters vary between 0.4 and 0.9 mm (Figure 1.5b). Regardless of the surgical application area, there is a need for efficient production of complex, multi-functional surgical instruments, in increasingly small sizes. The main challenge with such instruments is that the more complex they get, the more difficult it is to produce and assemble them. In addition, since MIS instruments are often used as disposable instruments, the costs of production should remain as low as possible.

1.3.2 Additive manufacturing of medical devices

The potential for geometrical complexity offered by AM is extremely suitable for the production of medical devices that are patient-, clinician-, or function-specific. Therefore, in recent years AM has grown in importance in the medical domain [34], and has been applied in fields such as drug delivery systems [35], implants [36], anatomical models [37], surgical guides [38], prostheses [39], and surgical instruments [40]. Besides from the possibility to create customized, one-off devices on demand, non-assembly AM offers a particular advantage for the production of miniature medical devices, by reducing the number of assembly steps and thereby production costs. Non-assembly medical devices have

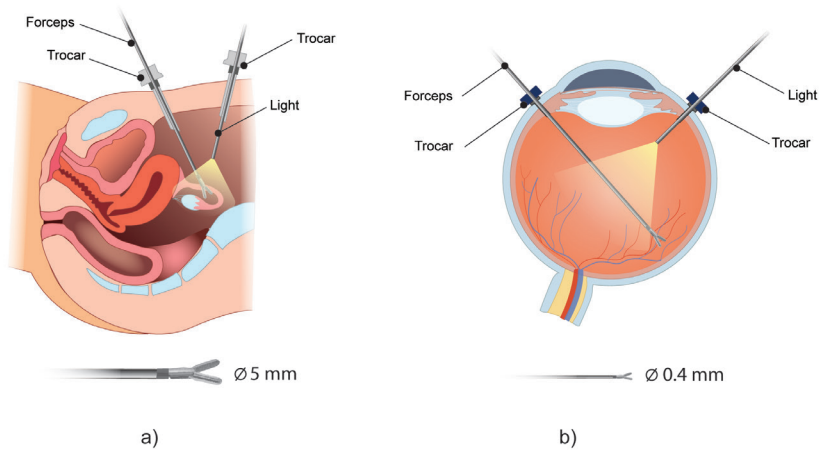


Figure 1.5: Typical set-ups for minimally invasive surgery (MIS). In both laparoscopic surgery (a) and in eye surgery (b), a similar set-up with similar general purpose instruments is used, although the scale of the instruments differ.

been explored for the design of advanced, steerable end-effectors for minimally invasive instruments [41]–[44], as well as deployable implants [45], [46], and hand prostheses [47], using different types of AM technology. These examples illustrate that non-assembly mechanisms can contribute to the production of complex geometrical designs containing many small parts, for which an advantage in production time and cost can be obtained.

1.4 GOAL OF THIS THESIS

Non-assembly AM has the potential to contribute to the design and production of complex, miniature medical devices, because it can reduce production time and efforts for assembly. Instead, these devices can be optimized for their function, providing they take the design considerations for the specific AM process into account [48]. However, increasing complexity also makes designing these mechanisms increasingly complex. Therefore, there is a need for new design strategies that focus on designing functional assemblies and mechanisms with all the design freedom that is provided by AM [49]–[51], instead of relying on the design knowledge for conventional production methods. Although various design methodologies for the design of non-assembly mechanisms have been proposed [49], [52], [53], none have truly succeeded to capture the difficulties and nuances of this level of design integration. Currently, there is no ‘one size fits all’ solution that can be applied to the design of such complex mechanisms. In addition, there are a number of challenges associated with the use of AM that can complicate non-assembly designs. For instance, the difficulty of creating tight tolerances and miniature features due to the limited manufacturing accuracy [54]–[56], the need for support structures [57], and the need for post-processing operations, such as surface finishing techniques [58]–[61].

The main goal of this thesis is to present and evaluate innovative device designs devel-

oped to explore the possible contributions of non-assembly AM to the production of complex medical devices. The designs are focused on utilizing the advantages of AM, while circumventing the limitations of the technology, such as the need for support structures and the poor surface quality. Through these explorations, the aim is to demonstrate that the free complexity offered by AM technology can be used to simplify the production chain, while at the same time advancing design opportunities for medical devices. This was summarized into two main research objectives:

- To investigate the state-of-the-art and identify the main challenges for implementation of non-assembly AM.
- To develop 3D printed prototypes of novel medical devices that demonstrate that the free complexity offered by AM can be used to simplify the production chain, while at the same time advancing design opportunities for medical devices.

1.5 THESIS OUTLINE

This thesis is divided into two parts: 1) background on designing with 3D printing with state-of-the-art of non-assembly mechanisms (Chapter 2 – 4); and 2) exploring design opportunities for non-assembly by means of the design of novel medical devices (Chapters 5 – 9).

The first part starts with a review of current examples of non-assembly mechanisms in Chapter 2, analysing the design strategies used to create and 3D print them. This led to a classification of different types of non-assembly mechanisms, as well as insight into design opportunities and limitations of current AM technology. In Chapter 3, we reviewed 3D printed springs. As functional, mechanical components, springs can play a vital role in non-assembly designs, but a lack of knowledge on how to design them can hinder their effective implementation into these mechanisms. Since there is a large hobbyist community of 3D print enthusiasts, we included both 3D printed spring designs from laymen as well as scientific results. One limitation for medical devices produced in metal is the rough surface finish that requires post-processing. Therefore, in Chapter 4, we study the effects of a post-processing technology on complex 3D printed parts by means of a novel visualization method.

The second part presents design opportunities for medical devices manufactured with different AM technologies. Chapter 5 explores the production of miniature medical devices, by means of 3D printing a trocar as used in eye surgery, while circumventing the inherent resolution limitations of the used AM technology. In Chapter 6, we present the design of a compliant steerable grasper with a pistol-grip, consisting of only five separate components. Chapter 7 expands on Chapter 5, by exploring the design of a miniature steerable light pipe for eye surgery that is printed in a single step, with a single actuation cable. In Chapter 8, a miniature, high-precision instrument used in eye surgery is redesigned for non-assembly AM, with a specific focus on obtaining the required properties of the mechanism using 3D printing materials in limited space. In Chapter 9, we present the

design of a completely non-assembly steerable instrument 3D printed in titanium, which does not require any post-processing steps. As such, the design is low-friction and does not require additional components such as cables. Finally, Chapter 10 discusses the main findings of this thesis.

REFERENCES

- [1] D. E. Whitney, *Mechanical Assemblies; their design, manufacture, and role in product development*. New York: Oxford University Press, 2004.
- [2] J. Heskett, *Industrial design*, 4th ed. London: Thames and Hudson Ltd., 1980.
- [3] R. Wood, "The Challenge of Manufacturing Between Macro and Micro," *Am. Sci.*, vol. 102, no. 2, p. 124, Mar. 2014.
- [4] A. J. Sánchez, "Handling for Micro-manufacturing," in *Micromanufacturing Engineering and Technology*, Elsevier, 2015, pp. 637–659.
- [5] L. Alting, F. Kimura, H. N. Hansen, and G. Bissacco, "Micro Engineering," *CIRP Ann.*, vol. 52, no. 2, pp. 635–657, Jan. 2003.
- [6] H. N. Hansen, M. Arentoft, and G. Tosello, "Micro-mechanical Assembly," in *Micromanufacturing Engineering and Technology*, Elsevier, 2015, pp. 581–595.
- [7] P. S. Sreetharan, J. P. Whitney, M. D. Strauss, and R. J. Wood, "Monolithic fabrication of millimeter-scale machines," *J. Micromechanics Microengineering*, vol. 22, no. 5, p. 055027, May 2012.
- [8] F. Zeynep Temel et al., "Pop-up-inspired design of a septal anchor for a ventricular assist device," 2017.
- [9] M. Wang, D. Ge, L. Zhang, and J. L. Herder, "Micro-scale Realization of Compliant Mechanisms: Manufacturing Processes and Constituent Materials—A Review," *Chinese J. Mech. Eng.*, vol. 34, no. 1, p. 85, Dec. 2021.
- [10] F. Gabler, D. D. Karnaushenko, D. Karnaushenko, and O. G. Schmidt, "Magnetic origami creates high performance micro devices," *Nat. Commun.*, vol. 10, no. 1, p. 3013, Jul. 2019.
- [11] "Fast, cheap nanomanufacturing | MIT News | Massachusetts Institute of Technology." [Online]. Available: <https://news.mit.edu/2014/manufacture-nanoscale-devices-cheaply-1003>. [Accessed: 25-Jul-2023].
- [12] "MEMS Video & Image Gallery - Microsystems Engineering, Science and Applications (MESA)." [Online]. Available: <https://www.sandia.gov/mesa/mems-video-image-gallery/>. [Accessed: 05-Jun-2023].
- [13] Y. M. Chukewad, J. James, A. Singh, and S. Fuller, "RoboFly: An Insect-Sized Robot With Simplified Fabrication That Is Capable of Flight, Ground, and Water Surface Locomotion," *IEEE Trans. Robot.*, vol. 37, no. 6, pp. 2025–2040, Dec. 2021.
- [14] I. Gibson, D. Rosen, and B. Stucker, *Additive Manufacturing Technologies*. New York, NY: Springer New York, 2015.
- [15] ISO/ASTM 52910, "Standard Guidelines for Design for Additive Manufacturing," *ASTM B. Stand.*, vol. 2017, pp. 1–14, 2017.
- [16] G. Jones, E. V. Kline, J. Schmelzle, E. W. Reutzel, T. W. Simpson, and C. J. Dickman, "(Re)Designing for Part Consolidation: Understanding the Challenges of Metal Additive Manufacturing," *J. Mech. Des.*, vol. 137, no. 11, p. 111404, 2015.

- [17] R. Becker, A. Grzesiak, and A. Henning, "Rethink assembly design," *Assem. Autom.*, vol. 25, no. 4, pp. 262–266, 2005.
- [18] J. Liu, "Guidelines for AM part consolidation," *Virtual Phys. Prototyp.*, vol. 11, no. 2, pp. 133–141, Apr. 2016.
- [19] J. S. Cuellar, G. Smit, D. Plettenburg, and A. Zadpoor, "Additive manufacturing of non-assembly mechanisms," *Addit. Manuf.*, vol. 21, no. February, pp. 150–158, 2018.
- [20] G. Sossou, F. Demoly, G. Montavon, and S. Gomes, "An additive manufacturing oriented design approach to mechanical assemblies," *J. Comput. Des. Eng.*, vol. 5, no. 1, pp. 3–18, Jan. 2018.
- [21] J. Cali et al., "3D-printing of non-assembly, articulated models," *ACM Trans. Graph.*, vol. 31, no. 6, p. 1, Nov. 2012.
- [22] A. Boschetto and L. Bottini, "Manufacturability of non-assembly joints fabricated in AlSi10Mg by selective laser melting," *J. Manuf. Process.*, vol. 37, no. September 2018, pp. 425–437, 2019.
- [23] X. Wei, Y. Tian, and A. Joneja, "A study on revolute joints in 3D-printed non-assembly mechanisms," *Rapid Prototyp. J.*, vol. 22, no. 6, pp. 901–933, Oct. 2016.
- [24] K. De Laurentis, C. Mavroidis, and F. F. Kong, "Rapid Robot Reproduction," *IEEE Robotics & Automation Magazine*, no. June, pp. 86–92, 2004.
- [25] Y. Yang, D. Wang, X. Su, and Y. Chen, "Design and Rapid Fabrication of Non-assembly Mechanisms," in *2010 International Conference on Manufacturing Automation*, 2010, vol. 1, pp. 61–63.
- [26] J. R. Kirkup, "The history and evolution of surgical instruments I Introduction Consultant Orthopaedic Surgeon, Bath Clinical Area," *Ann. R. Coll. Surg. Engl.*, vol. 63, no. 4, pp. 279–285, 1981.
- [27] A. Parisi et al., "Minimally invasive surgery for gastric cancer: A comparison between robotic, laparoscopic and open surgery," *World J. Gastroenterol.*, vol. 23, no. 13, p. 2376, Apr. 2017.
- [28] A. Biondi, C. Di Stefano, F. Ferrara, A. Bellia, M. Vacante, and L. Piazza, "Laparoscopic versus open appendectomy: a retrospective cohort study assessing outcomes and cost-effectiveness," *World J. Emerg. Surg.*, vol. 11, no. 1, p. 44, Dec. 2016.
- [29] M. M. Reza, J. A. Blasco, E. Andradas, R. Cantero, and J. Mayol, "Systematic review of laparoscopic versus open surgery for colorectal cancer," *Br. J. Surg.*, vol. 93, no. 8, pp. 921–928, Jul. 2006.
- [30] A. Park, G. Lee, F. J. Seagull, N. Meenaghan, and D. Dexter, "Patients Benefit While Surgeons Suffer: An Impending Epidemic," *J. Am. Coll. Surg.*, vol. 210, no. 3, pp. 306–313, Mar. 2010.
- [31] P. L. Anderson, R. A. Lathrop, and R. J. Webster III, "Robot-like dexterity without computers and motors: a review of hand-held laparoscopic instruments with wrist-like tip articulation," *Expert Rev. Med. Devices*, vol. 13, no. 7, pp. 661–672, Jul. 2016.
- [32] P. Puangmali, K. Althoefer, L. D. Seneviratne, D. Murphy, and P. Dasgupta, "State-of-the-art in force and tactile sensing for minimally invasive surgery," *IEEE Sens. J.*, vol. 8, no. 4, pp. 371–380, 2008.
- [33] J. Arata, Y. Saito, and H. Fujimoto, "Outer shell type 2 DOF bending manipulator using spring-link mechanism for medical applications," in *2010 IEEE International Conference on Robotics and Automation*, 2010, pp. 1041–1046.
- [34] C. Culmone, G. Smit, and P. Breedveld, "Additive manufacturing of medical instruments: A state-of-the-art review," *Addit. Manuf.*, vol. 27, pp. 461–473, May 2019.
- [35] M. Wallis, Z. Al-Dulimi, D. K. Tan, M. Maniruzzaman, and A. Nokhodchi, "3D printing for enhanced drug delivery: current state-of-the-art and challenges," *Drug Dev. Ind. Pharm.*, vol. 46, no. 9, pp. 1385–1401, Sep. 2020.

- [36] N. E. Putra et al., "Extrusion-based 3D printing of ex situ-alloyed highly biodegradable MRI-friendly porous iron-manganese scaffolds," *Acta Biomater.*, vol. 134, pp. 774-790, Oct. 2021.
- [37] P. G. McMenemy, M. R. Quayle, C. R. McHenry, and J. W. Adams, "The production of anatomical teaching resources using three-dimensional (3D) printing technology," *Anat. Sci. Educ.*, vol. 7, no. 6, pp. 479-486, Nov. 2014.
- [38] Y. Liu, L. Xu, H. Zhu, and S. S.-Y. Liu, "Technical procedures for template-guided surgery for mandibular reconstruction based on digital design and manufacturing," *Biomed. Eng. Online*, vol. 13, no. 1, p. 63, May 2014.
- [39] J. ten Kate, G. Smit, and P. Breedveld, "3D-printed upper limb prostheses: a review," *Disabil. Rehabil. Assist. Technol.*, vol. 12, no. 3, pp. 300-314, Apr. 2017.
- [40] S. Kondor et al., "On Demand Additive Manufacturing of a Basic Surgical Kit," *J. Med. Device.*, vol. 7, no. 3, p. 030916, 2013.
- [41] C. Culmone, P. W. J. Henselmans, R. I. B. van Starckenburg, and P. Breedveld, "Exploring non-assembly 3D printing for novel compliant surgical devices," *PLoS One*, vol. 15, no. 5, p. e0232952, May 2020.
- [42] N. P. Castledine, J. H. Boyle, and J. Kim, "Design of a Modular Continuum Robot Segment for use in a General Purpose Manipulator," in *2019 International Conference on Robotics and Automation (ICRA)*, 2019, pp. 4430-4435.
- [43] Y. Hu, L. Zhang, W. Li, and G.-Z. Yang, "Design and Fabrication of a 3-D Printed Metallic Flexible Joint for Snake-Like Surgical Robot," *IEEE Robot. Autom. Lett.*, vol. 4, no. 2, pp. 1557-1563, Apr. 2019.
- [44] D. B. Roppenecker, A. Pfaff, J. A. Coy, and T. C. Lueth, "Multi arm snake-like robot kinematics," in *2013 IEEE/RSJ International Conference on Intelligent Robots and Systems*, 2013, pp. 5040-5045.
- [45] S. Leeflang, S. Janbaz, and A. A. Zadpoor, "Metallic clay," *Addit. Manuf.*, vol. 28, no. February, pp. 528-534, Aug. 2019.
- [46] M. A. A. Leeflang, F. S. L. S. L. Bobbert, and A. A. A. Zadpoor, "Additive manufacturing of non-assembly deployable mechanisms for the treatment of large bony defects," *Addit. Manuf.*, vol. 46, p. 102194, Oct. 2021.
- [47] J. S. Cuellar, G. Smit, P. Breedveld, A. A. Zadpoor, and D. Plettenburg, "Functional evaluation of a non-assembly 3D-printed hand prosthesis," *Proc. Inst. Mech. Eng. Part H J. Eng. Med.*, vol. 233, no. 11, pp. 1122-1131, Nov. 2019.
- [48] H. Bikas, A. K. Lianos, and P. Stavropoulos, "A design framework for additive manufacturing," *Int. J. Adv. Manuf. Technol.*, vol. 103, no. 9-12, pp. 3769-3783, Aug. 2019.
- [49] S. Yang, Y. Tang, and Y. F. Zhao, "Assembly-Level Design for Additive Manufacturing: Issues and Benchmark," in *Volume 2A: 42nd Design Automation Conference*, 2016, pp. 1-13.
- [50] A. Rias, C. Bouchard, F. Segonds, B. Vayre, and S. Abed, "Design for Additive Manufacturing: Supporting Intrinsic-Motivated Creativity," in *Emotional Engineering*, Vol.5, vol. DS 84, Cham: Springer International Publishing, 2017, pp. 99-116.
- [51] S. Hällgren, L. Pejryd, and J. Ekengren, "(Re)Design for Additive Manufacturing," in *Proceedings of the 26th CIRP Design Conference*, 2016, vol. 50, pp. 246-251.
- [52] G. Sossou, F. Demoly, S. Gomes, and G. Montavon, "An Assembly-Oriented Design Framework for Additive Manufacturing," *Designs*, vol. 6, no. 1, p. 20, Feb. 2022.
- [53] H. Rodrigue and M. Rivette, "An Assembly-Level Design for Additive Manufacturing Methodology," in *Proceedings of IDMMME*, 2010.

- [54] A. Gatto, L. Iuliano, F. Calignano, and E. Bassoli, "Electrodischarge drilling performance on parts produced by DMLS," *Int. J. Adv. Manuf. Technol.*, vol. 58, no. 9-12, pp. 1003-1018, Feb. 2012.
- [55] N. Meisel and C. Williams, "An Investigation of Key Design for Additive Manufacturing Constraints in Multimaterial Three-Dimensional Printing," *J. Mech. Des.*, vol. 137, no. 11, Nov. 2015.
- [56] M. Ochoa, J. Zhou, R. Rahimi, V. Badwaik, D. Thompson, and B. Ziaie, "Rapid 3D-print-and-shrink fabrication of biodegradable microneedles with complex geometries," in *2015 Transducers - 2015 18th International Conference on Solid-State Sensors, Actuators and Microsystems (TRANSDUCERS)*, 2015, pp. 1251-1254.
- [57] J. Jiang, X. Xu, and J. Stringer, "Support Structures for Additive Manufacturing: A Review," *J. Manuf. Mater. Process.*, vol. 2, no. 4, p. 64, Sep. 2018.
- [58] H. Hassanin, F. Modica, M. A. El-Sayed, J. Liu, and K. Essa, "Manufacturing of Ti-6Al-4V Micro-Implantable Parts Using Hybrid Selective Laser Melting and Micro-Electrical Discharge Machining," *Adv. Eng. Mater.*, vol. 18, no. 9, pp. 1544-1549, Sep. 2016.
- [59] A. T. Beaucamp, Y. Namba, P. Charlton, S. Jain, and A. A. Graziano, "Finishing of additively manufactured titanium alloy by shape adaptive grinding (SAG)," *Surf. Topogr. Metrol. Prop.*, vol. 3, no. 2, p. 024001, Apr. 2015.
- [60] N. E. Uzan, S. Ramati, R. Shneck, N. Frage, and O. Yeheskel, "On the effect of shot-peening on fatigue resistance of AlSi10Mg specimens fabricated by additive manufacturing using selective laser melting (AM-SLM)," *Addit. Manuf.*, vol. 21, pp. 458-464, May 2018.
- [61] R. E. Williams and V. L. Melton, "Abrasive flow finishing of stereolithography prototypes," *Rapid Prototyp. J.*, vol. 4, no. 2, pp. 56-67, Jun. 1998.

PART 1.

ON DESIGNING WITH 3D PRINTING





A REVIEW ON 3D PRINTED NON-ASSEMBLY MECHANISMS

Additive Manufacturing (AM) or 3D printing has enabled the production of increasingly complex parts that are difficult to produce with conventional manufacturing methods. Its additive nature has made it possible to create interlocking parts in a single production step. This creates opportunities for new ways of designing and producing mechanisms, which do not need to be assembled after production, called non-assembly mechanisms. Non-assembly mechanisms are different from traditional mechanisms, since they show an unprecedented integration between geometry, material and structure. In this review, by means of a systematic literature search the current state-of-the-art of non-assembly mechanisms is reviewed and analyzed based on the challenges encountered in their design and production. The found examples were categorized according to types of mechanism that have similar production considerations. Per category is discussed what the challenges and opportunities are for the design of non-assembly mechanisms. This review aims to provide a helpful overview of best-practice examples that can be used as inspiration for further development of innovative non-assembly mechanisms.

Published as:

K. Lussenburg, A. Sakes, P. Breedveld, Design of non-assembly mechanisms: A state-of-the-art review, Addit. Manuf. 39 (2021) 101846.

2.1 INTRODUCTION

Additive Manufacturing (AM) or 3D printing is changing the way products are designed and manufactured. Recent developments in the quality and resolution of 3D printers have made AM a viable production method for parts and products, instead of only being used for prototyping. This has led to an increased interest in using AM for the production of functional assemblies.

Traditionally, most products can be seen as a collection of individually fabricated parts, which are subsequently assembled into a working product. The assembly step can take up a lot of time and costs. Improvements to this step can be made by designing parts optimized for assembly [1]. AM offers opportunities in this respect because no compromises have to be made to simplify parts for assembly, instead they can be optimized for their function, provided they take the design considerations for the specific AM process into account [2].

Two of the most common ways in which AM can contribute to the design of mechanical assemblies, is by considering an assembly as a collection of parts that either form 1) a rigid structure or 2) a movable mechanism [1]. In the case of a rigid structure, assembly is necessary because there is no efficient way to produce it as a whole, for instance due to limitations in materials, production techniques or costs. Although they consist of separate parts, they require stiffness and rigidity between the part connections [1]. For example, a table can be seen as a structural assembly, since the table top and the legs are often produced separately, consisting of different materials and made with different production processes. However, the end result functions as one product. The shape complexity offered by AM can eliminate some of these production limitations by combining multiple, separate parts, into one complex-shaped part; resulting in a reduction of the number of components [3,4]. This process is known as “part consolidation”, for which numerous design guidelines exist [3–8].

Moveable mechanisms, on the other hand, require assembling of multiple parts because there is a need for movement between the parts [1]. Traditionally, this has been achieved by separately fabricating parts with carefully measured out tolerances, and subsequently assembling them into a mechanism. AM has also brought new possibilities for the production of movable mechanisms. There are three different ways to produce movable mechanisms by AM. First, using a traditional approach, in which separate components are produced and afterwards assembled, resulting in the same workflow as for mechanisms produced by conventional manufacturing [9]. Second, using embedded assembly, in which one or more components, often of an electronic nature, are incorporated into the 3D printed part, while it is still being produced [10]. An example of embedded assembly is integrating batteries or motors in 3D printed robots [11,12]. Finally, in non-assembly 3D printing, fully functional assemblies or mechanisms are produced in a single production step [10,13]. These 3D printed mechanisms are functional immediately out of the 3D printer, although still some post-processing steps may be required, such as to remove support material [12,14–17].

In the past two decades, many examples of non-assembly mechanisms have appeared.

Often the term non-assembly is used to refer to multi-body mechanical assemblies [10]. However, any mechanism that is manufactured without an assembly step can be considered non-assembly. This includes mechanisms which do not need to be assembled by design, such as compliant mechanisms, which are monolithic structures consisting of only one part [18]. This shows that mechanisms do not necessarily need to consist of different parts, as long as they are able to transfer or transform motion [18]. Therefore, in this paper non-assembly mechanisms include all 3D printed devices that allow motion within their system, and can be produced in a single production step.

Designing non-assembly mechanisms requires re-thinking the way we design and manufacture traditional mechanisms. Specially developed design methodologies for AM have tried to come up with design guidelines to help with this [19-21]. These methodologies are often driven by the functionality of the mechanism, which in turn leads to the geometric design, material choice and specific AM process selection [5]. For the latter, additional models have been proposed that can be helpful for designers to select the most suitable AM process for their design [22-24], or to optimize the settings of the chosen AM process with respect to factors such as dimensional accuracy and mechanical properties [25]. However, these methodologies offer little to help designers and engineers navigate the immense design space that is provided by AM [19-21]. The recent interest in producing multi-functional, complex systems that are operational straight out of the 3D printer shows that there is already a lot of knowledge to overcome the most common AM challenges. Therefore, in this review we provide an overview of the current state-of-the-art of non-assembly mechanisms, with a focus on design solutions and production considerations to create fully functional designs. We categorize and analyze the mechanisms based on the described design challenges and design opportunities.

2.2 LITERATURE SEARCH METHOD

A systematic literature search was performed using the Scopus and the Web of Knowledge databases on the topic non-assembly 3D printed mechanisms. The search query consisted of three categories of keywords:

1. related to the production method: 3D print*, additive manufactur*, rapid manufactur*;
2. related to the way of producing: non*assembl*, print-in-place, assembl* free, without assembl*, fully assembled, monolithic, compliant, direct fabrication;
3. related to the product class: mechanism*, mechanical assembly, robot*, machine, joint*, device*.

The search was limited to articles in English, with no restrictions on the subject area or date, resulting in 744 articles from both databases. After eliminating duplicates, the scientific articles were selected on a number of eligibility criteria. For the production method, AM methods were accepted that can be used on a macro-scale, this excludes lithography

and direct writing methods related to the production of nanoscale sensors. Bio-printing methods were also excluded. Titles and abstract were scanned to select the articles in which a physical mechanism was created by means of non-assembly AM, and for which AM was also the intended production method. This excludes mechanisms for which 3D printing is merely the prototyping method and not the main production method. In addition, the designed mechanism itself needed to be 3D printed, not only casings or frames. From the selected articles, the references were scanned for additional relevant articles that were not found by the query. In the end, 84 articles on non-assembly mechanisms were analyzed with respect to the design and production considerations for this review.

2.3 CLASSIFICATION

The selected examples of non-assembly mechanisms span a wide range of different AM processes. Although each AM process has its own specific production guidelines, as is the case with every manufacturing process, there are a number of design considerations that are similar for all AM processes [2,26,27]. For example, maximum overhang angles, the need for support structures, and optimized build directions are all AM-specific production considerations. These will inevitably influence the design process for non-assembly mechanisms as well. Therefore, it is possible to cluster them into groups for which similar design challenges apply and similar design solutions can be used. The classification is visualized in Figure 2.1. Three main categories have been distinguished that are representative for AM non-assembly mechanisms: 1) geometry-based mechanisms, 2) material-based mechanisms, and 3) pattern-based mechanisms. Geometry-based mechanisms are a group of mechanisms where the functionality of the mechanism relies foremost on the geometry of the structure, which can be accomplished by using multiple bodies, such as for traditional mechanisms, or a single body, such as for compliant mechanisms. Material-based mechanisms are a group of mechanisms in which the material is predominantly responsible for the functionality of the mechanism, making use of either a single flexible material or a flexible material combined with other (rigid) materials. Pattern-based mechanisms describe a group of mechanisms for which a pattern or repetition of a simple base unit is responsible for the functionality of the mechanism. In the following sections, examples of non-assembly mechanisms per category are discussed, focusing on the encountered design and production challenges and the identified design opportunities.

2.4 GEOMETRY-BASED MECHANISMS

2.4.1 Multi-body

Design Challenges

Multi-body mechanisms closely resemble the design of ‘traditional’ mechanisms, since they consist of separate parts. The clearances between the separate parts are challenging for most 3D print processes. Therefore, design solutions are necessary to create functional

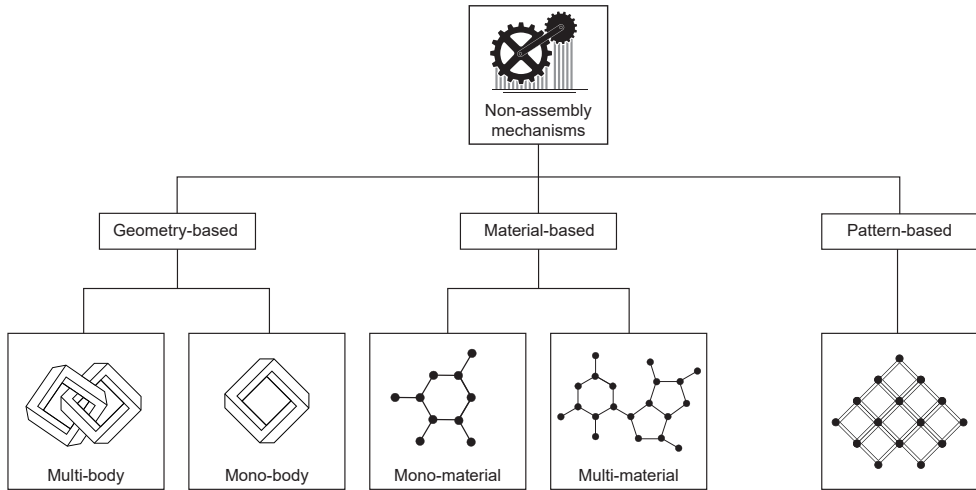


Figure 2.1: Classification of non-assembly mechanisms based on groups for which similar design challenges apply. Geometry-based is a group of mechanisms where the functionality relies foremost on the geometry of the structure, material-based is a group of mechanisms in which the material is dominant for its functionality, and pattern-based is a group of mechanisms where a pattern of a simple base unit is responsible for its functionality.

mechanisms. Table 2.1 summarizes the challenges for multi-body mechanisms and their proposed solutions.

Support structures are often necessary when designing multi-body mechanisms, since the bodies are separated from each other and cannot be printed in the air without support. The use of support structures has undesirable side effects: removing support material requires an extra post-processing step, the area underneath the support structures usually has a diminished surface quality, and support structures require additional material that often cannot be reused. In addition, for complex geometries it can become difficult to create sufficient room for access to remove all support structures. Therefore, to allow for removal of the support material, the geometry should be designed as open as possible [16,28,31], or specific holes for the release of support should be integrated in the design [32].

The surface finish of AM parts can be of poor quality, because of the ‘staircase effect’ caused by the layered print process, the relatively low resolution of 3D printers, and the presence of support material that is locally fixed to the surface. Poor surface quality can hinder the movement of joints, especially in the case of full surface contact. The ‘staircase effect’ can be lessened by using angular geometric shapes instead of round and organic shapes, as was illustrated by the design of a rectangular prismatic joint [13], or by reducing the angle on overhanging geometry [17]. Reducing the surface contact between moving parts by using protrusions in the surface or markers and dents can negate the effects of poor surface quality [29,30,32,35], as shown in Figure 2.2. Surfaces that interact with each other should ideally be kept free from support material in order to maintain the best pos-

Table 2.1: Challenges, general solutions and design solutions for the design of multi-body mechanisms, with corresponding references proposing/applying the solution.

Challenge	Solution	Design solution	Reference
Support structures	Prevent support structures	Reduce overhang angle	[17]
		Decrease clearances	[13]
	Allow support removal	Increase clearances	[16][28]
		Increase spacing between bodies	[16]
		Add features such as chamfers	[29][30]
		Use open geometry	[16][28][31]
		Add drainage/release holes	[32][33][34]
Surface finish	Reduce surface contact	Add protrusions/markers & dents	[30][29] [32] [35]
	Prevent ‘staircase’ effect	Reduce overhang angle	[17]
		Use rectangular geometric shapes in favor of organic ones	[13]
	Prevent supports	Keep interacting surfaces free from supports	[28]
Consider the build direction	Change the build direction to suit the design	[28][29] [33] [34]	
Clearances	Adjust geometry	Add markers and dents	[31][32][33] [35][36]
		Change main hinge shape	[17][37][13] [38] [32][39]
		Scale entire mechanism up	[16]
Strength	Adjust geometry	Optimize cross-section for the direction of movement	[28]
	Consider the build direction	Change the build direction to suit the design	[29][40]

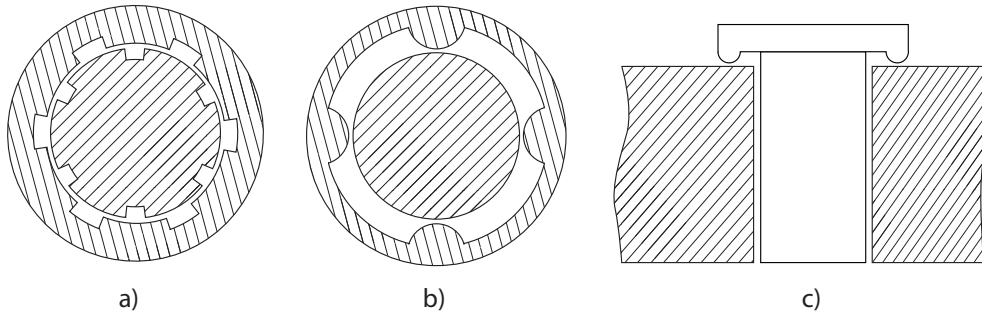


Figure 2.2: Markers and dents can be added to the inside of a pin joint to obtain a smaller clearance and negate the effect of poor surface finish, by reducing the amount of surface contact. a) Top view of a marker-dent construction within the pin-joint, adapted from [35]. b) Top view of a marker-dent construction within the pin-joint, adapted from [32]. c) Side view of protrusions underneath the top of the pin, adapted from [29,30].

sible surface finish [28]. In addition, rolling joints are less sensitive to poor surface finish as compared to sliding joints [28].

A small clearance can make a mechanism more accurate, but it might cause parts to fuse together while printing. A larger clearance can lead to less accurate movement in the final mechanism [37,41]. By changing the geometry of adjacent surfaces, it is possible to obtain the advantages of minimal clearances while preventing complete fusion. Adding markers and dents to moving surfaces is a successful strategy [31,32,35,36]. In this case, the clearance can be chosen slightly smaller than the minimum clearance needed to prevent fusion. After the markers and dents fuse while printing, there is only a small overlap of material which can easily be broken apart, Figure 2.2. Since the minimal clearance is a fixed value per AM process, Jansen et al. [16] noted that by scaling the entire mechanism up, the influence of clearances will be relatively smaller. However, scaling the design of an entire mechanism will also result in scaling of the clearance between the parts. Therefore, Li et al. [41] set up a parametric design to enable scaling of revolute, prismatic, spherical and gear joints. This enabled them to scale all parts of the mechanism up or down, while making sure the clearance remained at the same minimum value given the used 3D print process. Because of the layer-wise construction of AM, parts tend to have anisotropic properties. The chosen build direction is of large influence on the resulting strength of the parts [29]. Especially for moving parts, care should be taken to choose the best build direction and cross-section in order to obtain optimum strength [28].

Design opportunities

Design guidelines and best practice examples can be useful when designing multi-body mechanisms, in order to make sure the design is attuned to the specifications of the chosen AM process. Cuellar et al. [28] give a list of ten guidelines to keep in mind when designing non-assembly mechanisms for FDM printing. Their guidelines were applied to the design of a low-cost prosthetic hand for developing countries. The mechanism in the prosthetic

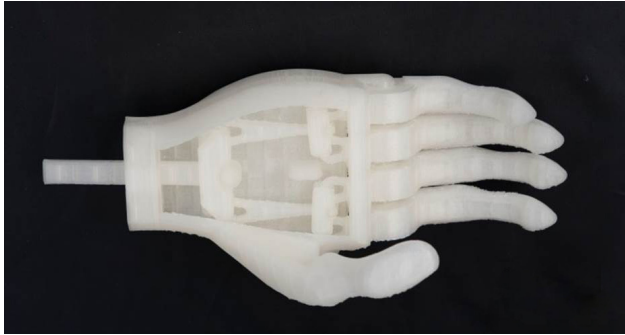


Figure 2.3: Prosthetic hand with a non-assembly mechanism. Although the mechanism has large clearances, the joints automatically align because of the driving force [19].

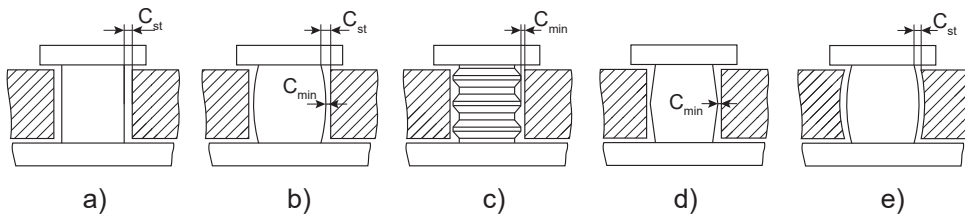


Figure 2.4: Different proposed shapes for a pin-joint in order to minimize the clearance in the mechanism. a) A standard pin joint shape with standard clearance (C_{st}). b) A drum-shaped pin-joint in which the minimum clearance (C_{min}) is smaller than the standard clearance. c) A worm-shaped pin-joint. d) A drum-shaped pin-joint with a sharp transition. e) A drum-shaped pin-joint with a constant clearance. Adapted from [17,30,37-39,43].

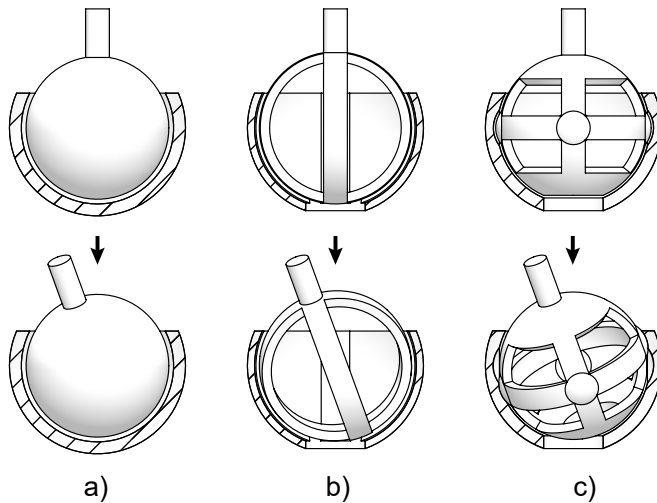


Figure 2.5: Examples of non-assembly ball joints. a) A regular ball joint. b) Design of a ball joint with open structure and ridges in order for it to be possible, adapted from [31]. c) Design of a ball joint with open structure and marker-dents in order for it to be possible, adapted from [36].

hand was designed with large clearances to be easily printable, but when activated by the driving force the joints automatically align (Figure 2.3). This way they were able to create a functional adaptive prosthetic hand, specifically optimized for 3D printing. Sossou et al. [34] propose a design methodology, which starts from the conceptual design of the product as an input. According to them, the functional constraints should be incorporated into the design context by means of an extensive functional analysis, while keeping in mind the constraints from the AM processes. By considering clearances, printing configurations, build direction and accessibility to clearances, the position of each component and their geometry can be finalized.

The design of multi-body mechanisms often starts with the design of a single joint [13]. Best practice examples for multi-body joints include revolute joints [17,30,32,38,39,42], ball joints [13,31,36], and universal joints [29,30,37,43]. Revolute joints and universal joints both make use of pins. Altering the shape of the pin can ensure proper movement within the joint, without hindering the printability or the removal of supports. Figure 2.4 shows a number of different pin shapes that have been proposed [16,17,30,37–39]. The goal is to design the pins with minimal clearance in the joint, while simultaneously allowing for support material to be removed and preventing the joint from fusing. Adding chamfers or fillets to the edges of the joint creates as much space as possible for the removal of support material [29,30]. A drum-shaped joint (Figure 2.4b) has proven a good alternative for a pin-shape [30,37,38]. The minimum clearance is determined by the widest part of the drum, which reduces instability, while leaving enough space to remove support material on both ends. 3D printed drum-shaped joints have been shown to achieve smaller clearances than regular pin joints [30], as well as more uniform stress distribution and lower stress concentrations [38]. Wei et al. [39] took the drum-shape a step further and proposed a worm-shaped joint (Figure 2.4c), which showed less axial movement than the drum-shape when subjected to an asymmetrical load. A cross-shaped pin instead of a round one has been shown to facilitate in the removal of support powder, although the cross-shaped pin rotates less smoothly than the round pin [16].

Non-assembly ball joints have been designed for joints that are posable in any position [31,36,44], as shown in Figure 2.5. By creating an open structure, the support powder used in the AM process can be drained. Markers and ridges were added in the ball joint to create sufficient friction for the joint to assume any pose, while simultaneously preventing fusion of the surfaces during printing.

An example of a ‘joint-centered’ design process was shown by Jansen et al. [16]. They redesigned a ‘Strandbeest’, a robotic walking mechanism, to be non-assembly 3D-printable (Figure 2.6). Since they felt existing guidelines for design for AM were not sufficient for their mechanism, their process was one of trial-and-error, starting from the joints. By adjusting and testing multiple small sections of the mechanism first, they were able to optimize the design and functioning of the joints, before applying them in the complete mechanism.

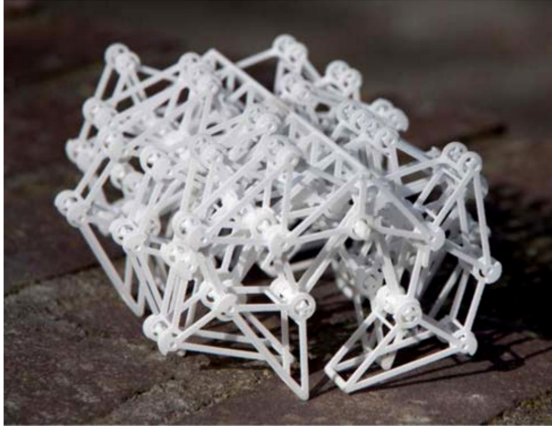


Figure 2.6: A non-assembly ‘Strandbeest’, a mechanical walking robot, by Jansen et al. [16].

2.4.2 Mono-body

Design Challenges

Challenges related to the design of mono-body mechanisms are summarized in Table 2.2. Mono-body mechanisms often suffer from limited mobility, due to rigidity of the material. By increasing the length of the flexural part of a hinge, it is possible to create a large displacement joint. Spirals and helices are an ideal shape for this, since they can have long flexural members, while maintaining a compact size. Scarcia et al. [45] optimized the design of a spiral torsion spring to obtain a deflection/bending angle of up to 90° , as illustrated in Figure 2.7a. Mirth [47] proposed a tri-spiral hinge, shown in Figure 2.7b, which is self-centering due to its structure. The design of the hinge allows multiple links to be stacked on top of one another with a connecting core, creating 2D-layered mechanisms that can be printed without support on an FDM printer. Different bending angles can be obtained by means of adjusting the core diameter, spiral angle, pitch and thickness. Bending angles of up to 180° were developed this way, although the authors noted that the joints limited to 90° were most stable.

A major disadvantage of increasing the range of motion of flexural joints is parasitic motion, which is out-of-plane, unwanted motion. To combat this, Tavakoli et al. [49] suggest avoiding elastomeric materials in favor of more rigid materials, since it is easier to control their bending direction. Mirth [50], Zhang et al. [52] and Tan et al. [51] have shown that by applying symmetry or by mirroring the geometry, parasitic motion can be reduced. Geometrical restrictions can be built into the design of a joint in order to ensure its stability [45,53]. Hu et al. [53] developed a flexible joint for snake-like instruments. A helical structure is used to obtain the mobility needed for a bending motion, while rolling contacts are added in the helix to prevent undesirable compression (Figure 2.7c). Merriam et al. [46] designed a pointer mechanism for use in space applications (Figure 2.8). In order to maintain a suitable range of motion, a thin, long flexure was used for the joints. For their application it was important that the mechanism had high precision and reliability. To achieve this, they made the structure surrounding the flexures as rigid as possible,

Table 2.2: Challenges and design solutions for mono-body mechanisms, with corresponding references proposing/applying the solution.

Problem	Design solution	Reference
Limited mobility	Increase flexure length	[45][46][47][48]
Parasitic motion	Avoid elastomeric materials	[49]
	Mirror the geometry/apply symmetry	[50][51][52]
	Design geometric restrictions	[45][53]
	Replace serial mechanisms with parallel mechanisms	[51][45]
	Increase structural stiffness of connecting structure	[46]
Support structures	Decrease overhang angle	[46][54][55]
	Scale part down	[53]
	Choose appropriate build direction	[55]
Poor fatigue life	Provide a uniform stress distribution	[53]
	Avoid motion in the plastic region of the material	[51]
	Choose appropriate build direction	[53] [51]
Limited material options	Adjust geometry according to material properties and choose suitable joints	[50][47][48]

which has been found to significantly improve the precision by reducing parasitic motion [46,56].

The need for supports is less of a problem for mono-body mechanisms than it is for multi-body mechanisms. However, supports can still be undesirable. Decreasing the overhang angle is the most effective way to reduce the need for supports [46,54,55]. For mechanisms that are sufficiently small, support material may not be necessary. An example is the flexible helix joint designed by Hu et al. [53]. They found that due to the small size of the helix, the helix could be printed without support, with only a small deformation. This deformation was small enough not to affect the functioning of the joint.

The fatigue life of flexural parts is directly influenced by the positioning on the build

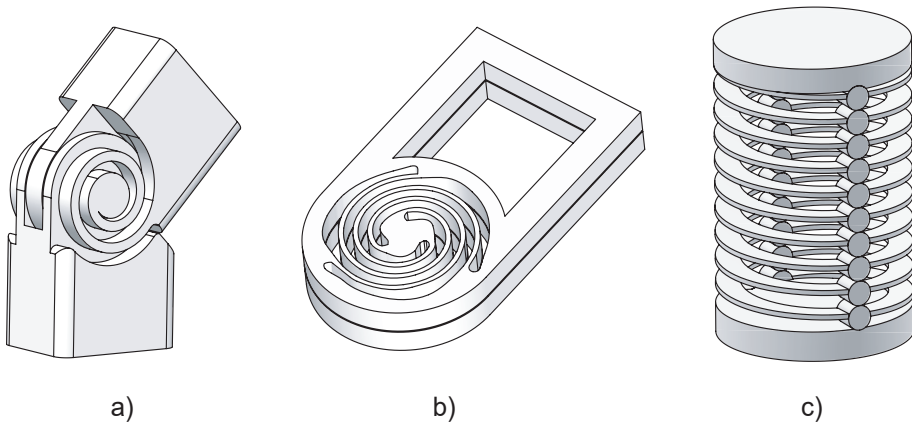


Figure 2.7: Examples of mono-body hinges. a) Spiral torsion spring, based on [45]. b) Tri-spiral hinge, based on [47]. c) Helical joint with rolling contacts, based on [53].

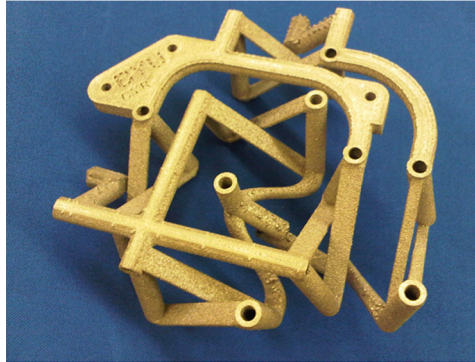


Figure 2.8: Design of a pointer mechanism for space applications by Merriam et al. [46]

plate [51,53]. Ideally, all flexure parts should be located in planes parallel to the build plate, in order to ensure that the stress of bending will be carried by the material itself instead of by the inter-layer adhesion [51]. This will provide the optimal strength to the mechanism, even if this would mean that more support material is necessary. Additionally, for the longest life cycle, motion in the plastic region of the material should be avoided [48,51]. Bai and Rojas [57] tested two versions of a compliant joint based on a cross-four-bar-linkage for a prosthetic finger. In order to mimic human joints, they added a contact surface in one instance and gear teeth in the other. A finite element analysis showed that the maximum stresses in the teeth-guided joint were 55% less than in the contact-aided joint, meaning that the gear teeth aided in distributing forces from the flexible compliant links.

Although the materials options for AM are increasing rapidly, there are still limited options to choose from. For mechanisms with flexural parts, it is important that the used material has a certain flexibility and is not too brittle [50]. The best way to create joints and flexural elements is to adjust the geometry according to the material properties [47,48,50]. Mirth [47,50] has shown that longer beam-type flexural elements can success-

fully be used for more brittle materials.

Design opportunities

Mono-body mechanisms are generally more difficult to produce with traditional manufacturing techniques than with AM [58]. However, they have many advantages, such as frictionless motion [45,46,51,58], fewer parts [58], and affordability [45,51,59]. Since there are no clearances for mono-body mechanisms, it is possible to generate a smooth displacement and an accurate, predictable range of motion [51,60]. Especially in the medical domain, this can be a great advantage. Zanaty et al. [61] designed a multi-stable device that can be used to puncture the retinal vein in the eye. Since this vein is extremely small, it is nearly impossible for a surgeon to accurately puncture inside the vein. The mono-body mechanism of Zanaty et al. [61] can be pre-programmed to specific puncture distances, eliminating the need for any force or displacement from the surgeon. Krieger et al. [62] showed that their monolithic robotic gripper could follow a predefined path. The structure they designed consists of solid segments, connected by thin flexure hinges. By changing the geometry of the contact surfaces between the solid segments from flat to an interlocking structure, a predefined end pose could be enclosed within the geometric design of the gripper.

Another advantage of mono-body mechanisms is the possibility of creating small sized or scalable mechanisms, which can be created without taking clearances into account [45,59]. Salem et al. [59] designed a microbiota sampling capsule, which needed to be small enough to be able to travel through the entire gastrointestinal tract. The capsule contains a small sponge, which, once in contact with liquids, swells and activates a bi-stable 3D-printed mechanism. The bi-stable mechanism closes the capsule, safely sealing in a microbiota sample.

2.5 MATERIAL-BASED MECHANISMS

For material-based mechanisms, a flexible material is used for the required mobility. The flexible material can be used for the entire mechanism, or in combination with other, of-

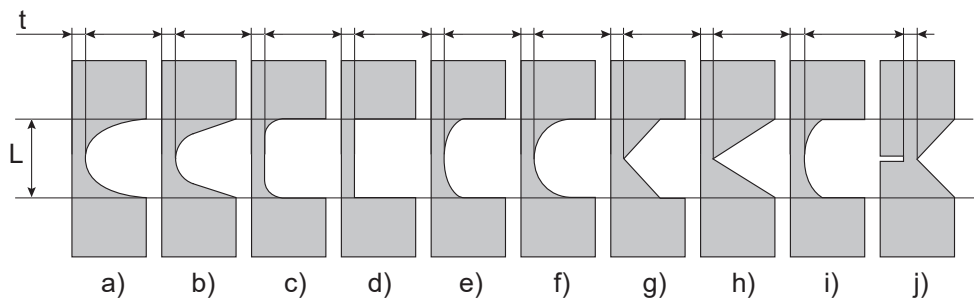


Figure 2.9: Side view of flexible hinges used in prosthetic fingers, with equal hinge thickness (t) and hinge length (L), the only difference is in hinge geometry. Adapted from Liu et al. [64] (a-i), Mutlu et al. [71] (a, c, f) and Zhou et al. [63] (j).

Table 2.3: Challenges and design solutions for material-based mechanisms, with corresponding references proposing/applying the solution.

Challenge	Design Solution	Reference
Limited mobility	Position hinge in the middle of the joint instead of at the edge	[63]
	Adjust hinge geometry	[63][64]
	Use functionally graded materials	[65]
Low rigidity/stiffness	Use multiple layers	[66][67]
Parasitic motion	Add elastomeric constraints	[68]
	Use appropriate cross-section	[69]
	Shorten length of hinge	[69]
Spring behavior	Add a negative stiffness counterbalance	[70]
Poor inter-material adhesion	Add a material gradient	[66]

ten rigid, materials. The challenges associated with the use of flexible materials are summarized in Table 2.3.

2.5.1 Mono-material

Design challenges

Hinges for the design of monolithically fabricated prosthetic fingers have been extensively researched with regards to their range of motion [63,64,71]. These non-symmetrical notch-type hinges allow for a bending motion with one degree of freedom, mimicking the motion of a real finger, as shown in 2.9. Liu et al. [64] compared nine different geometric shapes for the flexure hinges, which they 3D printed and tested for bending performance (9 a-j). Mutlu et al. [71] compared three different geometrical shapes by experimental testing of 3D printed models and by FEM analysis (2.9 a, c, f). Although Liu et al. [64] and Mutlu et al. [71] used the same 3D printing process and a similar material, their results differ. According to Mutlu et al. [71], an elliptical hinge shape showed the best bending angle, while Liu et al. [64] concluded that rectangular-shaped notches had the best bending angle. The difference in result may be due to the testing method: Liu et al. [64] used a tendon-driven testing set-up where a weight was connected to the tendon wire at a perpendicular angle, while Mutlu et al. [71] applied a force directly to one end of the hinge at an

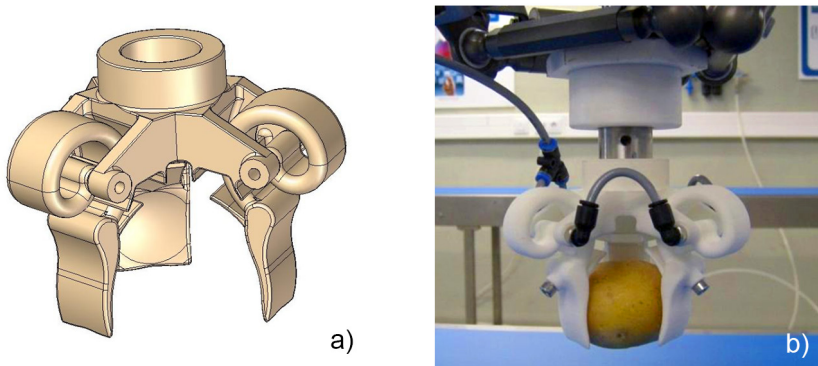


Figure 2.10: An example of a mono-material pneumatic gripper, utilizing a spiral-shaped air chamber and rotational links. a) CAD-model of the pneumatic gripper. b) The 3D printed prototype [48].

angle smaller than 90 degrees. Zhou et al. [63] considered only one flexure hinge geometry, but instead of placing the flexure hinge towards the edge of the joint, they positioned it towards the middle of the joint, as shown in 2.9j). While still maintaining a non-symmetrical bending motion, they reported that it provided a greater bending displacement, as well as a reduced chance of buckling.

The hinge designs shown in 2.9 have only one degree of freedom. When it is necessary to have two degrees of freedom, the flexural part of the joint needs to be slender in two directions, creating a fragile part in the joint and increasing the chance of parasitic motion. Zhou et al. [63] solved this for their opposable thumb design by using two consecutively placed one degree of freedom joints with slightly different bending axes to create the required range of motion. In order to combat the parasitic motion in their surgical end-effector, Johnson et al. [69] designed the flexible hinges with a cross-section that only allows deflection in a single plane. In their case this was a rectangular cross-section. In addition, by limiting the length of the flexible members they were able to reduce parasitic motion.

Low rigidity is one of the side-effects of using a flexible material. Liu et al. [72] used this to their advantage for a compliant finger designed to grasp fragile objects, since they found the finger could deform easily around objects, creating an increased contact region. Zhu et al. [66] designed a pneumatically driven robotic finger, in which they used the principle of layer jamming, in which multiple layers are pressed onto one another to create the required stiffness. Similarly, Mutlu et al. [67] integrated an extra wall into their pneumatic soft gripper to adjust the stiffness.

Design opportunities

The advantage of mono-material mechanisms compared to mono-body mechanisms, is their ability to achieve a greater range of motion in less space with a simpler geometry [69,73]. As a result, they can be produced in smaller size ranges [74]. Flexible materials have also proven to be useful for pneumatically actuated grippers, since soft materials are able to conform to the contours of an object [75]. AM makes it possible to design pneu-

matic actuators with a controlled bending motion by means of local changes in geometry. For mono-material mechanisms, this can be achieved by alternating straight sides, with sides with a bellows-like structure that is able to expand [75–77]. Mutlu et al. [67] created two pneumatic ‘fingers’ actuated by one central bellow that can exhibit bending motion. In these fingers an extra wall was added, perpendicular to the bending direction, which increased the bending stiffness and the gripping force of the gripper. Blanes et al. [48] presented a number of different pneumatic actuators utilizing air chambers and rotational links to obtain controlled motion for food grippers (Figure 2.10). They were successful in creating helical, spiral-shaped and bellows-shaped air chambers, which combined with rotational links created linear, rotational, and mixed motion.

2.5.2 Multi-material

Design challenges

The options for multi-material printing are limited to the available printers that can print multiple materials, and the available materials themselves. The most utilized combination of materials is the combination of two polymers, a rigid and a flexible one [68–70,73,78,79]. A combination of metals has also been used [65], as well as a flexible polymer combined with a magnetic-particle polymer composite [80].

It seems intuitive that the area of a multi-material structure that is most likely to fail is the border between the flexible and rigid material. However, Sakhaei et al. [73] found that for their ratchet-like mechanism this was not the case (Figure 2.11). Instead, failure occurred in the area with highest concentration of stress in the flexible material. They hypothesized that this is due to the fact that both materials were acrylate-based, resulting in a strong chemical bond between the materials since they have a similar base. To facilitate

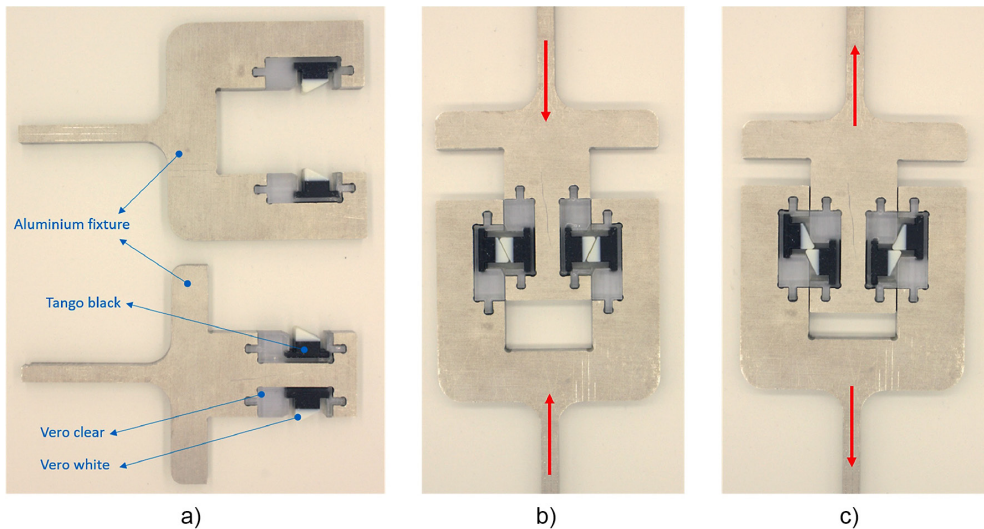


Figure 2.11: Multi-material ratchet mechanism by Sakhaei et al. [73]. a) The testing set-up for the mechanism with an aluminum fixture. b) Initial set-up. c) Locking direction.

proper border adhesion when a chemical bond is not possible, a material gradient can be used between the transition of the materials [69].

One of the properties of all material-based mechanisms is that the hinges will show spring-like behavior due to the elastic properties of the material. This can be an advantage, depending on the application, however, in applications where multiple stable positions are required, this might pose a challenge. In order to combat this, Bruyas et al. [70] designed a statically balanced compliant joint. They combined a mirrored helical structure made of a rigid material, with a core made of an elastic material. In order to create static balance, they added two spring-like elements to the sides, which exhibit bi-stable behavior. This way, they managed to create two stable positions for the joint.

The flexibility of the material can also be a challenge for the functionality of the mechanism. Castledine et al. [81] used multi-material AM to design a flexible segment for a robotic gripper, in which the flexible material was used for the core of the gripper, with rigid disks dispersed along it for guidance of the actuation tendons. However, the core proved to be too flexible to accurately steer the segment. Therefore, in order to create sufficient torsional rigidity, interlocking segments were added to the rigid disks.

Design opportunities

In all examples of multi-material mechanisms, the elastomeric material is used for the joints in the mechanism, while the rigid material provides the structural integrity. The advantage of using an elastomeric material for the joints in multi-material mechanisms is the same as for mono-material mechanisms, with the advantage that the addition of a rigid material makes it easier to increase the required rigidity for other parts of the mechanism. In addition, multi-material AM makes it possible to create functionally graded structures, in which two or more materials are mixed in different ratios to create varying material properties. This was applied by Jovanova et al. [65] to create compliant metal hinges with different bending angles.

Mirth [78] used a sheet metal design approach to create a multi-material mechanism. The mechanism can be printed entirely flat on the print bed, after which it is folded into

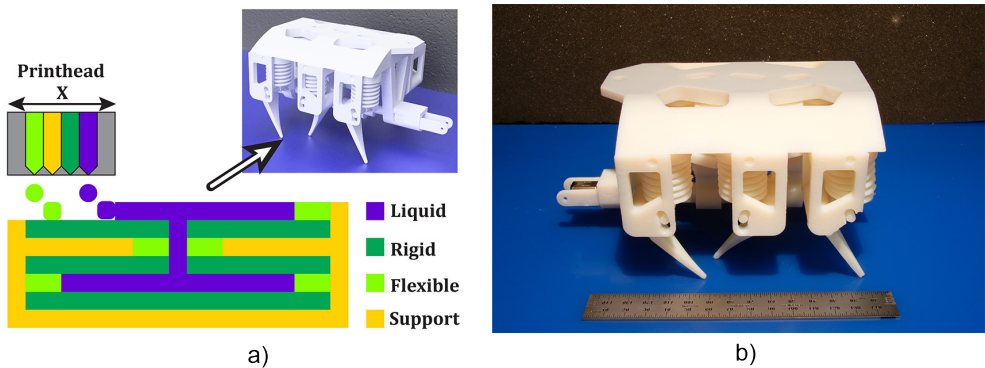


Figure 2.12: Non-assembly 3D printed hydraulic walking robot by MacCurdy et al. [82]. a) Showing the different materials and order in which the bellows were printed. b) The final prototype.

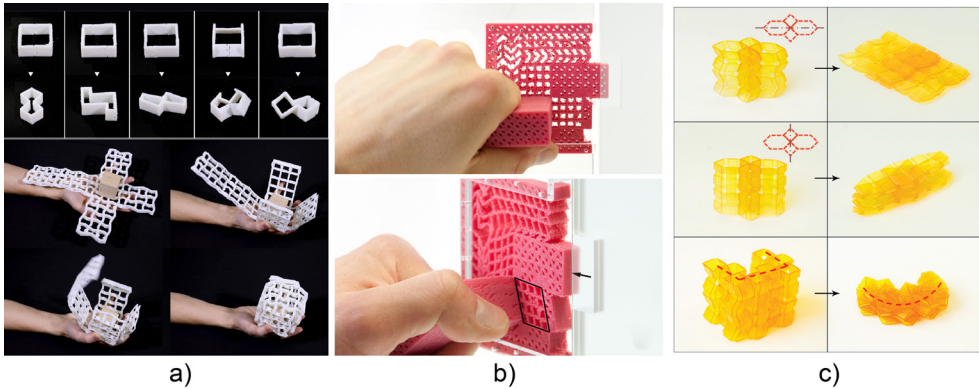


Figure 2.13: Examples of pattern-based mechanisms. a) Five different transforming configurations for a single cell (top), cells applied in a folding box design (bottom) [86]. b) Pattern-based door latch mechanism [84]. c) Different origami-based folding structures, the unfolded structure on the left, folded on the right [89].

its functional shape, much like the production of sheet metal parts. The design consists of a layer of flexible material that forms the base for the hinges, onto which a rigid material is printed for the structural parts. The advantage of this approach is that it significantly reduces the printing time and no support material is required.

Multi-material AM has also been used to create pneumatic and hydraulic mechanisms. The addition of a rigid material has certain advantages over only using a flexible material. MacCurdy et al. [82] adjusted a multi-material Polyjet 3D printer to print non-assembly hydraulic walking robots. To make the robot completely non-assembly, they also printed the hydraulic fluid inside the bellows by using a cleaning fluid provided by the printer manufacturer (Figure 2.12). A mix of materials with varying stiffness was used to create bellows that were flexible enough, but were also able to resist the fluid pressure. Similarly, Skylar-Scott et al. [83] created a pneumatically actuated walking robot by developing a new AM method for multi-material printing in which they could define per voxel which material to use. The walking robot uses both a flexible and rigid material for the air chambers. The flexible material allows the legs to ‘bend’, and because of the rigid material the robot is able to carry a weight of up to eight times its mass.

2.6 PATTERN-BASED MECHANISMS

Pattern-based mechanisms use a relatively simple mechanism as a basic building block, or cell, which is patterned or repeated to obtain a complex transformation. This can be useful to create modular mechanisms that can easily be adapted to different applications or tasks, since they use the same basic mechanism as building block.

Ion et al. [84,85] designed mechanisms inspired by metamaterials that allow for controlled directional movement. Their mechanisms consist of rectangular cells, which can either be rigid, connected by a living hinge, or be able to make a shearing motion. The cells were arranged in rectangular arrays. Alternating shearing, hinged and rigid arrays

resulted in mechanisms such as a door hinge (Figure 2.13b), pliers, and a switch. Ou et al. [86] also used rectangular cells as a basic building block, which they described as four-bar linkages. Placing hinges in different locations on the four sides of the rectangular cell, resulted in scaling, shearing, twisting and bending motions of the single cell, illustrated in Figure 2.13a. By combining and patterning different cell configurations, they were able to create displays with encoded messages, foldable boxes for packaging (Figure 2.13a) and a foldable helmet. Mark et al. [87] used 3D metamaterials with auxetic behavior to design a robot that can climb up and down in a tube. The robot contains one bellow actuator, which is connected to two metamaterial structures: the first behaves like an auxetic material with negative Poisson's ratio, and the other with a similar positive Poisson's ratio. Because of the contraction of the bellow actuator, the materials are either pushed or stretched; alternately taking on the role of anchor or walker. This way the robot is able to crawl up the tube. The two metamaterials were designed in such a way that they have an exact inverse Poisson's ratio. The structure did need supports, therefore the cells needed to be large enough for removal of the support material.

Liu et al. [88] and Zhao et al. [89] took inspiration from origami for their pattern-based mechanisms. Liu et al. [88] adapted a classic origami design, a twisted tower consisting of modular segments, for 3D printing. In the adapted design, the entire structure can be 3D printed as a pre-folded mechanism using multi-material AM, where the flexible material functions as the folds in the paper. The tower can be actuated by cables, and is able to generate linear, bending and twisting motions, making it suitable to function as a robotic arm. Zhao et al. [89] used an origami cube as a basic cell, with flexure hinges located along the edges of the cube. Variations in the configuration and structure of the cubes resulted in different transformations, as shown in Figure 2.13c.

The advantage of pattern-based mechanisms is that it is relatively easy to design the simple mechanism that can be used as the basic cell [90]. For FEM calculations, analyzing one segment requires less computational power than analyzing the entire structure [91]. They can also be adapted easily for different applications. In addition, the basic cell can function as a test-segment to optimize the production settings for 3D printing [92]. However, the real difficulty lies in designing the pattern within the mechanism. Simple functions can be designed by hand, but for more complex mechanisms this becomes a difficult task. Therefore, software programs and models that can generate the pattern based on an input and desired output are particularly useful for pattern-based mechanisms [84–86,90,93].

2.7 SELF-ASSEMBLY

In addition to mechanisms that do not need to be assembled after production, AM has given rise to mechanisms that can assemble themselves after printing. Self-assembling behavior can for instance be obtained by making use of shape-memory materials [94–96]. These materials have the capacity of holding a temporary shape, but will return back to their original shape when subjected to an external stimulus, such as heat [94]. This allows

the mechanism to both assemble and disassemble itself. Another approach is making use of the shrinking behavior of PLA to create self-assembling mechanisms [97,98]. 3D printed PLA shows shrinking behavior along the printing path direction [93], therefore by varying the printing direction within a part it is possible to use the shrinking behavior to design pre-programmed bending. Bending can be triggered by heating the material. A number of interesting mechanisms have been created using this approach, such as compliant forceps [93], chair legs that can lock themselves in place after assembling [93], self-tightening knots [94], and soft grippers inspired by natural tendrils [98]. The advantage of these examples of self-assembling mechanisms is that the starting configuration of the mechanism is often a simple structure that can easily be 3D printed without support structures, whereas the final assembled state would be more complex and difficult to print. In addition, assembly can be triggered whenever it is required [99].

2.8 DISCUSSION

2.8.1 Design solutions for non-assembly mechanisms

The use of AM technologies for the production of mechanisms is still experimental. Therefore, it is always necessary to thoroughly know the specifications of the chosen printing process in order to design a well-working mechanism [34]. Knowing the minimum resolution, overhang angle, minimum wall thickness and material properties is important for the printability of the design. The reviewed literature shows that there are a lot of best practice examples of non-assembly mechanisms, from which design solutions can be extrapolated to be implemented in future designs.

The design of joints is an important part of non-assembly mechanisms [16,17,29,30,32,33,35,37,39,43]. Often a single joint is designed, printed, and tested for its kinematic performance. When the joint is functioning satisfactorily, it is applied in the complete mechanism. However, there are a few downsides to this approach. First, build direction is an important consideration for the functioning of the joint. If the integrated mechanism contains joints at different construction angles, it might mean that the build direction is not the same as for the tested joint, and thus its performance might be affected. Second, integration of the joint into the mechanism may lead to unexpected surprises. For example, Jansen et al. [16] found that the single pin joint they had designed and tested as part of their 3D printed ‘Strandbeest’ worked with minimal clearances. However, when the entire integrated mechanism was 3D printed, it turned out to be impossible to remove all the support material from the joints, because they were blocked by other parts of the mechanism. As a result, the joints needed to be redesigned with larger clearances for cleaning. It is, therefore, important to consider the design of the mechanism as a whole.

With the developments in material suitable for AM, a large number of flexible and elastic materials have become available. These materials have been quickly adopted for the design of joints for typical ‘soft’ applications, such as prosthetic fingers [63,64,71] and soft robotics [66,67,80]. The advantage of a flexible material is that the joint geom-

etry can be less complex and more robust, as compared to mechanisms using only a rigid material. This leads to the possibility of scaling mechanisms down to a smaller size while still being 3D printable. The option to combine multiple materials in a single production step opens the door to a new range of possibilities, such as creating functional gradients between materials. This can be used for instance to control the bending behavior of joints [65], to reinforce transitions between materials, or to create fully functional advanced assemblies, such as the hydraulic robot of MacCurdy et al.[82], in which even the hydraulic fluid was printed. Multi-material AM also shows great potential for creating innovative bio-inspired designs, since in nature a combination between flexible and rigid materials is common.

Metal AM shows great potential for use in both rigid parts and flexures in non-assembly mechanisms. However, only a handful of the examples in this review make use of metal AM [17,37,38,46,53,56,65,100]. This may be because compared to conventional technologies, metal AM processes such as Powder Bed Fusion or Selective Laser Melting have a few distinct disadvantages. First, they leave the part with a relatively rough surface quality, which increases friction and wear on parts with surface-to-surface contact. This is especially problematic for multi-body mechanisms, since the wear on parts during use increases the clearances and can make the mechanism unstable [17]. Since non-assembly mechanisms also cannot be disassembled, most surface finishing processes will not be able to reach the internal surfaces of joints. Second, the resolution of AM metal processes is still quite poor. This makes it difficult to create tight clearances, or flexures that are thin enough to serve as a joint. With advances in AM it is expected that these disadvantages will decrease, although more research into design methods specifically for metal AM will be valuable for a wide adoption of metal AM mechanisms.

Pattern-based mechanisms make optimum use of the shape complexity offered by AM. Their design shows a lot of similarities to the design of metamaterials; structure and material are closely integrated. Further development of the pattern-based design approach could lead to a fusion between designed mechanisms and metamaterials. Technological advances in AM processes in terms of resolution and multi-material options offer many possibilities to create these types of mechanisms on a smaller scale with ever-increasing functionality.

One of the ways to deal with the immense design freedom offered by AM is using computational models and software to aid in the generation of functional mechanisms. As the design of mechanisms becomes more complex, and more components of an assembly are integrated, the more value these tools can add to the design process. Software editors, design tools, and libraries with a standardized selection of functions are being developed to make it easier to design and produce 3D printable mechanisms [84,101,102].

An effective, conventional solution to actuate any mechanism is by using cables to transfer movement from one part of the mechanism to the other. For non-assembly mechanisms, this means the mechanism itself is 3D printed, after which the tendons are manually inserted [49,53,58,63,64,69,71]. This can be a quite laborious process, depending on the complexity of the mechanism. Possibilities of integrating strings into 3D print-

ed parts that have been researched include the use of an embroidery machine as an extra production step [103], or by embedded 3D printing, in which the fibers are added during printing either manually [104] or by adding a fiber extrusion head to an existing 3D printer [105]. Additional research into this area is needed in order to eliminate the final assembly step for tendon-actuated mechanisms.

Self-assembly can be seen as the next step in the development of non-assembly mechanisms, since they can avoid some of the disadvantages associated with non-assembly. For instance, with self-assembly it is possible to print the casing of a mechanism as a flat structure with the required functional components pre-assembled on top, which folds exactly into place after printing, creating an enclosed mechanism without the disadvantages of needing a support structure. This could pave the way for structures that are simple to produce with AM and, after printing, self-assemble into a complex mechanism. In addition, being able to control the exact time when the mechanism assembles and, more importantly, disassembles, could be an enormous advantage, for instance for medical applications.

2.8.2 Advantages and disadvantages of non-assembly mechanisms

Non-assembly mechanisms provide many advantages, the most obvious being a reduction in manufacturing steps for complex products [28], leading to reduced costs. Non-assembly mechanisms lend themselves to being scaled down to sizes where assembly of separate parts is a difficult and tedious process. In addition, complex mechanisms can be produced without considering adjustments for assembly. This can improve reliability and safety, because of an elimination of additional assembly steps [14]. Non-assembly mechanisms have the potential to function instantly after fabrication, which is beneficial for plug-and-play solutions for urgent needs, or in remote locations [14]. Non-assembly also reduces the need for specialized assembly and fine tuning knowledge, reducing the need for training in production facilities and making production more accessible for laypeople [14].

However, there are also a number of disadvantages of non-assembly. In traditional mechanism design, the material choice and production process can be optimized for each part, since they are all produced separately. For non-assembly mechanisms, all parts are made with the same process and often the same material. Since most multi-material 3D printers are not yet capable of using more than two similar materials at the same time, such as two plastics or two metals, compromises in material and geometry have to be made. Even though no assembly after production is necessary, this does not always mean the mechanism is ready to use out of the printer. Usually, one or more post-processing steps, such as removing support material or polishing surfaces, are necessary. Especially removing supports can be a time-consuming process [88].

Since the design of these mechanisms is non-assembly, it also means that they cannot be disassembled. Therefore, replacing or servicing parts is difficult or impossible. Due to the current limited quality of 3D printed parts, this would suggest that currently non-assembly mechanisms are mostly applicable to non-critical products, disposable products or products with a short life span. A possible solution for products that need to be serviceable is printing them partially disassembled, or designing them in such a way that they can

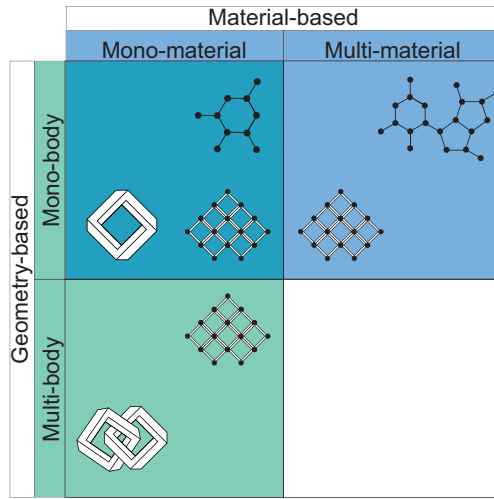


Figure 2.14: This figure shows the combined design space for geometry-based and material-based mechanisms. All examples discussed in this review fall within the blue and green fields. The icons represent the categories as presented in Figure 2.1. The fourth field, of multi-body multi-material mechanisms, remains empty, since no examples were found that fall within this category. This indicates a promising direction for future research.

be (partly) taken apart when necessary [16].

When the disadvantages of the non-assembly approach cannot be ignored for a design, it is always possible to combine this approach with parts that do need to be assembled. This should be a consideration based on the functional concerns, such as the kinematic and strength requirements of a joint, and manufacturing concerns, such as the required clearances and need for support material [33].

2.8.3 Future directions

As can be seen from the examples provided in this review, AM of non-assembly mechanisms is still in its infancy. We can distinguish a trend within our proposed categorization, from more traditional mechanism designs that consist of multiple bodies, to innovative designs that show an unprecedented integration between material, geometry and structure, embracing all opportunities that 3D printing brings.

An interesting perspective can be offered when combining the design opportunities as presented in this review for the category of geometry-based mechanisms and material-based mechanisms, as has been done in Figure 2.14. If we consider that each of the fields in this figure signifies the design space for the given categories, then the examples selected in this review all fall within the blue- and green-colored fields. The figure indicates that the design space for mono-body and mono-material mechanisms is overlapping, which is caused by the fact that there are many variations of flexibility when considering material properties. Depending on the properties of the material, the appropriate design solutions should be chosen.

Pattern-based mechanisms are a special case. Since the building block that they use is in essence a simple mechanism, when zooming in to this level, it can be seen that it is possible to classify the single cell as a geometry-based or a material-based mechanism. An example of a geometry-based cell is given in Figure 2.13a, where rigid-body hinges are used in the cell, and an example of material-based cells is given in Figure 2.13b, where a flexible material is used for the hinge. Therefore, the same design solutions can be applied as for geometry- and material-based mechanisms on a cell level, however for the overall mechanism overarching design solutions are necessary.

The fourth field in Figure 2.14 remains empty, since no examples of mechanisms have been found that combine the design opportunities of multi-body mechanisms with those of multi-material mechanisms. This shows a potential direction for future research. We imagine that inspiration for these kinds of mechanisms can be found in nature. For instance, joints in the human body can be described as multi-body multi-material joints: two rigid, separate bones, for which the movement is controlled or restricted by flexible tendons.

2.9 CONCLUSION

The advances in AM technologies have led to novel ways of creating fully-functional mechanisms that can be created in a single production step. These come with their own challenges for design and production. This review has provided a state-of-the-art of non-assembly mechanisms, in which special attention has been paid to the production challenges inherent to AM and the design solutions used to overcome these. Although each AM process has its own specific limitations and guidelines, from the examples found in literature it can be seen that for certain groups of mechanisms similar problems are encountered regardless of the technology, for which it is possible to use similar design solutions. Therefore, the found examples were categorized according to the type of mechanism to which similar design solutions can be applied. The examples in this review show that it is possible to create a wide range of mechanisms using AM, ranging from the traditional type of multi-body mechanism, to increasingly popular compliant mechanisms and futuristic mechanisms that are able to assemble themselves. The simplified production of non-assembly mechanisms makes them advantageous to use in many applications, such as healthcare and aerospace engineering. In order to continue the development and implementation of non-assembly mechanisms, it is important to pay attention to tools and methodologies that help designers and engineers navigate the immense design space offered by AM.

REFERENCES

- [1] D.E. Whitney, *Mechanical Assemblies; their design, manufacture, and role in product development*, Oxford University Press, New York, 2004.
- [2] H. Bikas, A.K. Lianos, P. Stavropoulos, A design framework for additive manufacturing, *Int. J. Adv.*

REFERENCES

- Manuf. Technol. 103 (2019) 3769–3783. <https://doi.org/10.1007/s00170-019-03627-z>.
- [3] F. Laverne, F. Segonds, N. Anwer, M. Le Coq, Assembly Based Methods to Support Product Innovation in Design for Additive Manufacturing: An Exploratory Case Study, *J. Mech. Des.* 137 (2015) 121701. <https://doi.org/10.1115/1.4031589>.
- [4] N. Boyard, M. Rivette, O. Christmann, S. Richir, A design methodology for parts using additive manufacturing, in: *Int. Conf. Adv. Res. Virtual Rapid Prototyp. (VRAP)*, Port., 2013.
- [5] M.K. Thompson, G. Moroni, T. Vaneker, G. Fadel, R.I. Campbell, I. Gibson, A. Bernard, J. Schulz, P. Graf, B. Ahuja, F. Martina, Design for Additive Manufacturing: Trends, opportunities, considerations, and constraints, *CIRP Ann.* 65 (2016) 737–760. <https://doi.org/10.1016/j.cirp.2016.05.004>.
- [6] G. Jones, E. V. Kline, J. Schmelzle, E.W. Reutzel, T.W. Simpson, C.J. Dickman, (Re)Designing for Part Consolidation: Understanding the Challenges of Metal Additive Manufacturing, *J. Mech. Des.* 137 (2015) 111404. <https://doi.org/10.1115/1.4031156>.
- [7] R. Becker, A. Grzesiak, A. Henning, Rethink assembly design, *Assem. Autom.* 25 (2005) 262–266. <https://doi.org/10.1108/01445150510626370>.
- [8] J. Liu, Guidelines for AM part consolidation, *Virtual Phys. Prototyp.* 11 (2016) 133–141. <https://doi.org/10.1080/17452759.2016.1175154>.
- [9] S. Coros, B. Thomaszewski, G. Noris, S. Sueda, M. Forberg, R.W. Sumner, W. Matusik, B. Bickel, Computational design of mechanical characters, *ACM Trans. Graph.* 32 (2013) 1. <https://doi.org/10.1145/2461912.2461953>.
- [10] J.S. Cuellar, G. Smit, D. Plettenburg, A. Zadpoor, Additive manufacturing of non-assembly mechanisms, *Addit. Manuf.* 21 (2018) 150–158. <https://doi.org/10.1016/j.addma.2018.02.004>.
- [11] K.J. De Laurentis, C. Mavroidis, K.J. De Laurentis, Rapid fabrication of a non-assembly robotic hand with embedded components, *Assem. Autom.* 24 (2004) 394–405. <https://doi.org/10.1108/01445150410562606>.
- [12] K.J. De Laurentis, F.F. Kong, C. Mavroidis, Procedure for Rapid Fabrication of Non-Assembly Mechanisms With Embedded Components, in: *Proc. DETC'02 Proc. DETC'02 ASME 2002 Des. Eng. Tech. Conf. ASME 2002 Des. Eng. Tech. Conf. Comput. Inf. Eng. Conf.*, 2002: pp. 1239–1245. <https://doi.org/10.1115/detc2002/mech-34350>.
- [13] C. Mavroidis, K.J. DeLaurentis, J. Won, M. Alam, Fabrication of Non-Assembly Mechanisms and Robotic Systems Using Rapid Prototyping, *J. Mech. Des.* 123 (2001) 516–524. <https://doi.org/10.1115/1.1415034>.
- [14] Y. Wei, Y. Chen, Y. Yang, Y. Li, Novel Design and 3-D Printing of Nonassembly Controllable Pneumatic Robots, *IEEE/ASME Trans. Mechatronics.* 21 (2016) 649–659. <https://doi.org/10.1109/TMECH.2015.2492623>.
- [15] F. Rosa, M. Bordegoni, A. Dentelli, A. Sanzone, A. Sotgiu, Print-in-place of Interconnected Deformable and Rigid Parts of Articulated Systems, in: *27th Int. Conf. Flex. Autom. Intell. Manuf.*, The Author(s), 2017: pp. 555–562. <https://doi.org/10.1016/j.promfg.2017.07.149>.
- [16] B. Jansen, E. L. Doubrovski, J. C. Verlinden, *Animaris Geneticus Parvus*, *Rapid Prototyp. J.* 20 (2014) 311–319. <https://doi.org/10.1108/RPJ-10-2012-0087>.
- [17] F. Calignano, D. Manfredi, E.P. Ambrosio, S. Biamino, M. Pavese, P. Fino, Direct Fabrication of Joints based on Direct Metal Laser Sintering in Aluminum and Titanium Alloys, *Procedia CIRP.* 21 (2014) 129–132. <https://doi.org/10.1016/j.procir.2014.03.155>.

- [18] L.L. Howell, Compliant Mechanisms, in: *Encycl. Nanotechnol.*, Springer Netherlands, Dordrecht, 2016: pp. 604–611. https://doi.org/10.1007/978-94-017-9780-1_302.
- [19] S. Yang, Y. Tang, Y.F. Zhao, Assembly-Level Design for Additive Manufacturing: Issues and Benchmark, in: *Vol. 2A 42nd Des. Autom. Conf.*, American Society of Mechanical Engineers, 2016: pp. 1–13. <https://doi.org/10.1115/DETC2016-59565>.
- [20] A. Rias, C. Bouchard, F. Segonds, B. Vayre, S. Abed, Design for Additive Manufacturing: Supporting Intrinsic-Motivated Creativity, in: *Emot. Eng. Vol.5*, Springer International Publishing, Cham, 2017: pp. 99–116. https://doi.org/10.1007/978-3-319-53195-3_8.
- [21] S. Hällgren, L. Pejryd, J. Ekengren, (Re)Design for Additive Manufacturing, in: *Proc. 26th CIRP Des. Conf.*, 2016: pp. 246–251. <https://doi.org/10.1016/j.procir.2016.04.150>.
- [22] Y. Wang, R. Blache, X. Xu, Selection of additive manufacturing processes, *Rapid Prototyp. J.* 23 (2017) 434–447. <https://doi.org/10.1108/RPJ-09-2015-0123>.
- [23] C.G. Mançanares, E. de S. Zancul, J. Cavalcante da Silva, P.A. Cauchick Miguel, Additive manufacturing process selection based on parts' selection criteria, *Int. J. Adv. Manuf. Technol.* 80 (2015) 1007–1014. <https://doi.org/10.1007/s00170-015-7092-4>.
- [24] U.K. uz Zaman, M. Rivette, A. Siadat, S.M. Mousavi, Integrated product-process design: Material and manufacturing process selection for additive manufacturing using multi-criteria decision making, *Robot. Comput. Integr. Manuf.* 51 (2018) 169–180. <https://doi.org/10.1016/j.rcim.2017.12.005>.
- [25] H. Bikas, P. Stavropoulos, G. Chryssoulouris, Additive manufacturing methods and modelling approaches: a critical review, *Int. J. Adv. Manuf. Technol.* 83 (2016) 389–405. <https://doi.org/10.1007/s00170-015-7576-2>.
- [26] P. Pradel, Z. Zhu, R. Bibb, J. Moultrie, A framework for mapping design for additive manufacturing knowledge for industrial and product design, *J. Eng. Des.* 29 (2018) 291–326. <https://doi.org/10.1080/09544828.2018.1483011>.
- [27] S. Yang, Y.F. Zhao, Additive manufacturing-enabled design theory and methodology : a critical review, *Int. J. Adv. Manuf. Technol.* 80 (2015) 327–342. <https://doi.org/10.1007/s00170-015-6994-5>.
- [28] J.S. Cuellar, G. Smit, A.A. Zadpoor, P. Breedveld, Ten guidelines for the design of non-assembly mechanisms: The case of 3D-printed prosthetic hands, *Proc. Inst. Mech. Eng. Part H J. Eng. Med.* 232 (2018) 962–971. <https://doi.org/10.1177/0954411918794734>.
- [29] Y.H. Chen, Z.Z. Chen, Major Factors in Rapid Prototyping of Mechanisms, *Key Eng. Mater.* 443 (2010) 516–521. <https://doi.org/10.4028/www.scientific.net/KEM.443.516>.
- [30] Y. Chen, C. Zhezhen, Joint analysis in rapid fabrication of non-assembly mechanisms, *Rapid Prototyp. J.* 17 (2011) 408–417. <https://doi.org/10.1108/13552541111184134>.
- [31] J. Cali, D.A. Calian, C. Amati, R. Kleinberger, A. Steed, J. Kautz, T. Weyrich, 3D-printing of non-assembly, articulated models, *ACM Trans. Graph.* 31 (2012) 1. <https://doi.org/10.1145/2366145.2366149>.
- [32] R. Krishna, D. Sen, DFM for non-assembly RP of mechanisms, in: *Proc. 14th IFToMM World Congr. Interdiscip. Top. DFM Non-Assembly RP Mech.*, Taipei, 2015. <https://doi.org/10.6567/IFToMM.14TH.WC.OS20.013>.
- [33] S.N. Ramasubramanian, K. Ramakrishna, D. Sen, Design for additive manufacturing of products containing articulated mechanisms, in: *2nd Int. 17th Natl. Conf. Mach. Mech.*, 2015: pp. 1–11.
- [34] G. Sossou, F. Demoly, G. Montavon, S. Gomes, An additive manufacturing oriented design approach to mechanical assemblies, *J. Comput. Des. Eng.* 5 (2018) 3–18. <https://doi.org/10.1016/j.jcde.2017.11.005>.

REFERENCES

- [35] X. Song, Y. Chen, Joint Design for 3-D Printing Non-Assembly Mechanisms, in: Vol. 5 6th Int. Conf. Micro- Nanosyst. 17th Des. Manuf. Life Cycle Conf., American Society of Mechanical Engineers, 2012: pp. 619-631. <https://doi.org/10.1115/DETC2012-71528>.
- [36] Y. Li, Y. Chen, Physical Rigging for Physical Models and Posable Joint Designs Based on Additive Manufacturing Technology, *Procedia Manuf.* 11 (2017) 2235-2242. <https://doi.org/10.1016/j.promfg.2017.07.371>.
- [37] Y. Yang, D. Wang, X. Su, Y. Chen, Design and Rapid Fabrication of Non-assembly Mechanisms, in: 2010 Int. Conf. Manuf. Autom., IEEE, 2010: pp. 61-63. <https://doi.org/10.1109/ICMA.2010.2>.
- [38] Y. Chen, J. Lu, Minimise joint clearance in rapid fabrication of non-assembly mechanisms, *Int. J. Comput. Integr. Manuf.* 24 (2011) 726-734. <https://doi.org/10.1080/0951192X.2011.592995>.
- [39] X. Wei, Y. Tian, A. Joneja, A study on revolute joints in 3D-printed non-assembly mechanisms, *Rapid Prototyp. J.* 22 (2016) 901-933. <https://doi.org/10.1108/RPJ-10-2014-0146>.
- [40] H. Lipson, F.C. Moon, J. Hai, C. Paventi, 3-D Printing the History of Mechanisms, *J. Mech. Des.* 127 (2005) 1029-1033. <https://doi.org/10.1115/1.1902999>.
- [41] X. Li, J. Zhao, R. He, Y. Tian, X. Wei, Parametric Design of Scalable Mechanisms for Additive Manufacturing, *J. Mech. Des.* 140 (2018) 022302. <https://doi.org/10.1115/1.4038300>.
- [42] F. De Crescenzo, F. Lucchi, Design for Additive Manufacturing of a non-assembly robotic mechanism, in: *Adv. Mech. Des. Eng. Manuf. Lect. Notes Mech. Eng.* Springer, Cham, Springer International Publishing AG 2017, 2017: pp. 251-259. https://doi.org/10.1007/978-3-319-45781-9_26.
- [43] X. Su, Y. Yang, D. Wang, Y. Chen, Digital assembly and direct fabrication of mechanism based on selective laser melting, *Rapid Prototyp. J.* 19 (2013) 166-172. <https://doi.org/10.1108/13552541311312157>.
- [44] R. Lynn, M. Dinar, N. Huang, J. Collins, J. Yu, C. Greer, T. Tucker, T. Kurfess, Direct Digital Subtractive Manufacturing of a Functional Assembly Using Voxel-Based Models, *J. Manuf. Sci. Eng.* 140 (2018) 021006. <https://doi.org/10.1115/1.4037631>.
- [45] U. Scarcia, G. Berselli, C. Melchiorri, M. Ghinelli, G. Palli, Optimal Design of 3D Printed Spiral Torsion Springs, in: Vol. 2 Model. Simul. Control. Bio-Inspired Smart Mater. Syst. Energy Harvest., American Society of Mechanical Engineers, 2016: p. V002T03A020. <https://doi.org/10.1115/SMASIS2016-9218>.
- [46] E.G. Merriam, J.E. Jones, S.P. Magleby, L.L. Howell, Monolithic 2 DOF fully compliant space pointing mechanism, *Mech. Sci.* 4 (2013) 381-390. <https://doi.org/10.5194/ms-4-381-2013>.
- [47] J.A. Mirth, An Examination of Trispiral Hinges Suitable for Use in ABS-Based Rapid Prototyping of Compliant Mechanisms, in: Vol. 5A 38th Mech. Robot. Conf., American Society of Mechanical Engineers, 2014: p. V05AT08A026. <https://doi.org/10.1115/DETC2014-34075>.
- [48] C. Blanes, M. Mellado, P. Beltran, Novel Additive Manufacturing Pneumatic Actuators and Mechanisms for Food Handling Grippers, *Actuators.* 3 (2014) 205-225. <https://doi.org/10.3390/act3030205>.
- [49] M. Tavakoli, A. Sayuk, J. Lourenço, P. Neto, Anthropomorphic finger for grasping applications: 3D printed endoskeleton in a soft skin, *Int. J. Adv. Manuf. Technol.* 91 (2017) 2607-2620. <https://doi.org/10.1007/s00170-016-9971-8>.
- [50] J.A. Mirth, Preliminary Investigations Into the Design and Manufacturing of Fully Compliant Layered Mechanisms (FCLMs), in: Vol. 6A 37th Mech. Robot. Conf., American Society of Mechanical Engineers, 2013: p. V06AT07A017. <https://doi.org/10.1115/DETC2013-12124>.
- [51] U.-X. Tan, W.T. Latt, C.Y. Shee, W.T. Ang, A Low-Cost Flexure-Based Handheld Mechanism for

- Micromanipulation, *IEEE/ASME Trans. Mechatronics*. 16 (2011) 773–778. <https://doi.org/10.1109/TMECH.2010.2069568>.
- [52] Z. Zhang, B. Liu, P. Wang, P. Yan, Design of an additive manufactured XY compliant manipulator with spatial redundant constraints, in: 2016 35th Chinese Control Conf., IEEE, 2016: pp. 9149–9154. <https://doi.org/10.1109/ChiCC.2016.7554814>.
- [53] Y. Hu, L. Zhang, W. Li, G.-Z. Yang, Design and Fabrication of a 3-D Printed Metallic Flexible Joint for Snake-Like Surgical Robot, *IEEE Robot. Autom. Lett.* 4 (2019) 1557–1563. <https://doi.org/10.1109/LRA.2019.2896475>.
- [54] A. Garaigordobil, R. Ansola, E. Vegueria, I. Fernandez, Overhang constraint for topology optimization of self-supported compliant mechanisms considering additive manufacturing, *Comput. Des.* 109 (2019) 33–48. <https://doi.org/10.1016/j.cad.2018.12.006>.
- [55] H. Saudan, L. Kiener, G. Perruchoud, J. Kruis, S. Liberatoscioli, M.M. Dadrás, K. Vaideeswaran, F. Cochet, Compliant mechanisms and space grade product redesign based on additive manufacturing, in: R. Geyl, R. Navarro (Eds.), *Adv. Opt. Mech. Technol. Telesc. Instrum. III*, SPIE, 2018: p. 101. <https://doi.org/10.1117/12.2312087>.
- [56] M. Tuan, Pham, T. Joo, Teo, S.H. Yeo, Investigation Of The Mechanical Properties Of 3D Printed Compliant Mechanisms, in: *Proc. 2nd Int. Conf. Prog. Addit. Manuf. (Pro-AM 2016)*, Research Publishing, Singapore, 2016: pp. 109–115. <http://hdl.handle.net/10220/41844>.
- [57] G. Bai, N. Rojas, Self-Adaptive Monolithic Anthropomorphic Finger with Teeth-Guided Compliant Cross-Four-Bar Joints for Underactuated Hands, in: 2018 IEEE-RAS 18th Int. Conf. Humanoid Robot., IEEE, 2018: pp. 145–152. <https://doi.org/10.1109/HUMANOIDS.2018.8624971>.
- [58] S. Hill, S. Canfield, An Assessment of Fused Deposition Modeling for the Manufacturing of Flexural Pivots in an Anthropomorphic Robotic Hand Design, in: *Vol. 5B 40th Mech. Robot. Conf.*, American Society of Mechanical Engineers, 2016: p. V05BT07A066. <https://doi.org/10.1115/DETC2016-60253>.
- [59] M. Ben Salem, G. Aiche, L. Rubbert, P. Renaud, Y. Haddab, Design of a Microbiota Sampling Capsule using 3D-Printed Bistable Mechanism, in: 2018 40th Annu. Int. Conf. IEEE Eng. Med. Biol. Soc., IEEE, 2018: pp. 4868–4871. <https://doi.org/10.1109/EMBC.2018.8513141>.
- [60] Y. Liu, Q. Xu, Design of a 3D-printed polymeric compliant constant-force buffering gripping mechanism, in: 2017 IEEE Int. Conf. Robot. Autom., IEEE, 2017: pp. 6706–6711. <https://doi.org/10.1109/ICRA.2017.7989793>.
- [61] M. Zanaty, T. Fussinger, A. Rogg, A. Lovera, D. Lambelet, I. Vardi, T.J. Wolfensberger, C. Baur, S. Henein, Programmable Multistable Mechanisms for Safe Surgical Puncturing, *J. Med. Device*. 13 (2019) 021002. <https://doi.org/10.1115/1.4043016>.
- [62] Y.S. Krieger, S. Schiele, S. Detzel, C. Dietz, T.C. Lueth, Shape Memory Structures-Automated Design of Monolithic Soft Robot Structures with Pre-defined End Poses, in: 2019 Int. Conf. Robot. Autom., IEEE, 2019: pp. 9357–9362. <https://doi.org/10.1109/ICRA.2019.8794035>.
- [63] H. Zhou, A. Mohammadi, D. Oetomo, G. Alici, A Novel Monolithic Soft Robotic Thumb for an Anthropomorphic Prosthetic Hand, *IEEE Robot. Autom. Lett.* 4 (2019) 602–609. <https://doi.org/10.1109/LRA.2019.2892203>.
- [64] S.Q. Liu, H.B. Zhang, R.X. Yin, A. Chen, W.J. Zhang, Flexure Hinge Based Fully Compliant Prosthetic Finger, in: Y. Bi, S. Kapoor, R. Bhatia (Eds.), *Proc. SAI Intell. Syst. Conf. 2016*, Springer International

- Publishing, Cham, 2018: pp. 839–849. https://doi.org/10.1007/978-3-319-56991-8_60.
- [65] J. Jovanova, S. Domazetovska, M. Frecker, Modeling of the Interface of Functionally Graded Superelastic Zones in Compliant Deployable Structures, in: Vol. 2 Mech. Behav. Act. Mater. Struct. Heal. Monit. Bioinspired Smart Mater. Syst. Energy Harvest. Emerg. Technol., American Society of Mechanical Engineers, 2018: p. V002T06A013. <https://doi.org/10.1115/SMASIS2018-8176>.
- [66] M. Zhu, Y. Mori, M. Xie, A. Wada, S. Kawamura, A 3D printed Two DoF Soft Robotic Finger With Variable Stiffness, in: 2018 12th Fr. 10th Eur. Congr. Mechatronics, IEEE, 2018: pp. 387–391. <https://doi.org/10.1109/MECATRONICS.2018.8495838>.
- [67] R. Mutlu, C. Tawk, G. Alici, E. Sariyildiz, A 3D printed monolithic soft gripper with adjustable stiffness, in: IECON 2017 - 43rd Annu. Conf. IEEE Ind. Electron. Soc., IEEE, 2017: pp. 6235–6240. <https://doi.org/10.1109/IECON.2017.8217084>.
- [68] A. Bruyas, F. Geiskopf, P. Renaud, Design and Modeling of a Large Amplitude Compliant Revolute Joint: The Helical Shape Compliant Joint, J. Mech. Des. 137 (2015) 085003. <https://doi.org/10.1115/1.4030650>.
- [69] B. V. Johnson, Z. Gong, B.A. Cole, D.J. Cappelleri, Design of Disposable 3D Printed Surgical End-Effectors for Robotic Lumbar Discectomy Procedures, in: Vol. 5A 42nd Mech. Robot. Conf., American Society of Mechanical Engineers, 2018: p. V05AT07A055. <https://doi.org/10.1115/DETC2018-85257>.
- [70] A. Bruyas, F. Geiskopf, P. Renaud, Towards Statically Balanced Compliant Joints Using Multimaterial 3D Printing, in: Vol. 5A 38th Mech. Robot. Conf., American Society of Mechanical Engineers, 2014: p. V05AT08A033. <https://doi.org/10.1115/DETC2014-34532>.
- [71] R. Mutlu, G. Alici, M. in het Panhuis, G.M. Spinks, 3D Printed Flexure Hinges for Soft Monolithic Prosthetic Fingers, Soft Robot. 3 (2016) 120–133. <https://doi.org/10.1089/soro.2016.0026>.
- [72] C. Liu, C.-H. Chiu, T.-L. Chen, T.-Y. Pai, M.-C. Hsu, Y. Chen, Topology Optimization and Prototype of a Three-Dimensional Printed Compliant Finger for Grasping Vulnerable Objects With Size and Shape Variations, J. Mech. Robot. 10 (2018) 044502. <https://doi.org/10.1115/1.4039972>.
- [73] A.H. Sakhaei, S. Kaijima, T.L. Lee, Y.Y. Tan, M.L. Dunn, Design and investigation of a multi-material compliant ratchet-like mechanism, Mech. Mach. Theory. 121 (2018) 184–197. <https://doi.org/10.1016/j.mechmachtheory.2017.10.017>.
- [74] A. Bruyas, F. Geiskopf, P. Renaud, Toward unibody robotic structures with integrated functions using multimaterial additive manufacturing: Case study of an MRI-compatible interventional device, in: 2015 IEEE/RSJ Int. Conf. Intell. Robot. Syst., IEEE, 2015: pp. 1744–1750. <https://doi.org/10.1109/IROS.2015.7353603>.
- [75] H.M.C.M. Anver, R. Mutlu, G. Alici, 3D printing of a thin-wall soft and monolithic gripper using fused filament fabrication, in: 2017 IEEE Int. Conf. Adv. Intell. Mechatronics, IEEE, 2017: pp. 442–447. <https://doi.org/10.1109/AIM.2017.8014057>.
- [76] C. Tawk, Y. Gao, R. Mutlu, G. Alici, Fully 3D Printed Monolithic Soft Gripper with High Conformal Grasping Capability, in: 2019 IEEE/ASME Int. Conf. Adv. Intell. Mechatronics, IEEE, 2019: pp. 1139–1144. <https://doi.org/10.1109/AIM.2019.8868668>.
- [77] B.A.W. Keong, R.Y.C. Hua, A Novel Fold-Based Design Approach toward Printable Soft Robotics Using Flexible 3D Printing Materials, Adv. Mater. Technol. 3 (2018) 1–12. <https://doi.org/10.1002/admt.201700172>.

- [78] J.A. Mirth, The Design and Prototyping of Complex Compliant Mechanisms via Multi-Material Additive Manufacturing Techniques, in: Vol. 5A 40th Mech. Robot. Conf., American Society of Mechanical Engineers, 2016: p. V05AT07A003. <https://doi.org/10.1115/DETC2016-59078>.
- [79] A.T. Gaynor, N.A. Meisel, C.B. Williams, J.K. Guest, Multiple-Material Topology Optimization of Compliant Mechanisms Created Via PolyJet Three-Dimensional Printing, *J. Manuf. Sci. Eng.* 136 (2014) 061015. <https://doi.org/10.1115/1.4028439>.
- [80] E.B. Joyee, Y. Pan, A Fully Three-Dimensional Printed Inchworm-Inspired Soft Robot with Magnetic Actuation, *Soft Robot.* 6 (2019) 333-345. <https://doi.org/10.1089/soro.2018.0082>.
- [81] N.P. Castledine, J.H. Boyle, J. Kim, Design of a Modular Continuum Robot Segment for use in a General Purpose Manipulator, in: 2019 Int. Conf. Robot. Autom., IEEE, 2019: pp. 4430-4435. <https://doi.org/10.1109/ICRA.2019.8794249>.
- [82] R. MacCurdy, R. Katzschmann, Youbin Kim, D. Rus, Printable hydraulics: A method for fabricating robots by 3D co-printing solids and liquids, in: 2016 IEEE Int. Conf. Robot. Autom., IEEE, 2016: pp. 3878-3885. <https://doi.org/10.1109/ICRA.2016.7487576>.
- [83] M.A. Skylar-Scott, J. Mueller, C.W. Visser, J.A. Lewis, Voxelated soft matter via multimaterial multi-nozzle 3D printing, *Nature.* 575 (2019) 330-335. <https://doi.org/10.1038/s41586-019-1736-8>.
- [84] A. Ion, J. Frohnhofen, L. Wall, R. Kovacs, M. Alistar, J. Lindsay, P. Lopes, H.-T. Chen, P. Baudisch, Meta-material Mechanisms, in: Proc. 29th Annu. Symp. User Interface Softw. Technol. - UIST '16, ACM Press, New York, New York, USA, 2016: pp. 529-539. <https://doi.org/10.1145/2984511.2984540>.
- [85] A. Ion, D. Lindlbauer, P. Herholz, M. Alexa, P. Baudisch, Understanding Metamaterial Mechanisms, in: Proc. 2019 CHI Conf. Hum. Factors Comput. Syst. - CHI '19, ACM Press, New York, New York, USA, 2019: pp. 1-14. <https://doi.org/10.1145/3290605.3300877>.
- [86] J. Ou, Z. Ma, J. Peters, S. Dai, N. Vlavianos, H. Ishii, KinetiX - designing auxetic-inspired deformable material structures, *Comput. Graph.* 75 (2018) 72-81. <https://doi.org/10.1016/j.cag.2018.06.003>.
- [87] A.G. Mark, S. Palagi, T. Qiu, P. Fischer, Auxetic metamaterial simplifies soft robot design, *Proc. - IEEE Int. Conf. Robot. Autom.* 2016-June (2016) 4951-4956. <https://doi.org/10.1109/ICRA.2016.7487701>.
- [88] T. Liu, Y. Wang, K. Lee, Three-Dimensional Printable Origami Twisted Tower: Design, Fabrication, and Robot Embodiment, *IEEE Robot. Autom. Lett.* 3 (2018) 116-123. <https://doi.org/10.1109/LRA.2017.2733626>.
- [89] Z. Zhao, X. Kuang, J. Wu, Q. Zhang, G.H. Paulino, H.J. Qi, D. Fang, 3D printing of complex origami assemblages for reconfigurable structures, *Soft Matter.* 14 (2018) 8051-8059. <https://doi.org/10.1039/C8SM01341A>.
- [90] Y. Li, Y. Chen, C. Zhou, Design of Flexible Skin for Target Displacements Based on Meso-Structures, in: Vol. 2 29th Comput. Inf. Eng. Conf. Parts A B, ASMEDC, 2009: pp. 611-624. <https://doi.org/10.1115/DETC2009-87137>.
- [91] C.R. de Lima, G.H. Paulino, Auxetic structure design using compliant mechanisms: A topology optimization approach with polygonal finite elements, *Adv. Eng. Softw.* 129 (2019) 69-80. <https://doi.org/10.1016/j.advengsoft.2018.12.002>.
- [92] J. Khurana, B. Hanks, M. Frecker, Design for Additive Manufacturing of Cellular Compliant Mechanism Using Thermal History Feedback, in: Vol. 2A 44th Des. Autom. Conf., American Society of Mechanical Engineers, 2018: p. V02AT03A035. <https://doi.org/10.1115/DETC2018-85819>.
- [93] G. Wang, Y. Tao, O.B. Capunaman, H. Yang, L. Yao, A-line: 4D Printing Morphing Linear Composite

- Structures, in: Proc. 2019 CHI Conf. Hum. Factors Comput. Syst. - CHI '19, ACM Press, New York, New York, USA, 2019: pp. 1-12. <https://doi.org/10.1145/3290605.3300656>.
- [94] M. Bodaghi, A.R. Damanpack, W.H. Liao, Adaptive metamaterials by functionally graded 4D printing, *Mater. Des.* 135 (2017) 26-36. <https://doi.org/10.1016/j.matdes.2017.08.069>.
- [95] M. Bodaghi, W.H. Liao, 4D printed tunable mechanical metamaterials with shape memory operations, *Smart Mater. Struct.* 28 (2019) 045019. <https://doi.org/10.1088/1361-665X/ab0b6b>.
- [96] Y. Mao, K. Yu, M.S. Isakov, J. Wu, M.L. Dunn, H. Jerry Qi, Sequential Self-Folding Structures by 3D Printed Digital Shape Memory Polymers, *Sci. Rep.* 5 (2015) 13616. <https://doi.org/10.1038/srep13616>.
- [97] Y. Jin, Y. Wan, Z. Liu, Surface polish of PLA parts in FDM using dichloromethane vapour, in: H.L. Yuan, R.K. Agarwal, P. Tandon, E.X. Wang (Eds.), *MATEC Web Conf.*, EDP Sciences, 2017: p. 05001. <https://doi.org/10.1051/mateconf/20179505001>.
- [98] W. Wang, C. Li, M. Cho, S.-H. Ahn, Soft Tendril-Inspired Grippers: Shape Morphing of Programmable Polymer-Paper Bilayer Composites, *ACS Appl. Mater. Interfaces.* 10 (2018) 10419-10427. <https://doi.org/10.1021/acsami.7b18079>.
- [99] Y. Zhou, W.M. Huang, S.F. Kang, X.L. Wu, H.B. Lu, J. Fu, H. Cui, From 3D to 4D printing: approaches and typical applications, *J. Mech. Sci. Technol.* 29 (2015) 4281-4288. <https://doi.org/10.1007/s12206-015-0925-0>.
- [100] S. Leeftang, S. Janbaz, A.A. Zadpoor, Metallic clay, *Addit. Manuf.* 28 (2019) 528-534. <https://doi.org/10.1016/j.addma.2019.05.032>.
- [101] J. Hergel, S. Lefebvre, 3D Fabrication of 2D Mechanisms, *Comput. Graph. Forum.* 34 (2015) 229-238. <https://doi.org/10.1111/cgf.12555>.
- [102] M. Hallmann, S. Goetz, B. Schleich, S. Wartzack, Optimization of Build Time and Support Material Quantity for the Additive Manufacturing of Non-Assembly Mechanisms, *Procedia CIRP.* 84 (2019) 271-276. <https://doi.org/10.1016/j.procir.2019.03.197>.
- [103] C.J. Kimmer, C.K. Harnett, Combining Strings and Fibers With Additive Manufacturing Designs, in: Vol. 4 21st Des. Manuf. Life Cycle Conf. 10th Int. Conf. Micro- Nanosyst., ASME, 2016: p. V004T05A014. <https://doi.org/10.1115/DETC2016-59569>.
- [104] N.A. Meisel, A.M. Elliott, C.B. Williams, A procedure for creating actuated joints via embedding shape memory alloys in PolyJet 3D printing, *J. Intell. Mater. Syst. Struct.* 26 (2015) 1498-1512. <https://doi.org/10.1177/1045389X14544144>.
- [105] T. Stalin, N.K. Thanigaivel, V.S. Joseph, P.V. Alvarado, Automated Fiber Embedding for Tailoring Mechanical and Functional Properties of Soft Robot Components, in: 2019 2nd IEEE Int. Conf. Soft Robot., IEEE, 2019: pp. 762-767. <https://doi.org/10.1109/ROBOSOFT.2019.8722752>.

3

A REVIEW ON 3D PRINTED SPRINGS

The rise of additive manufacturing technologies or 3D printing for functional applications has increased the demand for mechanical springs produced using this technology. This is not only a relevant topic in scientific communities, but also in hobbyist communities that have embraced 3D printing. The latter consists of hobbyists who exchange ideas and 3D models in online databases, where they build upon each other's work. We performed a systematic search for 3D printed springs, produced both by the scientific community and the hobbyist community. We analyzed the design, 3D print technology, materials, and 3D print settings of the springs. We divided the 3D printed springs into two main groups: planar and spatial designs. Planar designs contain zigzag, leaf, spiral, and ortho-planar springs, while spatial designs contain helical, wave, stacked, and rotation springs. Promising advantages of 3D printed springs are the ability to vary dimensions within one spring to customize the performance to the application, and integrating the spring into a functional design in a single production step. Springs encountered in the hobbyist database are more diverse and creative, and tend to focus more on planar designs, while springs encountered in the scientific database were more thoroughly evaluated, and focused more on spatial designs. The combined search results from scientific and hobbyist communities give a comprehensive overview of the possibilities and best practices for creating functional 3D printed springs and can be used as inspiration for further research.

3.1 INTRODUCTION

Springs are used in many applications, and can have a wide range of uses. The primary function of a spring is to deflect or distort under load, and to recover its original shape after the load is removed [1]. Some possible uses include storing energy, reducing impact, controlling vibrations, or improving connections between mechanical parts [2]. The elastic behaviour exhibited by a spring is caused by a combination of the spring shape and the material, both a helical shape made out of metal and a solid block of rubber can constitute a spring [2,3]. Spring steel is the most common choice of material for springs, along with other metal alloys, although it is possible to make springs out of a wide variety of materials. Commonly encountered mechanical spring designs are helical springs, leaf springs, flat springs, spiral springs, Belleville springs, and torsion-bar springs [1].

Additive manufacturing (AM) or 3D printing as a manufacturing technique for functional components is rising in popularity and use. In contrast to conventional manufacturing techniques, in AM material is deposited in a layer-wise fashion, which allows for the design of complex shapes without the limitations of the conventional production techniques. Although initially mostly used as a prototyping method, recently AM is also used to produce functional components and mechanical constructions [4]. Benefits of AM include the minimization of waste products, since it is not a subtractive method, the option to add complexity to a part without additional costs, and the ability to produce complete assemblies in a single build [4,5]. The rising interest to create complete, functional mechanisms with AM also increases demand for elastic elements that can be integrated into these mechanisms. This requires a new approach for the design of these elastic

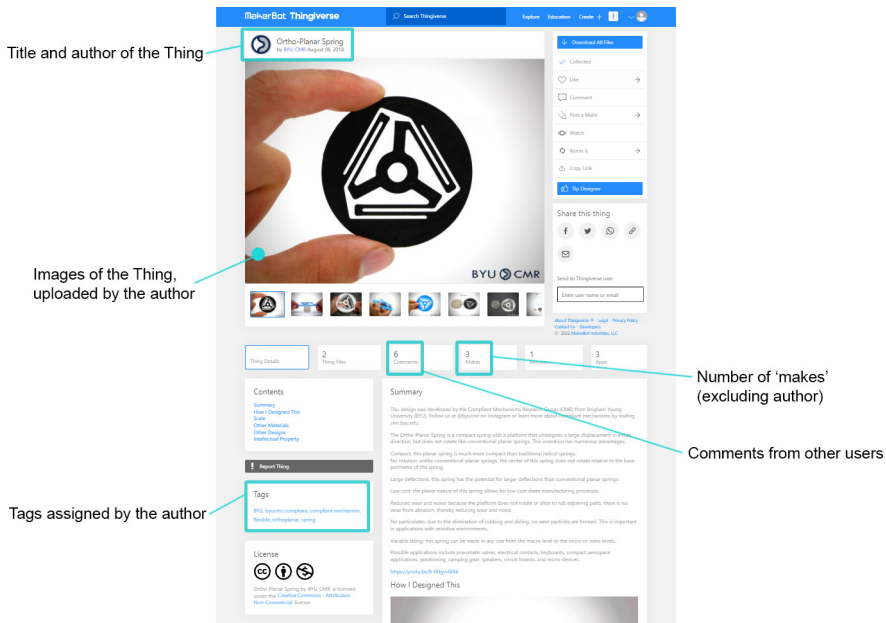


Figure 3.1: Example of a Thing-page from the website www.thingiverse.com [12]. The page shows the title and author of the Thing, along with a description, images, tags, and allows other users to upload their ‘makes’ and comments.

components, without the constraints of traditional manufacturing, while taking into account the new challenges that AM brings [6].

The interest in AM extends beyond only the scientific community. The availability of cheap extrusion-based 3D printers has dramatically increased in recent years, and these machines have been embraced by professionals and hobbyists alike [4,7]. These hobbyists, often referred to as the ‘Maker Movement’ [8], have embraced online websites in which they can exchange 3D models, 3D printer reviews, and tips and tricks for obtaining the best print results [9]. Characteristic of the maker movement is sharing of 3D files, which allows both hobbyists and professionals to build on each other’s models and ideas [9]. Hobbyists share their designs with online communities, allowing collaborative design to lead to a wide variety of solutions. In these large online 3D printing databases, many interesting 3D printed designs are made available for free [10], harbouring an immense wealth of creativity and exploration. Collective design can lead to quick innovations, although the lack of structure can also lead to many duplicates and repetitions [11]. For 3D printed springs this means that many innovative and functional spring designs can be found, applied in functional products, tested and approved by the collaborative design effort. In this review, we aim to provide a complete overview of 3D printed spring designs from both the scientific literature as well as the maker movement. Therefore, we have included both scientific articles researching 3D printed springs and 3D printed springs designed by hobbyists.

3.2 SEARCH METHOD

3.2.1 Scientific data

The Scopus database was used to search for scientific literature on 3D printed springs. The search query was organized in two parts: 1) related to the fabrication technology (*additive manufactur**, *3D print**, *rapid prototyp**) and 2) related to the application (*spring*, *springs*). The search term *spring** resulted in too many off-topic results, and was therefore replaced by *spring* or *springs*. The results were limited to articles written in English only, within the subject area ‘Engineering’.

3.2.2 Non-scientific data

Non-Scientific data in the form of 3D models was obtained from the Thingiverse platform (www.thingiverse.com, MakerBot Industries, New York, USA). Compared to other 3D model platforms, Thingiverse is the most popular and contains the most models, with over 2.2 million models at the time of writing [9,10]. Thingiverse is completely free and allows non-professionals to share their ideas and models. The 3D models are called Things, and all have a specific identification number called a Thing-id. All the information concerning a 3D model is displayed on the Thing-page, allowing other users to comment, directly download the files, and upload their own makes of the part (Figure 3.1). In addition, authors can add ‘tags’ to their uploads, to indicate which category their Thing belongs to.

The built-in search engine of Thingiverse limits the results for ‘spring’ to 10.000 results. Since anyone can upload files to this platform without restriction, and it is not required to test or 3D print the part before uploading them, it is likely that not all of the results are usable. To find the most relevant results, we utilized the built-in search engine in combination with filters. Search results can be sorted on popularity, relevance, exact text, newest, or most makes. Two of these relate directly to user-based metrics. Popularity shows results based on the number of likes the Thing received from users, with the most popular one first. Most makes shows results based on the number of times the Thing was made by other users. A make is registered only when a user uploads a photo of the printed Thing to the site, and can therefore be a good indication of the printability of the part.

For our search, we combined three search strategies in order to make our results as repeatable as possible while finding the most relevant results. First, we searched for ‘spring’, and filtered on ‘exact text’, which presents results that most closely match the search word. This provided us with mainly Things of springs, and it did not give us the most popular or printable Things. For the second search, we filtered the results for ‘spring’ by most makes. The top result in this search had 755 makes. Finally, we searched on all Things tagged with ‘spring’. These results are automatically sorted by popularity (number of likes), the most popular design received 25.752 likes. For each of the search queries, we evaluated the first 100 results, resulting in a total of 300 results for the three search queries.

3.2.3 Exclusion criteria

For the Scopus search, only results that included a prototype of a 3D printed spring were included, all results describing a conventional spring combined with a 3D printed part were omitted. We chose to include only the results in which the purpose of the author was

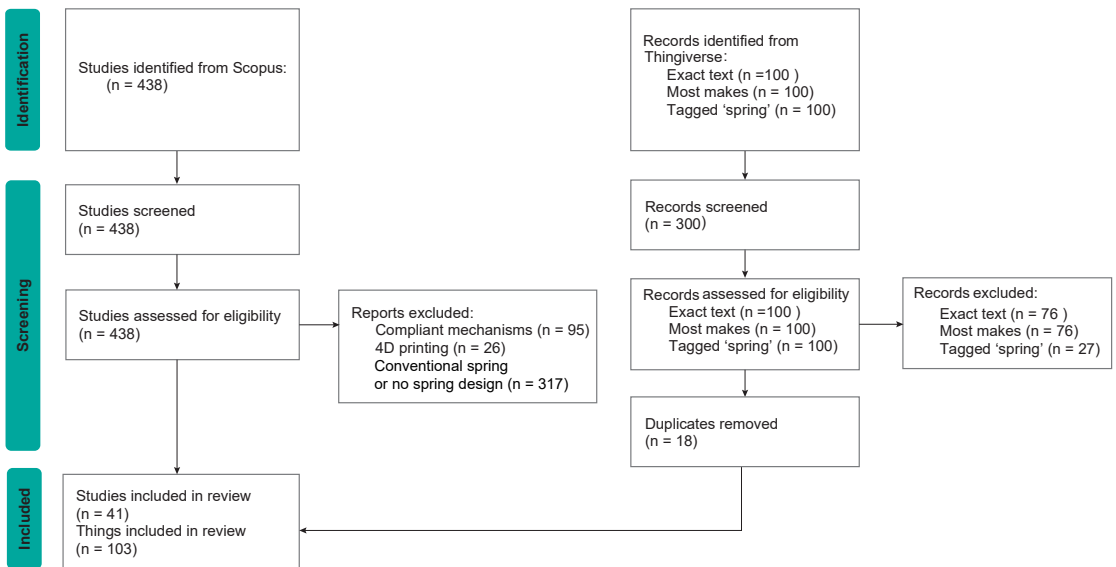


Figure 3.2: Schematic representation of the conducted systematic search.

to design or develop a spring; results in which a design or mechanism showed spring-like behaviour without it being one of the main purposes were omitted. Compliant mechanisms contain elastic members or flexures functioning as spring elements, which are thoroughly integrated and optimized for the design of the mechanism while being difficult to apply in other designs. Therefore, we excluded all mechanisms explicitly described as compliant for which the main purpose was not to function as a spring. Springs produced using 4D printing techniques, such as by using smart memory alloys, were also excluded, since this is considered to be out of the scope of this research. For the Thingiverse search, of the 300 evaluated results, only Things were included that showed an actual 3D printed spring with more than 10 likes. All results without any makes (including from the author) were omitted, as well as designs that require the use of a conventional spring to function. All duplicates and ‘remixes’, in which the author makes modifications to the design of another author, were excluded.

3.2.4 Search results

The search within the Scopus database resulted in 438 initial search results, of which the titles and abstracts were scanned for relevance. From these 438 results, we selected 41 articles that fulfilled the eligibility criteria. For the search in the Thingiverse database, we evaluated a total of 300 search results. To verify the repeatability of our search, we repeated it one month after the initial search, which led to no new search results. Based on

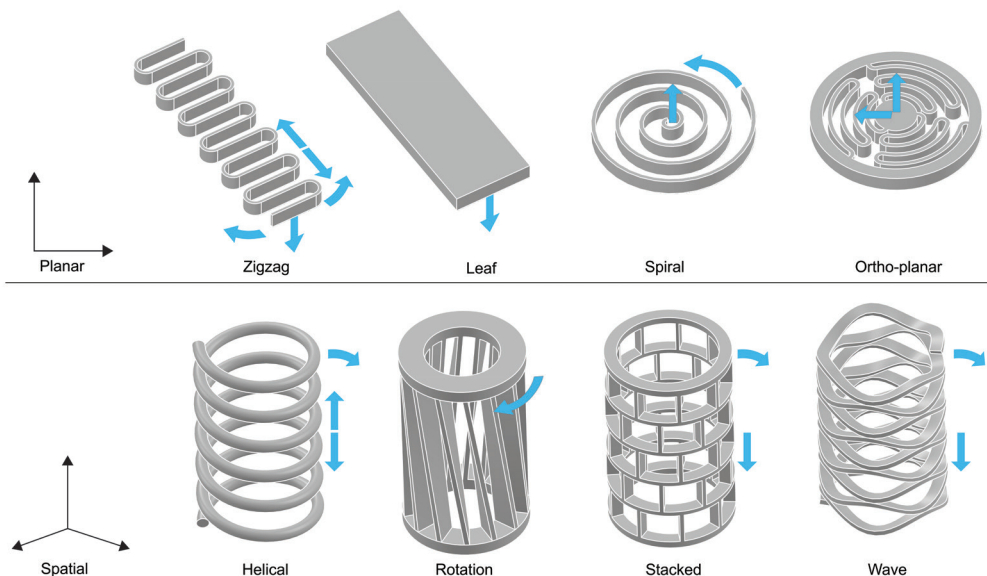


Figure 3.3: Overview of the division into different spring types. Two main categories were distinguished: planar and spatial spring designs. Zigzag, leaf, spiral and ortho-planar springs were encountered within planar designs; and helical, rotational, stacked, and wave springs within spatial designs. The arrows indicate the direction of motion of the springs as encountered in the search results.

the eligibility criteria, we included 103 Things. We analysed the included springs on the type of spring, manufacturing technique, and applications. The results of the systematic search are schematically shown in Figure 3.2.

3.3 TYPES OF 3D PRINTED SPRINGS

We subdivided the search results into planar and spatial spring designs, as shown in Figure 3.3, in which also the direction of motion of the springs as encountered in the search results is indicated with arrows. Planar springs include all designs that can be described as an extrusion of a 2-Dimensional (2D) shape, sometimes referred to as 2.5D, since they can be described as a 2D geometry with a given height. Within this category, we have found zigzag, leaf, spiral, and ortho-planar spring designs. Spatial spring designs include geometries that can only be described in a 3-Dimensional (3D) space. Within this category, we have encountered helical, rotational, wave, and stacked spring designs.

3.3.1 Planar designs

Zigzag springs

Zigzag springs owe their name to the zigzag shape of the structure, which is used to create long, slender flexures. Zigzag springs are a useful geometry for most AM technologies, since they can be printed lying flat on the build plate. This build direction aligns the layer lines with the direction of force of the spring, preventing breakage caused by poor layer adhesion. Cui et al. [13] showed that it is also possible to print zigzag springs protruding from the build plate, by taking the overhang angle into consideration. Tutum et al. [14] explored single-curve zigzag shapes to optimise a spring to launch a toy car, by means of an algorithm that optimized the spring to consistently propel the car forward over a certain distance.

Among the Things, zigzag springs were used by authors for compressive purposes, often in combination with linear constraints to prevent motion in other directions [15–24], for bending purposes such as in clamps and karabiners [25–31], and for use as flexible elements in toys [32–38]. One author designed zigzag springs with customized curves to use as a silencing suspension to dampen the noise of the extruder motor of the used material extrusion 3D printer (Figure 3.4a) [39], as well as vibration dampers to place underneath the printer’s feet [40]. The author mentioned that the suspension greatly reduced the noise from the extruder, although with both designs the material started to plastically deform after prolonged use. Another author designed a bag holder with zigzag springs as dampers to help carry heavy loads (Figure 3.4b) [41]. The use of six springs with different heights allows for an even load distribution, and the Thing author noted that it supported bags of at least 5 kg. An unusual type of zigzag spring is the honeycomb spring, in which negative stiffness honeycomb cells are designed in such a way that they are capable of elastic buckling, which allows them to recover their shape and properties after impact (Figure 3.4c) [42]. The research article on honeycomb springs was also encountered by a Thing-author, who decided to reverse engineer the structure to create a modifiable CAD-file that

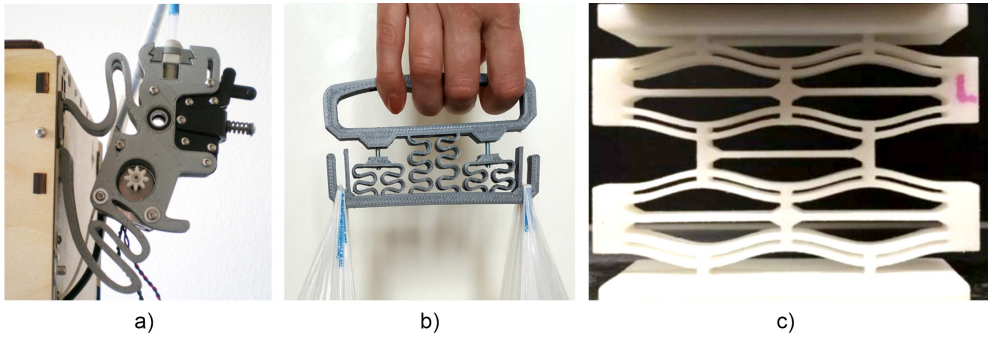


Figure 3.4: Designs with incorporated zigzag springs. a) A silencing suspension for an extruder motor using custom zigzag shapes [39]. b) A bag holder with zigzag springs, arranged in a way to create an even load distribution [41]. c) Negative stiffness honeycomb spring [44].



Figure 3.5: Examples of leaf springs. a) Crossed leaf springs applied in self-closing tweezers, based on [53]. b) Leaf springs applied in self-opening pliers, based on [52].

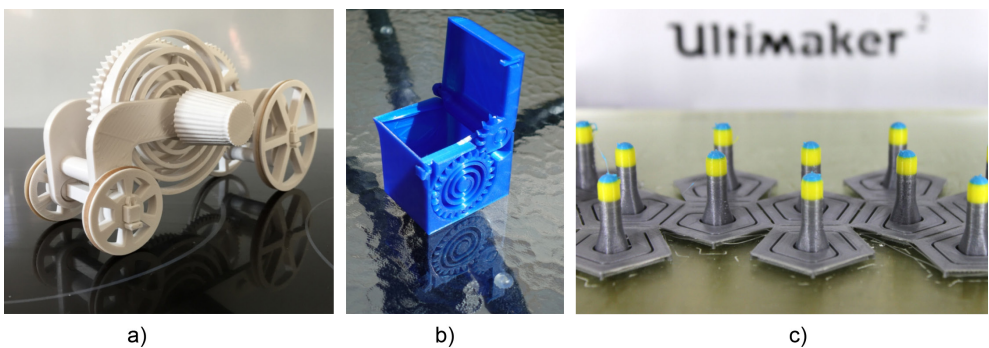


Figure 3.6: Examples of 3D printed spiral springs. a) Spring-propelled toy car [70]. b) Non-assembly spring loaded box with integrated spiral spring and gears [76]. c) Hexagonal shaped spirals connected to each other, which can be printed as a single sheet and afterwards folded into a 3D-shape [79].

can be used to explore the parameters of this structure, such as the thickness and number of spring elements [43].

Leaf springs

The design of leaf springs can range from a simple, straight beam, to a more complex stack of curved plates. A single, flat plate design is often encountered for 3D printed leaf springs, since this geometry is generally easy to print. This type of leaf spring can be loaded for bending by pushing or pulling one end, while fixating the other end in place. Besnea et al. [45] tested 3D printed leaf springs in rectangular and triangular shapes, in three different materials, showing a linear relation between force and deflection of the leaf springs. Garanger et al. [46] showed that a feedback-control system could be used to reach the desired stiffness for a stack of rectangular leaf springs, by controlling the infill density. Kessentini et al. [47] used finite element analysis to optimize the parameters of a mono leaf spring printed in carbon-filled PEEK, for use in a car suspension system. The leaf springs applied by Thing-authors in their designs were often used for opening or closing purposes by applying crossed leaf springs, such as for clamping toys [48–51], or for tools that can self-close (Figure 3.5a) or self-open (Figure 3.5b) [52–55]. Other purposes include clamping things in place with a single leaf spring, such as a business card holder [56] or a clamp with integrated ratchet mechanism [57], as well as using the stored energy of the leaf spring to move objects [58–60].

Spiral springs

Spiral springs were more frequently encountered in the Thingiverse database [61,62,71–79,63–70] than in the scientific database [80]. Spiral springs were often used by Thing-authors as energy storage mechanisms [68–76]. The spiral spring can be wound up to store energy, after which the energy is released to drive a mechanism. The use of gears reduces the spring force and ensures that the spring releases its energy at a lower rate. This principle has been used to propel toy vehicles (Figure 3.6a) [68–71], and to drive tourbillon mechanisms, which are used in clocks and watches to counteract the effect of gravity [72–74]. A non-assembly spring-loaded box, shown in Figure 3.6b, has a spiral spring with integrated gear teeth [76]. In this application, the spiral spring stores energy by means of closing the lid of the box, when pushing a button, the energy is released and the lid directly pops open. Alternatively, a horizontal spiral spring can be used as a compliant twist lock on a box [77]. Scarcia et al. [80] researched the behaviour of a 3D printed spiral spring, and concluded that the spring stiffness was dependent on the total length, thickness and height of the coil, and independent of the outer radius, pitch or coil number.

For most applications, spiral springs are loaded in the direction of the windings. Alternatively, a spiral spring designed by a Thing author shows loading of the spring in the out-of-plane direction, which allows it to be launched from the fingertip when released [78]. Furthermore, one Thing-author used hexagonal shaped spirals to create a structure that is printed flat on the build plate (Figure 3.6c), but is subsequently folded into a 3-di-

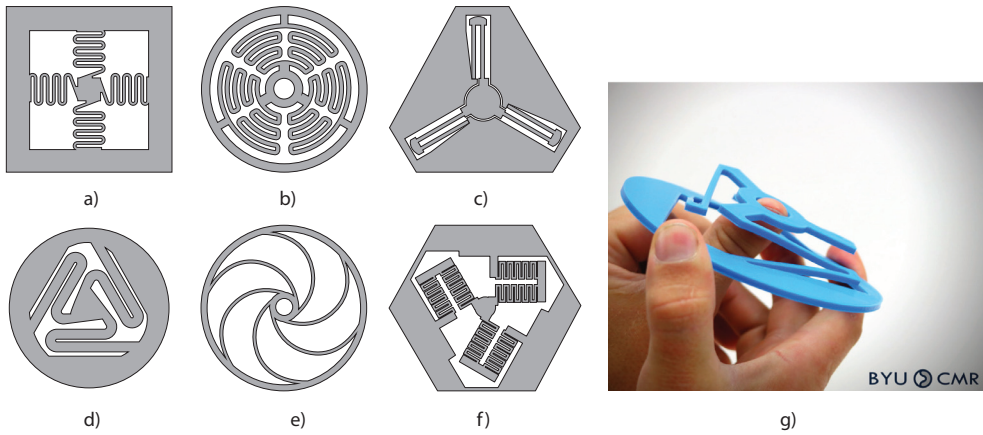


Figure 3.7: Examples of 3D printed ortho-planar spring designs. a) Ortho-planar spring design used for vibrational harvesting (based on [84]). b) Ortho-planar side-leg design (based on [85]). c) Ortho-planar spring design used in a parallel guidance mechanism (based on [82]). d) Ortho-planar spring design without application (based on [89]). e) Ortho-planar spring design used as airless tire (based on [86]). f) Ortho-planar spring without application (based on [81,90]). g) 3D printed ortho-planar spring showing its linear displacement [12].

mensional shape to function as a bouncing ball [79].

Ortho-planar springs

Ortho-planar springs typically have a central platform that is connected to a base by means of flexible segments, which can move in an out-of-plane direction [81]. Often an ortho-planar spring is expected to only allow a linear motion [82]. They can be designed in such a way that they ensure minimal planar rotation of the central platform, for example by using symmetry between the flexible segments. The spring forces resist the central platform from moving sideways. Yao et al. [83] used 3D printed ortho-planar springs to isolate vibrations, while Kawa et al. [84] tested various geometrical configurations of 3D printed ortho-planar springs for vibrational energy harvesting (Figure 3.7a). Qiu et al. [85] simulated the behaviour of 30 different ortho-planar spring designs, and applied a so-called side-leg design to use in a 3D printed continuum manipulator, since, besides from its large out-of-plane range of motion, the spring also has a large bending compliance and low torsional compliance (Figure 3.7b). Teichert and Jensen [82] used an ortho-planar spring in a parallel guidance mechanism printed in ABS, for added stability they used the same spring twice, rotated 60 degrees relative to each other (Figure 3.7c).

Designs for ortho-planar springs can be found on Thingiverse [12,86–89], although for most the Thing-authors have no application (examples in Figure 3.7d-e). One author modelled his ortho-planar spring [90] after the research work of Parise et al. [81] (Figure 3.7f). The Compliant Mechanisms Research Group from Brigham Young University uploaded a compact design with a large possible deflection and a fully linear displacement of the centre, which can be scaled to various sizes (Figure 3.7g) [12].

3.3.2 Spatial designs

Helical springs

Helical springs may be the most common type of spring. They can be used for compression, tension, bending and torsional purposes [1]. The 3D printed helical spring is the most encountered in both the scientific and the non-scientific search results. Helical designs allow themselves to be printed by a range of AM technologies, in different sizes. Considerable attention has been paid to investigating the correct process parameters for a given AM technology, such as for SLA [91], and material extrusion [92,93]. Nano AM methods, such as two-photonlithography, were used to create functional helical microsprings (Figure 3.8a) [94–97].

Disadvantages of helical springs are that they often require support material between the windings, and a round cross-section of the wire is difficult to print due to the layer-based nature of AM. Using 3D printing, the cross-section of the wire can easily be changed from circular to rectangular (Figure 3.8b) [98,99], the effects of which were investigated by Besnea et al. [100] and Enea and Moon [92], showing that better geometric accuracy could be achieved with the rectangular wire. Helical springs that do not require support material were often explored by Thing-authors, for instance springs with different main geometries, such as triangular cross-sections (Figure 3.8c) [101,102], rectangular cross-sections [103], and hexagonal cross-sections [104]. These cross-sections can be printed with a flat side laying on the build plate, and make use of self-supporting angles. Helical tension springs, in which all windings of the helix rest on top of each other, are popular with Thing-authors, due to the ability to print them without additional support material [101,105–107]. This is possible by ensuring a small gap of several layer thicknesses between the windings. The windings are carefully pried loose with a knife after printing.

Advantages of 3D printing helical springs are that they can be customized by altering the spring parameters, such as the wire thickness, pitch, and diameter, within one spring design, which influences the flexibility and elasticity of the spring [6,108–110]. Besides the use of different main geometries and wire cross-sections, AM also allows for the manufacturing of designs with additions to the basic helical shape, like barbs on the surface to anchor the spring in tissue [111].

Wave, stacked and rotation springs

Other spatial designs include wave [112–114], stacked [112,115,116], and rotation [117] springs, shown in Figure 3.8d–f. A conventional wave spring consists of a flat, corrugated ribbon, coiled into a helical shape. The advantage of wave springs over helical springs is that they require less material for similar properties in equal dimensions [118]. 3D printed wave springs forego the helical shape in exchange for a structure of stacked, corrugated rings. Wave springs are not the most convenient design to produce using AM, since they require support structures, and not all spring elements will be printed in the most favourable direction. This can for example result in the staircase effect alongside the curved geometries, which can initiate cracks while loading the spring [113]. To circumvent this,

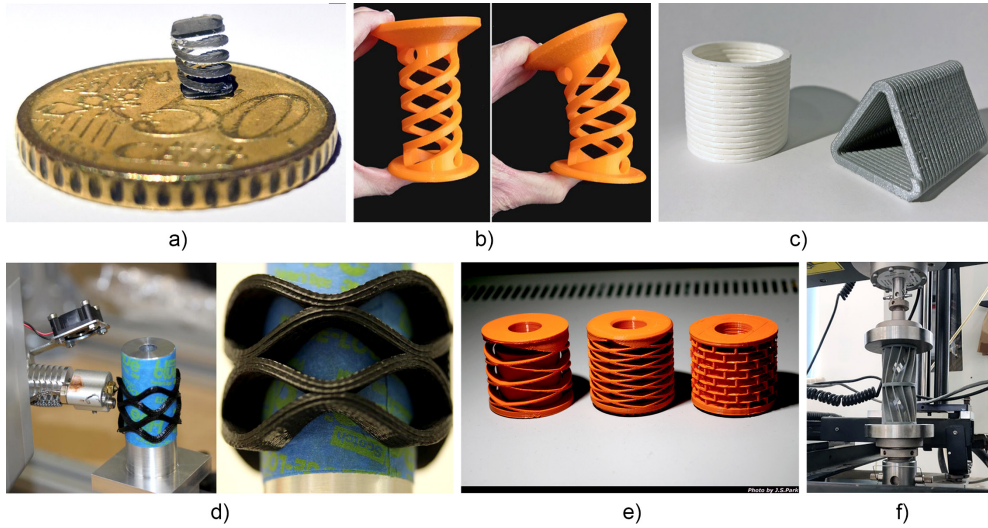


Figure 3.8: Examples of spatial 3D printed spring designs. a) Helical microspring [91]. b) Helical spring with rectangular wire cross-section [123]. c) Helical tension springs printed in upright (left) and horizontal (right) position [101]. d) Set-up to print a wave spring with optimized material extrusion direction (left) and close-up of the spring (right) [113]. e) Wave (left and middle) and stacked (right) springs [115]. f) Set-up for axial compression testing of a stack of two opposite rotation springs [117].

Gardner et al. [113] printed a wave spring using a modified 5-axis 3D printer, which is able to extrude material on top of a rotating cylinder perpendicular to its travel direction, thereby optimizing the extrusion direction (Figure 3.8d). The wave springs produced with this technique showed a 47% increase in strength under compression, as well as a significant increase in deflection until failure.

Haq et al. [119] compared a rectangular cross-section of the waves with a circular cross-section, and showed that the rectangular cross-section resulted in a 40% increase in compression stiffness. Chapkin et al. [112] compared 3D printed wave and stacked springs, sometimes called machined springs, for their bending response. The stacked spring design showed higher flexibility under bending, but also showed more parasitic motion while loaded, while the wave spring showed a higher bending stiffness. Things of wave and stacked springs were uploaded in various designs (Figure 3.8e) [115,116,120]. These springs proved printable and functional when using rigid plastics, although most designs required the use of support structures. One Thing author [116] noted that his stacked spring design was resistant to twisting, and became stiffer with more vertical bars added, while more stacked layers increased the range of motion.

Wang et al. [117] designed a rotation spring with curved surfaces (Figure 3.8f), similar in design to a flexible coupling, which is meant to convert compression into torsion. They investigated the effect of the slenderness ratio and the width of the curved surfaces. It was found that the width of the surfaces had little effect on the resulting torsion angle while under load, whereas an increased slenderness ratio of the curved surfaces increased the

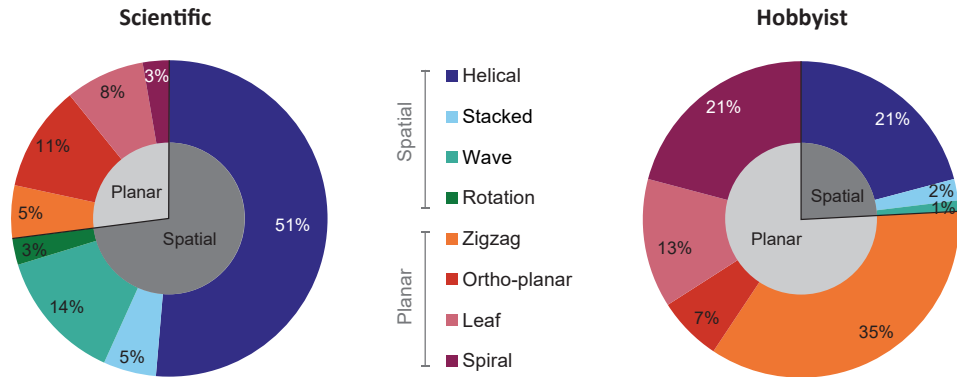


Figure 3.9: Distribution of the types of springs encountered in the scientific and non-scientific search results. A division is made between planar designs, which include zigzag, ortho-planar, leaf, and spiral designs, and spatial designs, which include helical, stacked, wave and rotational designs.

resulting torsion angle. Another type of rotation spring is based on an origami pattern for collapsible cylinders [121]. Khazaaleh et al. [122] printed this origami spring using multi-material printing, in which the sides were printed in a rigid material and the folds in a flexible material. They showed that the spring can exhibit linear, bi-stable, softening, and hardening behaviour, depending on the chosen geometrical dimensions of the spring.

3.3.3 Spring type distribution

The distribution of the types of springs identified in the scientific and hobbyist search results is shown in Figure 3.9. In the scientific search, helical springs were the most researched type of spring, with more than half of the articles focused on this spring type. The other types of springs were researched in more or less equal amounts. Furthermore, it can be seen that most attention has been paid to spatial springs, rather than planar springs. In the hobbyist search, the most encountered type of spring were zigzag type springs. This can be explained by the fact that zigzag springs are easy to design and produce using an inexpensive desktop printer, due to their 2.5-dimensional design. In contrast to the non-scientific literature, in the Thing-search the planar spring designs make up the majority of the results. The difference in focus between spatial and planar designs between the two search results might be contributed to the less expensive FDM printers used by the hobbyist community, which tend to work well with 2.5D-structures. In general, the spread of spring types from the Thing-results is more diverse than the spring types identified in the scientific results. From a qualitative perspective, we have also encountered more creative and diverse spring designs in the Thing results, as compared to the ones found in the scientific results. It should be noted that the functionality of the spring-Things is often not systematically tested, and it is therefore not possible to compare their performance to scientifically tested springs. However, the Thing-designs can be used as the starting point of investigations into different, more experimental springs and their application in functional designs, created by AM.

3.4 MANUFACTURING 3D PRINTED SPRINGS

3.4.1 3D print technologies

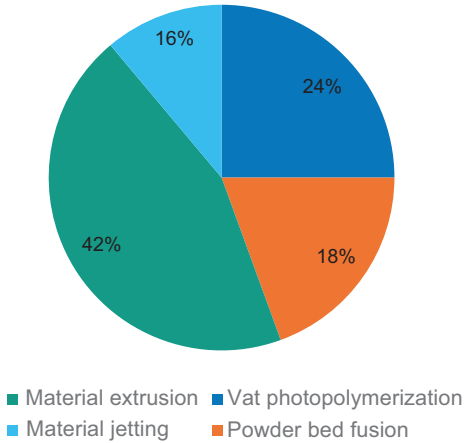


Figure 3.10: Distribution of the applied AM technologies identified in the scientific search results.

AM consists of a large group of layer-based technologies, which can be classified in numerous different ways. We followed the classification of the ASTM organization for clarity [124], which divides AM technologies into seven different groups: material extrusion, vat photopolymerization, material jetting, powder bed fusion, sheet lamination, directed energy deposition, and binder jetting. Figure 3.10 shows the division of different AM methods used to manufacture springs for the results from the scientific query, only four groups of AM technologies were encountered: material extrusion, material jetting, vat photopolymerization, and powder bed fusion. The results from the non-scientific

Thing-query are not included, since they all used material extrusion technology. The most applied technology in the scientific search is also material extrusion, used in about 42% of the spring designs. Material extrusion includes Fused Deposition Modelling (FDM), a commonly available and cheap-to-use type of printing, which can explain its popularity in both scientific and non-scientific communities. The second most used technique in the scientific results is vat photopolymerization, in which a resin is cured by a UV source. This technology is known for its high resolution. Less used are powder bed fusion and material jetting, identified in about 18% and 16% of the scientific results, respectively. These printing technologies have a high threshold to operate, requiring expensive equipment and expertise, which can explain their infrequent use. Sheet lamination, binder jetting, and directed energy deposition were not identified in our results. Although all scientific articles reported the used AM technology, often the choice of certain AM methods or materials is not substantiated.

3.4.2 Materials

The choice of material depends to a certain extent on the chosen AM technology. We distinguished two general groups of materials used to 3D print springs: polymer-based materials and metals. Polymer-based materials are the most commonly used materials in AM technologies, and can be used in the form of filaments, powders, or photo-sensitive resins. In 92% of the identified scientific articles polymer-based materials were used, whereas only in three instances metal was used. Danun et al. [125] designed custom springs consisting of separate building blocks printed in stainless steel. Saleh and Ragab [110] used

a titanium alloy to 3D print helical springs with different pitches, to investigate the influence of the geometry on the mechanical properties. Skylar-Scott et al. [126] showed that they were able to build support-free helical springs with different geometries using a Direct Ink Writing process with silver ink. Other attempts at producing metallic springs consisted of coating designs printed with polymer-based processes with a nickel or copper coating to improve conductivity [13,94], or printing with a PLA-based filament filled with copper particles [45].

Of the polymer-based materials, PLA is the most used type of polymer for both the scientific and non-scientific results. PLA is one of the main materials used for printing by FDM due to its low price, ease of processing, and lack of harmful substances when printing. A disadvantage of PLA is that it is fairly brittle, which makes it less suitable for the design of elastic components, such as springs. Some Thing-authors noted specifically that their designs should be printed in ABS [21,23, 33,36,41,116,120,127,128], because of its higher flexibility. However, others adjusted the design of the spring to comply with the properties of PLA, for instance by creating longer flexures [129], or recommended using PLA because of its higher stiffness [25,66,68,74]. PLA does tend to creep over time when a mechanical load is applied to it, therefore, some authors advised to not keep the spring under permanent loading conditions [39,40,66].

Polymeric materials often exhibit hysteresis, which in the case of 3D printed springs means that part of the spring energy is absorbed by the material [119]. The amount of hysteresis depends on the material and AM process. Nazir et al. [109] investigated helical springs printed with PA12 powder, and found that in the first hysteresis cycle a higher percentage of energy was lost as compared to the 20th cycle. They ascribed this to ‘setting’ of the material, as a consequence of porosity, residual stresses, or unfused powder, rather than permanent deformation. Other studies have noted similar behaviour, where the hysteresis loop reached equilibrium after a number of cycles, for a powder-based wave [119] and helical spring [108], and for a material extrusion helical spring [92]. For the latter, the hysteresis was less pronounced in stiffer springs. Helical microsprints fabricated using 2-photonlithography showed an increase in hysteresis for each additional load cycle, resulting in plastic deformation [94], while a wave spring printed in ABS showed barely any hysteresis after repeated testing [114].

3.4.3 Settings

On the Thing-pages, authors can give tips for which print settings to use to obtain the best results. These settings are valid only for FDM-type printers. The most discussed settings for springs are the number of ‘walls’, i.e. outer layers of the part, the amount of ‘infill’ used, which is a porous structure used for the interior of the part, and the settings for support structures. A high number of outer walls and high infill percentage (>50%) were often reported to lead to a spring with more strength and higher stiffness [17,49,55,68,123,130-133], as this adds more material to the spring, while a low infill percentage results in a low-stiffness spring [32]. A lower layer thickness was also recommended for a stronger spring [92].

Support structures are often seen as a necessary evil while 3D printing, since they utilize material that has to be removed in an additional post-processing step, in which delicate features of the spring risk breaking off [14,125]. Support structures are only required for spatial springs, since planar springs can be printed flat on the build plate. In most AM technologies, supports are required only if the angle with respect to the build plate is not self-supporting [125]. Both in the Things and scientific papers, 3D printing springs without support structures received a lot of attention. Helical springs can be designed in such a way that the angle of the windings is self-supporting, eliminating the need for support material [129–131,134,135]. A popular solution among the Things is to design the helix in such a way that each winding is resting on top of the previous winding, without fusing together [101,104–107], such as in the left spring of Figure 3.8c. After printing, the windings have to be pried loose using a spatula or a knife. This design solution results in tension-only springs, since the windings are already printed in their compressed state. Another strategy is to design the helical spring with a self-supporting rectangular or triangular cross-section, such as the right spring of Figure 3.8c, so that a flat side can be oriented on the build plate, preventing the need for support structures [101–103].

Farahani et al. [96] reviewed self-supporting helical microsprings, for which removing supports would be practically impossible due to the small size of the springs. He concluded that although multiple AM methods are capable of creating precise self-supporting microsprings, the highest precision was obtained when printing the helix on a rotating cylinder, which requires a specialized set-up. Danun et al. [125] showed that it was possible to create customized spatial springs consisting of separate building blocks using metal AM. By taking into account the maximum overhang angles, they created self-supporting structures, in order to avoid lengthy post-processing operations to remove the support material after printing. Inkjet-type printing, such as the relatively new StarJet technique, allows for the creation of support-free springs by carefully controlling the printing velocity, such that each droplet is deposited onto and supported by the previous one [136]. Skylar-Scott et al. [126] showed that they were able to build support-free helical springs with different geometries using a Direct Ink Writing process with silver ink utilizing this

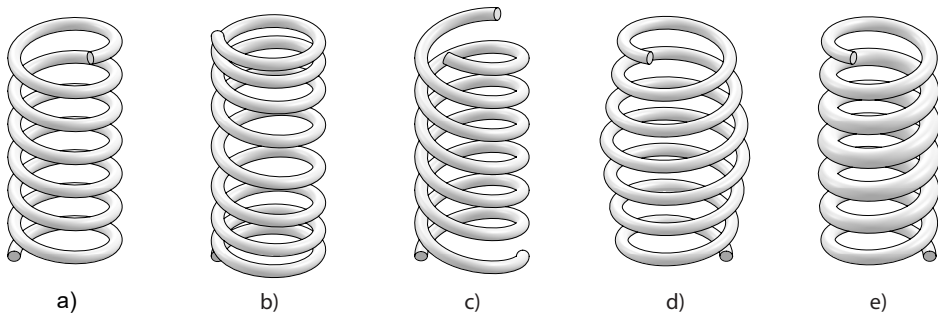


Figure 3.11: Examples of helical springs with variable dimensions. a) Standard helical spring. b) Helical spring with variable pitch. c) Helical spring with two helices intertwined. d) Helical spring with variable main diameter. e) Helical spring with variable wire diameter

strategy. For some AM technologies support structures are less of a problem, such as for powder-based technologies, in which the powder functions as support [118,119], or for multimaterial inkjet processes, for which custom support materials are available that can be dissolved in water, a chemical solution, or by means of heat [84]. In cases where support structures cannot be avoided, sometimes a better solution is to design custom supports that are easier to remove than the supports that are automatically generated by the slicing software [123].

3

3.5 ADVANTAGES OF 3D PRINTED SPRINGS

Advantages of 3D printed springs are that the springs can be made more complex or customized at no additional costs, especially in the case of varying the dimensions of springs to obtain specific characteristics. Several studies showed the advantages of helical springs with variable dimensions, such as pitch, main diameter, and wire diameter (Figure 3.11) [6,108,109]. Arshad et al. [6] compared springs with multiple helices, variable pitches, and variable diameters, but with identical mass. Their findings show that the stiffness of springs can be increased by adding more helices, increasing the pitch towards the centre, and increasing the wire diameter at the centre, although the higher stiffness comes at the cost of fatigue life. Nazir et al. [109] also tested variable dimension helical springs, their findings suggest that larger wire diameters can enhance the energy storage capacity of the springs, but it also makes them more prone to permanent deformation. Springs with variations in the main diameter showed a significantly higher load-bearing capacity, as compared to a standard helical spring. In the design of a new kind of shoe midsole, Ali et al. [108] compared the performance of 3D printed helical springs with uniform dimensions to 3D printed helical springs with variable dimensions, such as a varying diameter. They found that the variable dimension springs had a higher force bearing capacity, a lower deflection after loading, and better stability, which shows the advantage of using 3D printing to create specific properties based on the requirements of the design. Rather than vary the dimensions of the spring itself, one Thing-author created a functional suspension spring, by making use of two helical springs inside one another, in order to obtain the required properties [128].

3D printed helical springs often make use of a rectangular wire cross-section [92,95,127,130-132,135,137-139,98,100,101,103,105-107,123]. With AM technologies, rectangular cross-sections are easier to produce than circular cross-sections, due to the layer-wise nature of the process. An advantage of a rectangular wire is that it contains more material within a specified outer diameter, as compared to a circular wire, and therefore more energy can be stored within the same volume [1]. In addition, springs with a rectangular wire have a higher rigidity [2]. The elastic stress distribution is not as uniform as for a circular wire diameter, which can cause premature breakage of the wire. However, for springs with a short lifespan, such as is the case for 3D printed springs, this is less of a concern. A disadvantage of rectangular wire in a conventional manufacturing process is that the wire will deform due to coiling, and can take on a trapezoidal shape [1,2]. This

reduces the space efficiency and energy storage capacity. Since 3D printed springs are not coiled but built in a helical manner, this negative effect does not influence them.

Wave springs have the advantage that they can be produced in shorter lengths than helical springs, with similar mechanical properties, such as the stiffness. However, conventional production of wave springs is more complex than that of helical springs, and due to the production method, a small clearance exists between the waves [118]. In 3D printed designs, the waves are printed in a layer-wise manner, and can therefore be produced as a monolithic part. Haq, Nazir and Jeng [118] investigated 3D printing variable dimension wave springs (Figure 3.12a), and compared waves that were not connected to each other (D1 in Figure 3.12a) with waves that were fused together (D2-D10 in Figure 3.12a). They showed that the fused wave springs had improved properties over the non-contact wave springs, in terms of higher load-bearing capacity, higher stiffness and lower energy absorption. A larger overlap between the waves resulted in a higher stiffness. The tapered wave spring (D7 in Figure 3.12a) with variable diameter showed the best performance in terms of load-bearing capacity and energy absorption.

Another advantage of the use of AM is the ability to produce springs with built-in constraints [140]. He et al. [138] considered three basic deformations for a helical spring: linear, bend, and twist. They integrated constraints in their designs so that the springs were able to only deform in one of the specified directions, and implemented them into a parametric design tool that can automatically generate the constraints in CAD-software [141]. Springs with nonlinear behaviour, in which the stiffness of the spring decreases with higher force application, were designed and printed by Boehler et al. [142]. They used material jetting with multiple materials for the design, which allowed them to compare a helical spring made of a single, rigid material, with a bi-material spring consisting of

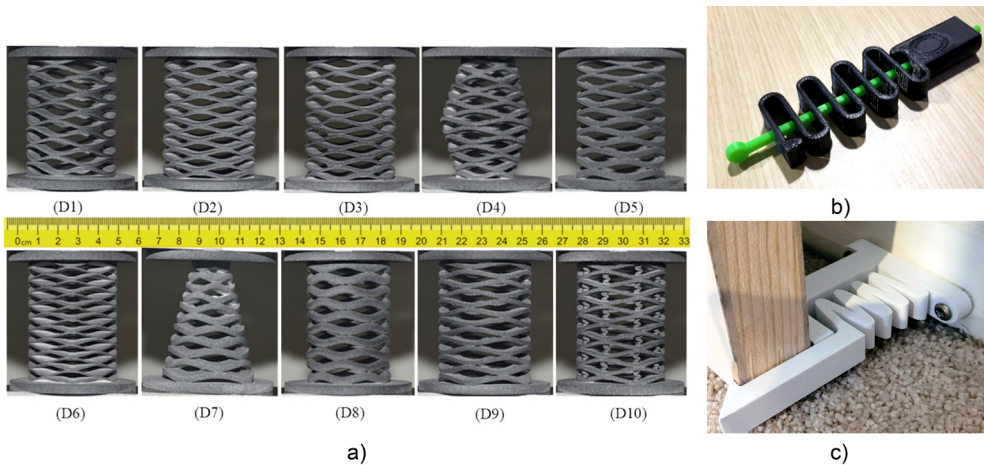


Figure 3.12: Advantages of 3D printed springs. a) Wave springs printed with variable dimensions and varying overlap in the waves, D1 with no overlap, D2-D10 with varying amounts of overlap [118]. b) Zigzag spring with built-in constraint to only allow linear motion [143]. c) 3D printed doorstop with built-in constraint to prevent it from buckling one way [17].

a rod of flexible material as the spring element. The bi-material spring showed a larger range of stiffness variation. A number of Thing-authors also incorporated deformation constraints into their designs, most commonly in combination with zigzag springs (Figure 3.12b-c) [17,18,21,143,144].

3.6 DISCUSSION AND CONCLUSION

This review article provides an overview of AM spring designs, as encountered in scientific articles and a hobbyist database, called Thingiverse. We categorized the springs we encountered in planar and spatial designs, and analysed their design, applications, and fabrication method. The design freedom of AM can be used to create more complex spring designs in less time as compared to conventional manufacturing. Most designs we have encountered are not original for AM, but rather based on conventional designs. However, other advantages of using AM have been utilized, such as varying the dimensions within one spring to customize the performance to the application, and integrating constraints. In addition, many of the hobbyist authors did not print a single spring, but integrated the spring into larger, functional designs that can be printed in one step, so-called print-in-place or non-assembly designs [20,21,76,131,135,145,22,26-28,30,52,64,66].

The limitations of AM technologies should always be taken into account to ensure the functional performance of the spring. Limitations related to the layer-wise nature of AM are particularly relevant for the design of springs consisting of relatively fragile wire structures, with relatively high deformation modes. The sensitivity of spring designs to the build plate orientation and layer directions can limit their mechanical properties [113], and as such their application in non-assembly mechanisms and integrated applications, where it is not always possible to orient the spring in the preferred way. The layered nature of 3D prints can also influence their longevity. Although the performance of 3D printed springs has been studied and modelled, relatively little attention has been paid to the fatigue life [6,92]. This is particularly relevant since plastics are the main used material for 3D printed springs. All found studies focused on a single AM method for their springs; comparisons between different printing techniques for equal designs were not found [92]. In addition, we encountered only a few comparisons between 3D printed springs and springs produced with conventional manufacturing.

The spring designs from the Thingiverse database were often not substantiated or systematically tested, however the models provided insight into a diverse range of possible 3D printed spring designs and potential applications. Moreover, these designs covered a much larger variety of geometries and possible applications than found in the scientific literature. The scientific articles, however, provided more insight into the performance of various spring designs, by systematically testing and describing all aspects of the design. We have encountered several cases in which a result from the hobbyist database was based on a scientific article, and vice versa. Therefore, both scientific and hobbyist results complement each other to give a complete overview of possible spring designs for AM, and can be used as inspiration for future research.

The lack of completely new spring designs that we encountered can be attributed to the difficulty of predicting the properties of 3D printed springs. Even for conventional designs, the AM process provides a number of uncertainties, due to its anisotropic nature, that make it difficult to theoretically model the behaviour of the spring. Considering that the spring behaviour will be different depending on the chosen AM process, material, orientation on the build plate, layer height, printer parameters, et cetera, the design of AM springs relies more on practical experiments than theoretical models. This means that it can be fairly time-consuming to develop a spring with the necessary properties for a given application. The hobbyist community can contribute in this respect to this practical approach, since they already adopted a hands-on trial-and-error approach towards printing of springs, and can be considered as a library of best-practice examples as a starting point for further development.

Due to the sheer number of Things available in Thingiverse, it is more than likely that we missed relevant and interesting results. However, since the number of models changes daily, it is unfeasible to sort through all results in an objective manner. In addition, the search engine of Thingiverse is notoriously unreliable, and will present different results on different days or in different browsers when searching only for 'relevant' results. The most stable metrics are popularity and number of makes, especially in the higher numbers, since it will take some time for a model to build up enough traction to receive many likes and makes. In order to get a significant number of likes, the print needs to be well designed, but also well-printable. As such, the designs that were included in this review have in a way been peer-reviewed by other users of the platform, because users will comment on mistakes, correct them with models of their own, as well as vote for well-thought-out designs.

REFERENCES

- [1] A.M. Wahl, *Mechanical springs*, McGraw-Hill, New York, 1963.
- [2] D. Gonen, A. Oral, M.C. Cakir, Investigating the benefits of using circular die springs instead of rectangular die springs, *Fatigue Fract. Eng. Mater. Struct.* 38 (2015) 799–812. <https://doi.org/10.1111/ffe.12269>.
- [3] R.C. Juvinall, K.M. Marshek, *Fundamentals of Machine Component Design*, 5th ed., Wiley, 2006.
- [4] I. Gibson, D.W. Rosen, B. Stucker, *Additive Manufacturing Technologies*, Springer US, Boston, MA, 2010. <https://doi.org/10.1007/978-1-4419-1120-9>.
- [5] J.S. Cuellar, G. Smit, D. Plettenburg, A. Zadpoor, Additive manufacturing of non-assembly mechanisms, *Addit. Manuf.* 21 (2018) 150–158. <https://doi.org/10.1016/j.addma.2018.02.004>.
- [6] A. Bin Arshad, A. Nazir, J.-Y. Jeng, Design and performance evaluation of multi-helical springs fabricated by Multi Jet Fusion additive manufacturing technology, *Int. J. Adv. Manuf. Technol.* 118 (2022) 195–206. <https://doi.org/10.1007/s00170-021-07756-2>.
- [7] H.-J. Steenhuis, L. Pretorius, Consumer additive manufacturing or 3D printing adoption: an exploratory study, *J. Manuf. Technol. Manag.* 27 (2016) 990–1012. <https://doi.org/10.1108/JMTM-01-2016-0002>.

- [8] J.I. Novak, P. Bardini, The Popular Culture of 3D Printing, in: 2019: pp. 188-211. <https://doi.org/10.4018/978-1-5225-8491-9.ch012>.
- [9] J.I. Novak, 500 days of Thingiverse: a longitudinal study of 30 popular things for 3D printing, *Rapid Prototyp. J. ahead-of-p* (2020). <https://doi.org/10.1108/RPJ-01-2020-0021>.
- [10] About - Thingiverse, (n.d.). <https://www.thingiverse.com/about> (accessed February 14, 2022).
- [11] A.G. Özkil, Collective design in 3D printing: A large scale empirical study of designs, designers and evolution, *Des. Stud.* 51 (2017) 66-89. <https://doi.org/10.1016/j.destud.2017.04.004>.
- [12] BYU_CM, Ortho-Planar Spring, Thingiverse. (2018). <https://www.thingiverse.com/thing:3007261> (accessed June 9, 2022).
- [13] J. Cui, J. Wang, Y. Zhong, L. Pan, J.A. Weibel, Metallized compliant 3D microstructures for dry contact thermal conductance enhancement, *J. Micromechanics Microengineering.* 28 (2018) 055005. <https://doi.org/10.1088/1361-6439/aaaf2e>.
- [14] C.C. Tutum, S. Chockchowwat, E. Vouga, R. Miikkulainen, Functional generative design, in: *Proc. Genet. Evol. Comput. Conf., ACM, New York, NY, USA, 2018*: pp. 1379-1386. <https://doi.org/10.1145/3205455.3205635>.
- [15] Breyton, Z Axis Return Spring, Thingiverse. (2014). <https://www.thingiverse.com/thing:615104> (accessed June 9, 2022).
- [16] Jakejake, Universal Phone Tripod Mount, Thingiverse. (2015). <https://www.thingiverse.com/thing:2423960> (accessed June 9, 2022).
- [17] HoustonAU, Spring Doorstop / Door Catch, Thingiverse. (2021). <https://www.thingiverse.com/thing:4920263> (accessed June 9, 2022).
- [18] Caganseval, micro spring door lock / latch, Thingiverse. (2017). <https://www.thingiverse.com/thing:2311908> (accessed June 9, 2022).
- [19] Radus, Battery box with printed spring, Thingiverse. (2014). <https://www.thingiverse.com/thing:374802> (accessed June 9, 2022).
- [20] Pixelle, Flexing Battery Holders with Integrated Spring, Thingiverse. (2017). <https://www.thingiverse.com/thing:2339441> (accessed June 9, 2022).
- [21] YXC, High current 18650/21700 holders with integrated spring, Thingiverse. (2017). <https://www.thingiverse.com/thing:2668159> (accessed June 9, 2022).
- [22] Oidan, Simple Sprung Bolt, Thingiverse. (2013). <https://www.thingiverse.com/thing:107959> (accessed June 9, 2022).
- [23] NirDobovizki, Durable Fully Printable Customizable Spring, Thingiverse. (2016). <https://www.thingiverse.com/thing:1795083> (accessed June 9, 2022).
- [24] Bandit-ed, spring ring, Thingiverse. (2014). <https://www.thingiverse.com/thing:446253> (accessed June 9, 2022).
- [25] Alerde, Door Closer, Thingiverse. (2018). <https://www.thingiverse.com/thing:2764294> (accessed June 9, 2022).
- [26] Briscoe28, s-carabiner, Thingiverse. (2013). <https://www.thingiverse.com/thing:165120> (accessed June 9, 2022).
- [27] Walter, Carabiner, Thingiverse. (2015). <https://www.thingiverse.com/thing:950426> (accessed June 9, 2022).
- [28] KidCrazy, Kcs clamp, Thingiverse. (2013). <https://www.thingiverse.com/thing:73469> (accessed June 9, 2022).

REFERENCES

- 2022).
- [29] Blakehaas, Spring Clip Stronger, Thingiverse. (2021). <https://www.thingiverse.com/thing:4908100> (accessed June 9, 2022).
- [30] Wuguigui, Clip, Thingiverse. (2021). <https://www.thingiverse.com/thing:4849576> (accessed June 9, 2022).
- [31] Eliask, Mini Hair Claw, Thingiverse. (2015). <https://www.thingiverse.com/thing:802586> (accessed June 9, 2022).
- [32] Landru, Springamathing 1.0, Thingiverse. (2011). <https://www.thingiverse.com/thing:12053> (accessed June 9, 2022).
- [33] PrettySmallThings, Spring Pins & Snake Pins, Thingiverse. (2012). <https://www.thingiverse.com/thing:17725> (accessed June 9, 2022).
- [34] Ghostsniper89, Braccialetto a molla - Bracelet spring, Thingiverse. (2015). <https://www.thingiverse.com/thing:954205> (accessed June 9, 2022).
- [35] OgoSport, Ogo Spring Connector, Thingiverse. (2014). <https://www.thingiverse.com/thing:369514> (accessed June 9, 2022).
- [36] Davision3d, Spring Things, Thingiverse. (2015). <https://www.thingiverse.com/thing:698639> (accessed June 9, 2022).
- [37] LeisureLuke, The Key - Puzzle Box, Thingiverse. (2020). <https://www.thingiverse.com/thing:4685893> (accessed June 9, 2022).
- [38] LeisureLuke, The Heist - Puzzle Box, Thingiverse. (2021). <https://www.thingiverse.com/thing:4826240> (accessed June 9, 2022).
- [39] Maxy, Ultimaker quiet retraction, Thingiverse. (2013). <https://www.thingiverse.com/thing:53690> (accessed June 9, 2022).
- [40] Maxy, Vibration Damper for Ultimaker, Thingiverse. (2013). <https://www.thingiverse.com/thing:90974> (accessed June 9, 2022).
- [41] TanyaAkinora, Bag holder with damper, Thingiverse. (2019). <https://www.thingiverse.com/thing:3420245> (accessed June 9, 2022).
- [42] D.M. Correa, C.C. Seepersad, M.R. Haberman, Mechanical design of negative stiffness honeycomb materials, *Integr. Mater. Manuf. Innov.* 4 (2015) 165-175. <https://doi.org/10.1186/s40192-015-0038-8>.
- [43] Abrokadabra, Honeycomb Spring, Thingiverse. (2015). <https://www.thingiverse.com/thing:1025626> (accessed June 9, 2022).
- [44] D.M. Correa, T. Klatt, S. Cortes, M. Haberman, D. Kovar, C. Seepersad, Negative stiffness honeycombs for recoverable shock isolation, *Rapid Prototyp. J.* 21 (2015) 193-200. <https://doi.org/10.1108/RPJ-12-2014-0182>.
- [45] D. Besnea, C.I. Rizescu, D. Rizescu, D. Comeaga, R. Ciobanu, E. Moraru, Study of deflection behavior of 3D printed leaf springs, *IOP Conf. Ser. Mater. Sci. Eng.* 444 (2018) 042008. <https://doi.org/10.1088/1757-899X/444/4/042008>.
- [46] K. Garanger, T. Khamvilai, E. Feron, 3D Printing of a Leaf Spring: A Demonstration of Closed-Loop Control in Additive Manufacturing, in: 2018 IEEE Conf. Control Technol. Appl., IEEE, 2018: pp. 465-470. <https://doi.org/10.1109/CCTA.2018.8511509>.
- [47] A. Kessentini, G.M.S. Ahmed, J. Madiouli, Design Optimization and FE Analysis of 3D Printed Carbon

- PEEK Based Mono Leaf Spring, *Micromachines*. 10 (2019) 279. <https://doi.org/10.3390/mi10050279>.
- [48] Muzz64, Wild Catz... with Jaws that Bite and Growl!, Thingiverse. (2015). <https://www.thingiverse.com/thing:988088> (accessed June 9, 2022).
- [49] Muzz64, SHARKZ... Fun Multipurpose Clips / Holders / Pegs with moving jaws that bite!, Thingiverse. (2015). <https://www.thingiverse.com/thing:910216> (accessed June 9, 2022).
- [50] Muzz64, PIRANHAZ, Thingiverse. (2016). <https://www.thingiverse.com/thing:1734347> (accessed June 9, 2022).
- [51] Muzz64, Minisaurus, Thingiverse. (2017). <https://www.thingiverse.com/thing:2476792> (accessed June 9, 2022).
- [52] ShawnGano, Pliers, Thingiverse. (2018). <https://www.thingiverse.com/thing:2749597> (accessed June 9, 2022).
- [53] Joo, cross tweezer, Thingiverse. (2012). <https://www.thingiverse.com/thing:25587> (accessed June 9, 2022).
- [54] George_collyer, Switch Knife, Thingiverse. (2019). <https://www.thingiverse.com/thing:3668073> (accessed June 9, 2022).
- [55] Charlie1982, Origami Carabiner by ddf3d.com, Thingiverse. (2016). <https://www.thingiverse.com/thing:1819242> (accessed June 9, 2022).
- [56] YSoft_be3D, BUSINESS CARD CASES, Thingiverse. (2016). <https://www.thingiverse.com/thing:1348371> (accessed June 9, 2022).
- [57] LoboCNC, Quick Clamp, Thingiverse. (2017). <https://www.thingiverse.com/thing:2477698> (accessed June 9, 2022).
- [58] CCCanyon, Crossbow, Western style, and Arrow, Thingiverse. (2016). <https://www.thingiverse.com/thing:1378783> (accessed June 9, 2022).
- [59] Muzz64, Spring Loaded Target for NERF Gun Fun!, Thingiverse. (2016). <https://www.thingiverse.com/thing:1239497> (accessed June 9, 2022).
- [60] MacGyver, TRAP! Improved Springs Stronger and No Support, Thingiverse. (2014). <https://www.thingiverse.com/thing:586182> (accessed June 9, 2022).
- [61] LeFabShop, Coil Spring, Thingiverse. (2015). <https://www.thingiverse.com/thing:746542> (accessed June 9, 2022).
- [62] DonaldJ, Springy Thing, Thingiverse. (2012). <https://www.thingiverse.com/thing:30182> (accessed June 9, 2022).
- [63] LeisureLuke, The Launch - Puzzle Box, Thingiverse. (2021). <https://www.thingiverse.com/thing:4722098> (accessed June 9, 2022).
- [64] Enif, Flexing battery holders with integrated spring, Thingiverse. (2014). <https://www.thingiverse.com/thing:456900> (accessed June 9, 2022).
- [65] LoboCNC, Improved One-piece Capo, Thingiverse. (2015). <https://www.thingiverse.com/thing:988513> (accessed June 9, 2022).
- [66] LoboCNC, One-Piece One-Handed Guitar Capo, Thingiverse. (2015). <https://www.thingiverse.com/thing:698317> (accessed June 9, 2022).
- [67] Makcumus, Spring_for_flux_gun, Thingiverse. (2017). <https://www.thingiverse.com/thing:2243343> (accessed June 9, 2022).
- [68] FULspeed, Spring propelled Catamaran, Thingiverse. (2015). <https://www.thingiverse.com/>

REFERENCES

- thing:1037341 (accessed June 9, 2022).
- [69] GreenDot, wind-up Bathtub Boat V4 - Badewannen Boot zum Aufziehen - Funktionsfähig, Thingiverse. (2019). <https://www.thingiverse.com/thing:3500845> (accessed June 9, 2022).
- [70] Benraay, PLA Spring motor, rolling car easy to mount, Thingiverse. (2016). <https://www.thingiverse.com/thing:1887099> (accessed June 9, 2022).
- [71] Johann517, Spring Plus, Thingiverse. (2014). <https://www.thingiverse.com/thing:448340> (accessed June 9, 2022).
- [72] TheGoofy, 3D-printed Watch with Tourbillon, Thingiverse. (2016). <https://www.thingiverse.com/thing:1249221> (accessed June 9, 2022).
- [73] A26, Triaxial Tourbillon Model II, Thingiverse. (2018). <https://www.thingiverse.com/thing:2761730> (accessed June 9, 2022).
- [74] A26, Flying Tourbillon Model 1.5, Thingiverse. (2018). <https://www.thingiverse.com/thing:2751917> (accessed January 17, 2022).
- [75] LtDan, Mechanical Counter, Thingiverse. (2015). <https://www.thingiverse.com/thing:824671> (accessed June 9, 2022).
- [76] Turbo_SunShine, PRINT-IN-PLACE SPRING LOADED BOX, Thingiverse. (2020). <https://www.thingiverse.com/thing:4382544> (accessed June 9, 2022).
- [77] 3d-printy, Twist Lock Coffin, Thingiverse. (2021). <https://www.thingiverse.com/thing:4967007> (accessed January 17, 2022).
- [78] Professor_pinball, Finger Springs, Thingiverse. (2017). <https://www.thingiverse.com/thing:2607235> (accessed June 9, 2022).
- [79] Jakejake, Springy Shape, Thingiverse. (2017). <https://www.thingiverse.com/thing:813365> (accessed June 9, 2022).
- [80] U. Scarcia, G. Berselli, C. Melchiorri, M. Ghinelli, G. Palli, Optimal Design of 3D Printed Spiral Torsion Springs, in: Vol. 2 Model. Simul. Control. Bio-Inspired Smart Mater. Syst. Energy Harvest., American Society of Mechanical Engineers, 2016: p. V002T03A020. <https://doi.org/10.1115/SMASIS2016-9218>.
- [81] J.J. Parise, L.L. Howell, S.P. Magleby, Ortho-Planar Linear-Motion Springs, Mech. Mach. Theory. 36 (2001) 1281. <https://scholarsarchive.byu.edu/facpub> (accessed January 17, 2022).
- [82] G.H. Teichert, B.D. Jensen, Design and fabrication of a fully-compliant mechanism for control of cellular injection arrays, Prod. Eng. 7 (2013) 561–568. <https://doi.org/10.1007/s11740-013-0475-1>.
- [83] Z. Yao, R. Zhao, V. Zega, A. Corigliano, A metaplate for complete 3D vibration isolation, Eur. J. Mech. - A/Solids. 84 (2020) 104016. <https://doi.org/10.1016/j.euromechsol.2020.104016>.
- [84] B. Kawa, K. Iiwa, V. Lee, Q. Shi, R. Walczak, Inkjet 3D Printed MEMS Vibrational Electromagnetic Energy Harvester, Energies. 13 (2020) 2800. <https://doi.org/10.3390/en13112800>.
- [85] C. Qiu, P. Qi, H. Liu, K. Althoefer, J. S. Dai, Six-Dimensional Compliance Analysis and Validation of Orthoplanar Springs, J. Mech. Des. Trans. ASME. 138 (2016). <https://doi.org/10.1115/1.4032580/474842>.
- [86] Tjhowse, Parametric airless tire, Thingiverse. (2012). <https://www.thingiverse.com/thing:17514> (accessed June 9, 2022).
- [87] Scanlime, 2D Spring Generator, Thingiverse. (2011). <https://www.thingiverse.com/thing:5713> (accessed June 9, 2022).
- [88] Thehans, Linear Stage Flexures, Thingiverse. (2015). <https://www.thingiverse.com/thing:1118407>

- (accessed June 9, 2022).
- [89] Jwillmer, Ortho-Planar Spring, Thingiverse. (2019). <https://www.thingiverse.com/thing:3648464> (accessed June 9, 2022).
- [90] Casteer, Ortho-planar linear spring, Thingiverse. (2015). <https://www.thingiverse.com/thing:1025241> (accessed June 9, 2022).
- [91] V. Bertana, G. De Pasquale, S. Ferrero, L. Scaltrito, F. Catania, C. Nicosia, S.L. Marasso, M. Cocuzza, F. Perrucci, 3D Printing with the Commercial UV-Curable Standard Blend Resin: Optimized Process Parameters towards the Fabrication of Tiny Functional Parts, *Polymers (Basel)*. 11 (2019) 292. <https://doi.org/10.3390/polym11020292>.
- [92] S. Enea, S.K. Moon, Guidelines for 3D printed springs using material extrusion, *Rapid Prototyp. J. ahead-of-p* (2021). <https://doi.org/10.1108/RPJ-04-2020-0078>.
- [93] L. He, H. Peng, M. Lin, R. Konjeti, F. Guimbretière, J.E. Froehlich, Ondulé: designing and controlling 3D printable springs, in: *Proc. 32nd Annu. ACM Symp. User Interface Softw. Technol.*, ACM, New York, NY, USA, 2019: pp. 739-750. <https://doi.org/10.1145/3332165.3347951>.
- [94] P. Schürch, R. Ramachandramoorthy, L. Pethö, J. Michler, L. Philippe, Additive manufacturing by template-assisted 3D electrodeposition: Nanocrystalline nickel microsprings and microspring arrays, *Appl. Mater. Today*. 18 (2020) 100472. <https://doi.org/10.1016/j.apmt.2019.100472>.
- [95] L. Jonušauskas, T. Baravykas, D. Andriječ, T. Gadišauskas, V. Purlys, Stitchless support-free 3D printing of free-form micromechanical structures with feature size on-demand, *Sci. Rep.* 9 (2019) 17533. <https://doi.org/10.1038/s41598-019-54024-1>.
- [96] R.D. Farahani, K. Chizari, D. Therriault, Three-dimensional printing of freeform helical microstructures: a review, *Nanoscale*. 6 (2014) 10470. <https://doi.org/10.1039/C4NR02041C>.
- [97] W. Ren, J. Xu, Z. Lian, X. Sun, Z. Xu, H. Yu, Localized electrodeposition micro additive manufacturing of pure copper microstructures, *Int. J. Extrem. Manuf.* 4 (2022) 015101. <https://doi.org/10.1088/2631-7990/ac3963>.
- [98] K. Ogawa, K. Tanaka, T. Minagawa, Y. Ochiai, Design method of digitally fabricated spring glass pen, in: *ACM SIGGRAPH 2018 Posters*, ACM, New York, NY, USA, 2018: pp. 1-2. <https://doi.org/10.1145/3230744.3230809>.
- [99] K. Tanaka, T. Ohshima, Y. Ochiai, Spring-pen, in: *SIGGRAPH Asia 2017 Posters*, ACM, New York, NY, USA, 2017: pp. 1-2. <https://doi.org/10.1145/3145690.3145732>.
- [100] D. Besnea, D. Rizescu, C. Rizescu, E. Dinu, V. Constantin, E. Moraru, Additive Technologies and Materials for Realization of Elastic Elements, in: *Lect. Notes Networks Syst.*, Springer, Cham, 2019: pp. 62-70. https://doi.org/10.1007/978-3-319-96358-7_7.
- [101] ImmersedN3D, Support Free SLINKY, Thingiverse. (2016). <https://www.thingiverse.com/thing:1528375> (accessed June 9, 2022).
- [102] Joeserdynski, Attempt at making PLA springs, Thingiverse. (2012). <https://www.thingiverse.com/thing:18965> (accessed June 9, 2022).
- [103] Pario, Fully Printable Rectangular Spring, Thingiverse. (2017). <https://www.thingiverse.com/thing:2668695> (accessed June 9, 2022).
- [104] JustinSDK, Toy spring, Thingiverse. (2017). <https://www.thingiverse.com/thing:2296745> (accessed June 9, 2022).
- [105] JustinSDK, Slinky dog, Thingiverse. (2017). <https://www.thingiverse.com/thing:2385869> (accessed

- June 9, 2022).
- [106] Desktop_Makes, Slinky, Thingiverse. (2017). <https://www.thingiverse.com/thing:2360999> (accessed June 9, 2022).
- [107] 3DP_PARK, Springy Rabbit (2), Thingiverse. (2019). <https://www.thingiverse.com/thing:4058182> (accessed January 17, 2022).
- [108] M. Ali, A. Nazir, J.-Y. Jeng, Mechanical performance of additive manufactured shoe midsole designed using variable-dimension helical springs, *Int. J. Adv. Manuf. Technol.* 111 (2020) 3273–3292. <https://doi.org/10.1007/s00170-020-06227-4>.
- [109] A. Nazir, M. Ali, C.-H. Hsieh, J.-Y. Jeng, Investigation of stiffness and energy absorption of variable dimension helical springs fabricated using multijet fusion technology, *Int. J. Adv. Manuf. Technol.* 110 (2020) 2591–2602. <https://doi.org/10.1007/s00170-020-06061-8>.
- [110] M. Saleh, A. Ragab, Ti-6 Al-4 V Helical Spring Manufacturing via SLM : Effect of Geometry on Shear Modulus, in: *Proc. Int. MultiConference Eng. Comput. Sci. Vol. 2, 2013*.
- [111] N. Huynh, G. Dubrovsky, J.D. Rouch, A. Scott, E. Chiang, T. Nguyen, B.M. Wu, S. Shekherdimian, T.M. Krummel, J.C.Y. Dunn, Three-dimensionally printed surface features to anchor endoluminal spring for distraction enterogenesis, *PLoS One.* 13 (2018) e0200529. <https://doi.org/10.1371/journal.pone.0200529>.
- [112] W.A. Chapkin, P. Walgren, G.J. Frank, D.R. Seifert, D.J. Hartl, J.W. Baur, Design and optimization of high-strain, cylindrical composite skins for morphing fuselages, *Mater. Des.* 187 (2020) 108395. <https://doi.org/10.1016/j.matdes.2019.108395>.
- [113] J.A. Gardner, T. Nethercott-Garabet, N. Kaill, R.I. Campbell, G.A. Bingham, D.S. Engstrøm, N.O. Balç, Aligning Material Extrusion Direction with Mechanical Stress via 5-Axis Tool Paths, in: *Solid Free. Fabr. 2018 Proc. 29th Annu. Int. Solid Free. Fabr. Symp. – An Addit. Manuf. Conf. Rev. Pap.*, 2018.
- [114] P. Sampath, E. De Silva, L. Sameera, I. Udayanga, R. Amarasinghe, S. Weragoda, A. Mitani, Development of a Conductive Polymer Based Novel 1-DOF Tactile Sensor with Cylindrical Arch Spring Structure Using 3D Printing Technology, *Sensors.* 19 (2019) 318. <https://doi.org/10.3390/s19020318>.
- [115] Jspark, Spring., Thingiverse. (2013). <https://www.thingiverse.com/thing:70881> (accessed June 9, 2022).
- [116] Bagelturf, Plastic spring, Thingiverse. (2013). <https://www.thingiverse.com/thing:39963> (accessed June 9, 2022).
- [117] Y.-B. Bin Wang, H.-T.T. Liu, Z.-Y.Y. Zhang, Rotation spring: Rotation symmetric compression-torsion conversion structure with high space utilization, *Compos. Struct.* 245 (2020) 112341. <https://doi.org/10.1016/j.compstruct.2020.112341>.
- [118] M.R. ul Haq, A. Nazir, J.-Y. Jeng, Design for additive manufacturing of variable dimension wave springs analyzed using experimental and finite element methods, *Addit. Manuf.* 44 (2021) 102032. <https://doi.org/10.1016/j.addma.2021.102032>.
- [119] M.R. ul Haq, A. Nazir, S.-C. Lin, J.-Y. Jeng, Parametric investigation of functionally gradient wave springs designed for additive manufacturing, *Int. J. Adv. Manuf. Technol.* (2021) 1–19. <https://doi.org/10.1007/s00170-021-08325-3>.
- [120] Magonegro, Customizable spring, Thingiverse. (2016). <https://www.thingiverse.com/thing:1690305> (accessed June 9, 2022).
- [121] A.S. Dalaq, M.F. Daqaq, Experimentally-validated computational modeling and characterization of

- the quasi-static behavior of functional 3D-printed origami-inspired springs, *Mater. Des.* 216 (2022) 110541. <https://doi.org/10.1016/j.matdes.2022.110541>.
- [122] S. Khazaaleh, R. Masana, M.F. Daqaq, Combining advanced 3D printing technologies with origami principles: A new paradigm for the design of functional, durable, and scalable springs, *Compos. Part B Eng.* 236 (2022) 109811. <https://doi.org/10.1016/j.compositesb.2022.109811>.
- [123] Muzz64, Springy Stand, Thingiverse. (2017). <https://www.thingiverse.com/thing:2432999> (accessed June 9, 2022).
- [124] ISO/ASTM 52910, Standard Guidelines for Design for Additive Manufacturing, ASTM B. Stand. 2017 (2017) 1-14. <https://doi.org/10.1520/ISO>.
- [125] A.N. Danun, P.D. Palma, C. Klahn, M. Meboldt, Building Block Synthesis of Self-Supported Three-Dimensional Compliant Elements for Metallic Additive Manufacturing, *J. Mech. Des.* 143 (2021). <https://doi.org/10.1115/1.4048220>.
- [126] M.A. Skylar-Scott, S. Gunasekaran, J.A. Lewis, Laser-assisted direct ink writing of planar and 3D metal architectures, *Proc. Natl. Acad. Sci.* 113 (2016) 6137-6142. <https://doi.org/10.1073/pnas.1525131113>.
- [127] NirDobovizki, 3D Printed Spring (Customizable), Thingiverse. (2016). <https://www.thingiverse.com/thing:1758631> (accessed June 9, 2022).
- [128] BME_Sundevil, Spring Suspension, Thingiverse. (2010). <https://www.thingiverse.com/thing:3551> (accessed June 9, 2022).
- [129] HeyVye, Printable Spring with Manual Support, Thingiverse. (2020). <https://www.thingiverse.com/thing:4591444> (accessed June 9, 2022).
- [130] Muzz64, Springy Apple Cable Savers, Thingiverse. (2015). <https://www.thingiverse.com/thing:1091637> (accessed June 9, 2022).
- [131] Muzz64, PIGZ, Thingiverse. (2018). <https://www.thingiverse.com/thing:2881420> (accessed June 9, 2022).
- [132] Laykanics, SPRING, Thingiverse. (2017).
- [133] Jashmakes, Spring, Thingiverse. (2017).
- [134] AntsinAfrica, Spring, Thingiverse. (2021). <https://www.thingiverse.com/thing:4846165> (accessed June 9, 2022).
- [135] Muzz64, "Bobblerz," Thingiverse. (2017). <https://www.thingiverse.com/thing:2396624> (accessed June 9, 2022).
- [136] B. Gerdes, R. Zengerle, P. Koltay, L. Riegger, Direct printing of miniscule aluminum alloy droplets and 3D structures by StarJet technology, *J. Micromechanics Microengineering.* 28 (2018) 074003. <https://doi.org/10.1088/1361-6439/aab928>.
- [137] HLOff, 3D Printed Working Spring, Thingiverse. (2021). <https://www.thingiverse.com/thing:5174545> (accessed June 9, 2022).
- [138] L. He, H. Peng, J. Land, M.D. Fuge, J.E. Froehlich, Designing 3D-Printed Deformation Behaviors Using Spring-Based Structures, in: *Adjun. Publ. 30th Annu. ACM Symp. User Interface Softw. Technol.*, ACM, New York, NY, USA, 2017: pp. 151-153. <https://doi.org/10.1145/3131785.3131836>.
- [139] E. Sacco, S.K. Moon, Modelling the stiffness of plastic springs manufactured via additive manufacturing, *Proc. Inst. Mech. Eng. Part B J. Eng. Manuf.* (2021) 095440542110382. <https://doi.org/10.1177/09544054211038282>.
- [140] M. Kimura, S. Nakatani, S.-I. Nishida, D. Taketoshi, N. Araki, 3D Printable Dry EEG Electrodes with

REFERENCES

- Coiled-Spring Prongs, *Sensors*. 20 (2020) 4733. <https://doi.org/10.3390/s20174733>.
- [141] L. He, H. Peng, M. Lin, R. Konjeti, F. Guimbretière, J.E. Froehlich, Ondulé, in: *Proc. 32nd Annu. ACM Symp. User Interface Softw. Technol.*, ACM, New York, NY, USA, 2019: pp. 739-750. <https://doi.org/10.1145/3332165.3347951>.
- [142] Q. Boehler, M. Vedrines, S. Abdelaziz, P. Poignet, P. Renaud, Parallel Singularities for the Design of Softening Springs Using Compliant Mechanisms, in: *Vol. 5A 39th Mech. Robot. Conf.*, American Society of Mechanical Engineers, 2015. <https://doi.org/10.1115/DETC2015-47240>.
- [143] BitsnBolts, Spring Flinger, Thingiverse. (2017). <https://www.thingiverse.com/thing:2367861> (accessed June 9, 2022).
- [144] Obijuan, Parameterized printable spring, Thingiverse. (2012). <https://www.thingiverse.com/thing:21234> (accessed June 9, 2022).
- [145] Thomasforsyth, Clip Peg - General purpose, Thingiverse. (2014). <https://www.thingiverse.com/thing:298955> (accessed June 9, 2022).

4 A STUDY ON POLISHING COMPLEX 3D PRINTED PARTS

Parts produced with metal additive manufacturing often suffer from a poor surface finish. Surface finishing techniques are effective to improve the quality of 3D printed surfaces, however they have as downsides that they also slightly change the geometry of the part, in an unpredictable way. This effect on the geometrical features of complex parts has received little attention. In this research, we illustrate a method to visualize the impact of surface finishing techniques on geometrical features, as well as their effectiveness on parts with high shape-complexity, by using centrifugal disk finishing as a case study. We designed and 3D printed test parts with different features using selective laser melting, which were coated with a blue metal lacquer prior to polishing. After polishing, the blue lacquer was eroded away from the spots that were easily reached by the polishing process, yet had remained on the surfaces that could not be reached by the process. We used measurements of material removal and image processing of the remaining blue lacquer on the surfaces to analyze these effects. Using this method, we were able to derive a number of specific design guidelines that can be incorporated while designing metal AM parts for centrifugal disk finishing. We suggest that this visualization method can be applied to different polishing methods to gain insight into their influence, as well as being used as an aid in the design process.

Published as:

K. Lussenburg, R. van Starckenburg, M. Bruins, A. Sakes, P. Breedveld, Polishing of metal 3D printed parts with complex geometry: Visualizing the influence on geometrical features using centrifugal disk finishing, PLoS One. 18 (2023) e0289730.

4.1 INTRODUCTION

Metal additive manufacturing (AM) processes allow for the production of components with a high shape complexity and with excellent mechanical properties. Most current metal AM processes use a metal powder that is fused together using a laser in the desired shape, which is referred to as powder bed fusion (PBF). Widespread adoption of metal AM for precision applications is hindered by the rough surface finish of as-built parts [1], caused by the powder-based nature of the process [2]. For high-precision mechanical parts, such as those used in medical instrumentation, a poor surface quality increases friction and wear on parts that interact with each other [3,4]. Relatively speaking, the influence of a poor surface quality is even more pronounced for small or miniaturized parts, where geometrical feature sizes are only a few times larger than the size of the metal particles. An example of this is shown in Figure 4.1.

4

Surface finishing techniques can be employed to improve the surface quality of these parts, by removing partially adhered particles from the surface, closing pores and micro-cracks, and diminishing visible layers and laser patterns [5-7]. Mechanical surface finishing techniques, in which a mechanical interaction with the surface is responsible for the polishing rather than a chemical or electrical interaction, are reported to be most effective for creating a high quality surface [8-10]. With mechanical polishing a mirror-like surface can be produced ($0.0254\ \mu\text{m}$) [11]. However, when applied to complex AM geometries, most mechanical processes have the disadvantage that they are extremely labor-intensive and require a lot of manual intervention [8], or they may not be able to reach all surfaces of the object at all. Therefore, they may be less suitable to process functional, complex 3D printed parts in a high volume [12], and they negate the advantages of the high shape complexity enabled by AM.

Mass Finishing (MF) processes offer a solution for these applications [12,13]. The working principle of MF is based on the use of abrasive polishing media, such as ceramic or plastic beads, agitated by mechanical means, often by rotation or vibration. The polishing media, in some cases combined with a liquid medium, comes into contact with the surface of the submerged parts and removes material from the surface by abrasion, as well

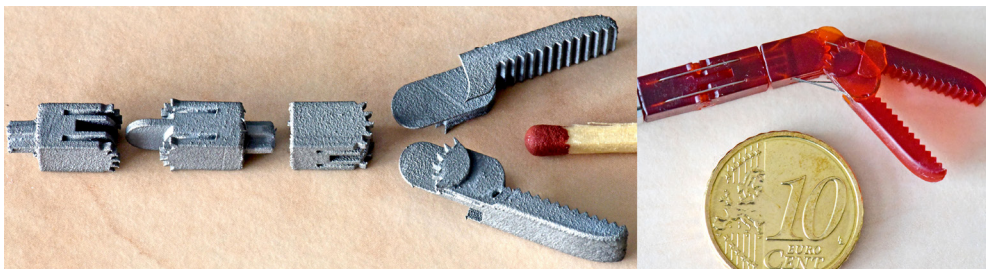


Figure 4.1: Example of the rough surface of parts printed with metal AM(left). The parts are meant to be used in a steerable, medical instrument, however they require extensive polishing before they can be used in a functional mechanism (match for scale). As comparison, on the right the same parts 3D printed using a polymer-based AM process.

as impart a polishing effect. Important processing parameters for MF processes are the size of the polishing media, speed of motion, and processing time. Generally, the use of larger sized particles results in a higher material removal rate and a better surface quality [14,15]. Prolonged contact with the abrasives in the form of a longer processing time results in the same effect [14,16,17], up to a limit [15]. Higher speeds are also associated with higher material removal rates, due to higher forces being applied to the workpieces [16,18,19]. The fill level of the container with polishing media was shown to have a negligible effect on material removal rates, higher load levels decreased the chance of contact between the abrasives and workpiece [14,18]. The advantages of MF processes are that the process is hands-off, it can process multiple parts at once, and it can be customized to the type of metal and surface finish required.

When the settings of MF processes are properly selected, surfaces with Ra of 0.52 to 5 μm Ra can be obtained [14]. However, as with any surface finishing process, unwanted side effects of MF processes include rounding of sharp edges, changes in part dimensions, decreased feature resolution, and changes in flatness [11,20]. These side effects are especially impactful for miniature parts, and become more prominent with longer processing times [13]. Surface improvements for internal surfaces are also less pronounced, unless they are designed significantly larger than the polishing media [18].

So far, research efforts into surface finishing processes for metal AM parts have focused on illustrating the improvements in surface finish only, executed on simple geometrical shapes such as cubes or discs [4,9,10,12,21-24]. As such, little information on the geometrical impact of surface finishing techniques on complex structures, such as those that can be produced with AM, is available. To apply PBF-printed parts in miniature, high-precision applications, it is important to not only know the surface roughness improvements that can be obtained with various methods, but also how effective these methods are on complex features, as well as the geometrical effects on features. This information can aid in the development of more robust design guidelines, facilitating higher quality in the AM process and the final components [13].

Making informed decisions early on in the design process is already commonly applied in design methodologies such as Design for Additive Manufacturing [25], although no such guidelines currently exist for post-processing methods. Therefore, in this study, we investigate how geometrical features are altered as a result of centrifugal disk finishing (CDF), a common MF process, and which types of features do not lend themselves well to polishing by CDF. In order to do so, we designed an experiment in which a miniature 3D printed test part with complex geometrical features was coated with a blue marking lacquer for metals, before undergoing polishing. After polishing, the remaining lacquer gives a visual pattern of the surfaces on the part to which the polishing media had access. The results led to a number of design guidelines that can be of help during the design process of SLM parts.

4.2 MATERIALS AND METHODS

4.2.1 Process

For this study, we designed a test part as shown in Figure 4.2a, which includes extruding features, recessed features, and mechanical features (gear teeth, ledges). The features were designed in such a way that none of them were obscured by other features, and all were large enough to allow theoretical access of polishing media. Twelve test parts were 3D printed by a commercial company, Materialise NV (Leuven, Belgium) on an EOS M280 (EOS GmbH, Germany), in stainless steel 316L. The parts were printed in the upright position shown in Figure 4.2a. Parts received a heat treatment to reduce internal stresses and were removed from the support structures using wire electrical discharge machining. The specific print and processing settings used for the test parts were not disclosed by the manufacturer. Instead, as a reference value, the surface roughness of the flat side on one of the test parts was measured (Mitutoyo SJ-301 SurfTest, Mitutoyo Corporation, Japan)

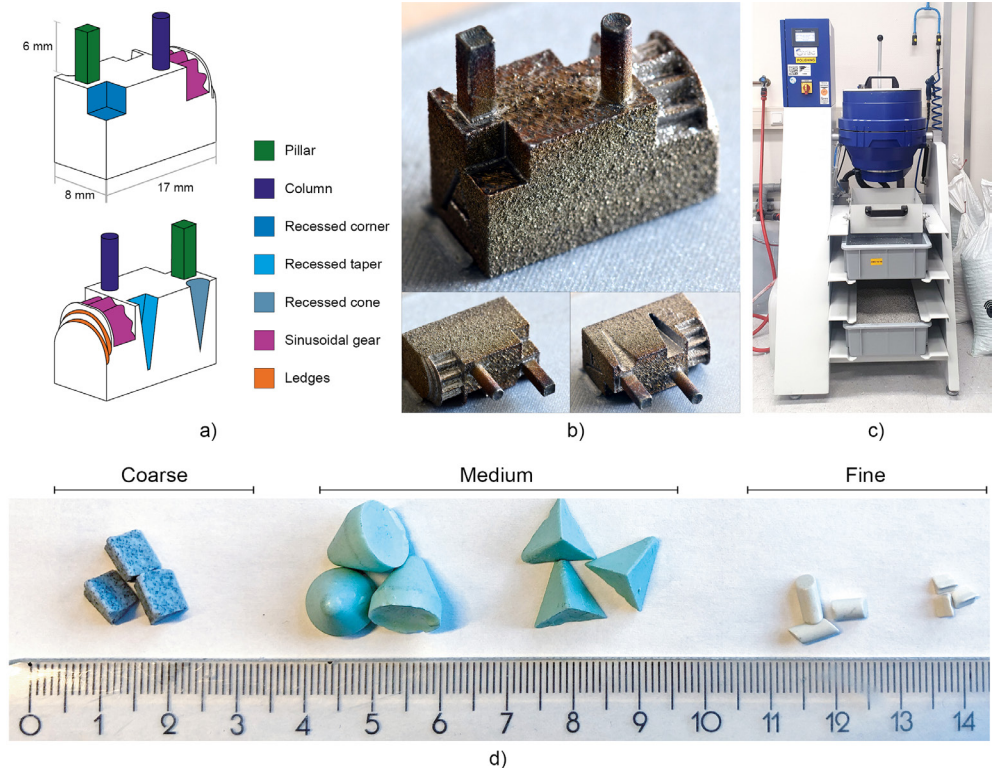


Figure 4.2: Test parts used in this study. a) The designed test part showing the different features that were implemented. b) An example of one of the test parts after printing. c) The CDF used in this study. d) The different types of polishing media used in this study, it should be noted that the distinction coarse, medium and fine refer to the removal of the surface material, not the size of the media. Media types: Coarse DZS 6/6, medium KM 10 and PM 10, fine ZSP 3/5 and DZP 3/3 SK (OTEC, Germany).

with a tolerance of $0.01\ \mu\text{m}$, across a length of 4 mm. An example of a printed test part is shown in Figure 4.2b.

Surface roughness is often used as a measure of the effectiveness of surface finishing processes, however this is difficult to measure on complex geometrical shapes. Since not all surfaces will be targeted equally, this would also require many measurements. In contrast, with the naked eye it is difficult to see which surfaces have been targeted by the polishing process and to what amount. The solution we found is to apply a blue marking lacquer for metals (Griffon, Bolton Adhesives, The Netherlands) on the parts that is eroded away in places that make contact with the polishing media. The coating will remain in places that are not in contact, or not in sufficient contact, with the media, leaving a visual pattern on the surface. The lacquer was applied on the parts after printing, with an approximate thickness of $0.05\ \text{mm}$. It should be noted that since the lacquer influences the effectiveness of CDF, a smaller improvement in surface finish will be expected.

The parts were polished using CDF (CF 1x18 B, OTEC, Germany), shown in Figure 4.2c. In CDF, the parts are submerged in a container with polishing media with or without a liquid, which is brought into motion by a rotating disk at the bottom. Several steps with different polishing media are usually applied for the best results. Generally speaking, larger abrasive media will be more effective on the external surfaces of the part and have a faster cut rate, while smaller media are able to reach into the interior regions and small features [11,26]. The size of the abrasive media is also important to keep the submerged parts separate from each other and prevent them from clashing [13]. The shape of the abrasive media should be chosen in such a way that it permits access to all surfaces of the part [13]. Based on preliminary tests and advice of the manufacturer of the CDF, we settled on a polishing schedule consisting of three steps of 120 minutes with coarse, medium, and fine polishing media with different shapes. In Table 4.1, the details of the used process steps are given, for each step fresh media was used. We investigated the influence of the coarseness of the media and the total duration of polishing on the geometrical features, by dividing the twelve parts into four groups of three that were polished in different polishing steps, as shown in Table 4.2. The order of the steps was in decreasing coarseness in all cases. The polishing media is shown in Figure 4.2d. It should be noted that while the KM 10 and PM 10 media are recommended as a second step for a less abrasive polish, the particles itself are larger in size than the coarse media.

4.2.2 Analysis

As a measure of the overall effectiveness of the CDF process, we measured the removed material on different places on the part. No additional surface roughness measurements were performed, since the applied lacquer would interfere with the measured roughness values. The overall width of the part, as well as the top and the base of the pillar and column, were measured before polishing and after each polishing step using a digital micrometer (Mitutoyo Digimatic IP65 0-25mm, Mitutoyo Corporation, Japan), across the entire length of the parts. The radius of one of the outer edges was measured using a digital microscope (Dino-Lite 3.0, AnMo Electronics Corporation, Taiwan). For the recessed

Table 4.1: Process details for the different centrifugal disk finishing polishing steps used. All materials are from OTEC, Germany.

	Coarse step	Medium step	Fine step
Polishing media	DZS 6/6	KM 10 and PM 10	ZSP 3/5 and DZP 3/3 SK
Size	6 x 6 mm	10 x 12 mm and 10 x 10 mm	3 x 5 mm and 3 x 3 mm
Compound	SC15	SC15	SC5
Speed	280 rpm	260 rpm	220 rpm
Water flow	10 L/h	10 L/h	10 L/h
Water concentration	3%	3%	3%
Type	Ceramic-bonded	Plastic-bonded	Ceramic-bonded

Table 4.2: The polishing steps and time for each of the test groups.

	No. of parts	Coarse	Medium	Fine	Total time
Group 1	3 parts	120 min	-	-	120 min
Group 2	3 parts	120 min	120 min	-	240 min
Group 3	3 parts	120 min	120 min	120 min	360 min
Group 4	3 parts	-	120 min	120 min	240 min

taper and cone, using the digital microscope we determined how deep into the feature the polishing media had reached, by measuring the distance from the top of the feature to the edge of where the blue lacquer was completely intact.

Images of different surfaces and features were used to visually compare where the coating was eroded away and with what intensity. To analyse the remaining blue colour on the parts, photos were taken of the sides of the test part and of the features using a digital microscope in standard office lighting (Figure 4.3a). The images were processed in Photoshop (Adobe Inc., USA) to extract only the blue tones. An RGB image contains three channels: red, green, and blue. The ‘Color Range’ command allows the user to select pixels of an image based on their colour channel. By selecting ‘Blues’ within the Color Range command, only pixels within the blue channel were selected. All other pixels were set to a white colour (Figure 4.3b). These images were saved as Bitmap images and processed in MATLAB R2021b (The MathWorks Inc., USA), using a script that converts the blue pixels to black, using the function `im2bw` with a threshold of 0.8 (Figure 4.3c) [27,28], after which the percentage of black pixels of the total pixels was calculated for each image. The areas that were analysed were one of the side surfaces, including the recessed corner, the top surface between the extruding features, the top view of the gears and ledges, and one side of the extruding pillar and column (Figure 4.3d).

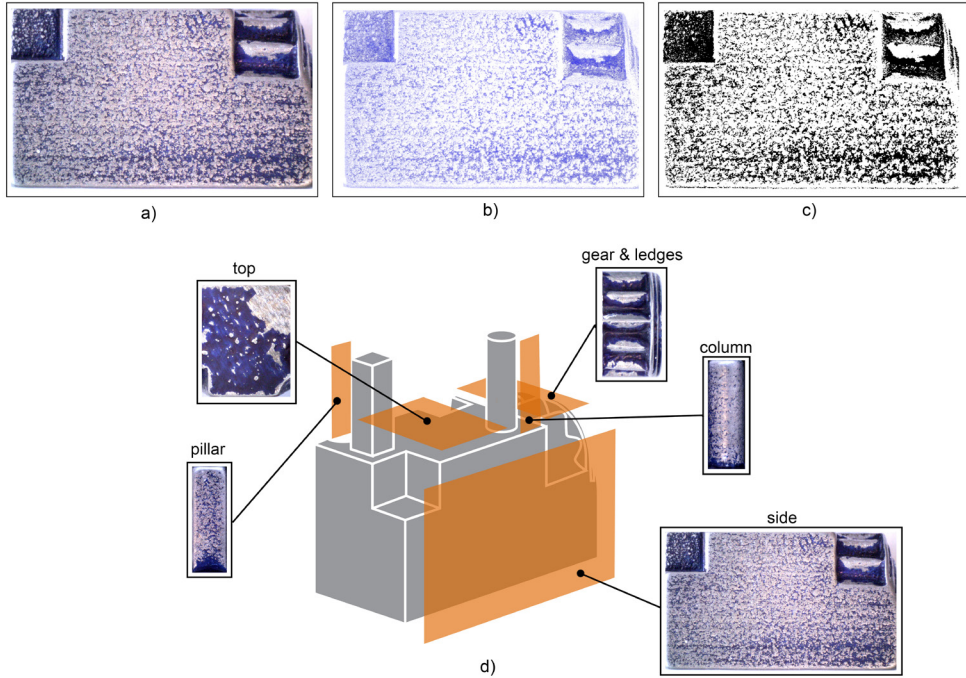


Figure 4.3: Image processing of the remaining blue color on different surfaces on the parts. a) Photo taken of the side of one of the test parts, shown here as an example. b) The same image with only the blue tones extracted. c) The image converted to black and white, in which the blue pixels are converted to black. These image were used to calculate the percentage of remaining blue on the surfaces. d) Location of the areas that were analyzed indicated in orange, with example photos of one of the test parts.

4.3 RESULTS AND DISCUSSION

4.3.1 Surface effects

The initial surface roughness on the side of the test part was $R_a = 9.49 \mu\text{m}$ before polishing, which is in line with reported roughness values between 2 and $15 \mu\text{m}$ R_a for SLM parts [14,29,30]. Figure 4.4a shows the normalized measurements of the width of the test parts before and after polishing, compared with the as-drawn width of the test part (horizontal axis). The average width of the as-printed test parts was $8.17 \text{ mm} \pm 0.05 \text{ mm}$ before polishing, compared to a designed width of 8.0 mm . After polishing, the average width of the parts in Group 1 to 4 was: $8.02 \pm 0.02 \text{ mm}$, $7.94 \pm 0.02 \text{ mm}$, $7.97 \pm 0.01 \text{ mm}$, and $7.97 \pm 0.01 \text{ mm}$, respectively. These results show that the CDF process can be used to correct for the dimensional error caused by the printing process. It should be noted that these measurements include the thickness of the layer of lacquer of approximately 0.05 mm that was partially polished away. Figure 4.4b shows that for Group 1 and Group 2 on average 0.21 mm material was removed from the width, for Group 3 on average 0.23 mm , and for Group 4 on average 0.14 mm . It is clear that the coarse polishing step is responsible for most of the material removal, which is in agreement with other studies [14], although for

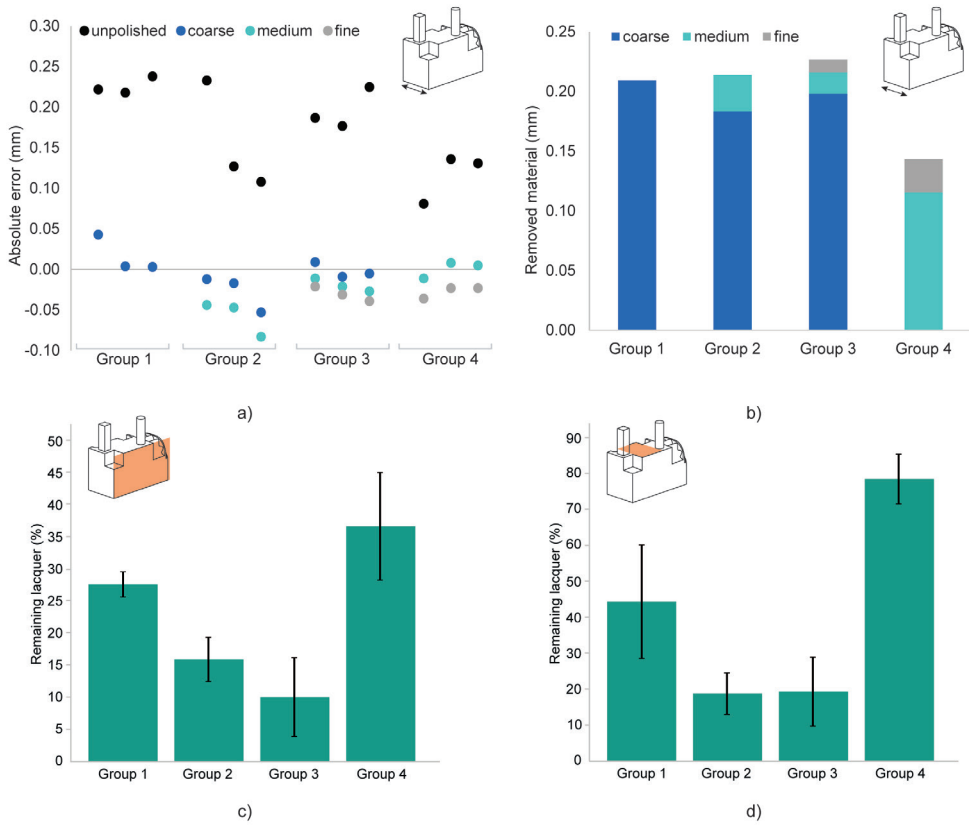


Figure 4.4: Material removal caused by polishing. a) Absolute dimensional error of the width of the test parts, unpolished refers to the coated parts before polishing. b) Material removal of the width of the parts per polishing step. c) Calculated percentage of remaining blue lacquer on the side of the part. d) Calculated percentage of remaining blue lacquer on top of the part between the two extruding features.

Group 4 it is noticeable that the medium step has more influence on the total material removal than for Groups 2 and 3. This implies that the first polishing step is responsible for most of the material removal, regardless of the coarseness of the polishing media. Rounded edges are a familiar side effect of mechanical polishing that is also present in our test parts. Only edges on the outside of the part (positive edges) experience this effect, because these edges are more exposed to the polishing media. All sharp outside edges have been rounded by the polishing process, while the internal edges were not polished. The average outer edge radius was 0.23 ± 0.03 mm after polishing. Group 4 experienced the smallest edge rounding with a radius of 0.20 ± 0.03 mm.

In all instances, after polishing blue lacquer has remained in the ‘pores’ on the surfaces of the parts (Figure 4.5). The calculated percentages of blue color on the analyzed top and side areas are given in Table 4.3 and Figure 4.4c-d. For the side of the part, the amount of remaining lacquer decreases from Group 1 to Group 3, as expected with additional polishing steps. The most lacquer remained on the test parts in Group 4, illustrating that

Table 4.3: Calculated percentage of blue lacquer remaining on the parts, based on different views of the test part.

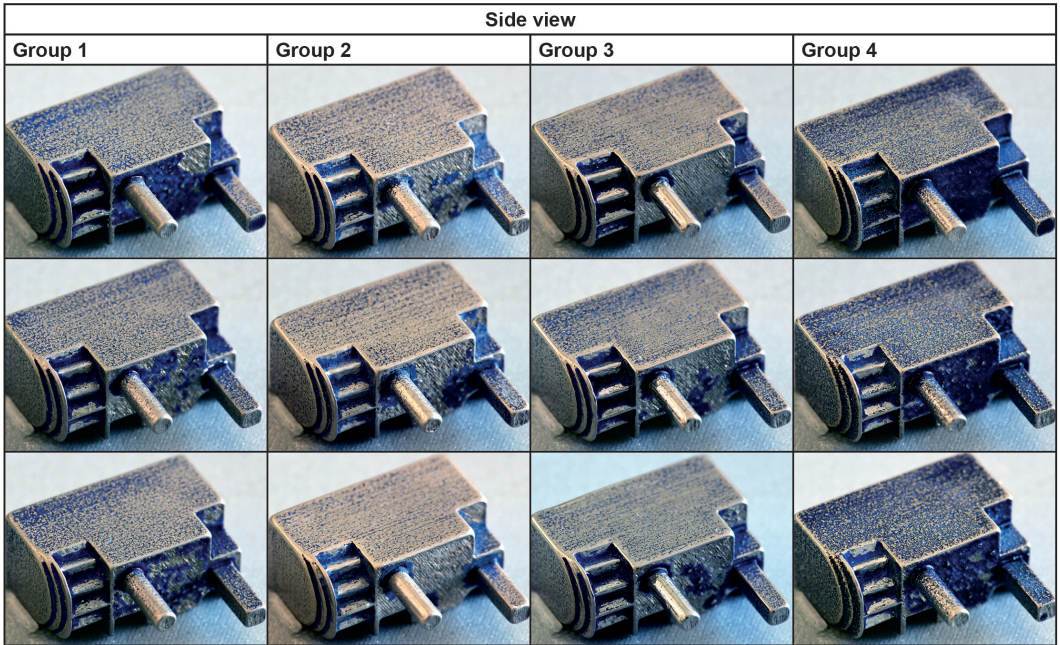
	Group 1	Group 2	Group 3	Group 4
Side	27.6 ± 2.0	15.9 ± 3.5	10.1 ± 6.1	36.6 ± 8.4
Top	44.3 ± 15.8	18.7 ± 5.9	19.2 ± 9.7	78.4 ± 7.0
Gear & ledges	59.2 ± 0.8	63.5 ± 6.8	56.2 ± 5.2	62.6 ± 6.7
Pillars	26.7 ± 2.0	25.4 ± 3.4	19.6 ± 6.4	38.4 ± 10.9
Columns	19.1 ± 4.0	17.3 ± 6.3	10.1 ± 2.7	22.1 ± 3.1

one course polishing step removes more material than a medium and fine step together. When comparing Figure 4.4b and Figure 4.4c-d, it can be seen that the remaining lacquer on the surface decreases with additional polishing steps, i.e. the surface quality increases, however for the material removal this connection is less distinct. This shows that the influence of additional, finer polishing steps on the amount of removed material stagnates, while the surface quality keeps improving. This is in line with other research suggesting larger particles are responsible for most of the material removal [14,15].

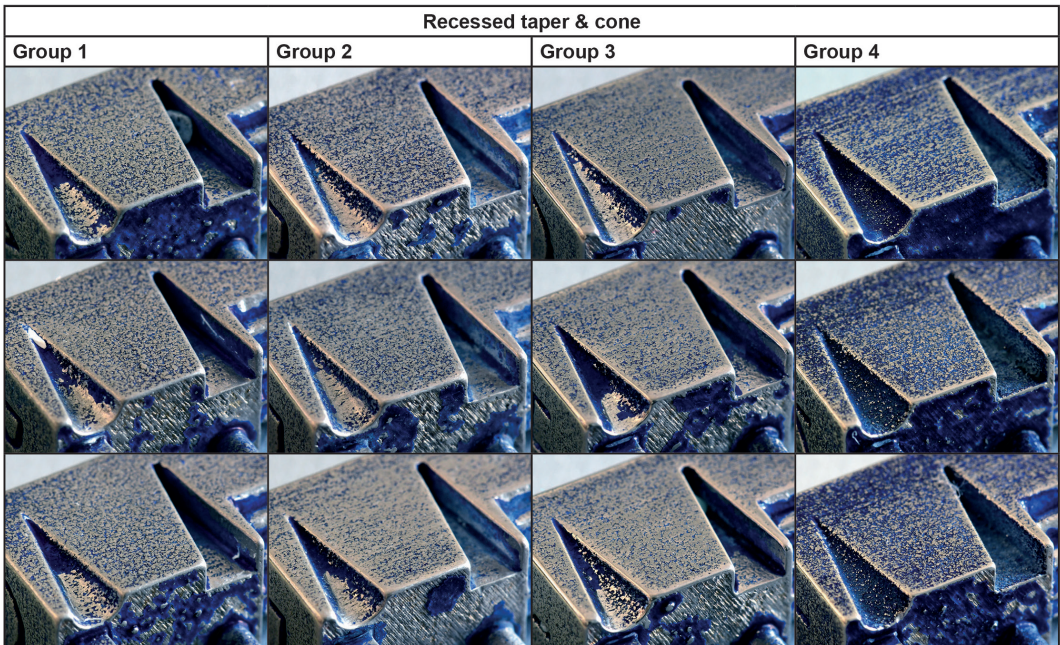
On the top surfaces, it is visible that the extruding features and protrusions have partly shielded the surrounding areas from being polished (Figure 4.5a). This is also clearly visible in the calculated blue color in the area between the extruding features in Figure 4.4d. The average of the remaining color for each group is higher than that for the side surfaces. This is most noticeable for Group 4, where the average percentage of remaining color is more than twice as high as on the side surface. A possible explanation is the size of the medium media, which is larger than the coarse media and therefore does not fit as well between the features. However, it is noticeable that this effect does not occur for Group 2, which has a significantly lower percentage blue left than Group 1. It is possible that the coarse media partly dislodges the lacquer, which is subsequently removed by the medium and fine media, while on their own the medium and fine media are not abrasive enough to remove the lacquer between the extruding features.

4.3.2 Feature effects

In Figure 4.5a-b, it is visible that more lacquer remains on the recessed features than on the extruding features. The mechanical features, i.e. the gear teeth and ledges, show a lot of remaining lacquer, indicating that the polishing media does not properly access them, although in theory the features were large enough to allow access. Figure 4.6a shows the calculated percentage of blue in the gears and ledges combined. Here the remaining lacquer is higher than for the flat surfaces, and there are no substantial differences between the four groups. Adding more polishing steps seems to have no significant advantage for the polishing of these features, which remain hard to access. Similar results were found for the recessed cone and taper. The extent to which these were polished was measured by the depth of the feature to which the polishing media reached. For Groups 1 to 3, the cone



a)



b)

Figure 4.5: Remaining blue lacquer on the test parts after polishing. a) Side view of all test parts per group. b) Close up of the recessed taper and cone on the other side of the test parts.

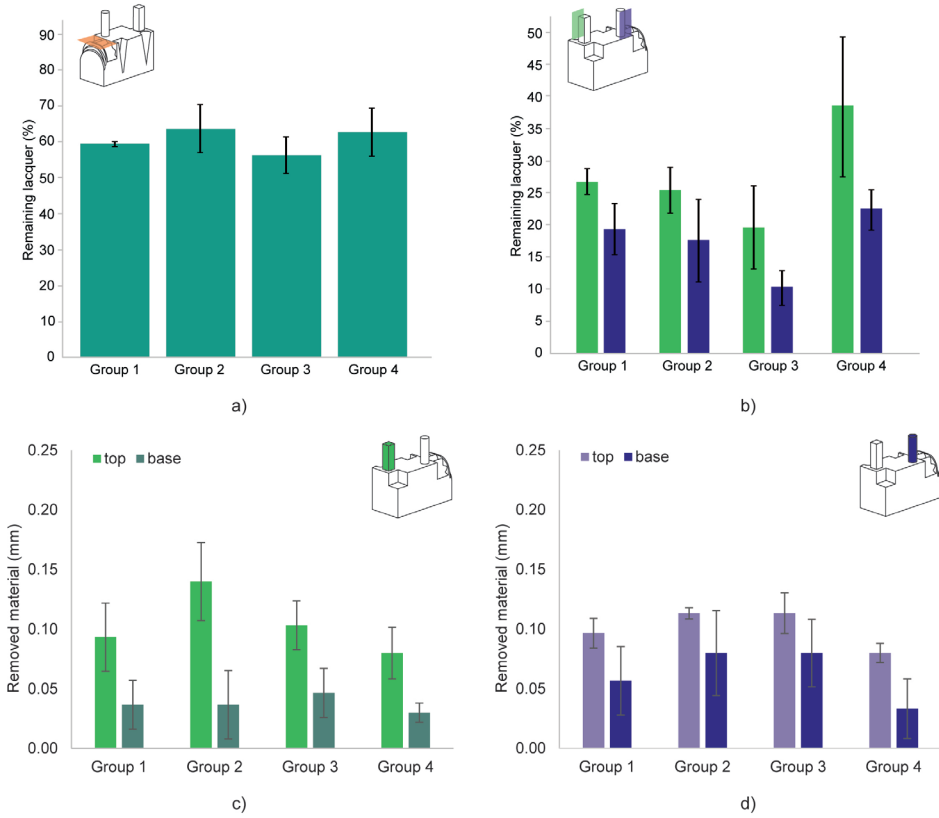


Figure 4.6: The effects of polishing on different features of the test part. a) Calculated percentage of remaining blue lacquer on the gear and ledges. b) Calculated percentage of remaining blue lacquer on the extruding pillar (green) and column (purple). c) Material removal of the pillar, on the top and the base. d) Material removal of the column, on the top and base.

was considerably more polished than the taper, with a depth of 3.67 ± 0.21 mm versus 3.04 ± 0.04 mm for Group 1, 4.39 ± 0.51 mm versus 2.69 ± 0.40 mm for Group 2, and 3.96 ± 1.15 mm versus 3.01 ± 0.16 mm for Group 3. In Group 4, none of the recessed features were polished beyond the top edge of the feature. In Figure 4.5, it can also be seen that more lacquer remains on the sides of the recessed features.

Figure 4.5a shows that the protruding columns appear more polished than the protruding pillars, which is confirmed by the calculated percentage of blue in the images (Figure 4.6b). However, the average material removal, measured at the cross-section of the top of both features is comparable: 0.10 mm \pm 0.02 for the column, and 0.10 mm \pm 0.03 for the pillar. This indicates that rounded features lend themselves better to polishing than similar angular features. When comparing the material removal at the top with the material removal at the base of both features, as shown in Figure 4.6c-d, for both features material removal at the top was on average 50% more than at the base. Protruding surfaces have a

higher chance of being in contact with the polishing media, which means that the diameter of such features will change along its length.

4.3.3 Limitations and recommendations

Visualization of polishing patterns using marking lacquer is a novel approach to further understanding the details of MFT processes. It is a simple and inexpensive method to observe differences in polishing compatibility for different geometries. However, there are still some limitations to this test. For instance, the marking lacquer was difficult to apply evenly across the part, and tended to pool in inside corners and the base of the gear teeth, leaving a thicker layer which could have influenced results. Different marking lacquers or coatings can be tested to obtain a more even application. In addition, the presence of the lacquer on the part will have influenced the effectiveness of the polishing process to some extent. Although the lacquer is less hard than the stainless steel of which the parts are made, this is still an additional layer that needs to be polished away. Therefore, it is an effective measure of visualizing the polishing patterns, but less suitable to determine the actual efficiency of the polishing process with regards to the surface roughness and the material removal rate. The image analysis method employed in this study is useful for comparison within batches, but due to sensitivity to lighting the absolute results may vary in different conditions. Additional research into other process parameters of CDF, such as rotational speed, and abrasive media shape and size, is required to provide insight into their effect on surface finish as well as geometrical features. We recommend that in order to optimize the processing settings for a specific design, test parts with representative features of the final design should be used [26].

Although in this study we focused on the CDF process, we imagine that the same workflow can be applied to different polishing methods in order to gain insight into the effect of the polishing method on the geometrical features and its effectiveness on a complex-shaped part. This method can be particularly helpful to design small, functional parts. Before committing to a final design, we imagine a test part with similar features should be designed and printed, and different polishing steps can be applied. This method can gain insight into which features are problematic for polishing, and should therefore be altered or avoided in the final design, as well as gain insight in which combination of polishing steps and duration is most suitable for the final part.

4.4 CONCLUSION

From the performed experiments, we can distill some general design guidelines that can be useful when designing metal AM parts that should be processed using CDF.

1. Extruding features shield the remaining surfaces from polishing, and should therefore not be placed next to functional surfaces or next to other extruding features.
2. The discrepancy between top and base of extruding features can be solved in the design phase by applying a negative draft angle to the feature.
3. Recessed features are difficult to polish, although the backside of these features is

- more easily accessible than the sides. When a functional surface is required in a recessed feature, the back surface of this feature is more suitable than the sides.
4. Rounded features lend themselves better to polishing than features with sharp corners, whether they are extruding or recessed.
 5. All extruding edges will be rounded by the CDF process, while recessed edges remain largely unpolished. This should be taken into account when relying on sharp edges for functional features. Since the exact amount of material removed from the edge cannot be controlled during polishing, it is better to apply a rounded edge in the design phase with a known value. Negative edges can be included in the design, although it should be noted that they will receive little polishing.
 6. Even if complex features, such as the gears in this study, are designed to allow access to the polishing media, they remain difficult to polish no matter the polishing cycles of CDF. Therefore, these should either be avoided or polished using a different polishing process.
 7. Additional polishing steps with fine media appear to have more influence on the surface quality than on the material removal, for the surfaces that can most easily be reached by the polishing media. Therefore, when a mirror-smooth surface is required, it should be sufficient to only take into account the material removal of the first polishing step in the design phase.

DATA AVAILABILITY

The data underlying this study are available at: DOI 10.4121/21401586

REFERENCES

- [1] Z. Baicheng, L. Xiaohua, B. Jiaming, G. Junfeng, W. Pan, S. Chen-nan, N. Muiling, Q. Guojun, W. Jun, Study of selective laser melting (SLM) Inconel 718 part surface improvement by electrochemical polishing, *Mater. Des.* 116 (2017) 531–537. <https://doi.org/10.1016/j.matdes.2016.11.103>.
- [2] A.P. Nagalingam, S.H. Yeo, Controlled hydrodynamic cavitation erosion with abrasive particles for internal surface modification of additive manufactured components, *Wear.* 414–415 (2018) 89–100. <https://doi.org/10.1016/j.wear.2018.08.006>.
- [3] M. Hanief, M.F. Wani, Effect of surface roughness on wear rate during running-in of En31-steel: Model and experimental validation, *Mater. Lett.* 176 (2016) 91–93. <https://doi.org/10.1016/j.matlet.2016.04.087>.
- [4] B. Sagbas, Post-Processing Effects on Surface Properties of Direct Metal Laser Sintered AlSi10Mg Parts, *Met. Mater. Int.* 26 (2020) 143–153. <https://doi.org/10.1007/s12540-019-00375-3>.
- [5] C. de Formanoir, S. Michotte, O. Rigo, L. Germain, S. Godet, Electron beam melted Ti–6Al–4V: Microstructure, texture and mechanical behavior of the as-built and heat-treated material, *Mater. Sci. Eng. A.* 652 (2016) 105–119. <https://doi.org/10.1016/j.msea.2015.11.052>.
- [6] Y. Kok, X.P. Tan, P. Wang, M.L.S. Nai, N.H. Loh, E. Liu, S.B. Tor, Anisotropy and heterogeneity of microstructure and mechanical properties in metal additive manufacturing: A critical review, *Mater.*

- Des. 139 (2018) 565–586. <https://doi.org/10.1016/j.matdes.2017.11.021>.
- [7] A. Mostafaei, S.H.V.R. Neelapu, C. Kisailus, L.M. Nath, T.D.B. Jacobs, M. Chmielus, Characterizing surface finish and fatigue behavior in binder-jet 3D-printed nickel-based superalloy 625, *Addit. Manuf.* 24 (2018) 200–209. <https://doi.org/10.1016/j.addma.2018.09.012>.
- [8] S. Bagehorn, J. Wehr, H.J. Maier, Application of mechanical surface finishing processes for roughness reduction and fatigue improvement of additively manufactured Ti-6Al-4V parts, *Int. J. Fatigue.* 102 (2017) 135–142. <https://doi.org/10.1016/j.ijfatigue.2017.05.008>.
- [9] J. Guo, M. Goh, Z. Zhu, X. Lee, M.L.S. Nai, J. Wei, On the machining of selective laser melting CoCrFeMnNi high-entropy alloy, *Mater. Des.* 153 (2018) 211–220. <https://doi.org/10.1016/j.matdes.2018.05.012>.
- [10] L. Löber, C. Flache, R. Petters, U. Kühn, J. Eckert, Comparison of different post processing technologies for SLM generated 316l steel parts, *Rapid Prototyp. J.* 19 (2013) 173–179. <https://doi.org/10.1108/13552541311312166>.
- [11] L.K. Gillespie, *Mass Finishing Handbook*, 1st ed., Industrial Press, New York, 2007. <https://www.globalspec.com/reference/68875/203279/mass-finishing-handbook> (accessed December 11, 2020).
- [12] Y. Kaynak, O. Kitay, The effect of post-processing operations on surface characteristics of 316L stainless steel produced by selective laser melting, *Addit. Manuf.* 26 (2019) 84–93. <https://doi.org/10.1016/j.addma.2018.12.021>.
- [13] M. Jamal, M. Morgan, Design Process Control for Improved Surface Finish of Metal Additive Manufactured Parts of Complex Build Geometry, *Inventions.* 2 (2017) 36. <https://doi.org/10.3390/inventions2040036>.
- [14] C. Fuchs, L. Kick, O. Leprevost, M.F. Zaeh, ASSESSMENT OF FINISH MACHINING AND MASS FINISHING AS POST-PROCESSING METHODS FOR PBF-LB/M-MANUFACTURED 316L, *MM Sci. J.* 2021 (2021) 5187–5194. https://doi.org/10.17973/MMSJ.2021_11_2021137.
- [15] M. Khorasani, I. Gibson, A. Ghasemi, M. Brandt, M. Leary, On the role of wet abrasive centrifugal barrel finishing on surface enhancement and material removal rate of LPBF stainless steel 316L, *J. Manuf. Process.* 59 (2020) 523–534. <https://doi.org/10.1016/j.jmapro.2020.09.058>.
- [16] W. Na, Z. Tingting, Y. Sheng-qiang, L. Wenhui, Z. Kai, Experiment and simulation analysis on the mechanism of the spindle barrel finishing, *Int. J. Adv. Manuf. Technol.* 109 (2020) 57–74. <https://doi.org/10.1007/s00170-020-05609-y>.
- [17] A. Boschetto, L. Bottini, F. Veniali, Surface roughness and radiusing of Ti6Al4V selective laser melting-manufactured parts conditioned by barrel finishing, *Int. J. Adv. Manuf. Technol.* 94 (2018) 2773–2790. <https://doi.org/10.1007/s00170-017-1059-6>.
- [18] M. Khorasani, A.H. Ghasemi, E. Farabi, M. Leary, I. Gibson, B. Rolfe, A comprehensive investigation of abrasive barrel finishing on hardness and manufacturability of laser-based powder bed fusion hollow components, *Int. J. Adv. Manuf. Technol.* 120 (2022) 3471–3490. <https://doi.org/10.1007/s00170-022-08903-z>.
- [19] F. Nalli, L. Bottini, A. Boschetto, L. Cortese, F. Veniali, Effect of Industrial Heat Treatment and Barrel Finishing on the Mechanical Performance of Ti6Al4V Processed by Selective Laser Melting, *Appl. Sci.* 10 (2020) 2280. <https://doi.org/10.3390/app10072280>.
- [20] I. Gibson, D. Rosen, B. Stucker, *Additive Manufacturing Technologies*, Springer New York, New York, NY, 2015. <https://doi.org/10.1007/978-1-4939-2113-3>.
- [21] H. Yamaguchi, O. Fergani, P.-Y.Y. Wu, Modification using magnetic field-assisted finishing of the

REFERENCES

- surface roughness and residual stress of additively manufactured components, *CIRP Ann.* 66 (2017) 305–308. <https://doi.org/10.1016/j.cirp.2017.04.084>.
- [22] A. Teramachi, J. Yan, Improving the Surface Integrity of Additive-Manufactured Metal Parts by Ultrasonic Vibration-Assisted Burnishing, *J. Micro Nano-Manufacturing.* 7 (2019). <https://doi.org/10.1115/1.4043344>.
- [23] K.L.L. Tan, S.H.H. Yeo, Surface modification of additive manufactured components by ultrasonic cavitation abrasive finishing, *Wear.* 378–379 (2017) 90–95. <https://doi.org/10.1016/j.wear.2017.02.030>.
- [24] V.A. Aleksandrov, S.K. Sundukov, D.S. Fatyukhin, A.A. Filatova, Ultrasonic Methods for Improving Object Surface Quality Prepared by Corrosion-Resistant Steel Powder Selective Laser Melting, *Met. Sci. Heat Treat.* 60 (2018) 381–386. <https://doi.org/10.1007/s11041-018-0287-1>.
- [25] A. Wiberg, J. Persson, J. Ölvander, Design for additive manufacturing – a review of available design methods and software, *Rapid Prototyp. J.* 25 (2019) 1080–1094. <https://doi.org/10.1108/RPJ-10-2018-0262>.
- [26] A. Boschetto, L. Bottini, L. Macera, F. Veniali, Post-Processing of Complex SLM Parts by Barrel Finishing, *Appl. Sci.* 10 (2020) 1382. <https://doi.org/10.3390/app10041382>.
- [27] P. van Assenbergh, C. Culmone, P. Breedveld, D. Dodou, Implementation of anisotropic soft pads in a surgical gripper for secure and gentle grip on vulnerable tissues, *Proc. Inst. Mech. Eng. Part H J. Eng. Med.* 235 (2021) 255–263. <https://doi.org/10.1177/0954411920971400>.
- [28] C. Culmone, K. Lussenburg, J. Alkemade, G. Smit, A. Sakes, P. Breedveld, A Fully 3D-Printed Steerable Instrument for Minimally Invasive Surgery, *Materials (Basel).* 14 (2021) 7910. <https://doi.org/10.3390/ma14247910>.
- [29] C. de Formanoir, U. Paggi, T. Colebrants, L. Thijs, G. Li, K. Vanmeensel, B. Van Hooreweder, Increasing the productivity of laser powder bed fusion: Influence of the hull-bulk strategy on part quality, microstructure and mechanical performance of Ti-6Al-4V, *Addit. Manuf.* 33 (2020) 101129. <https://doi.org/10.1016/j.addma.2020.101129>.
- [30] A. Soja, J. Li, S. Tredinnick, T. Woodfield, Surface finishing of additively manufactured stainless steel surgical instruments, *Rapid Prototyp. J.* 27 (2021) 59–70. <https://doi.org/10.1108/RPJ-01-2020-0009>.

PART 2.

ON DESIGNING TOWARDS NON-ASSEMBLY 3D PRINTING



5 HIGH-PRECISION 3D PRINTING: MINIATURE TROCAR

Stereolithography is emerging as a promising additive manufacturing technology for a range of applications in the medical domain. However, for miniature, medical devices such as those used in ophthalmic surgery, a number of production challenges arise due to the small size of the components. In this work, we investigate the challenges of creating sub-millimeter features for a miniature, functional trocar using Stereolithography. The trocar cannula system is used in eye surgery to facilitate a passage for other instruments. A standard trocar consists of a hollow cannula and a flexible check valve. The research was performed in two stages: in the first stage we investigated the effect of different materials and print settings on the current design of the cannula and the valve separately, and in the second stage we used these findings to optimize the design and production process. After the first investigation, it became apparent that even though the dimensions of the trocar are within the feature size range of Stereolithography, all hollow features tended to fuse shut during printing. This effect appeared regardless of the materials or print settings, and can be attributed to refraction of the laser source. In order to circumvent this, we identified two potential strategies: 1) increasing the negative space surrounding features; and 2) decreasing the surface area per layer. By applying these strategies, we tested a new design for the cannula and valve and managed to 3D print a functional trocar, which was tested in an artificial eye. The design of the 3D printed trocar allows for further personalization depending on the specific requirements of both patient and surgeon. The proposed strategies can be applied to different applications to create miniature features using Stereolithography.

Published as:

K. Lussenburg, M. Scali, A. Sakes, P. Breedveld, Additive Manufacturing of a Miniature Functional Trocar for Eye Surgery, Front. Med. Technol. 4 (2022).

5.1 INTRODUCTION

Additive manufacturing (AM) or 3D printing offers great flexibility in creating and producing complex parts and mechanisms. Especially in the medical domain, AM has been recognized for the benefits it offers in terms of personalization, additional functionalities, and production of increasingly complex structures [1,2]. In the field of ophthalmology, AM has been used for a variety of applications related to the eyes, such as the production of eye glasses, ocular prostheses, implants, and ophthalmic instruments, such as trocars [3–5]. For ophthalmic surgical instruments, which are often in the sub-millimeter-scale range, it is important that AM technologies offer accuracy and repeatability, in addition to a small manufacturing size. Among the commercially available AM techniques, vat photopolymerization processes, such as Stereolithography (SLA) or Digital Light Processing (DLP), have become popular in the medical domain. Their popularity can be attributed to a high resolution, currently in the range of 25 μm [6–8], and the availability of biocompatible materials [6]. Because of these factors, SLA and DLP are widely accepted in the medical domain, for applications ranging from patient specific implants to anatomical models [6,9].

Despite the advantages of SLA and DLP techniques, when the size of parts or features approach the maximum resolution, limitations in accuracy become apparent. Manuals of 3D printers and technical datasheets of the materials only give theoretical information about the obtainable minimum accuracy, which does not always reflect the actual result. The final accuracy of a part is influenced by many factors, such as the material, process parameters and even the specific 3D printer [10]. This means that it is likely that the 3D printed parts slightly deviate from the as-drawn dimensions. Therefore, for the design of miniature, functional devices, it is important to investigate the factors that influence the accuracy. In this research, we attempt to manufacture a miniature, functional trocar cannula system as used in ophthalmic surgery, while coping with minimal feature sizes of several micrometers and a high required accuracy [11].

5.1.1 Trocar design

The trocar cannula system is used in ophthalmic surgery to gain access to the interior section of the eye, by providing a working channel for other surgical instruments (Figure 5.1). The trocar is placed through the sclera, which is the outer protective layer of the eye, by means of a small incision made with an inserter knife. The trocar itself consists of a metal channel, the cannula, with a flexible valve on top (Figure 5.1b). After placement of the trocar, the channel is kept closed by the flexible closure valve. This is necessary in order to ensure that no fluids or gases are exiting the cannula, and to maintain a steady intraocular pressure during the surgery [11]. The valve has three functions: 1) compliancy to let an instrument enter the eye, 2) enough springback to close after the instrument is removed without permanent deformation, and 3) no open gaps when the valve is closed to prevent leakage, which can be achieved by a distance of less than 10 μm between the valve flaps. The inner diameter of the channel must be compatible with the industry standard sizes of instruments used during ophthalmic surgery, which are commonly 23G (0.64

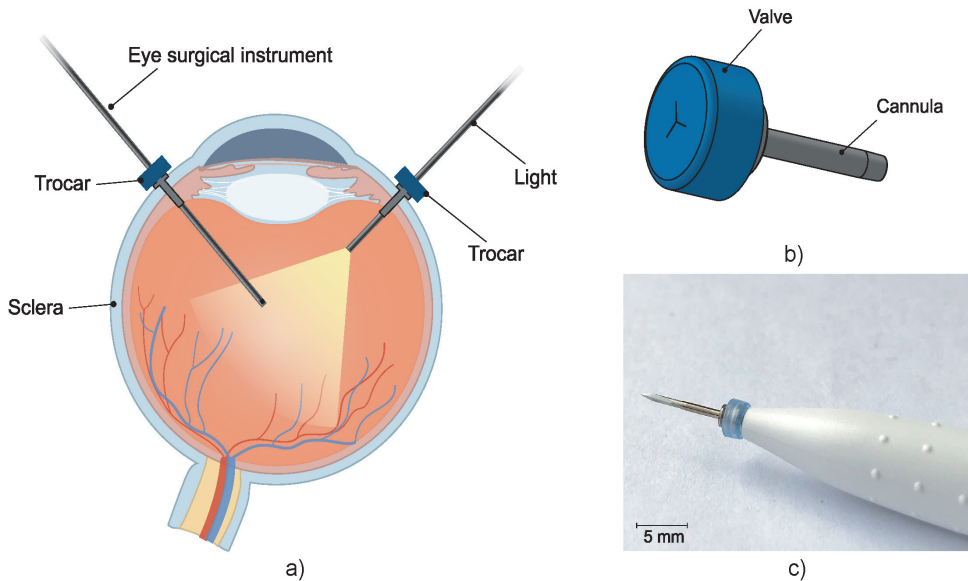


Figure 5.1: Trocar cannula system used in eye surgery, as developed by D.O.R.C. (Dutch Ophthalmic Research Center International (Zuidland, The Netherlands)). a) Schematic of a cross-section of the eye with a typical set-up for eye surgery. The trocars function as a channel into the eye for surgical instruments. Only the channel of the cannula is inserted into the eye, the top part of the cannula with the valve remains outside the eye. b) Schematic illustration of a trocar consisting of a valve (blue) and cannula (grey). c) Photograph of a trocar on the inserter knife, before insertion into the sclera.

mm), 25G (0.51 mm) and 27G (0.40 mm) [12]. Since other surgical instruments will be inserted through this channel, the internal accuracy is of greater importance than the outer accuracy, although a smaller outer diameter is preferred to minimize the size of the incision and the insertion forces. The length of the cannula channel is commonly around 4 mm, which is long enough to reach the internal cavity of the eye, but not too long to cause damage to internal structures [13].

5.1.2 Stereolithography

The principle behind SLA is vat photopolymerization, in which a liquid photopolymer is exposed to a light source that cures the material into a final object. The light is generated by a single laser spot, the size of this spot determines the minimum feature size [14]. The x,y-resolution is defined by the precision with which the laser spot can move, whereas the z-resolution is defined by the minimum layer thickness, i.e. the precision with which the z-axis can move. For this study, the SLA printer used was the Form 3B (FormLabs, USA), which has a reported x,y-resolution of 25 μm , and a minimum layer height of 25 μm [15]. A single laser is used for curing, with a laser spot size of 85 μm , 405 nm wavelength, and 250 mW power [15]. The FormLabs system is a closed system, which means that it is not possible to adjust settings such as laser power or scanning speed of the printer itself, rather

the slicing software will decide on the appropriate settings based on the chosen material.

Although often used interchangeably, there is a difference between the resolution of a 3D printer and the dimensional accuracy it can produce [16]. The resolution is a 3D printer-specific value, for which often the increments with which the laser spot can move are used, which can be used as an indication for the minimum feature size. The dimensional accuracy is dependent on many different factors, among which the material, laser intensity, calibration of the 3D printer, geometry of the part, color of the resin and even the settings of the file format used [16–18]. Due to these many factors, it is difficult to give a general value for the dimensional accuracy of a specific AM technique [16]. Previous studies have attempted to find the optimal process settings for increasing the accuracy of SLA processes, although it remains unlikely that these will be the same for all possible designs. The influence of process settings such as build orientations, printing direction, layer height, and material properties on the dimensional accuracy have been extensively studied [19–27].

The materials used in SLA are liquid photopolymer materials, engineered to cure under a light source. The exact composition of the materials is mostly proprietary information of the manufacturer, the materials are usually known by given names that describe one of their properties or applications. Little information is available on the mechanical properties of these resins, therefore selection of appropriate materials will often be on a trial-and-error basis. To remove residual liquid resin from the cured material after printing, the part is typically washed in isopropanol. Afterwards, a post-curing step takes place using heat and UV-light, to obtain the optimum mechanical properties of the material.

5

5.1.3 Challenges

For the trocar, there are a number of challenges in its current design. The design of the cannula relies on the successful printing of a small, open channel, and for the valve three open incisions need to be printed accurately. These type of hollow features with small dimensions ($>200\ \mu\text{m}$), i.e. negative features, proved difficult in the production of microneedles [28] and microfluidic devices [29,30]. Such enclosed channels are generally fused shut during the production process. In contrast, small, “positive” features can be produced accurately using SLA [31]. To investigate these limitations, the design and printing of the trocars was carried out in two stages. In the first stage, the design was printed as-is with minimal changes, to determine the most suitable print settings and materials, as well as indicate problematic areas that require a redesign. In the second stage, the design and process are optimized for SLA printing, in order to obtain a functional trocar.

5.2 INITIAL DESIGN

5.2.1 Initial design and method

First we investigated the effect of the used materials on the accuracy of positive and negative features of the trocar. The challenge in printing the cannula is obtaining an open

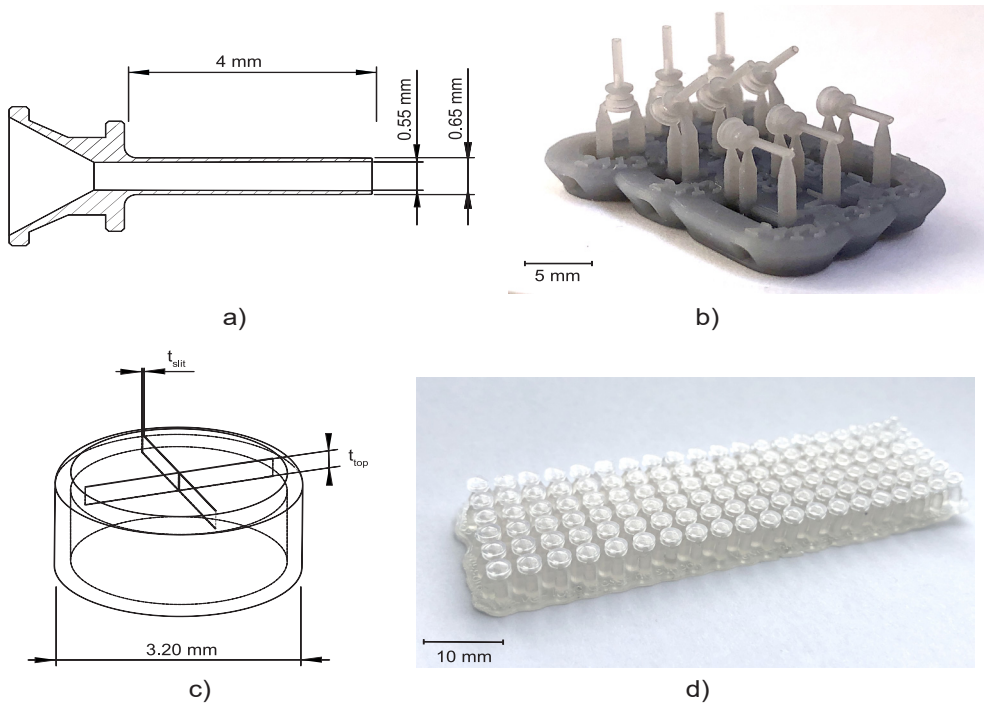


Figure 5.2: Overview of the 3D printed cannulas and valves. a) Design and dimensions of the printed cannula. b) Example of the 3D printed cannulas in three different orientations, still on their support structure. c) Design and the dimensions that were tested for the valve, in which t_{slit} is the thickness of the slits, and t_{top} is the thickness of the top. d) Example of the 3D printed valves with different dimensions, still on their support structure.

channel of the desired dimensions with the thin wall thickness required (Figure 5.2a). Four materials were investigated to 3D print the cannulas: Dental SG, Model, Grey Pro, and Durable, of which Dental SG and Model are both biocompatible materials. In addition, two process settings were tested: 1) the build orientation and 2) the layer height. The cannulas were printed in three different print orientations: 0° , in which the channel is positioned vertically, 45° , and 90° , in which the channel is positioned horizontally (Figure 5.2b). For the layer height, the smallest and largest layer heights were chosen. Depending on the material, the smallest layer height was $25\ \mu\text{m}$ or $50\ \mu\text{m}$, while the largest layer height was $100\ \mu\text{m}$ for all materials. For each print setting three cannulas were printed, resulting in a total of 18 printed cannulas per material. After printing the parts were washed and post-cured according to manufacturer instructions, and measurements were taken using a digital microscope.

The challenge in 3D printing the valve is to obtain separate valve flaps that can move independently, but are close enough together to prevent leakage. To facilitate this, we adjusted the design to be more suitable for 3D printing by maximizing the length of the slits to 2.6 mm, which is the maximum length without changing the size of the cap itself, and

by applying a four slit cross shape instead of the three slits in the original design in Figure 5.1b, to allow for more compliancy. The tested parameters were the top layer thickness and the slit thickness, illustrated in Figure 5.2c, since both influence the functions of the valve. The thickness of the top layer (t_{top}) was tested in thicknesses starting at 75 μm up to 200 μm , with increments of 25 μm . The thickness of the cuts of the slits (t_{slit}) ranged from 10 μm to 200 μm , with increments of 10 μm . The assumption here is that for the sizes larger than the desired slit size, the slits will be partially fused and end up approaching the desired slit size. Based on these dimensions, a total of 120 valves were printed per material (Figure 5.2d).

Four different materials were investigated to 3D print the valves: Dental SG, Durable, Elastic 50A, and Flexible 80A. A digital microscope was used to measure the t_{slit} of the valves for which the slits were as close together as possible, but not fused shut. Subsequently, a 27G hollow needle was used to test the valves' compliancy and level of springback, by

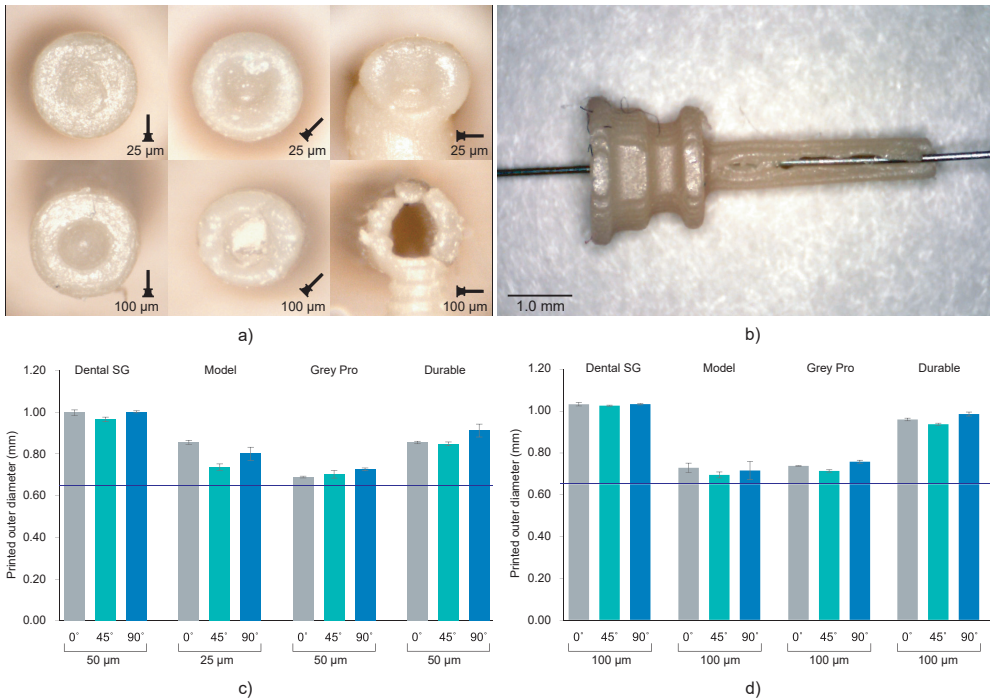


Figure 5.3: Results of the investigation into different materials and print settings for the cannulas. a) Example of the distal ends of the valves printed in Model, which was among the most successful materials, in different orientations and with different layer heights. For the cannulas in the 90° orientation, the support pillar is visible at the bottom. b) Cannula printed in Model with 100 μm layer height and open internal channel, although the wall is visibly torn. c) The average outer dimensions of the channel given per material and per build angle for the smallest layer height setting per material. The purple line indicates the as-drawn dimensions of the outer channel. d) The average outer dimensions of the channel given per material and per build angle for the largest layer height setting per material. The purple line indicates the as-drawn dimensions of the outer channel.

checking if the needle could be inserted without breaking the valve (level of compliancy) and if after the removal the valve could return to its initial position (level of springback).

5.2.2 Initial design results

The inner channels of the 3D printed cannulas were in almost all cases fused shut, regardless of material, layer height or build angle, with only an indentation visible at the distal end of the cannula (Figure 5.3a and Figure S5.1 in the supplementary material at the end of this Chapter). Only the cannulas printed with Model with a layer height of 100 μm in the 90° orientation had a visibly open channel. However, the walls were very fragile and tore immediately when inserting a hollow needle (Figure 5.3b). In the 90° orientation, for all other settings and materials, the cannulas had no open channel and were severely deformed. Since most of the cannulas were fused shut, only the dimensions of the outer channel were measured, for which the results are given in Figure 5.3c-d and Table S5.1 in the supplementary material. When compared to the as-drawn outer dimensions of the cannula (purple line in Figure 5.3c-d), Dental SG has the lowest accuracy for all print settings, while Model and Grey Pro have the highest accuracy. There appear to be no significant differences between the different orientation angles, although the 90° orientation shows a slightly lower accuracy for all materials.

The valves with the smallest top- and slit dimensions, for which the valve flaps were not fused together, were measured for Dental SG, Durable, and Elastic 50A (Dimensions of the valves with the smallest top-and slit dimensions. The printed slit thicknesses were measured using a digital microscope, and Figure 5.4), and their negative surface area was calculated (Figure S5.2 in the supplementary material). The valves printed in Flexible 80A were all completely fused, except for a hole in the center (Figure 5.4a). For the other materials, it was noticeable that although the printed openings of the slits were larger than drawn, a 10 μm increment smaller in drawn slit size would mean that the slits were partly or fully fused together. A possible explanation for this is material shrinkage, which can more easily occur when the valve flaps are not attached to each other. Insertion of the hollow needle into the valves showed that the materials Dental SG and Durable were too brittle, resulting in breakage of the valve flaps rather than deformation (Figure S5.3a in the supplementary material). Both Elastic 50A and Flexible 80A showed compliant behavior and flexibility (Figure S5.3b in the supplementary material), although Elastic 50A was so soft that it was easy to puncture.

Table 5.1: Dimensions of the valves with the smallest top-and slit dimensions. The printed slit thicknesses were measured using a digital microscope.

	Dental SG	Durable	Elastic 50A	Flexible 80A
Slit thickness as-drawn	140 μm	90 μm	150 μm	200 μm
Top thickness as-drawn	75 μm	75 μm	200 μm	75 μm
Printed slit thickness (max.)	248 μm	131 μm	261 μm	-

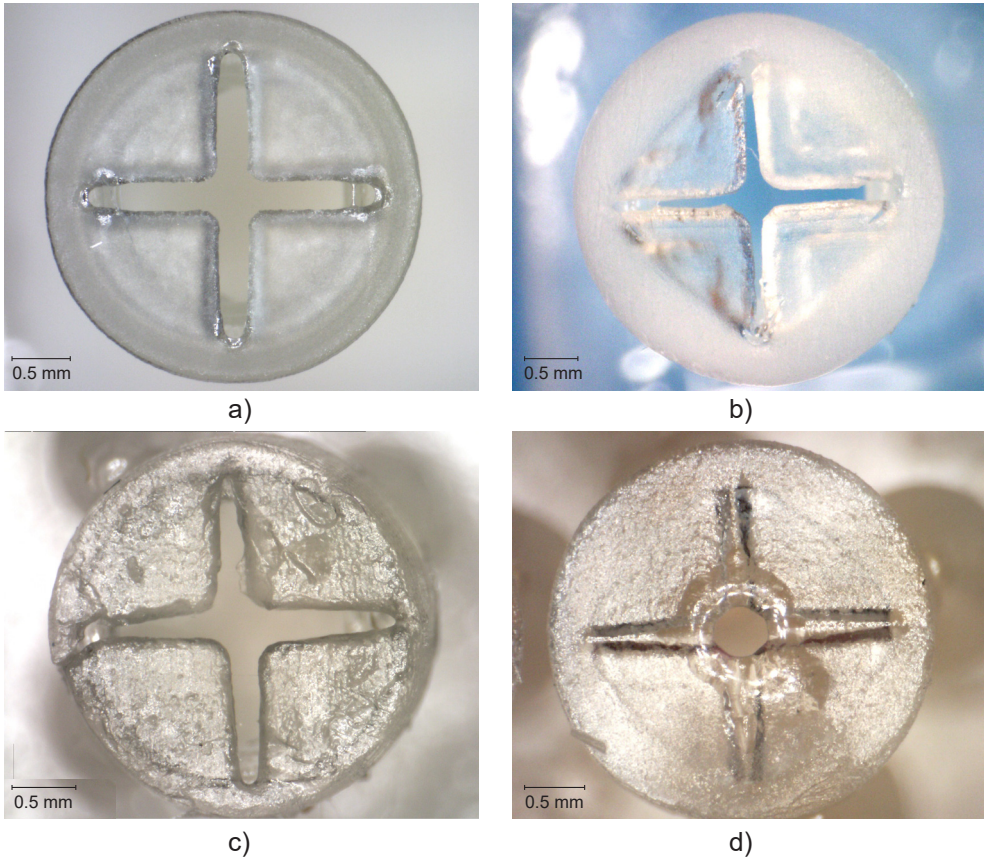


Figure 5.4: Top surfaces of the 3D printed valves with the smallest top-and slit dimensions for different materials. a) Valve printed in Dental SG. b) Valve printed in Durable. c) Valve printed in Elastic 50A. d) Valve printed in Flexible 80A, with only an opening in the centre of the valve.

5.2.3 Initial design discussion

Based on the 3D printing experiments, the design of the trocar as-is is incompatible with SLA, regardless of the material or print settings. We compared different materials, build orientations and layer heights for the cannula, but none resulted in a usable, opened internal channel. The measurements of the outer diameter showed that in all cases the cannulas were printed larger than drawn. Model and Grey Pro approached the drawn dimensions the closest, in which Model has the advantage of being biocompatible. Some studies have indicated that a higher layer thickness leads to a more accurate part [24, 25], however in our case the size of the layers relative to the part was too large to be functional. The build angles of 0° and 45° showed most promising results. The ones printed in 90° were more oval than round, and needed extra support pillars, which would cause the cannulas to break when removing them. Although multiple studies have researched factors that can improve the accuracy, our study shows that these can be conflicting for the purpose of a functional product. For instance, for the cannulas printed in Model, it was possible

to print an open channel with a higher layer thickness. However, a higher layer thickness also resulted in cannula walls that were too fragile, which resulted in a non-usable cannula.

None of the valves were printed with the required 10 μm slits thickness. In the cases the slits were not fused together, they were larger than drawn, and therefore not usable as a valve. A possible solution could be to use the valves that were mostly fused shut, since these have a lower percentage of open surface area. However, as was seen in the compliance test, this will lead to breakage of the valve when inserting an instrument. For Elastic 50A and Flexible 80A, which have a high flexibility, the hollow needle was able to puncture the top surface, however this resulted in a hole in the valve that cannot be closed off. Instruments compatible with this size of trocar have a diameter of 460 μm , which is only slightly smaller than the diameter of the internal channel of the cannula (550 μm), which would not be able to prevent leakage.

As previous studies have pointed out, refraction and diffraction of the laser spot can lead to an effect sometimes referred to as “false printing” [29,32], in which material outside of the laser spot is slightly cured. When printing a hollow tube, such as the cannula, the laser spot draws a circular shape around a negative space for each layer. Due to the small size of this negative space, the cumulative effect of false printing builds up and fully cures the internal channel as well. One option to obtain a functional trocar would therefore be to adjust the size of the cannula, for instance to 20G (0.81 mm). However, this size of trocar has been abandoned in eye surgery in favour of smaller sizes. In an attempt to circumvent the false printing effect and stretch the limits of the printing technology, we propose two solutions: 1) increase the size of the negative space surrounding the features; 2) decrease the curable surface area of each layer, and make sure this surface area is not in the same spot for each layer. Using these solutions, in the next section we present a new design for the cannula and the valve specified to the SLA process.

5.3 DESIGN OPTIMIZATION

5.3.1 Optimized design and method

To optimize the cannula for 3D printing, we explored the possibility of printing a trocar with a minimum curable surface area per layer and maximization of the negative space surrounding it. In our design, the cannula is composed of a helical structure (Figure 5.5a), so that each layer has a smaller surface area that needs to be cured, as compared to that of a hollow tube. In addition, considering the structure is printed in the vertical orientation, the to-be-cured surface area is not in exactly the same spot for each layer, which results in less cumulative build-up of false printing. The thickness of the helix, which is the wall thickness, is 100 μm , equal to the wall thickness. Although the original cannula design has a wall thickness of 50 μm , this is smaller than the size of the laser spot (85 μm), and can therefore not be produced in this size. Two vertical columns with the same thickness were added to function as custom support structure, to ensure printability, and to prevent the structure from acting as a spring. To prevent the sides of the channel from being

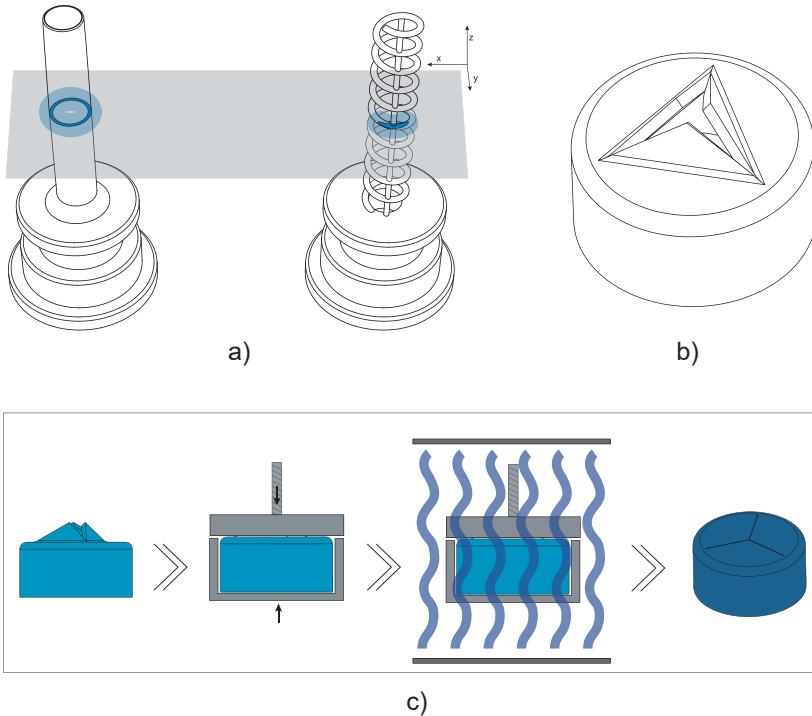


Figure 5.5: Overview of the optimized design and method for printing the trocars. a) The new helix design (right) of the cannula, which has a smaller surface area (dark blue) per layer than the previous cannula (left), and should therefore be less hindered by the effects of false printing (light blue). b) 3D model of the valve, in which the valve flaps are modelled to point upwards in order to create more negative space around them. c) New production process steps for the valves: after printing and cleaning, the valves are placed in a clamp which presses the flaps down; the entire clamp and valve are subsequently cured.

completely open, the pitch of the helix should be as small as possible, so that the windings of the helix will fuse together. To find the optimal value, we tested the helix with a pitch of 0.40 mm (10 revolutions), 0.33 mm (12 revolutions), 0.29 mm (14 revolutions), 0.25 mm (16 revolutions), 0.22 mm (18 revolutions), and 0.20 mm (20 revolutions). The new design was printed in Model, since this material showed accurate results in the previous tests and is biocompatible, in the vertical 0° orientation with a layer height of $50\ \mu\text{m}$. After printing the parts were washed and post-cured. Measurements were taken with a digital microscope and with a Scanning Electron Microscope (SEM) of the internal lumen and the wall thickness.

For the valve, we attempted to create more negative space surrounding the miniature features. We accomplished this by opening up the flexible flaps in the CAD file, so that they are positioned upwards (Figure 5.5b). This creates more negative space surrounding the flaps, while maintaining the right dimensions. Ideally, the flaps would be printed in a downward open position, so that the pressure in the eye causes them to close, however the limited space in the cap of the valve makes it impossible to print them separately from

each other in that position.

The flaps were opened under an angle of 60° , with a flap- and top thickness of 0.15 mm. In order to negate the effects of shrinkage, the flaps were designed to be slightly longer than required when printing them flat, 0.69 mm instead of 0.54 mm, which was experimentally determined after a number of try-outs. The valves were printed in Flexible 80A, which showed the best compliant behavior in our previous test, with a layer thickness of $50\ \mu\text{m}$. In the post-curing step after printing and cleaning, the flaps were pressed into their correct closed position, by placing them into an enclosure with a transparent lid. The entire enclosure was then cured, and after cooling the flaps remained in the desired, closed position. This process is schematically shown in Figure 5.5c. Measurements were taken with a digital microscope and with a Scanning Electron Microscope (SEM). The tests with insertion of the needle were repeated to determine their compliancy and springback.

5.3.2 Optimized design results

The new design of the cannula prevents false printing from fusing the internal lumen shut. With this design, all cannulas were printed with an opened internal lumen. The internal lumen was measured with a digital microscope, and the thickness of the printed helix with a SEM. In order to be used in eye surgery, the cannula should accommodate instruments of standard size, which can be $400\ \mu\text{m}$ at minimum. Therefore, the inner lumen of the trocar should be slightly larger than this size. As depicted in Figure 5.6b, the number of revolutions of the helix, and therefore the size of the pitch, influences the

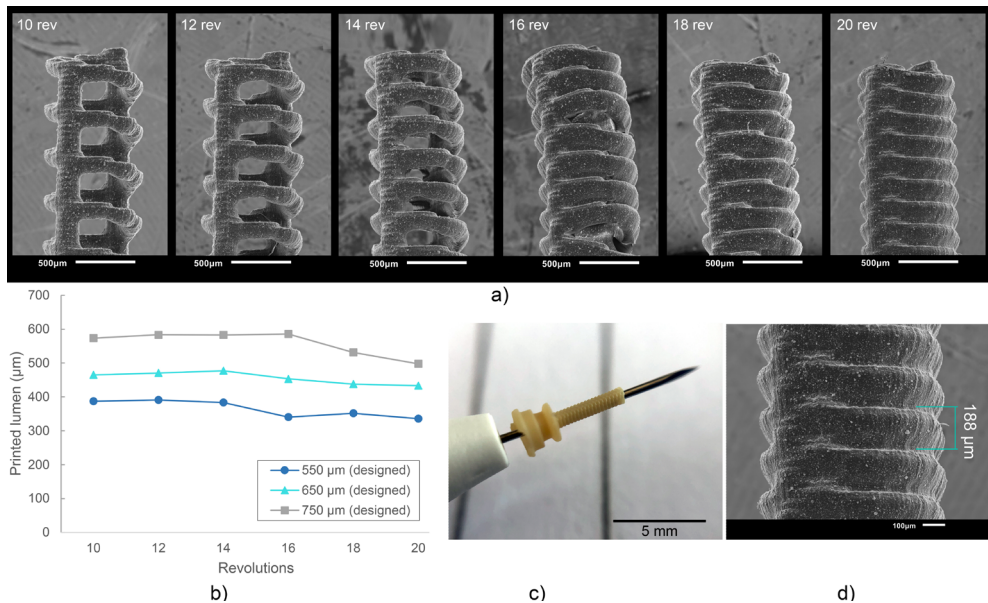


Figure 5.6: Results of the new cannula design. a) SEM images of the tips of the cannulas showing the effects of different numbers of revolutions of the helix. b) Influence of the number of revolutions on the size of the internal channel of the cannulas. c) Close up of a 3D printed helix cannula placed on the tip of a 27G inserter knife. d) SEM image and measurements of the helix cannula with 20 revolutions.

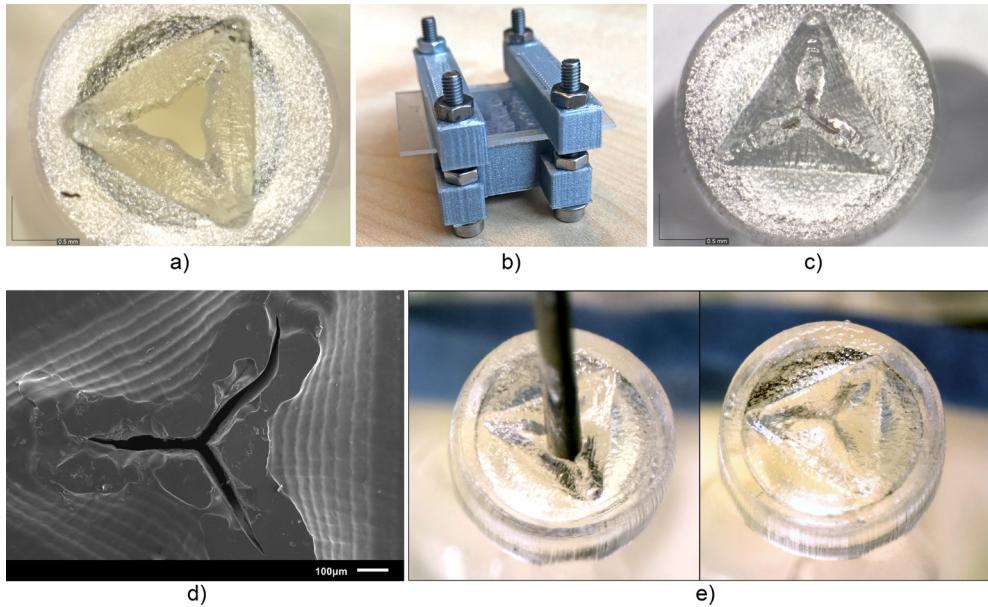


Figure 5.7: Results of the new valve 3D print process. a) Close up of a valve before curing, showing the opened valve flaps. b) Clamp set up for curing the valves. c) Close up of the valve after curing, the valve flaps have been pressed to their horizontal position, and no gap is visible between the flaps. d) SEM image of the valve after curing. e) Needle insertion test of the new valves, the needle can be easily inserted through the valve (left) and afterwards the flaps return to their horizontal position (right).

internal lumen of the cannula: the more revolutions, the smaller the remaining lumen. The difference between the printed diameter and the diameter as modelled increased from 175 μm on average with 10 revolutions, to 228 μm on average with 20 revolutions. As can be seen from this graph, in order to obtain a lumen of more than 400 μm , the helix should be designed with an inner diameter of 650 μm . This result is consistent with our approach of decreasing the size of the positive features, since more revolutions decrease the distance between the windings, and result in a larger surface area per layer. However, decreasing the revolutions leads to spacing between the windings (Figure 5.6a), which is also undesirable for our purpose. The helix with 20 revolutions shows no gaps in the side of the channel, and is therefore most suited for the cannula. The outer diameter of these cannulas was measured to be $828 \pm 13 \mu\text{m}$. It should be noted that with these settings the size of the inner diameter corresponds to a 27G trocar size, while the size of the outer diameter corresponds to the 23G trocar size.

The valves printed with the new process steps are shown in Figure 5.7. Measuring the slits in the valves using SEM (Figure 5.7d) shows that they range from 17 μm to 35 μm thickness. Although this is larger than the desired value of 10 μm , the open slits are not as long as in the original design, resulting in a smaller open surface area. The tests with insertion of the needle were also repeated, which showed that the material has enough compli-

ancy to allow an instrument to enter, and the flaps to return to their closed position when the needle is removed (Figure 5.7e).

5.4 EYE PHANTOM INSERTION

5.4.1 Insertion test method

The use of a polymer instead of metal to produce the cannula results in an inherently weaker design. This could mean that the cannula will break during insertion into the eye. The performance of the 3D printed trocar was tested by inserting it into an eye phantom (Eyecre.at GmbH, Ötztal, Austria), while measuring the insertion force, and comparing it with a commercially available trocar. The phantom eye was fixed onto a digital precision scale. The 3D printed trocar was assembled by placing the valve on top of the cannula, after which it was placed on the knife of a commercially available 27G trocar inserter (D.O.R.C., Zuidland, The Netherlands). The trocar was inserted into the scleral phantom by means of a single step, straight insertion. After insertion, a digital microscope was used to check whether there was no leakage of fluids from the valve. Subsequently, the trocars were removed using tweezers and examined under a digital microscope for signs of breakage. The test was performed with five 3D printed trocars. The maximum force as measured by the digital scale was recorded for each insertion test. Images of the test are shown in Figure 5.8. For comparison, commercially available 23G and 27G trocars (D.O.R.C., Zuidland, The Netherlands) were inserted in the same manner (n = 5).

5.4.2 Insertion test results

The maximum force measured during insertion for each of the trocars is shown in Table 5.2. The insertion force for the 3D printed trocar was almost 70% higher than for the commercially available 27G trocar, and almost 50% higher than for the 23G trocar. The higher force can be attributed to the larger wall thickness, which results in a larger step-difference between the knife inserter and the trocar, as well as the ‘ribbed’ outer wall that results from the helix design. It was visible as a larger deformation of the scleral phantom (Figure 5.8d), while the commercial trocars showed almost no deformation of the phantom. None of the 3D printed trocars broke during insertion or extraction. The valves did not show leakage while in the eye, although no additional pressure was applied. In eye surgery, the eye is artificially kept on a certain pressure, which can range from 0 to 120 mmHg, depending on the specific operation [33], however for higher pressures it is often required that the valve allows fluid to escape [13].

Table 5.2: Maximum forces measured during insertion of commercial and 3D printed trocars into an artificial eye phantom.

	Commercial 23G	Commercial 27G	3D printed 27G
Maximum insertion force (n = 5)	3.20 ± 0.37	2.82 ± 0.22	4.78 ± 0.26

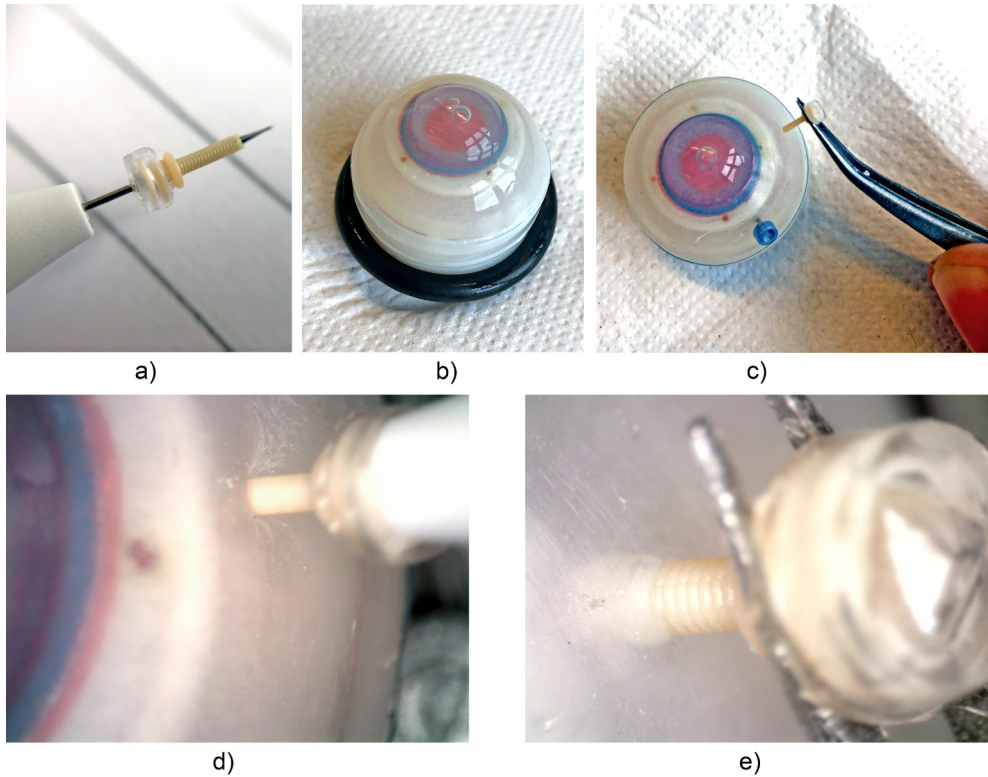


Figure 5.8: Insertion tests into an artificial eye phantom. a) Assembled trocar on a 27G commercial insert-er knife. b) Artificial eye for testing. c) Removal of the 3D printed trocar from the eye, showing that it is still intact. d) Magnification of the insertion of the 3D printed trocar, showing the deformation of the sclera. e) Magnification of the removal of the 3D printed trocar.

5.5 DISCUSSION

5.5.1 Process and method

Functional complexity is often considered one of the main advantages of 3D printing. The ability to produce a complete, functional product in a single production step can have many advantages for the manufacturing process. However, functional complexity does not always come easily. In this study, we aimed to investigate whether it would be possible to produce a trocar used in ophthalmology using 3D printing. SLA was chosen as best suited 3D printing technique for this study because is known for its ability to produce small features and the wide range of materials available. However, the theoretical information available about 3D printing techniques and materials does not present a full spectrum of what is possible with a certain 3D printing technique. Therefore, first we investigated the suitability of different materials and process settings for both the cannula and the valve. Materials with different properties were used, in order to gain more knowledge on the

minimum feature size achievable. Even within one 3D printing technology we have seen large differences between the accuracy and functionality that can be obtained for different materials. The main conclusion we can draw from this is that it is important for any successful 3D print design to be aware of the influence of the material choice in advance, therefore starting the design process with an investigation into these settings is recommended.

We succeeded in creating a functional trocar by circumventing the inherent limitations of the SLA process. The process we followed in order to accomplish this was 1) creating a thorough understanding of the challenges of the process; 2) exploring different materials and print settings to find the most suitable ones; 3) evaluating and adjusting which parts of the design still posed challenges for the chosen AM technology. This systematic approach for finding the relevant print settings, materials, and dimensions can be applied to any print method. We proposed two strategies, increasing the surrounding negative space and decreasing the surface area per layer, which are specific for SLA and circumvent the effects of false printing. Although these solutions were specific to our design and desired application, they have the potential for application in different fields for which miniature negative features are required. Increasing the surrounding negative space can be applied as a general strategy by folding the part open as we have shown here, dividing the part in different substructures, or even considering different build angles. Decreasing the surface area per layer can be applied by adjusting the structure as we have shown here, as well as adjusting the build angle. It should be noted that these changes may negatively affect the mechanical properties of the part, so a careful consideration is required.

We have investigated the effects of materials, build angles, and layer heights on the accuracy and functionality of our design. There are more factors that have been shown to influence the accuracy of SLA parts, such as exposure time and laser intensity [14,34], that we have not investigated. Since the used Form 3B printer is a closed system, it is not possible to change these printing parameters manually. The slicing software will determine the optimal printing parameters based on the material and layer height that are chosen. A disadvantage is that it is not possible to adjust these parameters to improve the accuracy of the results. However, the advantage of the closed system is that the printer manufacturer can optimize the materials and settings for specific applications, as has been happening for dental applications in recent years, which improves the ease-of-use for users. This has caused the FormLabs system to be widely accepted in commercial dental practices, and therefore we consider this a realistic scenario for further integration of 3D printing technology and healthcare.

5.5.2 3D printed trocar

The 3D printed trocar does have some inherent drawbacks caused by the changes to the design. The wall thickness is larger than in the original design, which is caused by the minimum feature size of the 3D printing process. In addition, the ribbed wall from the helical structure might cause damage in the eye. To prevent this, an extra processing step could be added to smooth out the outer wall, or alternatively, a rectangular cross-section for the

helix could be explored. Regardless, the tests in the phantom eye show that the plastic cannula has enough stiffness to be inserted and extracted into the sclera without breaking. This shows the feasibility of using a 3D printed trocar in ophthalmic surgeries, although more tests in for instance porcine eyes are required to determine the behavior of the trocar in actual tissue.

An additional challenge when producing miniature hollow features using SLA, is left-over resin becoming trapped [35], which we encountered when attempting to 3D print the initial design of the valve. In the new design of the valve, this was no longer a problem, since we opened up the valve flaps, creating sufficient space to clean out all excess resin. Although we added an additional process step in order to produce the valve by having to close the valve flaps, the advantage of better cleaning makes the process easier and leads to an improved end result. The same is true for the helical design of the cannulas. The design we used for testing with 20 revolutions showed that there was no spacing between the revolutions, however even with less revolutions it was possible to successfully print the design. The openness of the structure with less revolutions makes it more accessible to clean, which could also have contributed to the fact that less revolutions lead to a larger internal diameter.

The design of the 3D printed trocar allows for further personalization depending on the specific requirements of both patient and surgeon. For instance, the length of the cannula can be easily tailored to the thickness of the individual sclera. The thickness of the sclera can range from 0.39 mm to 0.67 mm [36], and it is important that the cannula is not too long to avoid damaging internal structures in the eye, yet long enough to reach the vitreous cavity. The design of the valve can be optimized to allow escape of fluids for certain pressures, by varying the length and thickness of the valve flaps. In addition, the trocars placed in the eye often have specific functions during the surgery, and AM enables that they can be adjusted for their specific function.

So far in this research, we have 3D printed a cannula and valve separately. In future work, it will be interesting to look into the additional benefit of 3D printing an entire assembly in one single production step. For the trocar, this would mean printing the cannula and valve as one part. Current commercially available SLA printers are limited to the production of only one material at a time, although multi-material SLA printers are in development [37]. For now, this means that both parts of the trocar need to be made from the same material. Since the cannula requires a certain stiffness, the best suggestion would be a redesign of the valve to work with a stiffer material, for instance a duckbill valve. Alternatively, other techniques, such as PolyJet printing, can be explored, in which it is possible to combine rigid and flexible materials in a single production step.

5.6 CONCLUSION

In this study, we attempted to 3D print a functional trocar intended for use in eye surgery, consisting of a hollow, stiff cannula, and a flexible valve. The trocar contains sub-millimeter scale features, which is why SLA was chosen as the preferred 3D printing technique

due to the high reported resolution and minimum feature size. We divided the research into two stages; in the first stage we investigated the effects of different materials and print settings on the unchanged conventional design, and in the second stage we used these findings to optimize the design and production process. The results of the first stage showed that the production of miniature, negative features was most problematic, regardless of materials or print settings. We determined that this is caused by an effect known as ‘false printing’, causing partial curing of surrounding layers. Therefore, in the second stage we presented a new design of the trocar that circumvents these effects by reducing the surface area per layer and creates more space surrounding the feature. With this new design, we succeeded in printing a miniature cannula with an open internal channel of 0.44 mm, and a functional, flexible valve. We evaluated the performance of this trocar on an eye phantom, which showed that it can be inserted and extracted from the eye without breakage. However, the measured insertion forces were 70% higher than from a commercial trocar, which can be attributed to the higher wall thickness and ribbed structure of the cannula.

Overall, in this work we have shown the potential of using SLA for the production of a miniature, functional trocar. We have shown an approach in which we systemically test relevant 3D print settings, materials, and part dimensions in order to obtain the required functionality and accuracy for our device. Although vat photopolymerization techniques are reported to have one of the highest theoretical resolutions, there are still a number of practical limitations hindering the adaptation of these technologies for miniaturized, functional devices. Mapping these limitations can help manufacturers and engineers to improve these AM techniques and develop materials and workflows for improved accuracy for functional designs.

REFERENCES

- [1] C. Culmone, G. Smit, P. Breedveld, Additive manufacturing of medical instruments: A state-of-the-art review, *Addit. Manuf.* 27 (2019) 461-473. <https://doi.org/10.1016/j.addma.2019.03.015>.
- [2] K. Lussenburg, A. Sakes, P. Breedveld, Design of non-assembly mechanisms: A state-of-the-art review, *Addit. Manuf.* 39 (2021) 101846. <https://doi.org/10.1016/j.addma.2021.101846>.
- [3] A. Pugalendhi, R. Ranganathan, A review of additive manufacturing applications in ophthalmology, *Proc. Inst. Mech. Eng. Part HJ. Eng. Med.* (2021) 1-17. <https://doi.org/10.1177/09544119211028069>.
- [4] C. Schubert, M.C. van Langeveld, L.A. Donoso, Innovations in 3D printing: a 3D overview from optics to organs, *Br. J. Ophthalmol.* 98 (2014) 159-161. <https://doi.org/10.1136/bjophthalmol-2013-304446>.
- [5] E. V. Navajas, M. ten Hove, Three-Dimensional Printing of a Transconjunctival Vitrectomy Trocar-Cannula System, *Ophthalmologica.* 237 (2017) 119-122. <https://doi.org/10.1159/000457807>.
- [6] F.P.W. Melchels, J. Feijen, D.W. Grijpma, A review on stereolithography and its applications in biomedical engineering, *Biomaterials.* 31 (2010) 6121-6130. <https://doi.org/10.1016/j.biomaterials.2010.04.050>.
- [7] I. Gibson, D. Rosen, B. Stucker, *Additive Manufacturing Technologies*, Springer New York, New York, NY, 2015. <https://doi.org/10.1007/978-1-4939-2113-3>.

- [8] M. Vaezi, H. Seitz, S. Yang, A review on 3D micro-additive manufacturing technologies, *Int. J. Adv. Manuf. Technol.* 67 (2013) 1721-1754. <https://doi.org/10.1007/s00170-012-4605-2>.
- [9] L.E. Diment, M.S. Thompson, J.H.M. Bergmann, Clinical efficacy and effectiveness of 3D printing: a systematic review, *BMJ Open.* 7 (2017) e016891. <https://doi.org/10.1136/bmjopen-2017-016891>.
- [10] J.S. Cuellar, G. Smit, A.A. Zadpoor, P. Breedveld, Ten guidelines for the design of non-assembly mechanisms: The case of 3D-printed prosthetic hands, *Proc. Inst. Mech. Eng. Part H J. Eng. Med.* 232 (2018) 962-971. <https://doi.org/10.1177/0954411918794734>.
- [11] U. Spandau, H. Heimann, *Practical Handbook for Small-Gauge Vitrectomy*, 2012. <https://doi.org/10.1007/978-3-642-23294-7>.
- [12] S. Mohamed, C. Claes, C.W. Tsang, Review of Small Gauge Vitrectomy: Progress and Innovations, *J. Ophthalmol.* 2017 (2017) 1-9. <https://doi.org/10.1155/2017/6285869>.
- [13] M.A. Klufas, *Trocar/Cannula Roundup*, *New Retin. MD.* (2016) 8-15.
- [14] C. Schmidleithner, D.M. Kalaskar, Stereolithography, in: *3D Print., InTech*, 2018. <https://doi.org/10.5772/intechopen.78147>.
- [15] High Resolution SLA and SLS 3D Printers for Professionals | Formlabs, (n.d.). <https://formlabs.com/> (accessed May 3, 2021).
- [16] EnvisionTEC, *Understanding 3D Printer Accuracy: Cutting Through the Smoke and Mirrors*, 2017. <https://envisiontec.com/wp-content/uploads/2017/08/Accuracy-versus-Resolution-0824172.pdf> (accessed February 19, 2021).
- [17] D. Dimitrov, W. Van Wijck, K. Schreve, N. De Beer, J. Meijer, An investigation of the capability profile of the three dimensional printing process with an emphasis on the achievable accuracy, *CIRP Ann. - Manuf. Technol.* 52 (2003) 189-192. [https://doi.org/10.1016/S0007-8506\(07\)60562-9](https://doi.org/10.1016/S0007-8506(07)60562-9).
- [18] C. Lynn-Charney, D.W. Rosen, Usage of accuracy models in stereolithography process planning, *Rapid Prototyp. J.* 6 (2000) 77-86. <https://doi.org/10.1108/13552540010323600>.
- [19] N. Alharbi, R. Osman, D. Wismeijer, Factors Influencing the Dimensional Accuracy of 3D-Printed Full-Coverage Dental Restorations Using Stereolithography Technology, *Int. J. Prosthodont.* 29 (2016) 503-510. <https://doi.org/10.11607/ijp.4835>.
- [20] T. Hada, M. Kanazawa, M. Iwaki, T. Arakida, Y. Soeda, A. Katheng, R. Otake, S. Minakuchi, Effect of Printing Direction on the Accuracy of 3D-Printed Dentures Using Stereolithography Technology, *Materials (Basel)*. 13 (2020) 3405. <https://doi.org/10.3390/ma13153405>.
- [21] E. Yankov, M.P. Nikolova, Comparison of the Accuracy of 3D Printed Prototypes Using the Stereolithography (SLA) Method with the Digital CAD Models, *MATEC Web Conf.* 137 (2017) 02014. <https://doi.org/10.1051/mateconf/201713702014>.
- [22] P.-H. Lee, H. Chung, S.W. Lee, J. Yoo, J. Ko, Review: Dimensional Accuracy in Additive Manufacturing Processes, in: *Vol. 1 Mater. Micro Nano Technol. Prop. Appl. Syst. Sustain. Manuf.*, American Society of Mechanical Engineers, 2014. <https://doi.org/10.1115/MSEC2014-4037>.
- [23] I. Cotabarren, C.A. Palla, C.T. McCue, A.J. Hart, An assessment of the dimensional accuracy and geometry-resolution limit of desktop stereolithography using response surface methodology, *Rapid Prototyp. J.* 25 (2019) 1169-1186. <https://doi.org/10.1108/RPJ-03-2019-0060>.
- [24] N. Nestler, C. Wesemann, B.C. Spies, F. Beuer, A. Bumann, Dimensional accuracy of extrusion- and photopolymerization-based 3D printers: In vitro study comparing printed casts, *J. Prosthet. Dent.* 125 (2021) 103-110. <https://doi.org/10.1016/j.prosdent.2019.11.011>.

REFERENCES

- [25] C.S. Favero, J.D. English, B.E. Cozad, J.O. Wirthlin, M.M. Short, F.K. Kasper, Effect of print layer height and printer type on the accuracy of 3-dimensional printed orthodontic models, *Am. J. Orthod. Dentofac. Orthop.* 152 (2017) 557-565. <https://doi.org/10.1016/j.ajodo.2017.06.012>.
- [26] E. Umaras, M.S.G. Tsuzuki, Additive Manufacturing - Considerations on Geometric Accuracy and Factors of Influence, *IFAC-PapersOnLine.* 50 (2017) 14940-14945. <https://doi.org/10.1016/j.ifacol.2017.08.2545>.
- [27] E.R. Khorasani, H. Baseri, Determination of optimum SLA process parameters of H-shaped parts, *J. Mech. Sci. Technol.* 27 (2013) 857-863. <https://doi.org/10.1007/s12206-013-0111-1>.
- [28] S.N. Economidou, M.J. Uddin, M.J. Marques, D. Douroumis, W.T. Sow, H. Li, A. Reid, J.F.C. Windmill, A. Podoleanu, A novel 3D printed hollow microneedle microelectromechanical system for controlled, personalized transdermal drug delivery, *Addit. Manuf.* 38 (2021) 101815. <https://doi.org/10.1016/j.addma.2020.101815>.
- [29] C. Yeung, S. Chen, B. King, H. Lin, K. King, F. Akhtar, G. Diaz, B. Wang, J. Zhu, W. Sun, A. Khademhosseini, S. Emaminejad, A 3D-printed microfluidic-enabled hollow microneedle architecture for transdermal drug delivery, *Biomicrofluidics.* 13 (2019) 064125. <https://doi.org/10.1063/1.5127778>.
- [30] A.K. Au, W. Lee, A. Folch, Mail-order microfluidics: evaluation of stereolithography for the production of microfluidic devices, *Lab Chip.* 14 (2014) 1294-1301. <https://doi.org/10.1039/C3LC51360B>.
- [31] D. Behera, S. Chizari, L.A. Shaw, M. Porter, R. Hensleigh, Z. Xu, N.K. Roy, L.G. Connolly, X. (Rayne) Zheng, S. Saha, J.B. Hopkins, M.A. Cullinan, Current challenges and potential directions towards precision microscale additive manufacturing - Part II: Laser-based curing, heating, and trapping processes, *Precis. Eng.* 68 (2021) 301-318. <https://doi.org/10.1016/j.precisioneng.2020.12.012>.
- [32] A. Kundu, T. Ausaf, S. Rajaraman, 3D Printing, Ink Casting and Micromachined Lamination (3D PICL μ M): A Makerspace Approach to the Fabrication of Biological Microdevices, *Micromachines.* 9 (2018) 85. <https://doi.org/10.3390/mi9020085>.
- [33] L.C. Moorhead, Dynamic Intraocular Pressure Measurements During Vitrectomy, *Arch. Ophthalmol.* 123 (2005) 1514. <https://doi.org/10.1001/archoph.123.11.1514>.
- [34] A. Davoudinejad, D.B. Pedersen, G. Tosello, Evaluation of polymer micro parts produced by additive manufacturing processes using vat photopolymerization method, in: *Dimens. Accuracy Surf. Finish Addit. Manuf.*, Euspen, 2017. www.euspen.eu (accessed January 19, 2021).
- [35] C. Culmone, P.W.J. Henselmans, R.I.B. van Starckenburg, P. Breedveld, Exploring non-assembly 3D printing for novel compliant surgical devices, *PLoS One.* 15 (2020) e0232952. <https://doi.org/10.1371/journal.pone.0232952>.
- [36] T.W. Olsen, S.Y. Aaberg, D.H. Geroski, H.F. Edelhauser, Human sclera: Thickness and surface area, *Am. J. Ophthalmol.* 125 (1998) 237-241. [https://doi.org/10.1016/S0002-9394\(99\)80096-8](https://doi.org/10.1016/S0002-9394(99)80096-8).
- [37] S. Waheed, J.M. Cabot, N.P. Macdonald, T. Lewis, R.M. Guijt, B. Paull, M.C. Breadmore, 3D printed microfluidic devices: enablers and barriers, *Lab Chip.* 16 (2016) 1993-2013. <https://doi.org/10.1039/C6LC00284F>.

SUPPLEMENTARY MATERIAL

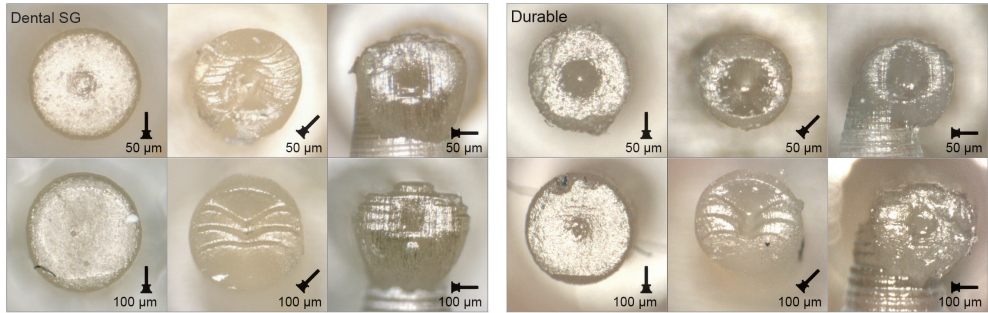


Figure S5.1: Example of the distal ends of the valves printed in Dental SG (left) and Durable (right), in different orientations and with different layer heights. For the cannulas in the 90° orientation, the support pillar is visible at the bottom.

5

Table S5.1: Measurements of the outer channel of the 3D printed cannulas for the different build orientations and layer heights per material (n = 3). The lowest layer height was 50 µm for the materials Dental SG, Grey Pro and Durable, and 25 µm for Model. The highest layer height was 100 µm for each material.

	Dental SG			Model			Grey Pro			Durable		
	0°	45°	90°	0°	45°	90°	0°	45°	90°	0°	45°	90°
Lowest layer height (µm)	997 ±14	965 ±11	1002 ±5	855 ±10	737 ±16	801 ±31	689 ±4	702 ±18	726 ±7	854 ±6	848 ±9	914 ±31
Highest layer height (µm)	1031 ±8	1025 ±2	1032 ±4	728 ±22	694 ±14	715 ±43	737 ±2	713 ±6	757 ±7	959 ±6	936 ±5	985 ±9

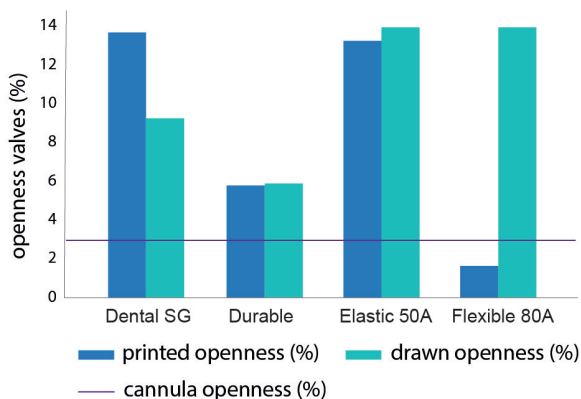
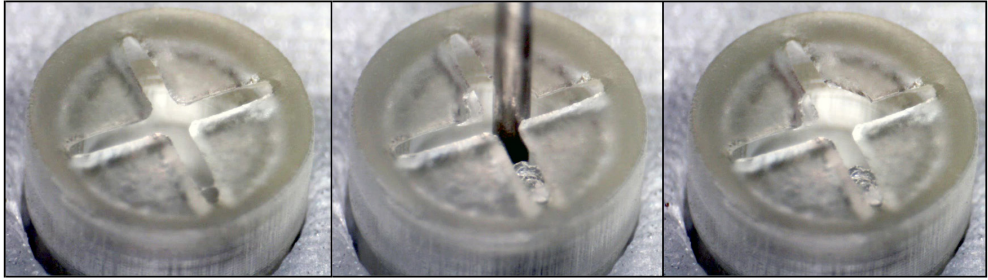
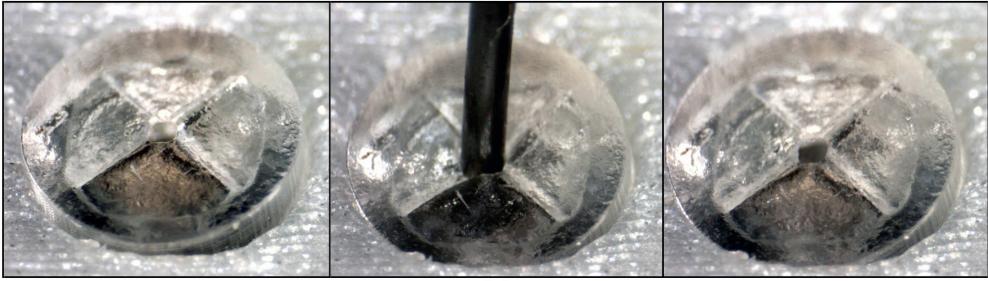


Figure S5.2: The percentage of openness of the valves as-printed compared to the openness of the valves as-drawn. The negative surface area, or “openness” of the top surface of the valve was calculated as a percentage of the top surface. The images taken with the digital microscope were converted into vector drawings, and imported in the CAD software, which was then used to calculate the surface area of the vectors. If the printed thickness of the slits is larger than 10 μm , the valve will not be able to sufficiently prevent leakage. For the ideal slit size of 10 μm , the openness value corresponds to 0.84%. The calculated openness for all materials is given in Figure S4b. When the printed openness is close to the drawn openness, the results show a better accuracy. None of the printed valves had an openness close to the desired openness, which was to be expected based on the measurements of the slits. Durable (5.8%) and Elastic 50A (13.2%) show the best accuracy, since their printed openness is close to the as-drawn openness (5.9% and 13.9%, respectively). The valve printed in Flexible 80A showed the least openness, however this was because only the central opening of the cross slits had been printed open. As a reference, the openness of a 25G cannula is given as a percentage of the total valve surface (purple line).



a)



b)

Figure S5.3: Results of the investigation into different materials and print settings for the valves. a) Example of a valve printed in Dental SG, showing the valve before, during, and after insertion of a needle. It can be seen that the valve flaps broke after insertion of the needle. b) Example of a valve printed in Flexible 80A, showing the valve before, during, and after insertion of a needle. It can be seen that the valve deforms, but does not break.

6 MINIMAL ASSEMBLY 3D PRINTING: STEERABLE GRASPER

In the field of medical instruments, additive manufacturing allows for a drastic reduction in the number of components while improving the functionalities of the final design. In addition, modifications for users' needs or specific procedures become possible by enabling the production of single customized items. In this work, we present the design of a new fully 3D printed handheld steerable instrument for laparoscopic surgery, which was mechanically actuated using cables. The pistol-grip handle is based on ergonomic principles and allows for single-hand control of both grasping and omnidirectional steering, while compliant joints and snap-fit connectors enable fast assembly and minimal part count. Additive manufacturing allows for personalization of the handle to each surgeon's needs by adjusting specific dimensions in the CAD model, which increases the user's comfort during surgery. Testing showed that the forces on the instrument handle required for steering and grasping were below 15 N, while the grasping force efficiency was calculated to be 10-30%. The instrument combines the advantages of additive manufacturing with regard to personalization and simplified assembly, illustrating a new approach to the design of advanced surgical instruments where the customization for a single procedure or user's need is a central aspect.

Published as:

C. Culmone, K. Lussenburg, J. Alkemade, G. Smit, A. Sakes, P. Breedveld, A Fully 3D-Printed Steerable Instrument for Minimally Invasive Surgery, Materials (Basel). 14 (2021) 7910.

6.1 INTRODUCTION

6.1.1 State of the art

The advent of Minimally Invasive Surgery (MIS) can be considered one of the most important innovations in the surgical field. In MIS, two or three small incisions, usually between 5 and 10 mm in diameter, act as an entry port to the human body, hereby avoiding a large incision, which is common in conventional open surgery. In the small incisions, a temporary port called trocar is used to facilitate the insertion of the instruments. This minimally invasive approach reduces the risk of complications such as infections or hemorrhages, decreases the hospitalization time, and minimizes the size of the scar, reducing the pain for the patient [1,2]. However, different from open surgery where the surgeon has direct visualization and access to the operation area, in MIS, the indirect visualization and the limited operational space to maneuver the instruments influence the surgeon's performance.

Instruments conventionally used in MIS are characterized by three main components: a handle to maneuver the device, a long and straight shaft to reach the operation area, and an end-effector to operate, usually containing a grasper or a cutting mechanism. The rigid and slender instruments used in MIS severely reduce the dexterity of the surgeon due to the loss of wrist articulation and the restriction posed by the small incision size. The number of degrees of freedom (DOF) is limited from six in open surgery to four in MIS (Figure 6.1): (1) and (2) pivoting on the incision in two perpendicular planes, (3) axial translation, and (4) axial rotation [3]. Aside from the reduced number of DOF, the surgeon has to cope with the fulcrum effect: the inversion of the handle movements at the end-effector due to the pivot point created by the trocar in the abdominal wall.

6.1.2 Challenges in minimally invasive surgery

Solutions have been proposed to overcome the limitations of MIS by enhancing the dexterity of instruments using wrist-like mechanisms. Robotic devices, such as the da Vinci robotic system (Intuitive Surgical Inc., Sunnyvale, CA, USA), have the ability to diminish the fulcrum effect and enhance the surgeon's dexterity by providing two additional DOF

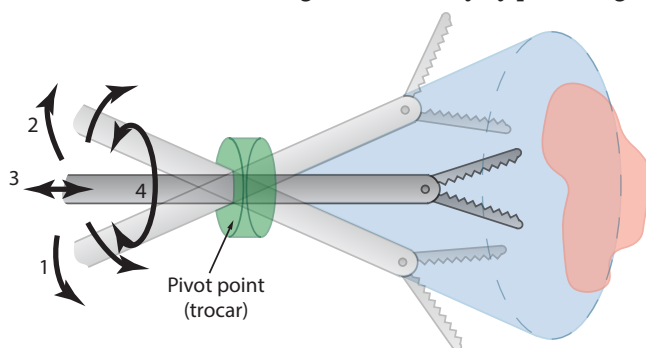


Figure 6.1: Instrument degrees of freedom in Minimally Invasive Surgery: (1) and (2) pivoting around the incision in two perpendicular planes, (3) axial translation and (4) axial rotation.

to the end-effector of the robotic arm using the so-called EndoWrist mechanism. Still, the high initial costs and the limited lifespan of the robotic instruments [4] push researchers to find solutions able to guarantee the advantages of robotic devices while reducing the costs [5]. Great attention has been given to handheld mechanically actuated steerable instruments. Examples are the laparoscopic instruments Maestro [6] and the LaparoFlex (TU Delft and DEAM B.V., Amsterdam, The Netherlands). Both these instruments use rigid joints in their steering mechanism to achieve bending motion in two orthogonal planes, similar to the human wrist. Rigid joints are robust and solid and therefore widely used in conventional instruments. However, when it comes to MIS, the inability to further miniaturize mechanical components due to friction limits their applications [7].

Next to the limited DOF of conventional MIS instruments, the radically different design and operation of instruments for MIS often cause ergonomic inconveniences for surgeons [8-11]. These inconveniences range from muscle fatigue and musculoskeletal pains to neural injury and worsened performance [10,12,13]. Instrument handles are the primary physical interface for the surgeon, and therefore, many studies have been dedicated to this topic [12]. One of the main conclusions of these studies points to the need for the personalization, or at the very least adaptability, of instrument handles [10,13], since it is impossible to create one handle design that suits every possible hand. Due to the high manufacturing costs associated with the conventional manufacturing of personalized products, this has long been out of reach.

6.1.3 Additive manufacturing for surgical devices

Additive manufacturing (AM) or 3D printing provides new opportunities to change the design paradigm of medical devices. AM allows a 3D model to be directly converted from a Computer-Aided Design (CAD) into an object built with a layer-by-layer process. The possibility of producing complex shapes allows the number of components to be drastically reduced, in addition to increasing the functionality of the entire medical instrument. Examples of 3D-printed medical devices are the continuum robots presented by Kim et al. [14] and the 2-DOF steerable grasper DragonFlex created by Jelinek et al. [3]. A comprehensive overview of 3D-printed surgical instruments has been published previously by our group [15]. AM allows for the possibility of using different approaches, such as non-assembly 3D-printed mechanisms [16,17] or 3D-printed compliant solutions [18], which already have been successfully applied in prosthetics [19] and surgical forceps [20]. In addition, AM enables the production of personalized items at no extra cost [21,22]. Ranganathan et al. [23] 3D-printed customized forceps handles based on eight anthropometric hand parameters of Indian males. González et al. [24,25] presented and tested the design of an ergonomic pistol-grip handle that was customized to the surgeon's specific hand size. They concluded that the use of their ergonomic handle reduced muscle fatigue and improved the ease of use of the instrument. Similarly, Sánchez-Margallo et al. [26] compared customized 3D-printed handles with standard handles and reported that the customized handles aided the surgeon's hand-eye coordination and led to shorter execution times.

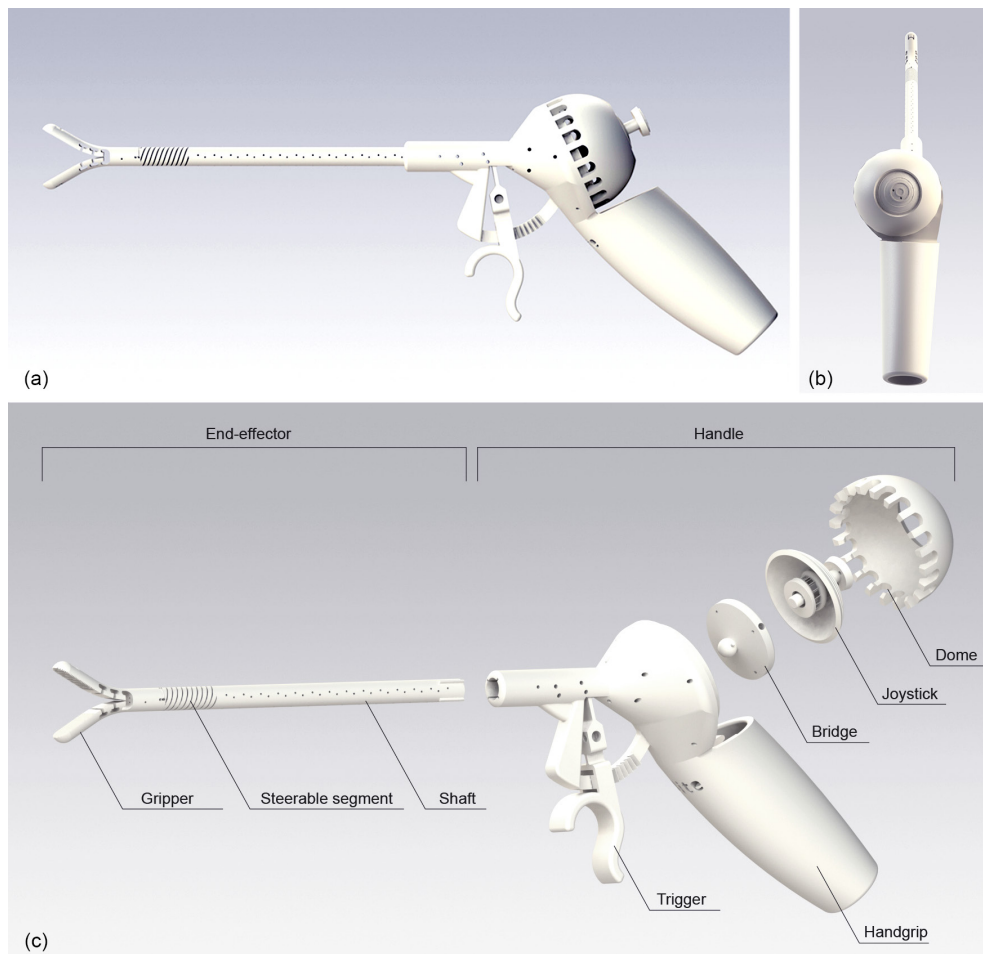


Figure 6.2: Design of 3D-GriP. (a) Side view. (b) Back view. (c) Exploded view with the names of the parts indicated.

6.1.4 Objective and requirements

In this work, we propose a design of a handheld 2-DOF cable-driven steerable instrument for MIS that maximizes the advantages of AM by making use of non-assembly design principles. The new steerable instrument (Figure 6.2), which we called 3D-GriP (company, city, abbr. state if US, country), is mechanically actuated by means of cables and was designed for AM to minimize the number of assembly steps. In order to comply with the constraints of the laparoscopic environment, it has a maximum omnidirectional bending angle of the end-effector between 40 and 60 degrees [5,27], an opening angle of the gripper of 60 degrees [28], and a shaft diameter of 8 mm [28–30]. The surgical instrument allows for single-hand control of both the grasping and steering mechanisms, while the design of

the handle is based on ergonomic guidelines and can be customized to specific hand sizes due to the use of AM. We used Solidworks as CAD software to design the 3D-Grip.

6.2 3D-GRIP DESIGN

6.2.1 Gripper design

For the design of our instrument, compliant joints are used wherever possible in favor of rigid body joints. The advantage of compliant joints is that they do not suffer from the problems with clearances that occur in non-assembly rigid body joints [16,17]. An additional advantage is that compliant joints can be produced as a single, monolithic part without assembly and therefore can reduce the number of components and assembly steps. Moreover, by using flexible components to achieve motion, friction between sliding elements within the joint can be eliminated [31–34].

The compliant gripper was designed in such a way that in the relaxed position, it is in a fully open configuration with a 60-degree opening angle. This way, the forces applied on the actuation cables to close the gripper are directly translated to a (gripping) force on the tissue and thus can be easily controlled by the surgeon. Using a half-open position, as proposed by Lassooij et al. [32], has the advantage of reducing the stress on the compliant beam during operation. However, the half-open position is less convenient, as it requires the surgeon to move the gripper both to grasp and to release the tissue. In the fully open configuration, the jaws will passively return to their initial open configuration after the control input is seized due to the compliant flexures, reducing the number of active movements for the surgeon.

The design of the gripper joint was based on a compliant beam, as shown in Figure 6.3a, and it consists of two gripper jaws with a closed diameter of 8 mm and length of 20 mm. The tooth profile has a height of 0.5 mm and a tooth angle of 60 degrees, similar

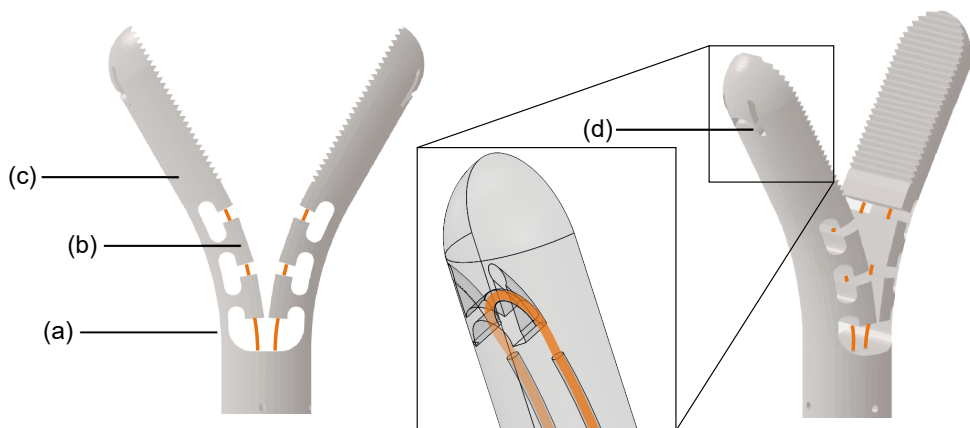


Figure 6.3: Gripper. (a) Compliant beam. (b) T-shape guiding section for the actuation cables. (c) Jaw. (d) Cable fixation point with its close-up made transparent with black outline. Teeth have been removed for clarity.

to those seen in commercial grippers for MIS [35]. The compliant beam has a thickness of 0.8 mm, in order to minimize the bending stress, while the width was kept as large as possible, to provide torsional and lateral stability. The closing of the gripper is actuated by two \varnothing 0.25 mm actuation cables, which loop around the distal end of the gripper (Figure 6.3d) to avoid gluing or soldering on the jaws. T-shaped guiding sections were added to the compliant beams in order to gently guide the actuation cables through the joint without affecting their bendability; see Figure 6.3b.

6.2.2 Steerable segment design

In order to equip the instrument with two additional DOF, a steerable segment was integrated into the shaft of the device. The steerable segment used in this study was designed to achieve high torsional and axial stiffness, to avoid misalignment between the gripper and the shaft, whilst keeping a low bending stiffness to guarantee easy maneuverability. A detailed description of the design of the steerable segment is given by Culmone et al. [36]; however, for the clarity of this work, a summary follows. The steerable segment combines a compliant continuous central backbone for high axial stiffness with four helicoids evenly placed around the centerline for high torsional stiffness, homogeneously distributed (Figure 6.4a). The helicoids have a T-shaped cross-section (Figure 6.4b). The T-shaped cross-section is thinnest close to the backbone and increases in thickness toward the outer side of the segment. This guarantees a low bending stiffness while at the same time limiting the maximum bending angle, which prevents failure due to excessive bending.

Two cables are used for steering, which loop around the top of the steerable segment and back down to the shaft (Figure 6.4c). A cross-shaped groove in the top of the segment was used to fixate the cables in place by means of friction to avoid soldering or gluing (Figure 6.4d). The 20 mm long steerable segment was printed as one part with the rigid shaft, in which dedicated channels guide the steering and gripper cables toward the handle.

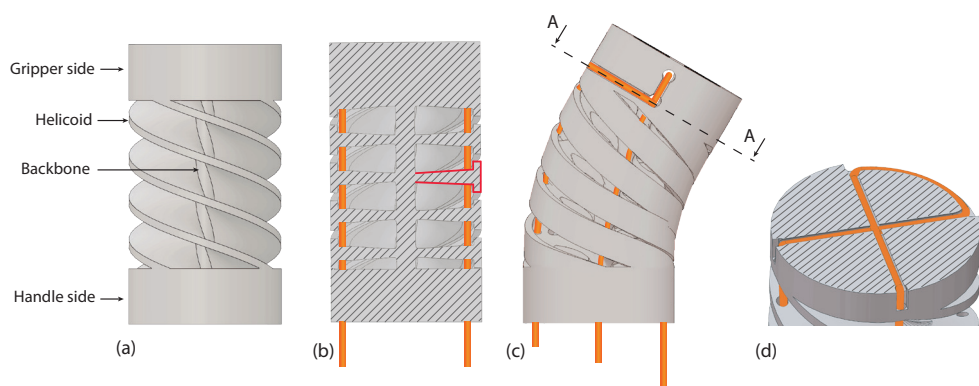


Figure 6.4: Steerable segment design. (a) Central backbone with four helicoids evenly placed around. (b) Cross-section of the segments showing the T-shape of the helicoids, highlighted in red. Cables are shown in orange. (c) Due to the T-shape, the helicoids touch each other at the inner curve of the segment, limiting the bending angle. (d) Cross-section A-A shows the cable fixation point with the looped cables.

6.2.3 Handgrip ergonomics

A pistol-grip is used for the main shape of the handle (Figure 6.2), which is the preferred design for complex or multifunctional instruments [9,10,12,39]. The handle is specifically designed for right-handed use: the asymmetric grip allows for a straight alignment of the thumb and the wrist during steering, which increases the user's comfort (Figure 6.2b) [37,38]. It can easily be converted to left-handed use by mirroring the design [10]. The handgrip has a bulbous shape that follows the shape of the hand [10,24] without any specific finger grooves for positioning the fingers [39], since the latter limits the positions in which it can be held. Changing the dimensions of the handle length, width, and size of the trigger allows for customization to different hand sizes.

6.2.4 Steering control

A joystick is used for the steering system, which is actuated by the thumb. In the field of steerable surgical instruments, thumb actuation allows for more precise control in terms of motion, accuracy, and the perception of steering [40,41,43,44]. The steering mechanism itself consists of the joystick with an integrated spring, which is connected to a ball and socket joint and covered by a dome. The top part of the ball and socket joint, the bridge (Figure 6.5a), is the point of fixation for the cables. Rotating the joystick pulls and releases the actuation cables to steer the end-effector. In order to lock the steerable segment into

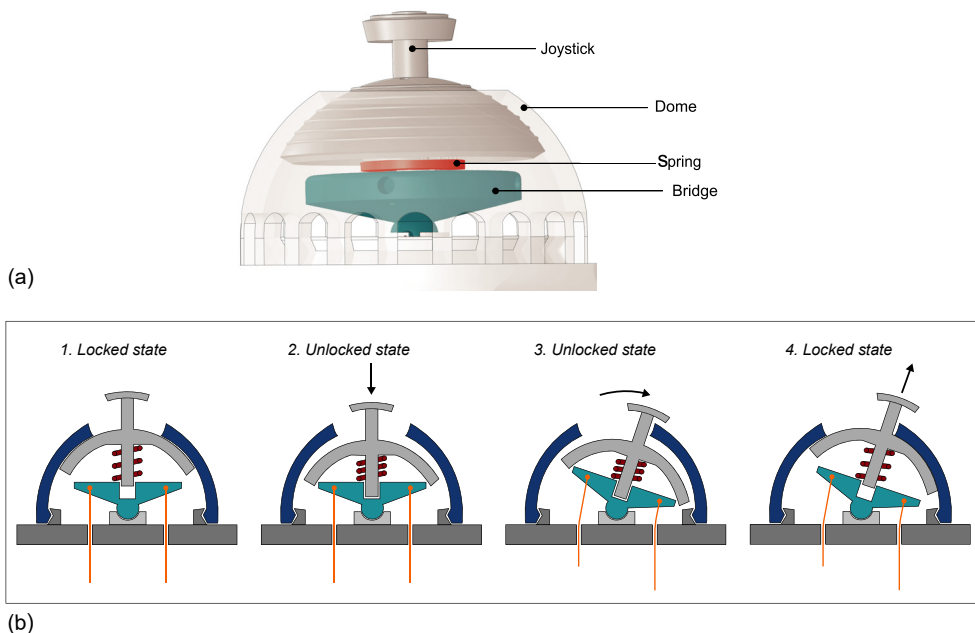


Figure 6.5: Working principle of the steering mechanism. (a) Three-dimensional (3D) render of the assembled joystick, showing the joystick, the dome (transparent to show the underlying components), bridge (blue), and spring (red). (b) Schematic drawing of the working principle of the friction lock showing the bridge (blue), spring (red), and cables (orange). (1)–(4) show the actions taken to move and lock the steerable segment.

any angle, an active friction lock mechanism was implemented. When no normal pressure is applied to the joystick, it is held in place by the friction between the joystick and the dome, which is caused by pre-tension in the spring (Figure 6.5b). This pre-tension is generated during the assembly when the dome is placed over the joystick mechanism and snapped into place. By applying pressure to the joystick, the friction lock is released, allowing for steering of the end-effector. Releasing the joystick will automatically lock the steerable segment into any angle up to 60 degrees.

The rotation of the thumb when steering, and therefore the rotation of the joystick, should be smaller than 45° in order to retain an ergonomic position [40]. Considering the desired steering angle for the end-effector of 60° , the rotation angle of the joystick cannot be transferred in a 1:1 ratio to the end-effector. Therefore, an amplification of the joystick rotation was implemented within the steering control system. To achieve this amplification, the cables' radial distance toward the centerline of the bridge was designed to be three times larger than the cables' radial distance toward the end-effector's centerline. The result of this is that when rotating the joystick 20° in one direction, the end-effector will bend 60° .

6.2.5 Gripper control

The grasping motion of the gripper is driven by a trigger, which is actuated by the index and/or middle finger (Figure 6.6) [41]. The trigger is automatically locked in position by means of a ratchet mechanism. In order to release the ratchet lock, the trigger needs to be moved sideways until the teeth disengage. Two orthogonal bending flexures were designed to allow the trigger to move in these two required directions (Figure 6.6c). As a result of the compliancy of the bending flexures, the trigger moves automatically back to the initial position when released, opening the compliant gripper. This means that only

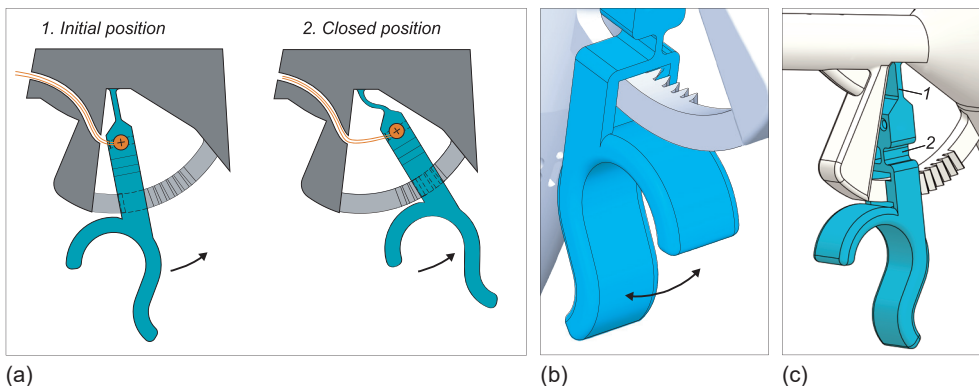


Figure 6.6: Working principle of the trigger mechanism, the trigger and flexures are highlighted in blue, the cables are shown in orange. a) 1. In the initial position of the trigger, the ratchet is not locked, and the gripper is opened. 2. By moving the trigger towards the palm, the gripper closes, and the trigger is locked when the ratchet teeth are engaged. b) Close-up of the internal ratchet-teeth in the locked position. c) Render of the trigger indicating the two orthogonal bending flexures.

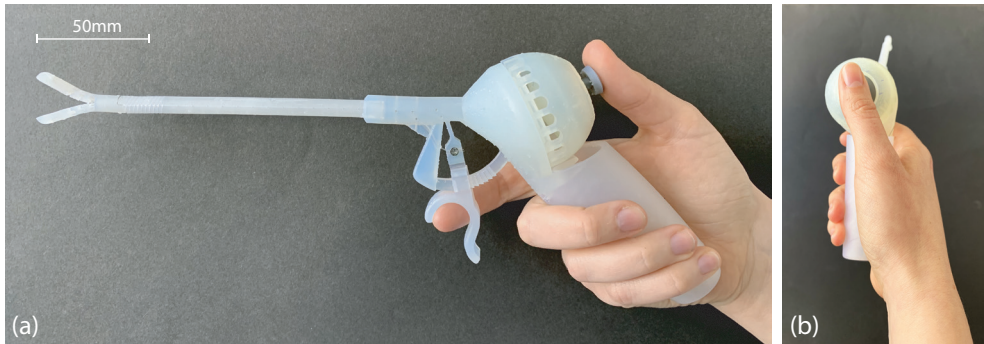


Figure 6.7: The assembled prototype. (a) Front view, (b) side view that shows the alignment of the wrist and the thumb.

active movement for the surgeon is required to close the gripper. The actuation cables were fixated in the rigid part between the bending flexures. Although it is common in laparoscopic instruments to place the trigger mechanism inside the handle, in this case, we opted to place it outside the handle to be able to produce it with as few assembly steps as possible.

6.2.6 Prototype fabrication and assembly

The instrument was manufactured using a commercially available Form 3B (Formlabs, Somerville, MA, USA) 3D printer, which uses stereolithography (SLA) technology. SLA is a process in which a light source, typically a laser, hardens a liquid photopolymer in layers [42]. The handgrip, dome, bridge, and end-effector were printed using the Durable FLD-CL02 resin (Formlabs, Somerville, MA, USA), exploiting the high elongation properties of the material for the compliant joints. The total volume for the parts printed with the Durable resin was 132 mL. The joystick with incorporated spring was printed with the Tough 1500 FLTO1501 resin (Formlabs, Somerville, MA, USA), with a total volume of 8.85 mL, due to its ability to produce parts that spring back under loading cycles. All parts were printed with a 50 μm layer height. The print time for the parts in Durable was 43 h, whereas the joystick was printed in 3 h and 45 min. After printing, isopropanol alcohol was used to remove the uncured resin from the prototype. Only the joystick was cured for 60 min at 70 $^{\circ}\text{C}$ in the curing chamber to enhance the spring back properties of this component.

The final prototype consists of five 3D-printed parts: (1) the end-effector, (2) handgrip with trigger, (3) bridge, (4) joystick with spring, and (5) dome. The end-effector and the handgrip could not be printed as one part because they exceed the printer's build volume. Therefore, they were separated into two pieces and connected by a form-fit closure. The channels for the actuation cables run along the entire length of the shaft and handgrip. In order to be able to remove excess material from inside these channels, we added small drainage holes of 0.1 mm in diameter at regular intervals along the shaft (Figure 6.2). Furthermore, the shaft and the handgrip were printed with the long axis of the cable holes parallel to the vertical z-axis of the printer. This orientation proved best to keep the cable

channels open along their entire length. The joystick and the spring were consolidated so that they could be 3D printed as one part. However, this configuration made it difficult to remove the standard support material generated by the Formlabs software. Therefore, we created custom support pillars between the coils of the spring that could be easily removed after printing.

To assemble the prototype (Figure 6.7), first, the shaft was coupled with the handgrip using the form-fit connection. To actuate the steerable segment, we used stainless steel cables (\varnothing 0.30 mm). The four ends of the cables were fixed using dog point screws into dedicated grooves of the bridge. Before fixation, the cables were straightened by means of weights. The gripper jaws are actuated with nitinol wires (\varnothing 0.25 mm) because, due to their high rigidity, they can be used to close the jaws and help open them. These wires were fixed to the trigger by means of dog point screws. After insertion and fixation of the cables, the joystick and dome were snapped into place

6.3 EXPERIMENTAL METHODS AND RESULTS

To assess the functionalities in steering and grasping, we performed three different measurements. First, we verified the maximum bending angle of the end-effector in four main directions, with different external loads applied to the end-effector. Second, we evaluated the required steering force applied by the user on the joystick when different external loads were applied to the end-effector, simulating steering in a surgical setting. Third, we evaluated the grasping force of the gripper on artificial tissue in relation to the required force applied by the user on the trigger.

6.3.1 Bending angle measurements

We analyzed the maximum bending angle of the end-effector by steering the joystick to its maximum position in the four main directions: upward and downward in the vertical yz-plane and right and left in the horizontal xy-plane. We repeated the measurement three times for each plane. The end-effector was able to reach an angle of approximately $\pm 50^\circ$ in both directions in the xy-plane (Figure 6.8b) and $\pm 45^\circ$ in the yz-plane (Figure 6.8c),

Table 6.1: Vertical bending evaluation with different loads applied. Vertical bending in the yz-plane with no load, 5 g, 10 g, and 20 g.

	No Load (Degrees)		5 g (Degrees)		10 g (Degrees)		20 g (Degrees)	
	upward	downward	upward	downward	upward	downward	upward	downward
rep. 1	47.0	46.0	42.3	51.2	40.4	49.7	37.0	45.5
rep. 2	46.2	48.7	43.7	50.3	35.8	52.2	34.3	50.8
rep. 3	46.5	53.4	43.9	50.6	36.1	49.5	28.7	52.3
aver.	46.6 \pm 0.3	49.4 \pm 3.8	43.3 \pm 0.9	50.7 \pm 0.5	37.4 \pm 2.5	50.4 \pm 1.5	33.3 \pm 4.3	49.5 \pm 3.5

rep. = repetition, aver. = average.

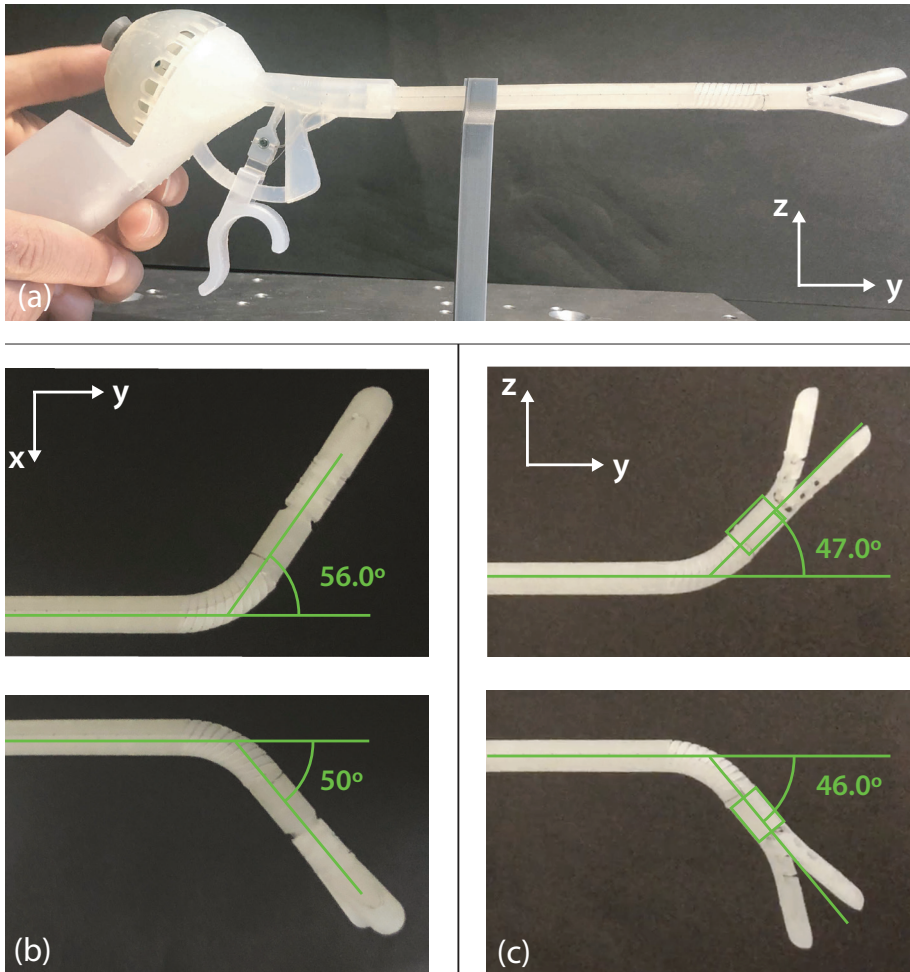


Figure 6.8: Lateral bending evaluation. (a) Set-up. (b) Lateral left/right bending in the horizontal xy -plane without load and (c) in the vertical yz -plane without load.

which is somewhat lower than the desired $\pm 60^\circ$. The video linked by the QR code at the end of this Chapter illustrates the omnidirectionality and the smoothness of the motion.

In addition, we evaluated the effect of different external loads on the bending performance by attaching different weights to the end of the steerable segment. Three load conditions were tested: (1) 5 g, (2) 10 g, and (3) 20 g. The load was suspended from the distal end of the steerable segment in order to only test its effects on the steerable segment and not the compliant gripper. Only the bending angle in the yz -plane was evaluated, since the direction of the load does not influence bending in the xy -plane. To measure the bending angle, we moved the joystick to its maximum up- and downward position and repeated this three times for each load condition. It was found that an increase in load decreased the bending angle in the upwards direction: 7.1% for 5 g, 19.8% for 10 g, and 28.5% for 20

g (Table 6.1). No considerable differences in the average of the maximum bending angle (0–2%) were observed when the steerable segment was steered downwards, regardless of the applied load.

6.3.2 Steering force test

Method

In a surgical procedure, it is often necessary to move or stretch the gripped tissue. Therefore, we evaluated the force necessary to operate the joystick with the thumb in relation to the effect of different loads on the steerable segment. For this test, we applied again a load to the end of the steerable segment and moved the joystick in the four main directions (upward, downward, left, and right), after which we registered the force required for these four movements combined. We tested the following load conditions: (1) no load, (2) 5 g, (3) 10 g, and (4) 20 g. The force required to operate the joystick was measured by placing a piece of pressure foil with a sensitivity of 0.05 MPa (4LW Fujifilm Prescale, ALTHEN BV Sensors & Control, Leidschendam, The Netherlands) between the fingertip and the joystick (Figure 6.9a). The foil changes color when pressure is applied in a specific location. The pressure foil can be used to calculate the applied force by analyzing the density of the colored pixels. Using the pressure chart as provided by the manufacturer of the foil, the pressure value corresponding to the density can be determined. In order to calculate the total force on the joystick, the pressure is multiplied by the surface area of the joystick head.

During the test, the instrument was placed on a support that constrained the base of the handle, kept the shaft in straight position, and left the end-effector free to move. The test was performed by one of the authors and repeated three times per load condition. Although the joystick has a circular flat head with a diameter of 20 mm, we used a square piece of foil for the joystick analysis to avoid false imprints while placing and removing the foil during the test. Only the circular area of the pressure foil corresponding to the joystick head was analyzed. The acquired imprints on the pressure foil were digitalized using a calibrated scanner (Canonscan LiDE 110, Canon Netherlands N.V., 's-Hertogenbosch, The Netherlands) and analyzed using MATLAB R2020a (The MathWorks, Inc., Natick, Massachusetts, USA) in order to find the corresponding density. We translated the images into black and white, with a threshold of 0.8, as used in previous studies [43] where the black pixels represented the colored locations (Figure 6.9b-c). Then, the images were masked with a circle with the same diameter as the joystick head (Figure 6.9d). The digitalized figures were divided into nine portions to analyze the force distribution on the joystick, indicating on which part of the joystick the most pressure was applied by the user; see Figure 6.9e-f. The average black-pixel density over the three repetitions was calculated per portion and normalized for the total number of pixels.

Results

Figure 6.10a shows the pressure concentration per portion for the different load conditions. For all load conditions, the black-pixel density peaks on the edges of the flat head,

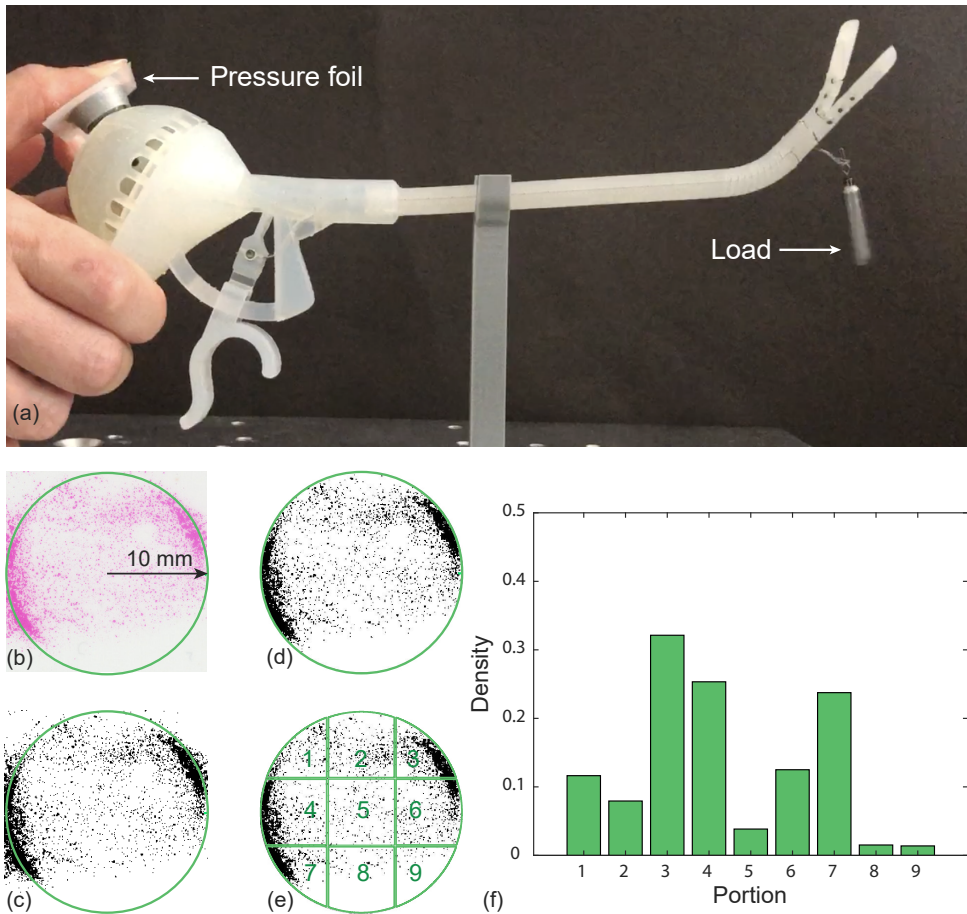


Figure 6.9: Method of force analysis on the joystick during steering. The example shown in this figure is the first repetition at the no load condition. (a) Set-up of the steering force measurements. (b) Scan of the imprinted pressure foil. The green circle represents the joystick area, the pink color shows the pressure distribution. (c) Black-and-white conversion of the scanned foil. (d) Applied mask used to analyze the circular area corresponding to the joystick area. (e) Segmentation of the pressure foil into nine portions. (f) Density of the black pixels per portion for the pressure foil for the no load condition.

especially in the top right and bottom left corner (portions 4 and 7), whereas in the central vertical portions (portions 2, 5 and 8), the applied pressure reaches the lowest value.

Subsequently, we analyzed the density of the colored pixels for the entire measured area for the different load conditions (Figure 6.10b). The plot shows that there are no significant differences in black-pixel density (D) when increasing the load: $D0_{steer} = 0.17 \pm 0.05$, $D5_{steer} = 0.09 \pm 0.04$, $D10_{steer} = 0.12 \pm 0.03$, $D20_{steer} = 0.10 \pm 0.02$. Based on the density of the black pixels and the known surface area of the joystick head, we calculated the applied force using the pressure chart given by the manufacturer. The applied force was between 12.5 and 23.5 N, considering the 10 mm radius of the joystick head. These results indicate

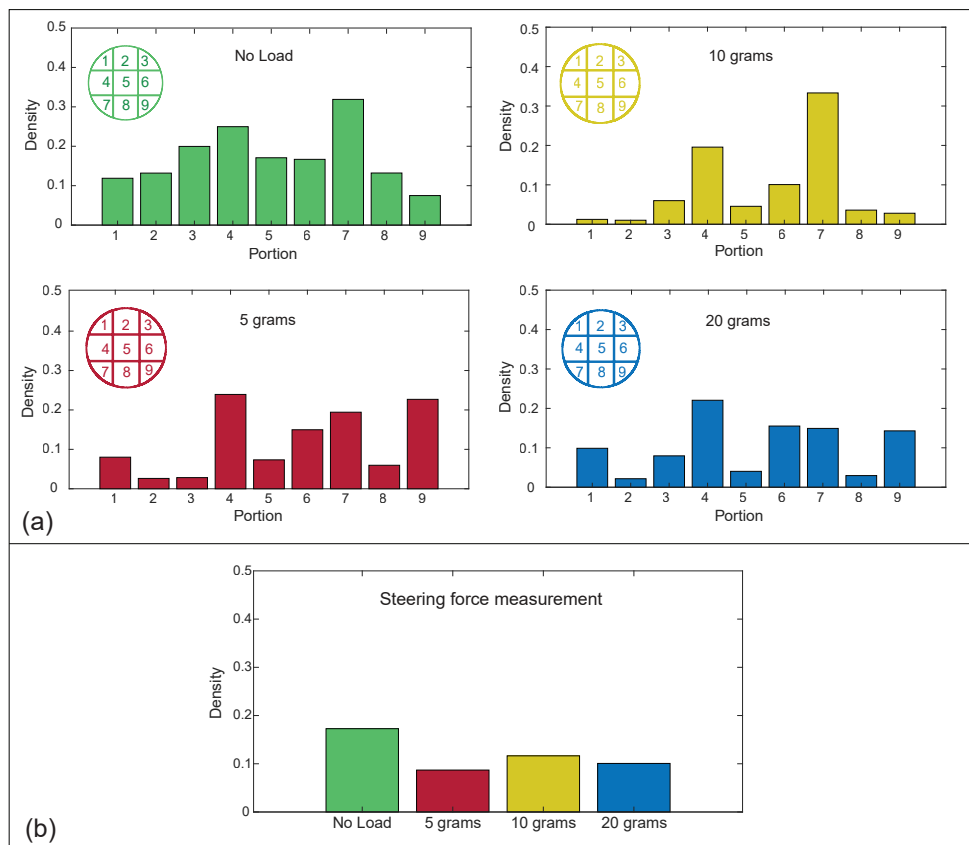


Figure 6.10: Steering force measurement. (a) Average of the black-pixel density per portion for each tested condition: no load (green), 5 g (red), 10 g (yellow), and 20 g (blue) applied load. (b) Average of the black-pixel density for each load condition on the entire area of the pressure foil.

that the user does not need to increase the applied force to steer the joystick when the load increases in the measured range.

6.3.3 Grasping force test

Method

Another important aspect during surgery is the force applied by the user in relation to the force at the gripper used to grasp the tissue; i.e., the efficiency of the instrument. To evaluate the grasping functionality in different scenarios, we tested the prototype on artificial silicon-based tissue (DOTFOX Snc, Siena, Italy) with three different thicknesses: 1–2 mm, 2–3 mm, and 3–4 mm. We used a set-up similar to the one used for the steering force measurement (Figure 6.11). Since the pressure foil is one-sided and the grasping force on both jaws of the gripper is identical when gripping, we decoupled the cables actuating the lower jaw of the gripper from the trigger and fixed the lower jaw onto customized support

to prevent it from moving. Moreover, we placed a rigid tube around the steerable segment to prevent bending and analyze only the grasping functionality. We placed the artificial tissue and a piece of pressure foil with a minimum sensitivity of 0.006 MPa (5LW Fujifilm Prescale) between the jaws. The forces exerted by the user on the trigger were also measured using the same type of pressure foil. To digitalize and analyze the acquired imprints, we used the same methodology as for the imprints of the steering test described in Section 3.2.1.

Results

The imprints for the gripper show that the pressure was concentrated at the proximal side, close to the steerable segment (portions 7, 8, and 9). For the trigger, the pressure was equally distributed among all the portions with a slightly smaller concentration on the top part of the trigger (portions 1 and 3); see Figure 6.12.

Using the average of the black-pixel density and the surface area of the gripper and the trigger, we calculated the applied force using the pressure chart given by the manufacturer. To calculate the total force exerted by the gripper, we only used portions 7, 8, and 9, since the black-pixel density was close to zero for the gripper on the top and central parts. Therefore, the surface area of the other portions was not included in the calculation to obtain a more realistic value. The average black-pixel density (D) for portions 7, 8, and 9 was $D_{1-2_{\text{grripper}}} = 0.04 \pm 0.01$ for 1-2 mm, $D_{2-3_{\text{grripper}}} = 0.06 \pm 0.01$ for 2-3 mm, and $D_{3-4_{\text{grripper}}} = 0.09 \pm 0.01$ for 3-4 mm tissue thickness. The average black-pixel density for the trigger was $D_{1-2_{\text{hand}}} = 0.24 \pm 0.001$ for 1-2 mm, $D_{2-3_{\text{hand}}} = 0.21 \pm 0.03$ mm for 2-3 mm, and $D_{3-4_{\text{hand}}} = 0.27 \pm 0.07$ for 3-4 mm tissue thickness (Figure 6.13). Based on these values, the force generated by the gripper on the tissue samples was between 1 and 4.4 N, and the force applied by the user on the trigger was between 10.8 and 13.2 N. We calculated that the mechanical efficiency, and therefore the efficiency of our instrument, ranges between 10% and 30%.

6.4 DISCUSSION

6.4.1 Production and customization

3D-GriP was designed for use as a disposable instrument; therefore, the production process must be as fast and simple as possible. A non-assembly design can save time and costs for the total production process. In our design, the trigger mechanism is completely non-assembly, due to the use of compliant joints. For the fastest route to the total assembly of the instrument, we decided to produce the joystick mechanism out of three separate parts, which gave us access to remove supports and excess material, and place the cables through the instrument. The separate parts can be positioned easily and snapped into place. The solutions that we used for the fastest and simplest assembly can be summarized as the following design rules: (1) make use of compliant joints to create monolithic parts; (2) consolidate parts where possible; (3) ‘expose’ moving parts to ensure the material can be drained and supports removed; (4) when an assembly is unavoidable, make use of smart

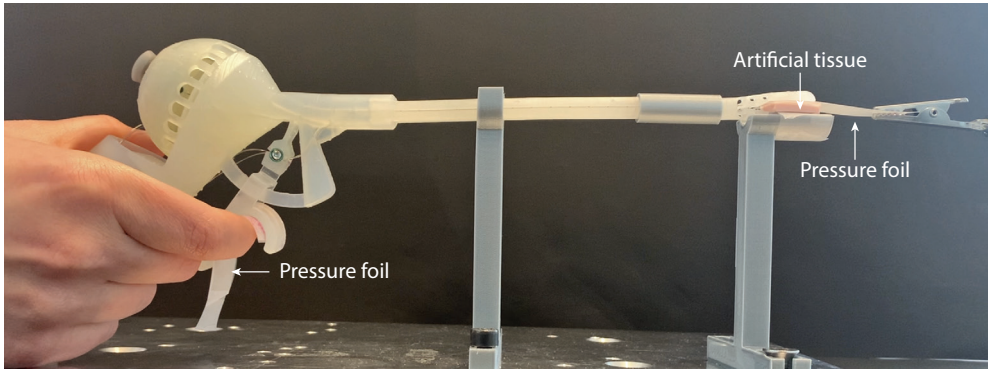


Figure 6.11: Set-up of the grasping force measurement.

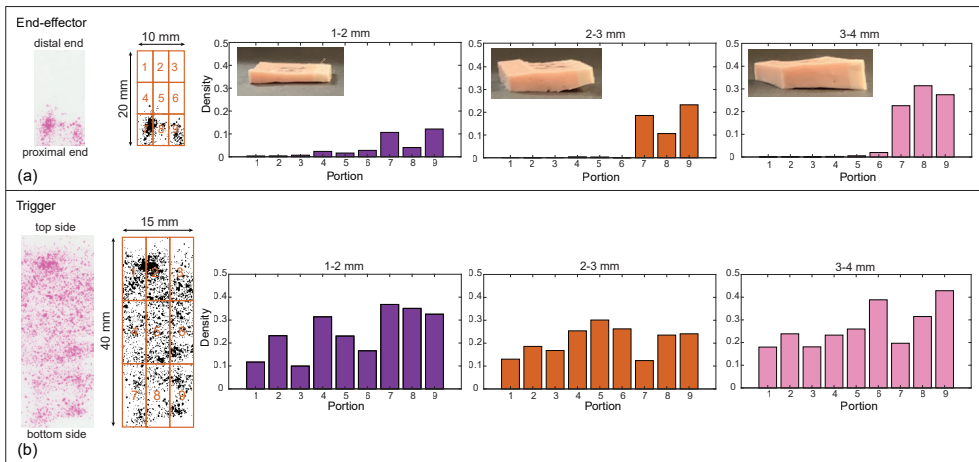


Figure 6.12: Grasping force measurements. From left to right: example of a scan of the imprinted pressure foil for 2-3 mm condition; the segmentation of the corresponding scanned foil converted into a black-and-white image; average of the black-pixel density per portion for each tested condition: 1-2 mm (purple), 2-3 mm (orange), and 3-4 mm (pink) tissue thickness. (a) Gripper results. (b) Trigger results.

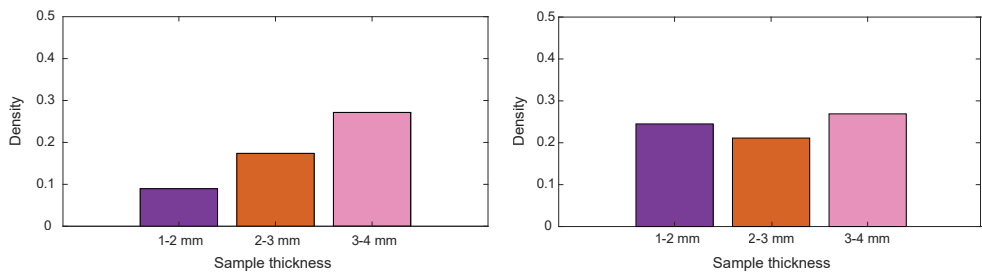


Figure 6.13: Average black-pixel concentration for the grasping force measurements. Left, the average of the black-pixel concentration of the gripper considering portions 7, 8, and 9. Right, the black-pixel concentration of the trigger for each tested tissue thickness: 1-2 mm (purple), 2-3 mm (orange), and 3-4 mm (pink).

solutions such as snap-fit connections for quick and easy assembly.

Being 3D printed, the instrument can be customized to the patient, the procedure, and the needs of the surgeon, for instance, by changing the gripper into a needle holder or fenestrated grasping forceps. Customization of the handle depending on the surgeon's hand size is also possible. Although we took care in our handle to adhere to ergonomic principles, it is impossible to design one handle that fits all. On the other hand, it is not necessary to change the entire design for each surgeon, since the main functionality remains the same. We addressed the customization by enabling certain specific dimensions to be easily adjustable. For instance, the length and width of the handle can be adjusted to the palm size of the surgeon, and the distance of the trigger to the handgrip can be adjusted to the length of the index finger. In addition, by mirroring the trigger design, it can be changed from right- to left-handed. For future implementation, we envision surgeons recording some of their relevant hand measurements in a personal portfolio, which can be easily implemented in the CAD design and 3D printed on demand to create surgeon-specific instruments.

6.4.2 Performance and improvements

The low bending stiffness of the steerable segment reduces the forces required for steering and increases the ease of maneuverability. In the steering force test, we found that the force required for steering the end-effector is between 12.5 and 23.5 N, with the maximum applied force measured in no load condition. This result is counter-intuitive, but since this was the first condition tested, it might be explained by the user's inexperience, which led to an excessive force being applied. In fact, excluding the no-load condition, the applied force ranges between 12.5 and 15.7 N. The maximum measured force applied by the user on the trigger to operate the gripper was 13.2 N. This force is comparable to the measured forces as applied by the surgeon while using conventional instruments in a laparoscopic setting that varies between 9 and 15 N for gentle pinch [42,48,49]. No data are available on the force required to steer the end-effector on commercially available steerable handheld laparoscopic instruments with fully mechanical actuation. In a future study, it would be interesting to perform a test to compare the results of the 3D-Grip to commercially available laparoscopic devices, which are especially related to the steering force.

An important aspect related to the surgeon's comfort during laparoscopic surgery is the handle-to-tip force ratio [44]. In the grasping force test, we measured the grasping efficiency as the control-force-to-gripper-force ratio. We found that the efficiency ranges between 10% and 30%. This efficiency is comparable to common laparoscopic graspers [45]. However, this efficiency should still be improved: a higher force transmission ratio has been associated with lower muscle fatigue in the forearm, which improves the surgeon's comfort [44], higher force feedback [46], as well as prevention of tissue slipping from the gripper, which improves performance [47]. A possible reason for a low force transmission ratio is the friction of the cables in the cable channels. Since the cable channels are difficult to clean after printing, the leftover resin may remain in the channels, which cannot be easily removed or cured. Additional drainage holes and more thorough cleaning could

aid in this respect.

Using the pressure foil, we were also able to evaluate the pressure distribution on the joystick, trigger, and gripper jaws. The imprints of the joystick showed that the pressure concentration was higher on the edges, especially on the top/right and bottom/left. This result seems to indicate that more force is required for steering in the up- and downwards direction compared to the left/right direction, which can be attributed to the applied load. More research is needed to indicate whether a more equal pressure distribution can be obtained with for instance a customized joystick head. For the trigger imprints, the concentration was equally distributed over all the portions. The imprints of the gripper showed a pressure concentration of the forces at the proximal end of the jaws, which caused localized pinch force on the tissue. The limited areas of the imprints in the other portions of the gripper were too small to evaluate using the pressure foil, considering the supplier's guidelines. To quantitatively evaluate this pressure, a possible solution would be using a pressure sensor on the gripper such as the one used by Jin et al. [48]. An interesting option to obtain a uniform distribution of the gripper forces would be an adaptable gripper such as the one proposed by Sun et al. [20].

6.4.3 Limitations and future studies

The verification of 3D-GriP showed that it functions comparably to existing laparoscopic instruments; however, there are some limitations to the design and tests described in this article. Since our instrument was designed for disposable use, we did not carry out a dedicated fatigue test for the compliant joints. However, we observed the compliant joint behavior and durability after repeated use of the prototype in both steering and grasping during the tests. The prototype did not experience any sign of fatigue or breakage; however, more testing is required to determine the joint fatigue and optimal dimensions for the compliant joints.

For the fixation of the cables, we initially used thread inserts and dog point screws. However, after executing the tests, the metal thread inserts in the trigger tore the material apart. In future instruments, we will experiment with alternative methods of fixating the cables, for instance by applying a small amount of the same photopolymer resin used to print the instrument at the fixation point and letting it cure. The advantage of this method is that it is quicker to apply than the thread inserts and screws, and it requires fewer parts and materials. Testing should find out whether this fixation will hold up in repeated use.

The design of the pistol-grip handle is based on well-documented ergonomic principles. However, we did not perform any tests with users to verify its comfort level. We suggest that future tests require multiple participants, preferably surgeons, as they are familiar with laparoscopic instruments, with an equal number of instruments customized to their specific hand sizes in order to verify its potential as an ergonomic instrument.

The 3D printer used for our design was a Form 3B, which is based on SLA technology and optimized for biocompatible materials. However, biocompatible materials that also have the possibility to be sterilized with different technologies, such as autoclave or

gamma radiation, are limited. Moreover, since we found that the available biocompatible materials were too brittle for use in the compliant flexures, we decided to print our prototype using non-biocompatible materials to analyze the functionality of our design. In the future, we hope that new biocompatible and sterilizable materials will become available with characteristics similar to the materials we used in this study for truly biocompatible 3D printed surgical instruments.

6.5 CONCLUSION

In this work, we have proposed a design of a handheld steerable instrument for MIS that can be fully 3D printed. The new steerable instrument, called 3D-GriP, is fully mechanically actuated using cables. It complies with standard specifications for laparoscopic instruments, such as an omnidirectional bending between 40 and 60 degrees, a gripper opening of 60 degrees, and a shaft diameter of 8 mm. We designed a handle for the instrument based on ergonomic principles, which allows for single-hand control of both grasping and steering. Using AM allows personalizing the handle to the surgeon's preference by adjusting specific dimensions in the CAD model. This flexibility allows the production of customized handles to increase the surgeon's comfort. In addition, the use of AM enables a minimal part count by making use of compliant joints and snap-fit connectors. We tested the required forces to steer and operate the instrument by measuring both the input actuation force and the output grasping force. The results show that the operating forces on the handle remain below 15 N for both steering and grasping, resulting in a grasping efficiency of 10-30% for the force transmission. Although the instrument was developed for laparoscopy, our design can be easily adapted to other fields of minimally invasive surgery.

REFERENCES

- [1] V. Velanovich, Laparoscopic vs open surgery, *Surg. Endosc.* 14 (2000) 16-21.
- [2] A. Parisi, D. Reim, F. Borghi, N.T. Nguyen, F. Qi, A. Coratti, F. Cianchi, M. Cesari, F. Bazzocchi, O. Alimoglu, J. Gagnière, G. Pernazza, S. D'Imporzano, Y.-B. Zhou, J.-S. Azagra, O. Facy, S.T. Brower, Z.-W. Jiang, L. Zang, A. Isik, A. Gemini, S. Trastulli, A. Novotny, A. Marano, T. Liu, M. Anecchiarico, B. Badii, G. Arcuri, A. Avanzolini, M. Leblebici, D. Pezet, S.-G. Cao, M. Goergen, S. Zhang, G. Palazzini, V. D'Andrea, J. Desiderio, Minimally invasive surgery for gastric cancer: A comparison between robotic, laparoscopic and open surgery, *World J. Gastroenterol.* 23 (2017) 2376. <https://doi.org/10.3748/wjg.v23.i13.2376>.
- [3] F. Jelinek, R. Pessers, P. Breedveld, DragonFlex Smart Steerable Laparoscopic Instrument, *J. Med. Device.* 8 (2014) 015001. <https://doi.org/10.1115/1.4026153>.
- [4] R. Prewitt, V. Bochkarev, C.L. McBride, S. Kinney, D. Oleynikov, The patterns and costs of the Da Vinci robotic surgery system in a large academic institution, *J. Robot. Surg.* 2 (2008) 17-20.
- [5] P.L. Anderson, R.A. Lathrop, R.J. Webster III, Robot-like dexterity without computers and motors: a review of hand-held laparoscopic instruments with wrist-like tip articulation, *Expert Rev. Med.*

- Devices. 13 (2016) 661–672. <https://doi.org/10.1586/17434440.2016.1146585>.
- [6] P.L. Anderson, R.A. Lathrop, S.D. Herrell, R.J. Webster, Comparing a Mechanical Analogue With the Da Vinci User Interface: Suturing at Challenging Angles, *IEEE Robot. Autom. Lett.* 1 (2016) 1060–1065. <https://doi.org/10.1109/LRA.2016.2528302>.
- [7] J. Arata, Y. Saito, H. Fujimoto, Outer shell type 2 DOF bending manipulator using spring-link mechanism for medical applications, in: 2010 IEEE Int. Conf. Robot. Autom., IEEE, 2010: pp. 1041–1046. <https://doi.org/10.1109/ROBOT.2010.5509705>.
- [8] L. Santos-Carreras, M. Hagen, R. Gassert, H. Bleuler, Survey on surgical instrument handle design: Ergonomics and acceptance, *Surg. Innov.* 19 (2012) 50–59. <https://doi.org/10.1177/1553350611413611>.
- [9] F.M. Sánchez-Margallo, J.A. Sánchez-Margallo, Ergonomics in Laparoscopic Surgery, in: *Laparosc. Surg., InTech*, 2017. <https://doi.org/10.5772/66170>.
- [10] U. Matern, P. Waller, Instruments for minimally invasive surgery, *Surg. Endosc.* 13 (1999) 174–182. <https://doi.org/10.1007/s004649900934>.
- [11] S. Choi, A Review of the Ergonomic Issues in the Laparoscopic Operating Room, *J. Healthc. Eng.* 3 (2012) 587–604. <https://doi.org/10.1260/2040-2295.3.4.587>.
- [12] R. H. M. Goossens, M. A. van Veelen, Assessment of ergonomics in laparoscopic surgery, *Minim. Invasive Ther. Allied Technol.* 10 (2001) 175–179. <https://doi.org/10.1080/136457001753192303>.
- [13] A.G. Gonzalez, D.R. Salgado, L.G. Moruno, Optimisation of a laparoscopic tool handle dimension based on ergonomic analysis, *Int. J. Ind. Ergon.* 48 (2015) 16–24. <https://doi.org/10.1016/j.ergon.2015.03.007>.
- [14] Y. Kim, S.S. Cheng, J.P. Desai, Towards the development of a spring-based continuum robot for neurosurgery, *Med. Imaging 2015 Image-Guided Proc. Robot. Interv. Model.* 9415 (2015) 94151Q. <https://doi.org/10.1117/12.2082193>.
- [15] C. Culmone, G. Smit, P. Breedveld, Additive manufacturing of medical instruments: A state-of-the-art review, *Addit. Manuf.* 27 (2019) 461–473. <https://doi.org/10.1016/j.addma.2019.03.015>.
- [16] J.S. Cuellar, G. Smit, D. Plettenburg, A. Zadpoor, Additive manufacturing of non-assembly mechanisms, *Addit. Manuf.* 21 (2018) 150–158. <https://doi.org/10.1016/j.addma.2018.02.004>.
- [17] K. Lussenburg, A. Sakes, P. Breedveld, Design of non-assembly mechanisms: A state-of-the-art review, *Addit. Manuf.* 39 (2021) 101846. <https://doi.org/10.1016/j.addma.2021.101846>.
- [18] T. Thomas, V. Kalpathy Venkiteswaran, G.K. Ananthasuresh, S. Misra, Surgical Applications of Compliant Mechanisms-A Review, *J. Mech. Robot.* (2020) 1–21.
- [19] J.S. Cuellar, G. Smit, A.A. Zadpoor, P. Breedveld, Ten guidelines for the design of non-assembly mechanisms: The case of 3D-printed prosthetic hands, *Proc. Inst. Mech. Eng. Part H J. Eng. Med.* 232 (2018) 962–971. <https://doi.org/10.1177/0954411918794734>.
- [20] Y. Sun, Y. Liu, L. Xu, Y. Zou, A. Faragasso, T.C. Lueth, Automatic Design of Compliant Surgical Forceps With Adaptive Grasping Functions, *IEEE*, 2020.
- [21] I. Gibson, D.W. Rosen, B. Stucker, *Additive Manufacturing Technologies*, Springer US, Boston, MA, 2010. <https://doi.org/10.1007/978-1-4419-1120-9>.
- [22] L. Toth, A. Schiffer, M. Nyitrai, A. Pentek, R. Told, P. Maroti, Developing an anti-spastic orthosis for daily home-use of stroke patients using smart memory alloys and 3D printing technologies, *Mater. Des.* 195 (2020) 109029. <https://doi.org/https://doi.org/10.1016/j.matdes.2020.109029>.
- [23] S. M.P., R. Ranganathan, A. Pugalendhi, Individual customization strategy accomplished by develop-

- ing prototype of a laparoscopic forceps handle using additive manufacturing, *Rapid Prototyp. J.* 26 (2020) 689–697. <https://doi.org/10.1108/RPJ-06-2019-0157>.
- [24] A. González, D. Salgado, L. García Moruno, A. Sánchez Ríos, An Ergonomic Customized-Tool Handle Design for Precision Tools using Additive Manufacturing: A Case Study, *Appl. Sci.* 8 (2018) 1200. <https://doi.org/10.3390/app8071200>.
- [25] A.G. González, J. Barrios-Muriel, F. Romero-Sánchez, D.R. Salgado, F.J. Alonso, Ergonomic assessment of a new hand tool design for laparoscopic surgery based on surgeons' muscular activity, *Appl. Ergon.* 88 (2020) 103161. <https://doi.org/10.1016/j.apergo.2020.103161>.
- [26] J.A. Sánchez-Margallo, A. González González, L. García Moruno, J.C. Gómez-Blanco, J.B. Pagador, F.M. Sánchez-Margallo, Comparative Study of the Use of Different Sizes of an Ergonomic Instrument Handle for Laparoscopic Surgery, *Appl. Sci.* 10 (2020) 1526. <https://doi.org/10.3390/app10041526>.
- [27] F.M. Sánchez-Margallo, J.A. Sánchez-Margallo, A. Szold, Handheld Devices for Laparoscopic Surgery, *New Horizons Laparosc. Surg.* (2018) 75.
- [28] DEAM, LaparoFlex steerable laparoscopic instrument, (2020).
- [29] R. Zhu, M. Maréchal, I. Yamamoto, M.J. Lawn, T. Nagayasu, K. Matsumoto, Evaluation of laparoscopic forceps jaw contact pressure and distribution using pressure sensitive film, *Comput. Assist. Surg.* 24 (2019) 105–116.
- [30] A. Schneider, H. Feussner, Operative (Surgical) Laparoscopy, in: A. Schneider, H.B.T.-B.E. in G.S. Feussner (Eds.), *Biomed. Eng. Gastrointest. Surg.*, Elsevier, 2017: pp. 269–327. <https://doi.org/10.1016/B978-0-12-803230-5.00007-5>.
- [31] L.L. Howell, Compliant Mechanisms, in: *Encycl. Nanotechnol.*, Springer Netherlands, Dordrecht, 2016: pp. 604–611. https://doi.org/10.1007/978-94-017-9780-1_302.
- [32] J. Lassooij, N. Tolou, G. Tortora, S. Caccavaro, A. Menciasci, J.L. Herder, A statically balanced and bi-stable compliant end effector combined with a laparoscopic 2DoF robotic arm, *Mech. Sci.* 3 (2), 2012. (2012).
- [33] J. Dearden, C. Grames, B.D. Jensen, S.P. Magleby, L.L. Howell, Inverted L-Arm gripper compliant mechanism, *J. Med. Device.* 11 (2017).
- [34] S. Kota, K.-J. Lu, Z. Kreiner, B. Trease, J. Arenas, J. Geiger, Design and application of compliant mechanisms for surgical tools, (2005).
- [35] H. Chen, L. Zhang, D. Zhang, P. Zhang, Z. Han, Bioinspired surface for surgical graspers based on the strong wet friction of tree frog toe pads, *ACS Appl. Mater. Interfaces.* 7 (2015) 13987–13995.
- [36] C. Culmone, P.W.J. Henselmans, R.L.B. van Starckenburg, P. Breedveld, Exploring non-assembly 3D printing for novel compliant surgical devices, *PLoSOne.* 15 (2020) e0232952. <https://doi.org/10.1371/journal.pone.0232952>.
- [37] L.M. Okken, M.K. Chmarra, E. Hiemstra, F.W. Jansen, J. Dankelman, Assessment of joystick and wrist control in hand-held articulated laparoscopic prototypes, *Surg. Endosc.* 26 (2012) 1977–1985. <https://doi.org/10.1007/s00464-011-2138-7>.
- [38] C. Fan, H. Clogenson, P. Breedveld, J.J. van den Dobbelen, J. Dankelman, Comparison of Two Control Methods for Minimally Invasive Surgical Instruments, *J. Med. Device.* 6 (2012). <https://doi.org/10.1115/1.4006544>.
- [39] M.A. van Veelen, D.W. Meijer, I. Uijtewaal, R.H.M. Goossens, C.J. Snijders, G. Kazemier, Improvement of the laparoscopic needle holder based on new ergonomic guidelines, *Surg. Endosc. Other Interv.*

- Tech. 17 (2003) 699-703. <https://doi.org/10.1007/s00464-002-9186-y>.
- [40] A.R. Tilley, Henry Dreyfuss, H.D.A. Alvin R. Tilley, *The Measure of Man and Woman: Human Factors in Design*, Revised Edition, John Wiley & Sons, New York, 1994. <https://www.wiley.com/en-us/The+Measure+of+Man+and+Woman%3A+Human+Factors+in+Design%2C+Revised+Edition-p-9780471099550> (accessed May 18, 2021).
- [41] M.A. van Veelen, D.W. Meijer, R.H.M. Goossens, C.J. Snijders, New Ergonomic Design Criteria for Handles of Laparoscopic Dissection Forceps, *J. Laparoendosc. Adv. Surg. Tech.* 11 (2002) 17-26. <https://doi.org/10.1089/10926420150502896>.
- [42] J. Gardan, Additive manufacturing technologies: state of the art and trends, *Int. J. Prod. Res.* 54 (2016) 3118-3132.
- [43] P. van Assenbergh, C. Culmone, P. Breedveld, D. Dodou, Implementation of anisotropic soft pads in a surgical gripper for secure and gentle grip on vulnerable tissues, *Proc. Inst. Mech. Eng. Part H J. Eng. Med.* 235 (2021) 255-263. <https://doi.org/10.1177/0954411920971400>.
- [44] R. Berguer, S. Gerber, G. Kilpatrick, An ergonomic comparison of in-line vs pistol-grip handle configuration in a laparoscopic grasper, *Surg. Endosc.* 12 (1998) 805-808. <https://doi.org/10.1007/s004649900717>.
- [45] W. Sjoerdsma, J.L. Herder, M.J. Horward, A. Jansen, J.J.G. Bannenberg, C.A. Grimbergen, Force transmission of laparoscopic grasping instruments, *Minim. Invasive Ther. Allied Technol.* 6 (1997) 274-278.
- [46] J.L. Herder, M.J. Horward, W. Sjoerdsma, A laparoscopic grasper with force perception, *Minim. Invasive Ther. Allied Technol.* 6 (1997) 279-286. <https://doi.org/10.3109/13645709709153076>.
- [47] E.P. Westebring-van der Putten, J.J. van den Dobbelen, R.H.M. Goossens, J.J. Jakimowicz, J. Dankelman, Effect of laparoscopic grasper force transmission ratio on grasp control, *Surg. Endosc.* 23 (2009) 818-824. <https://doi.org/10.1007/s00464-008-0107-6>.
- [48] X. Jin, J. Zhao, M. Feng, L. Hao, Q. Li, Snake-like surgical forceps for robot-assisted minimally invasive surgery, *Int. J. Med. Robot. Comput. Assist. Surg.* 14 (2018) e1908.

Video of the omnidirectionality and the motion smoothness of the 3D-GriP (download).





SMALL SCALE 3D PRINTING: STEERABLE LIGHT PIPE

Additive Manufacturing or 3D printing presents unique capabilities in producing intricate shapes and mechanisms, particularly advantageous in the domain of miniature, high-precision instruments, such as those utilized in eye surgery. Despite the benefits of Additive Manufacturing, challenges persist in miniaturized applications, stemming from size constraints and the accuracy limitations of current 3D printers. This paper introduces a novel approach to develop an ultraslender steerable light pipe, named Acci, for eye surgery using conventional 3D print technology. Acci's design addresses challenges in manufacturing miniature negative features using Stereolithography, by employing a helical structure. The optical fiber, essential for illumination, also serves as the actuation cable, eliminating additional parts and assembly steps. The non-assembly 360-degree precision-grip handle, designed for single-step printing, enhances maneuverability. Acci was tested successfully in an artificial eye, demonstrating its illumination capabilities and the potential for further customization. This design illustrates the capacity of non-assembly Additive Manufacturing to create tailored medical instruments for specific applications at the intersection of the capabilities of Additive Manufacturing and medical device design boundaries.

Submitted as:

K. Lussenburg, P. Breedveld, A. Sakes, Development of a Novel 3D-Printed Steerable Light Pipe for Eye Surgery.

7.1 INTRODUCTION

Additive Manufacturing (AM) or 3D printing provides significant flexibility in the creation of intricate shapes and mechanisms. This capability is particularly advantageous in applications involving miniature, high-precision instruments, such as those used in eye surgery. AM offers numerous benefits, including the ability to produce customized products and increased complexity. However, the primary challenges associated with AM in miniature applications lie in the constraints of manufacturing size and the accuracy limitations of current 3D printers [1, 2].

In the realm of eye surgery, where instruments and components are exceptionally small, the majority of currently available AM technologies struggle to produce features at this scale. While progress has been made in nanoscale AM methods like 2-photon lithography, these techniques are limited to sub-millimetre build volumes [3]. For applications in the millimetre-scale range, such as those for eye surgery, only a few print methods are potentially suitable. Among the commercially available AM techniques, vat photopolymerization processes boast some of the highest reported resolutions, currently reaching as small as 25 μm [3-5]. However, when the size of parts or features approach the maximum resolution, limitations in accuracy become apparent. The final accuracy of a part will be influenced by many factors, such as the material, process parameters and even the specific 3D printer [6].

In this paper, we describe a novel way to develop an ultraslender steerable light pipe for use during eye surgery, nicknamed Acci, using conventional 3D print technology. The function of a light pipe is to illuminate the inside of the globe of the eye during surgical procedures. As of now, only rigid light pipes exist for eye surgery. By adding steerability, the light can be directed more precisely to the surgical location without placing high forces on the trocar, as well as prevent shadows caused by the other instruments.

7.2 MATERIALS AND METHODS

Stereolithography (SLA) excels in accurately manufacturing miniature positive features. However, it encounters challenges when attempting to create miniature negative features, even when falling within the reported accuracy range of 3D printers. Printing ultrathin cannulas proves to be particularly challenging, mainly due to the potential fusion of the lumen. Our previous study [7] revealed that this difficulty can be traced back to residual heat emanating from the laser spot, correlating with the total surface area of the negative feature and the number of layers.

Based on this observation, we designed Acci in the form of a helical structure (Figure 1a). By applying this design, each layer has a smaller surface area that needs to be cured, as compared to that of a solid hollow tube with a smaller perimeter. The laser spot also does not encircle the entire negative space, which results in less cumulative heat build-up. The helical thread has a circular cross section of 100 μm . A vertical backbone with the same diameter as the helical thread was added to function as a custom support structure, ensuring printability, add axial stiffness to the shaft, and allow for single-sided 1 Degree of

Freedom (DoF) bending of the shaft using a single cable connected to the tip of the end-effector (Figure 7.1a).

Instead of using a metal actuation cable, as is common in steerable instruments, in this case the optical fibre required for illumination was used for actuation, thereby eliminating the need for additional parts and assembly steps. The bare optical fibre of a commercial light pipe, with a diameter of 1.75 mm, was reused for this purpose (D.O.R.C., Zuidland, The Netherlands). The plastic sleeve of the optical fibre was stripped, leaving the core and cladding, with a total diameter of 120 μm . This was inserted through the end-effector. The distal end of the optical fibre was attached to the tip of the end-effector, using the same resin as used for printing, the proximal end to the handle (Figure 7.1b).

A non-assembly 360-degree precision-grip handle was designed in such a way that

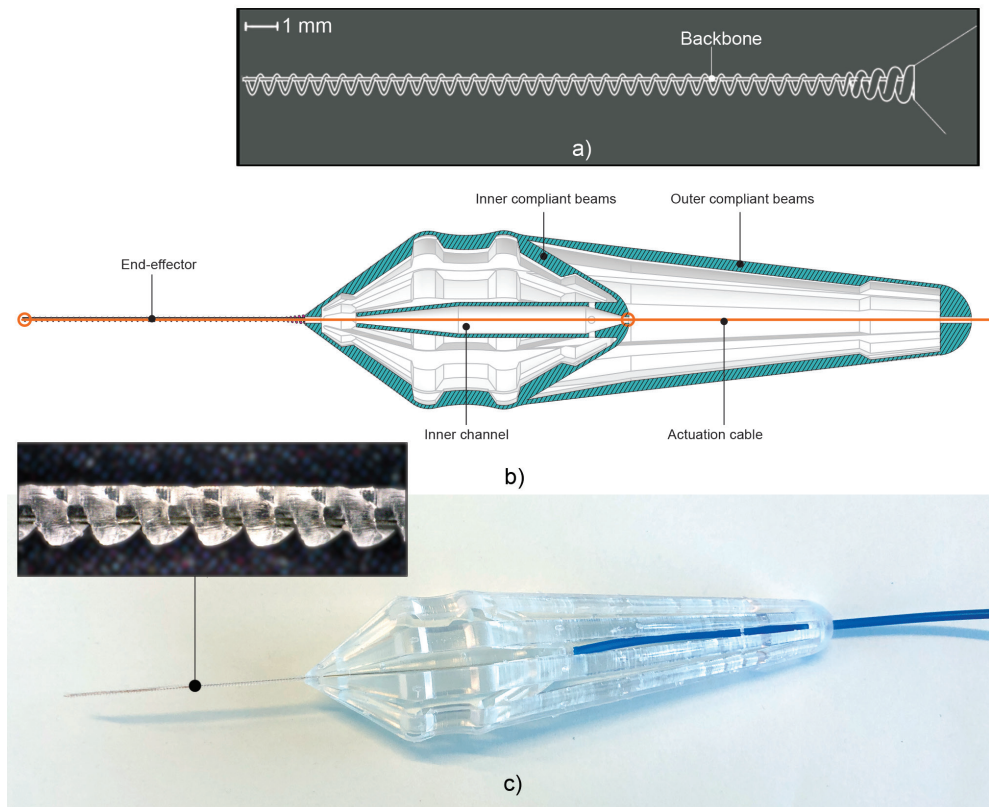


Figure 7.1: Design of the steerable light pipe Acci. a) Schematic design of the shaft, which consists of a helical structure and a straight backbone. b) Cross-section of the entire instrument. The green parts indicate the double compliant beams and the inner channel which serves as a guide for the optical actuation fibre (orange). The orange circles indicate where the optical fibre is attached to the instrument. c) 3D printed prototype of the steerable light pipe, printed in a transparent material. The blue cable is the protective cover of the optical fibre. The close-up (75x magnified) shows the end-effector with the core of the optical fibre in metallic and the printed structure in the transparent material, the backbone is located on the top of the helix.

it could be printed in the same orientation as the end-effector (Figure 7.1b). The precision-grip handle consists of a double layer of compliant beams, oriented in a circular manner. By pinching the handle between two fingers, the diameter decreases, and the handle elongates because of the compliant beams, thereby pulling on the actuation cable and as a result steering the end-effector. The 360-degree precision-grip handle also allows the surgeon to rotate the instrument between their fingers without compromising an ergonomic position and adds another DOF to the end-effector.

7.3 TESTING AND EVALUATION

Acci was printed in a single step on a commercially available Formlabs 3B SLA printer, in the material Clear, with a layer height of 50 micron (Figure 7.1a). After printing, the design was thoroughly cleaned in isopropyl alcohol and a wire was used to carefully push any remaining resin out of the end-effector. The final printed prototype Acci has an outer diameter of 0.75 mm, which allows it to fit through an industry standard trocar size of 20G. It can reach a maximum bending angle of up to 90° (Figure 7.2a) to steer the illuminated tip (Figure 7.2b).

Acci was tested in an artificial eye, by inserting the end-effector through a 20G trocar (Figure 7.2c, a link to a video is available at the end of this Chapter). It was possible to steer the instrument inside the eye, and the movement of the illuminated tip was visible from the outside.

7.4 RESULTS AND DISCUSSION

Acci was able to illuminate the full surface of the inside of the eye by using the steerable tip. From the tests it became clear that the end-effector of Acci is slightly too long. The Acci was designed with a shaft length of 40 mm, similar to other eye surgical instruments. However, it was found that there is no need for the light pipe to actually reach all the way to the back of the eye for clear illumination. Therefore, a short shaft length of 15 - 20 mm is preferred.

The end-effector was illustrated to have a very low stiffness. Usually, low stiffness is considered a negative feature in surgical instruments, however for eye surgery the rule is “when you feel something, you have gone too far”. A low-stiffness instrument can mitigate forces and prevent damage to internal ocular structures, in case the light pipe accidentally touches the side of the eye. However, when part of the end-effector remained outside of the eye, the low stiffness complicated maintaining the correct position with respect to the trocar. This can be mitigated by reducing the shaft length or by designing a variable stiffness end-effector, with a stiffness gradient from the proximal to the distal end. This can be accomplished by varying the pitch or thread thickness of the helix.

The design of Acci shows the potential of using non-assembly AM to create custom medical instruments for specific applications and is an example of how exploring the boundaries of AM can lead towards a new innovative design. The use of the optical fibre

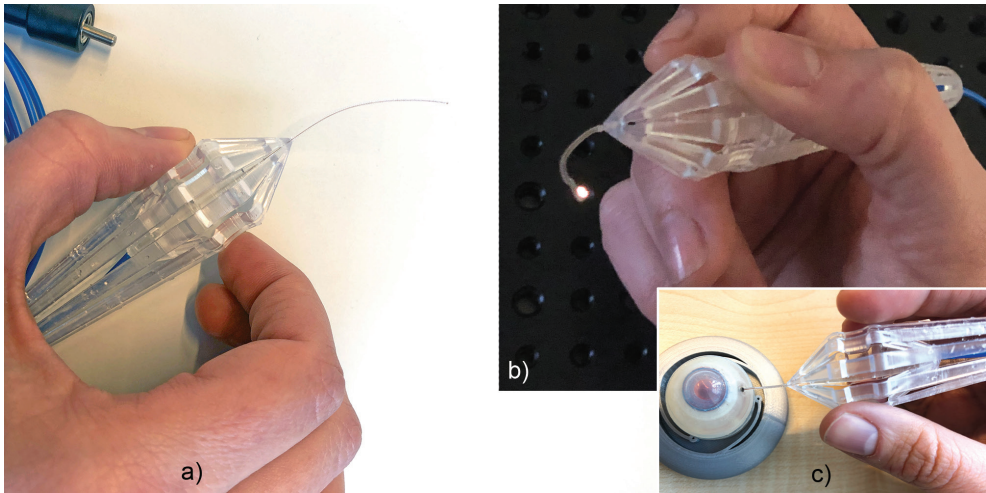


Figure 7.2: The full instrument with embedded light fibre. a) Pinching of the handle results in bending of the end-effector. b) The instrument with illuminated tip.

as actuation cable combines two functions into one and ensures a quick and simple production process. The handle has the potential for further customization, for instance to the surgeon's hand size, and the desired pinching force to operate the handle. Additional functionality can be added to the end-effector by adding a forceps to the distal end, by varying the pitch of the helix to control the bending angle, or by adjusting the helical structure to form two or more channels in order to include an irrigation channel, for example.

REFERENCES

- [1] C. Culmone, G. Smit, P. Breedveld, Additive manufacturing of medical instruments: A state-of-the-art review, *Addit Manuf.* 27 (2019) 461–473. <https://doi.org/10.1016/j.addma.2019.03.015>.
- [2] K. Lussenburg, A. Sakes, P. Breedveld, Design of non-assembly mechanisms: A state-of-the-art review, *Addit Manuf.* 39 (2021) 101846. <https://doi.org/10.1016/j.addma.2021.101846>.
- [3] M. Vaezi, H. Seitz, S. Yang, A review on 3D micro-additive manufacturing technologies, *The International Journal of Advanced Manufacturing Technology.* 67 (2013) 1721–1754. <https://doi.org/10.1007/s00170-012-4605-2>.
- [4] F.P.W. Melchels, J. Feijen, D.W. Grijpma, A review on stereolithography and its applications in biomedical engineering, *Biomaterials.* 31 (2010) 6121–6130. <https://doi.org/10.1016/j.biomaterials.2010.04.050>.
- [5] I. Gibson, D. Rosen, B. Stucker, *Additive Manufacturing Technologies*, Springer New York, New York, NY, 2015. <https://doi.org/10.1007/978-1-4939-2113-3>.
- [6] J.S. Cuellar, G. Smit, A.A. Zadpoor, P. Breedveld, Ten guidelines for the design of non-assembly mechanisms: The case of 3D-printed prosthetic hands, *Proc Inst Mech Eng H.* 232 (2018) 962–971. <https://doi.org/10.1177/0954411918794734>.
- [7] K. Lussenburg, M. Scali, A. Sakes, P. Breedveld, Additive Manufacturing of a Miniature Functional Trocar for Eye Surgery, *Front Med Technol.* 4 (2022). <https://doi.org/10.3389/fmedt.2022.842958>.



Video of the motion and testing of the Acci (download).



MULTI-MATERIAL 3D PRINTING: RECIPROCATING VITRECTOME

A vitrectome is a commonly used instrument in eye surgery, which is used to cut and aspirate the vitreous body out of the eye. The mechanism of the vitrectome consists of miniature components that need to be assembled by hand due to their size. Non-assembly 3D printing, in which fully functional mechanisms can be produced in a single production step, can help create a more streamlined production process. We propose a vitrectome design based on a dual diaphragm mechanism, which can be produced with minimal assembly steps using PolyJet printing. Two different diaphragm designs were tested to fulfil the requirements of the mechanism: a homogenous design based on ‘digital’ materials, and a design using an ortho-planar spring. Both designs were able to fulfil the required displacement for the mechanism of 0.8 mm, as well as cutting forces of at least 8 N. The requirements for the cutting speed of the mechanism of 8000 RPM were not fulfilled by both designs, since the viscoelastic nature of the PolyJet materials resulted in a slow response time. The proposed mechanism shows promise to be used in vitrectomy, however more research into different design directions is required.

Published as:

K. Lussenburg, M. Scali, M. Stolk, D. Robijns, A. Sakes, P. Breedveld, Exploring High-Precision Non-Assembly Mechanisms: Design of a Vitrectome Mechanism for Eye Surgery, Materials (Basel). 16 (2023) 1772.

8.1 INTRODUCTION

The vitreous body is a gel-like substance that fills the inside of the eye, consisting out of water (99%) and a collagen fibre network intermixed with hyaluron (Figure 8.1a) [1]. Its main function is to stabilize the eye and absorb shocks from movement or mechanical impact that can reach the retina or lens [2]. The collagen fibres are connected to internal structures of the eye, such as the retina, creating a more dense network towards the outer edges of the eye [3]. In certain operations in the posterior segment of the eye it is necessary to remove part or all of the vitreous, for instance to gain a clear path of access to the retina, without applying traction to the delicate internal structures. For this, a vitrectome or vitreous cutter is used, which simultaneously cuts the vitreous in smaller pieces and aspirates it through the instrument out of the eye (Figure 8.1b-c). Such an instrument generally consists of a small hollow knife which is placed inside the eye, with a driving and aspiration mechanism inside the handle which remains outside of the eye.

The vitrectome, as well as other instruments commonly used in ophthalmology, consists of very small components with strict requirements regarding their precision and alignment. To produce these type of devices, manual assembly is still the most feasible solution, however this is time-consuming, expensive, and susceptible to human error [4]. Automatic assembly processes are generally too costly to implement in the manufacture of small and intricate surgical instruments, such as a vitrectome, as they ask for highly advanced robotized assembly systems that would require too high investments for medium-scale manufacture [4]. As an alternative, the use of additive manufacturing (AM) or 3D printing offers potential to streamline the production process, since its potential for high geometrical complexity allows for a high integration between parts with different functionalities, thereby reducing the need for assembling multiple parts [5]. AM can contribute to the optimization of the production and assembly chain for medical devices, since fully functional mechanisms can be produced in a single production step, without needing to be assembled [5,6]. These so-called non-assembly mechanisms make production cheaper and easier, reducing the need for specialized knowledge for the assembly and fine-tuning of the mechanism.

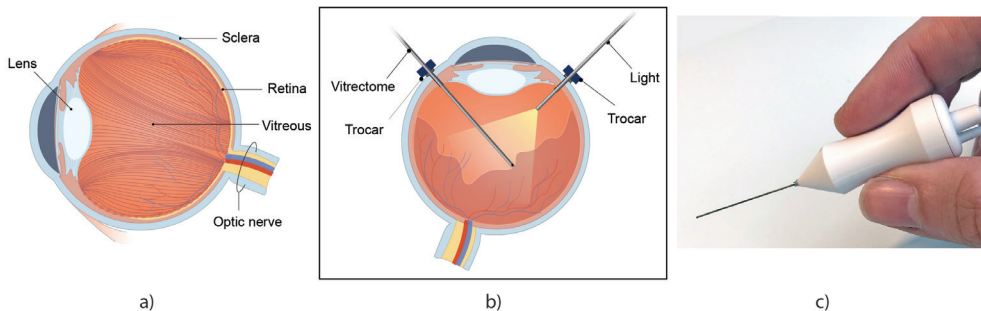


Figure 8.1: Vitrectomy surgery. a) Schematic cross-section of the anatomy of the eye, showing the orientation of the collagen fibre network in the eye, based on [3]. b) Schematic of the set-up during a typical vitrectomy. c) An example of a commercially available vitrectome as produced by D.O.R.C. (Dutch Ophthalmic Research Centre, Zuidland, The Netherlands).

Non-assembly designs have successfully been explored for the design of advanced, steerable end-effectors for minimally invasive instruments [7-10], as well as deployable implants [11,12], using different types of AM technology. So far, there have been only few attempts towards 3D printing instruments for eye surgery. Some examples are miniature 3D printed trocars [13,14], and a surgical puncturing needle, which can puncture a retinal vein with a programmable stroke length [15]. The difficulty in creating non-assembly, 3D printed instruments for eye surgery is that these instruments require specific, precise functionalities, in a relatively small design space. This requires a high level of integration between components, which effectively means a new design has to be created specific for AM, in which both functionality and manufacturability are taken into account [16]. In this study we explore the use of AM for the design and development of a non-assembly vitrectome mechanism used in eye surgery, with the intention of simplifying its fabrication and assembly process to facilitate its use as a low cost disposable product. Special attention is paid to attempting to fulfil the specific requirements of the vitrectome, in order for it to be feasible to use in eye surgery.

8.2 DESIGN AND FABRICATION

8.2.1 Specifications

A vitrectome generally consists of two hollow tubular knives and a driving mechanism. The outer knife is stationary and has a closed, blunt tip, with an aspiration opening (port) on the side. The driving mechanism moves the inner knife within the outer knife, with a guillotine-like linear cutting motion to cut the vitreous. A linear cutting motion of the inner knife is preferred over a rotary motion, to prevent traction of vitreous that is pulled between the shearing blades [17]. Modern vitrectomes have both an aspiration port in the outer knife, as well as in the inner knife, to double the effectiveness of the cut (Figure 8.2). The end of the inner knife is connected to an aspiration system, through which the vitreous is removed from the eye. Sizes of outer knives currently used in eye surgery vary

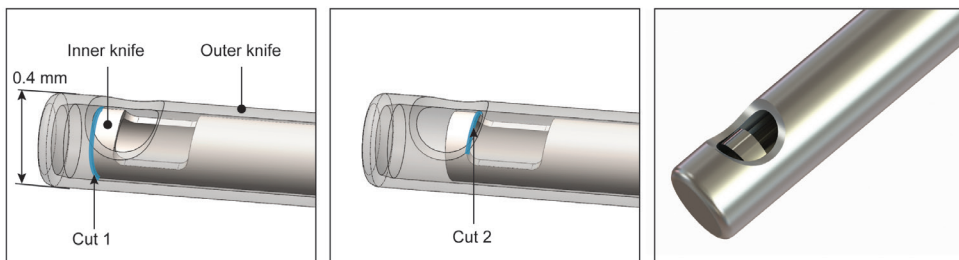


Figure 8.2: Close-up of the cutting principle of a vitrectome. The inner knife moves with a linear cutting motion within the stationary outer knife. Both knives have an opening on the side called an aspiration port, these two ports cause the inner knife to create two cuts instead of one per reciprocating motion (the cutting sides of the inner knife are highlighted with a blue line).

between 23G (0.65 mm) and 27G (0.4 mm) [18].

The mechanism that drives the cutting motion of the knives is located in the handle. Although different driving mechanisms are used in vitrectomes currently on the market, the most common drive systems are powered by an external pneumatic system [19], which is operated during surgery by means of a foot pedal. The system generates short pressure pulses, causing a linear, vibrating motion of the inner knife. Vitrectomes on the market today have a pulse rate of the driving mechanism that varies between 0 and 8000 pulses per minute, which results in 16000 cuts per minute when two aspiration ports are used (as illustrated in Figure 8.2) [18]. A low cut rate is used for operations such as retinal shaving, where precision and control are important, whereas a high cut rate can be used to remove the central part of the vitreous. High cut rates result in less traction on the retina and are also associated with better removal of the vitreous, resulting in a shorter duration of the surgery [20,21].

The stroke length of the driving mechanism is based on the geometries and tolerances of the aspiration ports, with a safety factor to ensure that the vitrectome always fully opens both aspiration ports. The cutting force generated by the driving mechanism should be approximately 8 N in the forward and backward direction. Since the force to cut the actual vitreous is very low, the majority of the cutting force is required to overcome the friction between the knives and within the driving mechanism. The handle of the vitrectome needs to be small enough for operation by a one-handed precision-grip by the surgeon while enabling rotation between the fingers to position the aspiration port of the outer knife in different orientations.

8.2.2 Driving mechanism

Design

In order to design a non-assembly vitrectome suitable for AM, we started from a simplified vitrectome design, which we adjusted for the different functions of the vitrectome and the manufacturing requirements of AM. A simple design for a pneumatically actuated translating system is a piston, shown implemented in a vitrectome in Figure 8.3a. The piston moves forward and backward when air pressure is applied to an airtight chamber on either side of the piston. Since most pneumatic systems used in vitreoretinal surgery only supply a positive pressure pulse, the vitrectome should either contain two air inlets with regulated valves, one on each side of the piston, or the mechanism should be designed in such a way that the return stroke does not require pressure. To keep the design as simple as possible, a spring can be implemented to provide the return stroke (Figure 8.3b).

Although the piston-spring design has the potential to fulfill the functional requirements of a vitrectome, there are some problems using AM to create such a system. First, sliding surfaces are problematic for 3D printed parts, due to the presence of visible layer lines in the part, often called the staircase effect. This can hinder the sliding motion of the piston, or create unacceptably high friction forces. Second, very tiny clearances need to be present between the piston and the walls of the housing as to allow the piston to move while keeping an airtight chamber. Since the goal is to create a non-assembly mechanism,

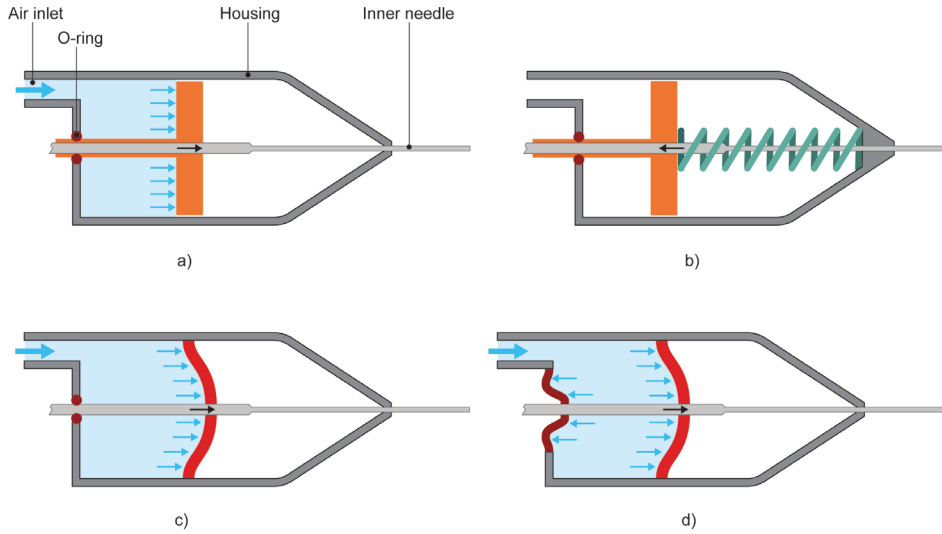


Figure 8.3: Evolution of the design for the non-assembly vitrectome driving mechanism. a) Schematic design of a simple, pneumatically actuated driving system with a piston (orange) delivering a forward motion for the inner needle by means of air pressure. b) Same design in which the backward force is delivered by a spring (green). c) Piston-spring system replaced by a flexible diaphragm, which fulfills both the function of the piston and the spring. d) Dual diaphragm system in which the back of the instrument is also sealed with a diaphragm.

these clearances need to be incorporated within one 3D printed part. Small clearances printed in such a way run the risk of fusing of parts, while large clearances will not create an airtight chamber. To solve this, the piston-spring design was replaced by a flexible diaphragm, which can theoretically fulfill the function of both the piston and the spring, as shown in Figure 8.3c. The advantages of a diaphragm mechanism are that it is easier to print, since the parts are attached to each other, the diaphragm creates an effective seal for the air chamber, and a separate spring is no longer required.

Since the inner knife needs to be connected to an aspiration system at the distal end, the knife needs to extend beyond the driving mechanism. This exit should allow the inner knife to move, while remaining airtight, which can conventionally be solved by using a rubber O-ring. This creates effectively the same manufacturing problems as described above for the piston. As a solution, here a diaphragm was implemented as well to provide both an airtight seal, and allow movement of the inner knife (Figure 8.3d). The resulting design can be described as a dual diaphragm actuator. The additional advantage of this design is that it obtains a linear guidance for the inner knife, without the high required precision that is difficult to achieve using AM.

Working principle

The two diaphragms form an enclosed chamber, to which the pneumatic pressure pulse is applied. The inner knife is attached to the center of the diaphragms. When a pressure

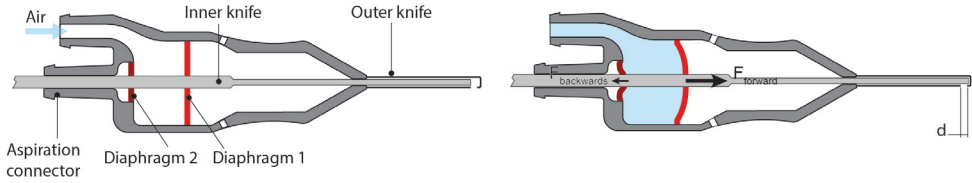


Figure 8.4: Working principle of the dual diaphragm mechanism. Left: schematic dual diaphragm design showing the various components of the design, before air pressure is applied. Right: air pressure is applied to the chamber, causing both diaphragms to exert an opposite force on the inner knife. The larger diameter of Diaphragm 1 results in a net forward force, causing a displacement “d” of the inner knife.

pulse is applied, the diaphragms are forced outwards, thus applying an opposite force on the needle. For two diaphragms of equal size, the force on the inner knife is equal in both directions, resulting in zero motion. In order to create a resulting force to move the inner knife in one direction, the diaphragms should have a different surface area. For the net force to point to the right at a positive pressure in the air chamber in Figure 8.4, Diaphragm 1 should have a larger surface area than Diaphragm 2. The net force developed by the mechanism in the forward direction (F_{net}) is equal to the difference between the force applied to the needle by the large ($F_{forward}$) and small ($F_{backward}$) diaphragms:

$$F_{net} = F_{forward} - F_{backward} \quad (8.1)$$

The large diaphragm (Diaphragm 1) has multiple functions: 1) it converts the applied pressure to a forward motion of the inner knife; 2) it stores the spring energy required for exerting a force and movement in the backward direction; 3) it encloses the air chamber by forming a seal; 4) it holds the inner knife in the central position. The small diaphragm in the back of the instrument (Diaphragm 2) only functions as a seal that allows translation of the inner knife and keeps it centered.

8

8.2.3 3D print technology

Considering the design of the driving mechanism, the used AM technology should be able to produce both rigid and flexible structures in the same production step. Although for some materials flexibility can be created by producing a thin, slender structure, this depends on the minimum feature thickness that can be produced by an AM technology. For the small size of the vitrectome, it does not appear to be feasible to produce a diaphragm with a sufficient slenderness ratio. Another strategy is to combine stiff and flexible materials in one 3D printing step. Material jetting, often referred to as PolyJet printing (Stratasys Ltd, USA), is capable of depositing two or more different materials on a pixel-by-pixel level, referred to as a ‘digital material’ [22], which allows for the creation of monolithic, multimaterial structures in a single processing step. Therefore, this process was chosen to produce the non-assembly vitrectome.

In the PolyJet process, an ink-jet print head moves in the horizontal xy-plane above the build platform. The ink-jet print head accurately deposits photopolymeric resin drop-

lets on the build platform, which are instantly cured by ultraviolet (UV) light. The ink-jet print head has multiple nozzles that deposit different types of material in the same print, including a support material. Although the advantage of the process is that it can combine rigid and flexible materials in a single printing step, the behavior of these materials is difficult to predict, since they are heavily influenced by the settings of the 3D printer [23], such as the orientation on the build plate [24,25], UV exposure during printing [24,26], and the presence of support material [27]. In addition, the materials used in the PolyJet process exhibit viscoelastic behavior [27], and are both frequency- and temperature dependent [28]. Based on these factors, it is difficult to predict the final behavior of a mechanism in advance.

8.2.4 Non-assembly vitrectome design

Knives

Although the PolyJet process is able to produce small features with high resolution, it is not possible to produce the knives with the required tolerances and size, or with sufficient stiffness. Therefore, the decision was made to use off-the-shelf knives (D.O.R.C., Zuidland, The Netherlands), which will be attached in the final mechanism. These particular knives require a stroke length of the driving mechanism of 0.8 mm. The inner knife is connected to the rigid carrier in the center of the diaphragms, while the outer knife is connected to the housing in the front and is stationary.

Main body and housing

Using PolyJet printing, the diaphragms can be produced in a flexible material, while the rest of the handle can be produced in a rigid material. The design of the diaphragms is experimentally explored in Section 3. The handle of the vitrectome should facilitate handling by the surgeon by means of a precision grip, therefore we limited the outer diameter to 16 mm at its widest point, with a slight inward slope that allows for placement of the fingers. For sufficient rigidity, the handle was given a wall thickness of 1 mm. On the back of the handle are two connector ports, one to connect the aspiration channel to the hollow needle, and one to connect the air chamber to the pneumatic system. To ensure that no pressure can build up outside the enclosed air chamber, two venting holes are located behind the large diaphragm, to ensure this part of the vitrectome remains at atmospheric pressure (Figure 8.5a). A rigid center portion, called the carrier in Figure 8.5a, is added to be able to hold the inner knife in the center of the diaphragms. The carrier is attached to both diaphragms, but not to the outer housing.

In the PolyJet process, support material is always required for enclosed chambers [29], which means all internal cavities of the non-assembly vitrectome will be filled with support material. The support material is, however, water soluble and can be removed by soaking the part in water combined with mechanical removal, commonly pressure washing with water is used. To provide sufficient access for the pressure washer, multiple

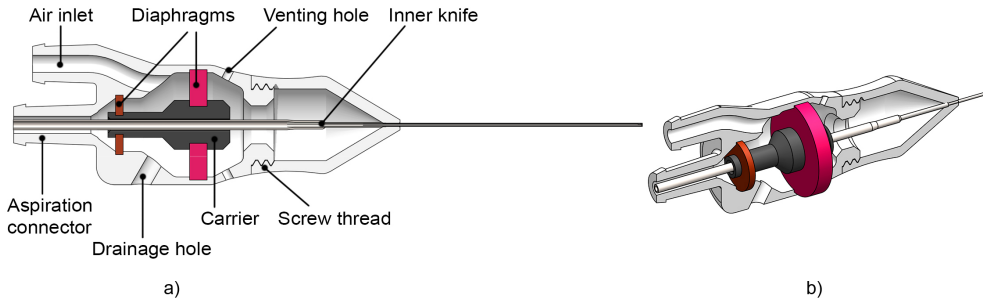


Figure 8.5: Design of the non-assembly vitrectome. a) Cross-section showing the various components of the design. b) Half cross-section showing the full dual diaphragm mechanism. Diameter outer knife 0.4 mm, length outer knife 28 mm, length entire 3D printed vitrectome 80 mm.

drainage holes should be added to create a continuous path for the water [29]. The dual diaphragm design shown in Figure 8.5a-b contains two internal cavities: one between the two diaphragms, and one between the large diaphragm and the tip of the instrument. For the first internal cavity, we opted to create a continuous channel by using the air inlet and adding one additional drainage hole of 2.5 mm diameter, as illustrated in Figure 8.5a. The drainage hole is closed off after removing the support to create an airtight cavity.

For the second internal cavity between the large diaphragm and the tip of the instrument, in theory the venting holes can be used to remove the support material. However, since the knives cannot be printed, the carrier has to be accessible from the outside so that the inner knife can be mounted to it. To facilitate this, we added a screw connection in front of the large diaphragm, which is integrated into the two halves of the housing. Although this adds an assembly step to the design, screw thread is simple and quick to assemble without any tools. In addition, it will save time and effort in removing the support material.

8

Initial prototype

A prototype of the vitrectome was 3D printed to test the clearances and whether support could be removed from all chambers. The prototype (Figure 8.6) was printed on an Objet260 Connex 3 (Stratasys, Ltd., Minnesota, USA), using Vero, a rigid material, Agilus30, a flexible material, and support material 706b. It was possible to remove most of the support material, although a thin layer remains on all surfaces, which is noticeable when scratching it with a finger nail. The outer knife was glued to the tip, and the inner knife to the carrier. The total prototype has a weight of 4.6 g.

8.3 EXPERIMENTAL EVALUATION

8.3.1 Diaphragm requirements

In this section, we explore the mechanical properties of the dual diaphragm mechanism.

The mechanism has a number of specific requirements that need to be fulfilled by the diaphragms, as discussed in Section 6.2.1. The requirements of the large diaphragm are the following: 1) Provide a displacement of 0.8 mm; 2) Provide a forward force of 8 N as a result of the applied air pressure; 3) Provide a backward force of 8 N; 4) Obtain a cutting speed of ideally up to 8000 pulses per minute. Based on these requirements, the large diaphragm should be flexible enough to allow a forward motion with limited pressure, but also stiff enough for a sufficient spring constant for a fast backward motion. For the small diaphragm, the only requirement is that it needs to be as flexible as possible while providing an airtight seal. When air pressure is applied, this diaphragm will generate a force in the opposite direction, therefore this force should be minimized by means of a low stiffness and small surface area.

Because of the near-unlimited possibility of mixing materials in any ratio and any design, and the lack of specific data on the material properties of PolyJet materials, we adopted an exploratory process, in which we tested different versions of the diaphragm to get a sense of the range of mechanical properties that the mechanism can obtain. The variables for these experiments are the design and material of the large diaphragm, while the rest of the mechanism is kept constant.

8.3.2 Prototype design and production

A simplified prototype of the dual-diaphragm mechanism was designed for the tests (Figure 8.7a-c). The outer casing was converted to a rectangular shape, to enable easy fixation of the prototype during the tests. The design of this prototype was kept constant, while we tested different versions of the large diaphragm. The prototypes were printed using an Objet260 Connex 3 multi-material printer, using Agilus30, a flexible material, and Vero, a rigid material. For the support of the inner cavity, the water-soluble support material 706b was used. To remove the support material, the samples were soaked in water for 2 days, after which the rest of the support was manually removed with a micro pressure washer. The drainage hole was sealed using a standard bolt after cleaning. The cutting knives were not included in this prototype.

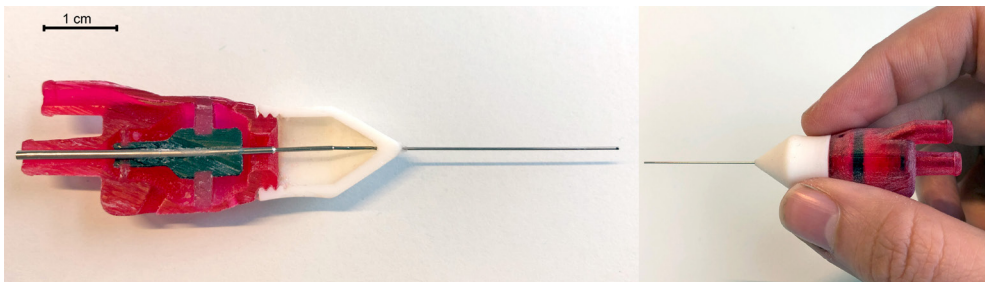


Figure 8.6: Initial prototype of the non-assembly vitrectome. Left: 3D printed model of the vitrectome cut in half, showing the two knives, the carrier in black, and the diaphragms in light red. Right: 3D printed model of the vitrectome. The attachment of the outer diaphragm can be seen as a black line through the red housing. Diameter outer knife 0.4 mm, length outer knife 28 mm, length entire 3D printed vitrectome 80 mm.

8.3.3 Experimental design and procedure

Initial experiments were conducted to test the proof-of-principle of the dual diaphragm mechanism. First of all, the goal was to investigate whether a non-leaking air chamber could be printed, and whether the sufficient displacement in the forward direction could be obtained. In addition, the forward cutting force, the backward cutting force, and cutting speed of the mechanism were determined. During the tests, measurements were performed on the carrier, which is the part of the mechanism that propels the inner knife.

Forward cutting force

The first experiment measured the forward cutting force. This was tested by applying air pressure to the inner chamber, and measuring the force generated by the mechanism without a displacement. A pressurized air supply (PACE 5000, General Electric Company, Boston, United States) connected to a valve was used to apply a constant air pressure to the prototype. The prototypes were horizontally clamped in a custom aluminum platform to which a mini load cell (Futek, Irvine, United States) was mounted in contact with the carrier, connected to an analog signal conditioner (Figure 8.8a). First, a baseline pressure was determined per prototype by testing the response on a range of different pressure levels to obtain a displacement of 0.8 mm. Then, to determine the forward force, fixed levels of pressure were stepwise applied for a duration of 20 seconds, causing the carrier to exert a force on the load cell, after which the pressure was relieved. Whenever possible, three different prototypes were tested at least three times, unless a prototype ruptured during the tests.

Backward cutting force and spring coefficient

The backward cutting force was measured using a tensile tester (Lloyd LS1EH, AMETEK STC, Berwyn, Pennsylvania, U.S.A.) with an attached 50 N load cell (AMETEK STC, Berwyn, Pennsylvania, U.S.A.). The prototype was clamped vertically to the base of the tensile tester and a blunt needle was attached to the load cell, which was used to displace the carri-

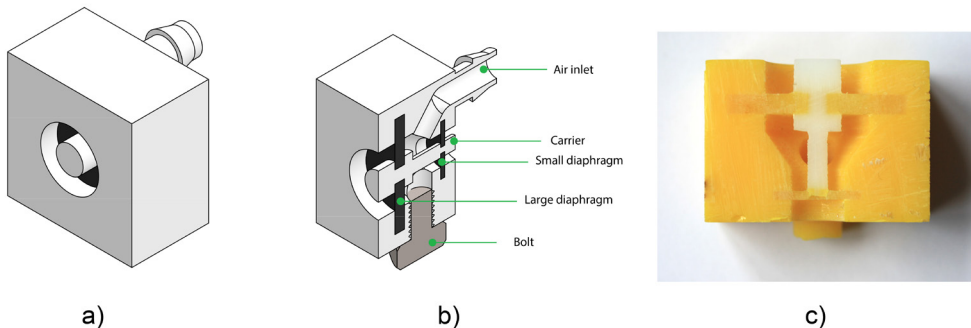


Figure 8.7: Prototypes of the dual diaphragm mechanism used for the experimental evaluation. a) 3D model of the prototype. b) Cross-section of the 3D model showing the various parts. c) Cross-section of the 3D printed prototype.

er of the prototype from the outside (Figure 8.8b). The tensile tester was set to displace the carrier downwards by 0.9 mm with a speed of 0.6 mm/min. After reaching the maximum displacement, the tensile tester moved upwards while the load cell registered the force exerted by the carrier. The tests were repeated three times per prototype from the front and three times from the back. The measured data was plotted in a force-displacement plot (an example is given in Figure 8.8c). The slope of the loading curve of each measurement was used to determine the spring coefficient of the diaphragm.

Cutting speed

A similar setup as in the forward cutting force test was used to measure the cutting speed, except in this case a laser sensor (ILD1420-10, Micro-Epsilon, Ortenburg, Germany) was used to measure the displacement of the carrier. Again the baseline pressure level was determined per prototype and applied in pulses of different pressure levels. The displacement of the carrier and the time required to reach this displacement were recorded from the moment a constant pressure level was applied. When the pressure was lifted, the displacement and time were recorded until the carrier had returned to its base position. This resulted in a response time for the forward motion as a result of the pressure, and a response time for the backward motion as a result of the spring constant of the diaphragm. Whenever possible, three different prototypes were tested at least three times, unless a prototype ruptured during the tests.

8.3.4 Digital material diaphragms

Design

The first design that was explored was a diaphragm made of a homogenous material with a simple disk-geometry, in which the material properties are responsible for the functioning of the mechanism. This design direction was used to determine the base characteristics, such as the displacement, force required for cutting, and speed, of a dual-diaphragm mechanism. Based on design guidelines for the PolyJet process, a “safe” thickness for a self-supporting wall is 1 mm [30]. Since the small diaphragm should have less stiffness, it

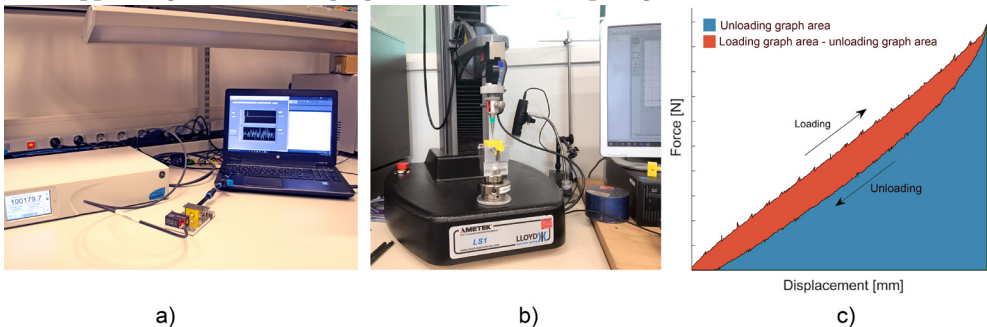


Figure 8.8: Set-ups used in the experimental evaluation. a) Set-up for the forward cutting force test and cutting speed test. b) Set-up for the backward cutting force test. c) Example of a force displacement plot used to calculate the spring coefficients of the prototypes.

was given this thickness of 1 mm. The outer diameter of the small diaphragm was set to 7 mm. The outer diameter of the large diaphragm was set to 14 mm, which is the maximum size based on the diameter of the housing, and given a thickness of 2.3 mm. The carrier has a diameter of 6.5 mm in the large diaphragm, and 3 mm in the small diaphragm. We tested three different digital material mixtures: 1) a flexible version of 20% Vero and 80% Agilus30, 2) a medium version of 50% Vero and 50% Agilus30, and 3) a stiff version of 80% Vero and 20% Agilus30, as indicated in Table 8.1.

Table 8.1: Ratios of the different material mixtures used for the diaphragms in the prototypes.

Name	Composition Vero	Composition Agilus30	Stiffness indication
80Agilus20Vero	20%	80%	flexible
50Agilus50Vero	50%	50%	medium
20Agilus80Vero	80%	20%	stiff

Results

All of the tested digital material prototypes were able to reach a minimum displacement of 0.8 mm. The backward cutting force, spring coefficient, and pressure to reach the displacement per prototype are summarized in Table 8.2. Figure 8.9a shows the average maximum measured forward force generated by the digital material diaphragms on different pressure levels. The graph shows that the forward force output of all the tested prototypes is nearly identical. All prototypes were able to reach a forward force of more than 8 N when an air pressure of 250 kPa was applied.

Table 8.2: Results of the digital material diaphragms, showing the average backward cutting force, the average spring coefficient, and the average pressure required to displace the carrier by 0.8 mm. In addition, the fastest obtained forward and backward response for a displacement of 0.8 mm are given.

Prototype name (stiffness indication)	Backward cutting force (n=18)	Spring coefficient (n=18)	Pressure to reach 0.8 mm displacement (n=2)	Fastest forward response 0.8 mm (n=1)	Fastest backward response 0.8 mm (n=1)
20Agilus80Vero (stiff)	8.9 ± 0.92 N	11.7 ± 1.53 N/mm	257 kPa	0.567 s	30.5 s
50Agilus50Vero (medium)	3.6 ± 0.27 N	5.2 ± 0.28 N/mm	171 kPa	0.156 s	9.7 s
80Agilus20Vero (flexible)	3.3 ± 0.16 N	4.5 ± 0.18 N/mm	156 kPa	0.110 s	9.2 s

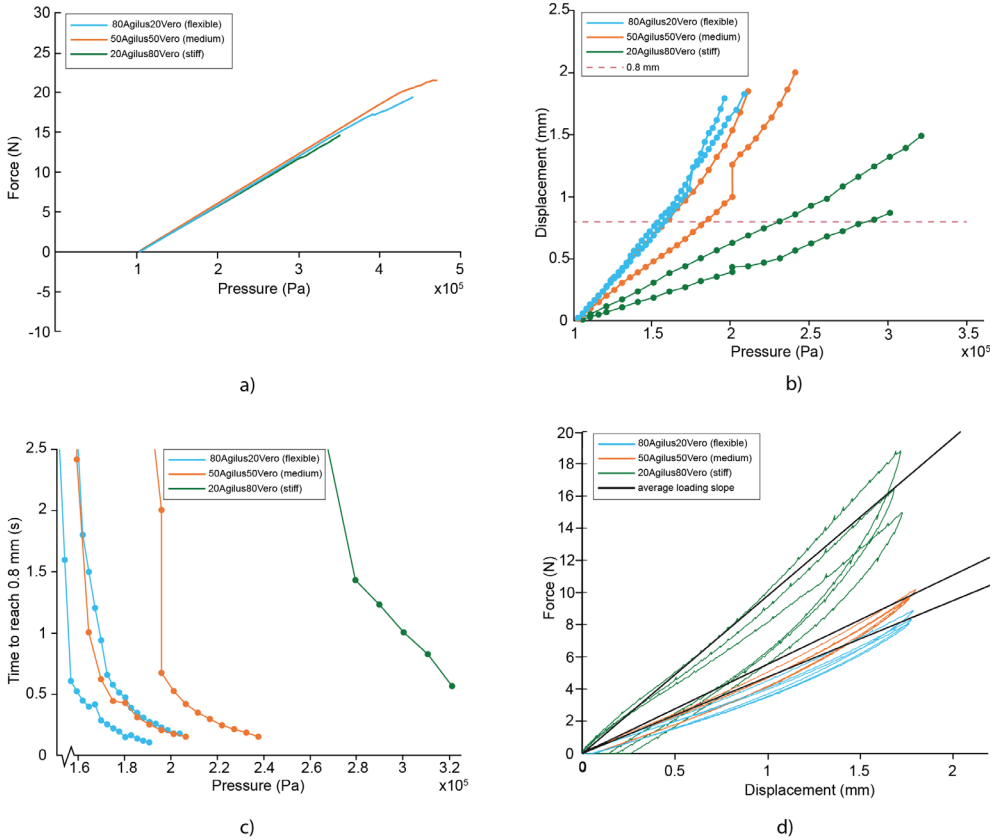


Figure 8.9: Test results of the digital material diaphragms. a) The average forward force as a function of the pressure. b) The displacement of the carrier as a function of the pressure. Only two prototypes for each material could be tested due to failure. c) The time it took the carrier to reach a forward displacement of 0.8 mm as a function of different pressure levels. Only two prototypes for each material could be tested due to failure for the medium and stiff materials, and only one of the stiff prototypes (20Agilus80Vero) is plotted, the other prototype failed during the test. d) The loading and unloading curves of the prototypes, illustrating the hysteresis present in the mechanism.

The relationship between the applied pressure and the forward displacement of the carrier is fairly linear, as shown in Figure 8.9b. The stiff prototypes (20Agilus80Vero) required a higher pressure to move the carrier than the flexible material (80Agilus20Vero), as expected. In Figure 8.9c, it can be seen that a higher pressure also resulted in a faster response for each prototype. However, the stiff prototypes did not have a faster response than the flexible prototypes. The flexible prototypes were more responsive for both the forward and backward movement than the medium or stiff prototypes. The fastest time recorded in the tests was 0.11 seconds in the forward motion for the flexible prototype, before the diaphragm failed.

Figure 8.9d shows the average force-displacement curves for the prototypes. The loading part of the cycle corresponds to the force required to displace the carrier, which is fairly linear in all cases. The unloading part of the cycle is the backward force generated by the diaphragms. The stiff prototypes reached the highest backward cutting force of 8.9 N on average at a deflection of 0.8 mm, while the medium and flexible prototypes showed values of 3 – 4 N on average. The calculated spring coefficients of the diaphragms are given in Table 8.2, and are in a range between 4.5 N/mm for the most flexible prototypes, and 11.7 N/mm for the stiffest prototypes. These spring coefficients show that the stiffness of the mechanism does not increase linearly with the percentage of Vero. The difference between the loading and the unloading curves indicates hysteresis in the system, which is negative for the efficiency of the design. This results in a longer time for the diaphragm to return to its initial position, as well as a lower backward cutting force. The results suggests that Agilus30 is more capable of storing and releasing energy than Vero, as the prototypes with the highest percentage of Agilus30 have the smallest average hysteresis area.

The results obtained in these first experiments show that it is possible to create a dual diaphragm mechanism using PolyJet printing, with the required displacement and forward force. However, the backward force and cutting speed do not yet fulfill the requirements. We speculate that this can be attributed to the viscoelastic nature of the digital materials. Therefore, we designed and tested another version of the large diaphragm in which the functions of the diaphragm are separated from the materials.

8.3.5 Spring reinforced diaphragms

Design

The second design was aimed at improving the speed characteristics of the mechanism. For this design, we separated the function of storing spring energy for the backward motion and the function of airtight enclosing of the air chamber. In this case, a flexible membrane of 100% Agilus30 with a thickness of 0.5 mm is responsible for sealing the air chamber, while an ortho-planar spring printed directly on top in 100% Vero is responsible

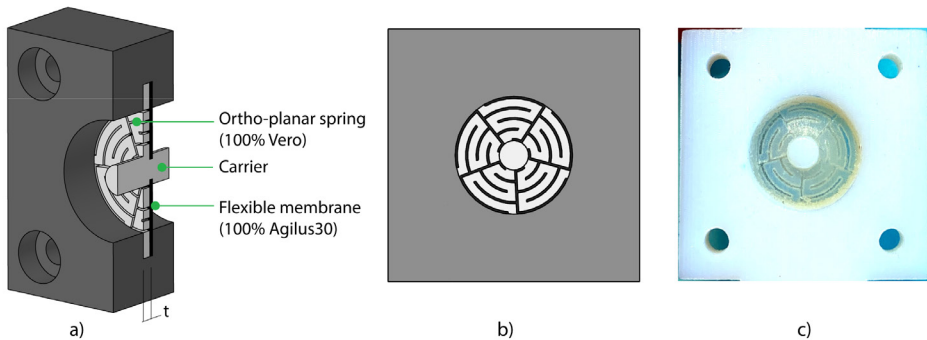


Figure 8.10: Design of the spring-reinforced diaphragms. a) 3D model showing the cross-section of the prototype, with a flexible membrane printed in 100% Agilus30, and on top an ortho-planar spring printed in 100% Vero. b) Top view of the spring design. c) Photograph showing the printed prototype.

for the speed and backward motion (Figure 8.10a). Ortho-planar springs are a type of planar spring, which typically have a central platform connected to a base by means of flexible segments [31], allowing a linear, out-of-plane motion [32]. The design of the spring is shown in Figure 8.10b-c. The spring covers as much of the surface of the diaphragm as possible, in order to prevent the flexible membrane from being pushed through the gaps under air pressure, by using minimum clearances of 0.25 mm, in accordance with PolyJet design guidelines.

The spring stiffness can be varied by changing the thickness of the ortho-planar spring printed on top of the diaphragm. To investigate the influence of the thickness, we used Finite Element Modelling (FEM) (SolidWorks, Dassault Systemes SolidWorks Corp., Waltham MA) to calculate different thicknesses, using the material properties of Vero as supplied by the manufacturer [22]. First, we calculated the thickness required for a completely solid diaphragm made of 100% Vero in order to deliver a backward force of 8 N, this thickness was calculated to be 0.28 mm. Since the spring shape will be weaker than a completely solid diaphragm, we also calculated the required thickness of our spring design to deliver 8 N, which was 1.12 mm. Based on these values, we tested three different thicknesses of the spring, summarized in Table 8.3: one with the same thickness as a completely solid diaphragm (Z0.28), one with the calculated thickness to deliver 8 N (Z1.12), and one with double this thickness (Z2.24).

Table 8.3: Properties of the ortho-planar spring designs used in the second test round.

Name	Thickness spring	Material spring	Thickness membrane	Material membrane
Z0.28	0.28 mm	100% Vero	0.50 mm	100% Agilus30
Z1.12	1.12 mm	100% Vero	0.50 mm	100% Agilus30
Z2.24	2.24 mm	100% Vero	0.50 mm	100% Agilus30

Results

For the spring diaphragms, only the tests for the cutting speed, both forward and backward, and the backward cutting force were repeated. Table 8.4 summarizes the results of these tests.

Table 8.4 and Figure 8.11a illustrate that the thicker springs show a higher backward force at 0.8 mm displacement. However, the results do not correspond with the FEM calculations. The Z1.12 design was expected to show a force of 8 N, but instead shows only 4 N. The Z0.28 prototypes show a large deviation between tests, which could indicate that the prototypes were not printed fully airtight. The Z2.28 prototype is the only design that can fulfil the requirement of 8 N. The results show that a thicker spring leads to a higher spring coefficient, however this does not scale linearly.

For the forward speed, the fastest response times for the entire 0.8 mm displacement are given in Table 8.4. The Z0.28 prototype did not reach an extension of 0.8 mm before breaking. For the Z1.12 and Z2.24 prototypes, only one test could be performed before

the prototypes broke, at pressures of 270 Pa and 600 Pa respectively. For the backward motion, the speed for the entire 0.8 mm could only be measured for the Z1.12 prototypes, since the other prototypes were not able to make the entire displacement due to breakage or plastic deformation. In general, the results from the cutting speed test show extremely large deviations between the results, more than was seen with the digital material diaphragms.

Figure 8.11b gives an example of the time-displacement graph of the Z1.12 design of the entire movement of the diaphragm, in which the forward motion is a result from the applied pressure, and the backward motion is a result of the spring force of the diaphragm. The initial forward displacement as a result of the pressure up to approximately 0.7 mm happens rapidly, after which the speed stagnates for the final 0.1 mm displacement. An explanation for this might be viscoelastic creep within the material [33]. Comparable curves are obtained for all prototypes. Examining these curves shows that within the first 0.4 mm of the forward motion, all prototypes exhibit linear behavior and are able to reach a displacement of 0.4 mm within 0.01 seconds. The fastest response times are given in Table 8.5.

Similarly, the initial backward response of the diaphragm as a result of the spring force of the diaphragm happens rapidly, with a stagnation in response time at around 0.2 mm. Table 8.5 shows the fastest backward response times for the displacement between 0.6 mm and 0.2 mm. Although these responses are significantly faster than for the entire 0.8 mm displacement, the results show that increasing the stiffness of the spring does not increase the backward speed of the mechanism.

8.4 DISCUSSION

8.4.1 Production

The goal of this study was to explore the possibility of creating a non-assembly vitrectome mechanism that is able to fulfil the specific requirements of the vitrectome. We have presented a design that was in theory non-assembly, however in practice required some assembly steps due to the chosen AM technology and the need to include off-the-shelf knives. Without any assembly steps, the post-processing time would increase due to the difficulty of removing the support material, placing the knives, and the need to seal multiple drainage holes after cleaning. The division into two parts using screw thread makes it easier to remove all the support material and to attach the knives, resulting in a shorter total production time. Since the screw thread is integrated into the printed part, the assembly is easy and straightforward, and no specific alignment of parts is required. The screw thread is located in the part of the vitrectome that is at atmospheric pressure, therefore the air tightness of the connection is not of concern. For these type of designs, we suggest that rather than focusing on eliminating assembly altogether, the focus should be on creating ‘smart’ assembly solutions, which can reduce the overall production time and simplify the production process [34]. Future developments in AM technology, for in-

DISCUSSION

Table 8.4: Results of the spring diaphragm tests, showing the backward cutting force, spring coefficient, fastest forward response for 0.8 mm displacement, and fastest backward response for 0.8 mm displacement. If no values are given, the prototypes were unable to fulfill the entire 0.8 mm displacement due to leakages occurring before the test could be completed.

Name	Backward cutting force (n=3)	Spring coefficient (n=3)	Fastest forward response 0.8 mm (n=1)	Fastest backward response 0.8 mm (n=1)
Z0.28	0.48 ±0.48 N	0.6 ±0.60 N/mm	-	-
Z1.12	4.00 ±0.25 N	5.0 ±0.32 N/mm	37.7 s	47.0 s
Z2.24	11.01 ±0.49 N	13.8 ±0.61 N/mm	3.1 s	-

Table 8.5: Fastest response times obtained for half of the 0.8 mm displacement.

Name	Fastest response between 0 and 0.4 mm forward (n=1)	Fastest response between 0.6 and 0.2 mm backward (n=1)
Z0.28	0.0019 s	0.4 s
Z1.12	0.0070 s	5.4 s
Z2.24	0.0056 s	2.5 s

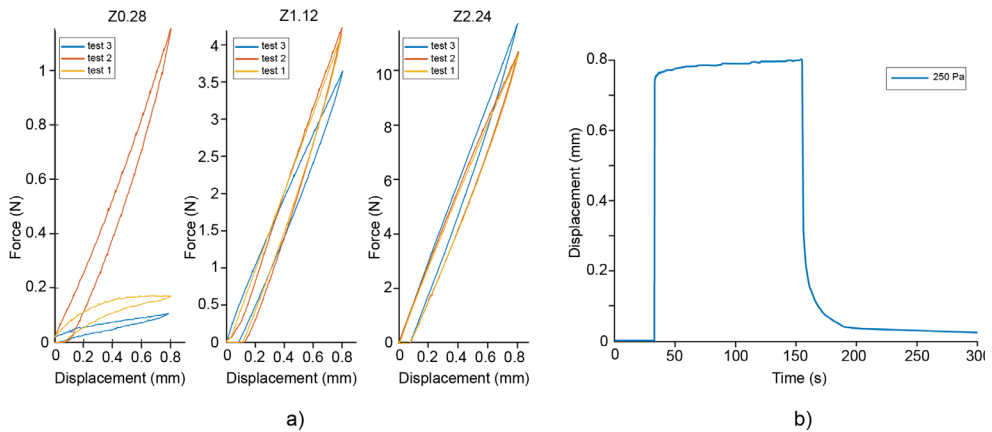


Figure 8.11: Results from the spring-reinforced diaphragm tests. a) The force displacement curves for the three different prototypes: Z0.28 (left), Z1.12 (middle), Z2.24 (right). Note the different scaling of the y-axis. b) Example of a time-displacement curve for the Z1.12 prototype at 250 Pa pressure.

stance in the area of printing truly different materials, such as combinations of polymers and metals, could lead to better applicability of completely non-assembly designs.

The advantage of the PolyJet process is the ability to print with multiple materials in the same printing step, which provides opportunities for miniature, complex mechanisms, where there is less design space to influence the material behavior by geometry.

Unfortunately, there is limited information available on how PolyJet materials behave, especially considering the near-limitless design possibilities of 3D printing, and therefore it is hard to predict how they will respond. In addition, the challenge of creating a high-precision mechanism using AM is that it is difficult to control all variables in order to get a reproducible result, as was evidenced by the breakage of multiple prototypes. This means still a lot of research is needed to be able to produce these kinds of mechanisms consistently and reliably.

8.4.2 Performance

Cutting force

The initial tests with the digital material diaphragms showed that a forward force of at least 8 N can be created by the mechanism. The force was shown to be linearly related to the applied pressure. In theory, a higher cutting force can be obtained by means of a higher pressure, as long as the diaphragms are able to withstand this pressure. To obtain the required backward cutting force, a higher stiffness of the diaphragm is necessary, as was illustrated by both the digital material diaphragms and spring diaphragms. A higher percentage of Vero increases the stiffness of the mechanism for the digital material diaphragms, however, the stiffness of the mechanism does not increase linearly with the percentage of Vero. To obtain the required backward cutting force with the tested dimensions of the diaphragm, a material mixture of minimally 80% Vero is required. For the spring diaphragms, a thicker spring results in a stiffer diaphragm, although again this does not increase linearly. The spring diaphragm with a thickness of 2.24 mm showed a higher backward force than the stiffest digital material diaphragm with similar thickness, indicating that the used material has a significant influence on the backward force.

Cutting speed

The cutting speed of the mechanism still poses a challenge. For the digital material diaphragms, the most flexible prototypes were more responsive for both the forward and backward motion than the medium or stiff prototypes. The time it took for each of the prototypes to reach a forward displacement of 0.8 mm depends on the applied air pressure, however the diaphragms failed before a high enough pressure could be applied to reach the required response time. The stiffer prototypes required a higher pressure to move the carrier forward than the flexible prototypes. However, this did not result in a faster response time than the flexible prototypes, in both forward and backward directions they were slower. Therefore, it can be concluded that the Vero material has a negative influence on the movement speed of the mechanism. Although even the flexible prototypes were almost 15 times too slow as compared to the desired cutting speed, the stiff prototypes were 75 times too slow. The spring diaphragms performed worse in general. The forward speed was slower than for the digital material diaphragms. This was partially caused by the fragility of the spring diaphragms, therefore less pressure could be applied before the prototypes broke. We saw no improvements in backward time, and multiple spring prototypes

were not able to displace the entire 0.8 mm, due to breakage or permanent deformation.

When examining the motion of the spring diaphragms further, it was noticeable that the last 0.2 mm of each movement contributed significantly more to the total cutting speed than the first part of the movement. When omitting the first and last 0.2 mm, a more realistic approximation of the speed of the mechanism is obtained. For the first 0.4 mm forward motion, the required time for this motion was lower than 0.01 seconds. A similar effect was seen for the backward response, although this still remains too slow to obtain the desired cutting speed. The test results show no clear relation between the thickness of the spring and the backward speed, since the fastest response was obtained by the thinnest spring. Regardless, these results indicate that there is potential to improve the cutting speed by allowing the mechanism a longer stroke length. More tests are necessary to investigate this effect and determine an appropriate stroke length. Once the required cutting speed is met, high-speed durability tests have to be carried out to investigate how long our 3D printed mechanism will last as compared to conventional vitrectome designs

Materials and design

The viscoelastic behavior of the printing materials is clearly visible in the response times of the prototypes. Contradictory to our expectations, the stiffer diaphragm designs did not show a faster response, both when a stiffer material mixture was applied and when a thicker diaphragm was applied. It appears that Vero exhibits more hysteresis than Agilus30, which is visible in Figure 8.9d. This leads to two contradictory requirements: a stiffer diaphragm is necessary to obtain the required backward cutting force, however the stiff diaphragms show a poor response time and cannot obtain the desired cutting speed. The influence of the material properties of the PolyJet materials on the requirements cannot be disregarded, and cannot be solved by design alterations alone. This illustrates that for precision mechanisms produced using PolyJet, more research is necessary into the response of these materials [33].

Between the two diaphragm designs, it seems that the digital material diaphragms performed somewhat better than the spring designs. The separation of the different functions of the large diaphragm does not appear to provide a benefit in the performance of the mechanism. FEM calculations were not able to predict the behavior of the springs, therefore we can assume that other forces are at play within the material, or that the influence of the flexible membrane changes the behavior of the system. Another effect that might be at play is the connection between the flexible membrane and the rigid material of the spring, which could result in shear forces. The digital material prototypes were more robust and could withstand multiple rounds of testing, however it should be tested whether they are able to withstand repeated cycles during actual use.

As an alternative to 3D printing in resins, metal 3D printing could also be interesting to investigate. Although manufacturing the flexible diaphragms out of metal could potentially solve our issues with viscoelasticity, 3D printing in metal could also result in new challenges related to printability, surface roughness, brittleness and resolution, leading to relatively high required wall thickness and too high stiffness.

8.4.3 Limitations of the tests

Breakage of the prototypes may have limited the accuracy of the test results. A leak was only noted after the diaphragm completely broke or the diaphragm could not be moved forward sufficiently by pressure. Therefore, it is possible that a small leak in the diaphragm was present during testing, which might have influenced the speed of the forward motion. In addition, it was possible for the ortho-planar springs to break without leakage of the flexible membrane, which could only be noticed by visual inspection after performing the tests, without knowing at which point the breakage occurred.

The test setup only examined one single forward and backward motion. This does not match the behavior of the actual vitrectome during use. During the tests with air pressure, the pressure was applied until a complete extension was reached. In an actual use scenario, the external pressure supply system will give multiple short pressure pulses in short succession. This means that at the same pressure level, the diaphragm might not completely extend. Moreover, it is likely that the 3D printed mechanism will not have returned to its start position before the next pulse is given. More testing is necessary to determine the response of the mechanism in a more realistic use scenario, as well as to examine the influence of the time dependency of the materials in this scenario.

The time dependency and viscoelasticity of the materials could also have influenced the test results. Since for each different prototype a new baseline pressure had to be determined, relaxation effects could have occurred caused by the initial extension of the diaphragm. In addition, the duration of the tests differed per prototype, since the diaphragms were pressed forward until an extension of 0.8 mm was obtained, regardless of the time it took. These effects could also have occurred due to previous tests performed with the same prototype. Although we attempted to use new prototypes for each test, this was not always possible due to breakage of the prototypes. These effects could account for the deviations between the results of some of the tests. The inaccuracies of the tests also partly reflect the main problem of producing this design using PolyJet, showing fast breakage and a lack of consistency between prototypes.

8.4.4 Future design directions

In the experiments, we have seen that the closer the displacement is to the zero-position of the diaphragm, the slower the movement of the diaphragm. We hypothesize that by shifting the displacement away from the zero-position by applying a pre-tension, we can obtain a faster return stroke. This way, the translation of the diaphragm will take place from for instance 0.2 mm to 1.0 mm, instead of from 0.0 mm to 0.8 mm. To accomplish this, a pre-displacement can be applied to the diaphragm in a mechanical or pneumatic way. Mechanically this can be accomplished by integrating a ‘pillar’ in the top half of the vitrectome body, which during assembly of the screw thread will displace the carrier by a predetermined amount. An integrated 3D printed helical spring could serve both as displacement as well as aid in the backward motion, and could therefore be a promising direction to explore further. Although preliminary tests showed that applying a pre-displacement has a positive effect on the backward response time, it may also reduce the lifespan

of the diaphragm. More extensive testing should find an optimum balance between response time and lifespan. In addition, the effect of creep of this solution will need to be examined, as this may reduce the effect of the pre-tension over time.

It is clear that the presence of the Vero material, although it has a higher stiffness, slows the response time. An alternative could be to only use the flexible material Agilus30 for the diaphragm, with a larger thickness to provide the necessary stiffness. However, this type of diaphragm runs the risk of having a short lifespan due to tensile stresses in the material [35]. Alternatively, a corrugated diaphragm design could be tested. Due to the limitations to the size of the vitrectome, it would be necessary to obtain a lower wall thickness to create corrugations within the available space in the vitrectome body. In addition, the proper material mixture for this type of design should be investigated. Both diaphragm designs that were tested in this research have a cross-section with a constant thickness, however a variable thickness for the diaphragm can also be implemented. The largest deflection should be at the center of the diaphragm, and the smallest deflection on the edges, therefore a variable thickness with the highest thickness on the edges could be investigated to adjust the stiffness of the diaphragm.

To circumvent the slow backward response of the diaphragm, an alternative design can be created that functions with dual air pulses: one for the forward motion and one for the backward motion. This would require an additional air chamber, with flexible seal, as well as an additional air inlet. Vitrectomes based on this mechanical principle are already on the market. Although mechanically this would seem the most simple solution, this would complicate fabrication due to the additional air chambers from which support material needs to be removed. However, the performance of such a mechanism relies less on the spring characteristics of a 3D printed diaphragm than the current design, and therefore this could be a promising direction to further explore.

The outcomes of our research show the pros and cons of using 3D printing for fine-mechanical medical devices. We introduced a design methodology that can be used as a guideline for 3D printing of springs for various medical and industrial applications. Furthermore we have explored possibilities for minimal-assembly 3D printing principles to circumvent challenges with tight tolerances and for dealing with support material in small internal cavities. Although there are still challenges to overcome, these are important steps towards real-life implementation of functional 3D printed devices in medicine.

8.5 CONCLUSION

In this study, we explored the possibility of creating a non-assembly vitrectome mechanism for eye surgery. The pneumatically actuated dual diaphragm mechanism that we proposed to generate the linear motion required for this mechanism, was successfully produced using multi-material PolyJet printing. To more efficiently produce the design, we considered the characteristics of the AM process by including features that allow the removal of support material, such as drainage holes and a screw connection. Although this adds an assembly step to the design, it provides access to remove and reduce support

material and therefore decreases the total production time, therefore we preferred these ‘smart assembly’ solutions over non-assembly. The two design directions for the dual diaphragm mechanism that were explored showed that the mechanism shows promise in terms of displacement and cutting force, although the cutting speed requirement could not be fulfilled. The viscoelastic properties of the materials influence the performance of the mechanism, which cannot be overcome by redesigning the diaphragms alone. The requirement of high stiffness for a suitable backward force leads to a contradictory, low speed response in the diaphragms. More research is needed to optimize the design for the required cutting speed.

ACKNOWLEDGEMENTS

We would like to thank Michael Richard from 3DLifePrints for his help in 3D printing the prototypes, and Mart Gähler for his assistance in performing the tests.

REFERENCES

- [1] R.S. Snell, M.A. Lemp, *Clinical Anatomy of the Eye*, Blackwell Science Ltd., Oxford, UK, 1997. <https://doi.org/10.1002/9781118690987>.
- [2] Z. Ahmed, G.A. Luttly, *Anti-Angiogenic Properties of Vitreous*, in: *Ref. Modul. Neurosci. Biobehav. Psychol.*, Elsevier, 2017: pp. 112-119. <https://doi.org/10.1016/B978-0-12-809324-5.01307-9>.
- [3] M.M. Le Goff, P.N. Bishop, *Adult vitreous structure and postnatal changes*, *Eye*. 22 (2008) 1214-1222. <https://doi.org/10.1038/eye.2008.21>.
- [4] H.N. Hansen, M. Arentoft, G. Tosello, *Micro-mechanical Assembly*, in: *Micromanufacturing Eng. Technol.*, Elsevier, 2015: pp. 581-595. <https://doi.org/10.1016/B978-0-323-31149-6.00024-4>.
- [5] I. Gibson, D. Rosen, B. Stucker, *Additive Manufacturing Technologies*, Springer New York, New York, NY, 2015. <https://doi.org/10.1007/978-1-4939-2113-3>.
- [6] C. Culmone, G. Smit, P. Breedveld, *Additive manufacturing of medical instruments: A state-of-the-art review*, *Addit. Manuf.* 27 (2019) 461-473. <https://doi.org/10.1016/j.addma.2019.03.015>.
- [7] C. Culmone, P.W.J. Henselmans, R.I.B. van Starckenburg, P. Breedveld, *Exploring non-assembly 3D printing for novel compliant surgical devices*, *PLoS One*. 15 (2020) e0232952. <https://doi.org/10.1371/journal.pone.0232952>.
- [8] N.P. Castledine, J.H. Boyle, J. Kim, *Design of a Modular Continuum Robot Segment for use in a General Purpose Manipulator*, in: *2019 Int. Conf. Robot. Autom., IEEE*, 2019: pp. 4430-4435. <https://doi.org/10.1109/ICRA.2019.8794249>.
- [9] Y. Hu, L. Zhang, W. Li, G.-Z. Yang, *Design and Fabrication of a 3-D Printed Metallic Flexible Joint for Snake-Like Surgical Robot*, *IEEE Robot. Autom. Lett.* 4 (2019) 1557-1563. <https://doi.org/10.1109/LRA.2019.2896475>.
- [10] D.B. Roppeneker, A. Pfaff, J.A. Coy, T.C. Lueth, *Multi arm snake-like robot kinematics*, in: *2013 IEEE/RSJ Int. Conf. Intell. Robot. Syst., IEEE*, 2013: pp. 5040-5045. <https://doi.org/10.1109/IROS.2013.6697085>.
- [11] S. Leeflang, S. Janbaz, A.A. Zadpoor, *Metallic clay*, *Addit. Manuf.* 28 (2019) 528-534. <https://doi.org/10.1016/j.addma.2019.05.015>.

REFERENCES

- org/10.1016/j.addma.2019.05.032.
- [12] M.A. Leeflang, F.S.L. Bobbert, A.A. Zadpoor, Additive manufacturing of non-assembly deployable mechanisms for the treatment of large bony defects, *Addit. Manuf.* 46 (2021) 102194. <https://doi.org/10.1016/J.ADDMA.2021.102194>.
- [13] K. Lussenburg, M. Scali, A. Sakes, P. Breedveld, Additive Manufacturing of a Miniature Functional Trocar for Eye Surgery, 4 (2022). <https://doi.org/10.3389/fmedt.2022.842958>.
- [14] E. V. Navajas, M. ten Hove, Three-Dimensional Printing of a Transconjunctival Vitrectomy Trocar-Cannula System, *Ophthalmologica*. 237 (2017) 119-122. <https://doi.org/10.1159/000457807>.
- [15] M. Zanaty, T. Fussinger, A. Rogg, A. Lovera, D. Lambelet, I. Vardi, T.J. Wolfensberger, C. Baur, S. Henein, Programmable Multistable Mechanisms for Safe Surgical Puncturing, *J. Med. Device*. 13 (2019) 021002. <https://doi.org/10.1115/1.4043016>.
- [16] L. Alting, F. Kimura, H.N. Hansen, G. Bissacco, *Micro Engineering*, *CIRP Ann.* 52 (2003) 635-657. [https://doi.org/10.1016/S0007-8506\(07\)60208-X](https://doi.org/10.1016/S0007-8506(07)60208-X).
- [17] M. Comaratta, S.M. Hariprasad, R. Reddy, The Evolution of Vitreoretinal Surgery Platforms, *Ophthalmic Surgery, Lasers Imaging Retin.* 48 (2017) 532-538. <https://doi.org/10.3928/23258160-20170630-03>.
- [18] P.R.C. de Oliveira, A.R. Berger, D.R. Chow, Vitreoretinal instruments: Vitrectomy cutters, endoillumination and wide-angle viewing systems, *Int. J. Retin. Vitr.* 2 (2016) 1-15. <https://doi.org/10.1186/s40942-016-0052-9>.
- [19] A.C. Barnes, C.M. DeBoer, P.R. Bhadri, O. Magalhaes, R.M. Kerns, M.T. McCormick, L.P. Chong, M.S. Humayun, 25-Gauge Instrumentation: Engineering Challenges and Tradeoffs, in: 2009: pp. 9-29. https://doi.org/10.1007/978-3-540-68586-9_2.
- [20] A. Teixeira, L.P. Chong, N. Matsuoka, L. Arana, R. Kerns, P. Bhadri, M. Humayun, Vitreoretinal Trac-tion Created by Conventional Cutters during Vitrectomy, *Ophthalmology*. 117 (2010) 1387-1392.e2. <https://doi.org/10.1016/j.ophtha.2009.11.004>.
- [21] S. Rizzo, F. Genovesi-Ebert, C. Belting, COMPARATIVE STUDY BETWEEN A STANDARD 25-GAUGE VITRECTOMY SYSTEM AND A NEW ULTRAHIGH-SPEED 25-GAUGE SYSTEM WITH DUTY CYCLE CONTROL IN THE TREATMENT OF VARIOUS VITREORETINAL DISEASES, *Retina*. 31 (2011) 2007-2013. <https://doi.org/10.1097/IAE.0b013e318213623a>.
- [22] Stratasys, PolyJet Parts On Demand, (2022). <https://www.stratasys.com/en/stratasysdirect/technologies/3d-printing/polyjet/> (accessed September 27, 2022).
- [23] A. Pilipovi, P. Raos, M. Šerčer, Experimental analysis of properties of materials for rapid prototyping, *Int. J. Adv. Manuf. Technol.* 40 (2009) 105-115. <https://doi.org/10.1007/s00170-007-1310-7>.
- [24] M.W. Barclift, C.B. Williams, EXAMINING VARIABILITY IN THE MECHANICAL PROPERTIES OF PARTS MANUFACTURED VIA POLYJET DIRECT 3D PRINTING, in: *Int. Solid Free. Fabr. Symp.*, 2012.
- [25] A. KSY, J. KOTLISKI, Mechanical properties of parts produced by using polymer jetting technology, *Arch. Civ. Mech. Eng.* 10 (2010) 37-50. [https://doi.org/10.1016/S1644-9665\(12\)60135-6](https://doi.org/10.1016/S1644-9665(12)60135-6).
- [26] J. Mueller, S.E. Kim, K. Shea, C. Daraio, Tensile Properties of Inkjet 3D Printed Parts: Critical Process Parameters and Their Efficient Analysis, in: *Vol. 1A 35th Comput. Inf. Eng. Conf.*, American Society of Mechanical Engineers, 2015. <https://doi.org/10.1115/DETC2015-48024>.
- [27] D. Blanco, P. Fernandez, A. Noriega, Nonisotropic experimental characterization of the relaxation

- modulus for PolyJet manufactured parts, *J. Mater. Res.* 29 (2014) 1876–1882. <https://doi.org/10.1557/jmr.2014.200>.
- [28] K.K. Reichl, D.J. Inman, Dynamic Mechanical and Thermal Analyses of Objet Connex 3D Printed Materials, *Exp. Tech.* 42 (2018) 19–25. <https://doi.org/10.1007/s40799-017-0223-0>.
- [29] N.Meisel, C.Williams, An Investigation of Key Design for Additive Manufacturing Constraints in Multi-material Three-Dimensional Printing, *J. Mech. Des.* 137 (2015). <https://doi.org/10.1115/1.4030991>.
- [30] Materialise, Design Guidelines for Composite Materials | PolyJet, (2022). <https://www.materialise.com/en/academy/industrial/design-am/composite-materials> (accessed October 3, 2022).
- [31] J.J. Parise, L.L. Howell, S.P. Magleby, Ortho-Planar Linear-Motion Springs, *Mech. Mach. Theory.* 36 (2001) 1281. <https://scholarsarchive.byu.edu/facpub> (accessed January 17, 2022).
- [32] G.H. Teichert, B.D. Jensen, Design and fabrication of a fully-compliant mechanism for control of cellular injection arrays, *Prod. Eng.* 7 (2013) 561–568. <https://doi.org/10.1007/s11740-013-0475-1>.
- [33] N. Muthuram, P. Sriram Madhav, D. Keerthi Vasani, M.E. Mohan, G. Prajeeth, A review of recent literatures in poly jet printing process, *Mater. Today Proc.* (2022). <https://doi.org/10.1016/j.matpr.2022.08.090>.
- [34] E.H. Childs, A. V. Latchman, A.C. Lamont, J.D. Hubbard, R.D. Sochol, Additive Assembly for PolyJet-Based Multi-Material 3D Printed Microfluidics, *J. Microelectromechanical Syst.* 29 (2020) 1094–1096. <https://doi.org/10.1109/JMEMS.2020.3003858>.
- [35] M. Di Giovanni, Flat and corrugated diaphragm design handbook, M. Dekker, New York, 1982.



NON-ASSEMBLY 3D PRINTING: STEERABLE METAL GRASPER

Metal additive manufacturing is a promising technology for the production of functional medical products, due to its high shape complexity and resolution, and ability to withstand sterilization temperatures. This study explores the possibility of designing a completely non-assembly steerable surgical instrument using Selective Laser Melting. Despite its advantages for medical devices, the rough surface quality of unfinished parts can be problematic for non-assembly designs, leading to increased friction and wear in rigid body mechanisms and tendon-actuated mechanisms. We investigated printing of rolling contact joints with crossed flexures as low-friction joints, adjusted for printing in titanium for the design of the instrument. Grid-based lattice structures were incorporated as miniature flexures, and we explored the influence of various grid sizes on the flexibility and bending stiffness of the lattices. Based on this exploration, we altered the rolling joint configuration from two crossed flexures to a single straight flexure for our design. The resulting steerable surgical instrument design is completely non-assembly, including its actuation, facilitates easy removal of support structures, and requires no surface finishing steps. It has a diameter of less than 20 mm, facilitates opening and closing of a grasper, and steering of the grasper by 20 degrees.

Published as:

K. Lussenburg, R. van Starckenburg, A. Sakes, P. Breedveld, 3D printer-driven design of a non-assembly titanium surgical instrument using compliant lattice flexures, Materials & Design 240 (2024).

9.1 INTRODUCTION

9.1.1 Additive manufacturing

Additive manufacturing (AM) or 3D printing has emerged as a promising technology for the production of functional, medical products. It has been applied in a number of medical fields, among which personalized implants, anatomical models, surgical guides, prostheses, and surgical instruments [1]. 3D printed medical products can reduce surgical time and improve medical outcome [2]. The ability to create highly complex parts makes it possible to create personalized medical products for both patient and surgeon, as well as for advanced functionalities in terms of usability. In addition, AM enables the creation of non-assembly designs, which are functional mechanisms that can be produced in a single production step [3]. Non-assembly designs have some advantages over traditional assembly-based designs, as they reduce the processing time and costs, and allow for an increase in complexity of the design. In the medical field, non-assembly designs enable the creation of increasingly complex devices that can facilitate a wide range of complex operations.

The most widely utilized AM technologies in the medical domain are those that use polymers as a base material [1]. While many polymer-based AM technologies have been explored for medical designs, these materials are often challenging to sterilize and often suffer from poor mechanical properties. Therefore, for some medical applications, metals are preferred over polymers, because of their high stiffness, biocompatibility, and ability to withstand high temperatures during the sterilization process [4]. Metal AM processes, described by the umbrella term Selective Laser Melting (SLM), allow for the production of components with a high shape complexity and resolution. This makes the process ideal for the production of medical and surgical instruments, which can benefit from the advantages of SLM to produce complex, personalized instruments at lower costs as compared to conventional manufacturing for small batch sizes [5]. So far, medical applications of SLM include customized implants [6,7], surgical guides [8], forceps [9,10], surgical clamps [11], grasper jaws [12,13] and (parts of) steerable surgical instruments [5,14,15].

Although SLM shows many advantages for the production of medical devices, unfinished parts have a rough surface quality that can be problematic for use in non-assembly designs. Especially in mechanisms with interacting surfaces, such as rigid body joints and mechanisms actuated by tendons, a rough surface finish increases friction and wear and can hinder the operation of the mechanism [16]. The influence of a rough surface finish is even more noticeable for small or miniaturized parts, where geometrical feature sizes are only a few times larger than the size of the metal particles. One way to improve the surface quality of SLM parts is by employing industrial surface finishing techniques, such as grinding or mechanical polishing [17,18]. However, in non-assembly designs mechanical surfaces are often inaccessible by these techniques, since the designs cannot be disassembled to allow for easy access to the inner geometry [19]. Thus, while SLM-based non-assembly designs may reduce production time and costs, the complex post-processing required can offset these gains.

9.1.2 Steerable surgical instruments

Medical non-assembly mechanisms are particularly promising for the production of instruments with steerable end-effectors. Current surgical practices have seen a shift from open surgery to minimally invasive surgery (MIS), in which only three small incisions are required instead of one large incision. Conventional surgical instruments, consisting of a handle, straight shaft, and rigid end-effector, severely reduce the dexterity of the surgeon in MIS, due to restrictions posed by the small incision size. In response, steerable end-effectors have been developed [20–24], which provide the surgeon with additional degrees of freedom (DOF), without sacrificing the advantages of small incision sizes. Steerable instruments usually consist of many small, complex parts that provide the end-effector with the additional DOF. Non-assembly AM is a promising approach to increase the speed and ease of production of these miniature devices.

Steerable end-effectors usually rely on tendon-actuation, which is a cheap and efficient choice, since tendons require little space and can be easily embedded in various designs due to their high tensile strength and flexibility. However, in non-assembly designs, tendons have to be inserted into the designs after printing, since current AM technologies are less suited to 3D print long, thin, flexible structures with a high tensile strength. Accurately inserting tendons in a 3D printed device can be a considerably lengthy task that usually has to be performed manually [20]. Furthermore, it has proven difficult to precisely 3D print hollow small diameter channels through which the tendons are guided, due to the risk of them fusing shut, which hinders miniaturization of the instrument [21,25]. In the case of SLM, friction between the tendons and the rough surface of internal geometries inaccessible to surface finishing techniques can lead to premature failure of the tendons.

In this work, we describe the design and 3D print process for a steerable surgical instrument made of titanium, specifically tailored for the SLM process. Given the extensive design possibilities afforded by AM, which often can be challenging to implement and exploit, our approach involved a thorough analysis of the boundaries of the SLM process. This analysis allowed us to incorporate process-specific guidelines from the start, rather than after the conceptual design phase, establishing a framework we categorize as a 3D printer-driven design process. The resultant instrument design, which is completely non-assembly, including its actuation, facilitates easy removal of support structures and requires no surface finishing steps. As the instrument design was driven by the specifications of the SLM process, our design decisions were driven by the process specifications and design guidelines.

9.2 MATERIALS AND METHODS

9.2.1 Instrument requirements

Our main goal was to design a steerable instrument that does not require any assembly steps and a minimal number of post-processing steps. We define an assembly step as at-

taching two or more separate parts to each other by any means. The instrument has the following requirements:

1. Actuation: The actuation system of the instrument is completely 3D printed.
2. Post-processing: The only post-processing that we allowed is the unavoidable removal of the support structures.
3. Friction: Considering the rough surface of SLM parts, the instrument contains no sliding surfaces and is preferably entirely frictionless.
4. Dimensions: The maximum diameter of the instrument shaft is 20 mm. Although this is large considering the size of current surgical instruments, which typically have a diameter less than 8 mm, it will give us more design freedom in this exploratory design without being hindered by SLM size limitations.
5. Functionality: The instrument should contain a grasper that can be opened with a maximum opening angle of 60° , and that can be steered by an angle of at least 45° with one DOF (planar bending).
6. Material: The instrument will be printed in titanium, because of its high stiffness and biocompatibility.

9.2.2 SLM design guidelines

The SLM process uses a thin layer of metal powder deposited for each layer, which is sintered by means of a focused laser beam. In this study, the SLM printer used is the Lasertec 30 SLM 2nd Gen (DMG Mori, Bielefeld, Germany), with a laser spot size of 73 micron and 600 W laser unit. The metal powder used is Ti6Al4V grade 23 (Carpenter Additive, Widnes, United Kingdom). In addition to the requirements for the instrument, we comprised an inventory of design guidelines for SLM. The following list was drawn up from literature as well as from preliminary experiments with the used SLM printer. It should be noted that these values can differ depending on the specific 3D printer used, and that they are often conservative estimates to ensure the successful printability of the part.

1. Support structures: Supports are required to anchor the workpiece to the base plate, for heat dissipation, and to reduce residual stresses [26]. Supports that are placed on flat surfaces reduce the complexity of support removal and result in a better surface finish than when removing them from a curved surface [26].
2. Overhang: To prevent the use of supports, features can be designed as ‘self-supporting’ when they have an overhang of less than 45° with respect to the build plate.
3. Clearance: Clearances between adjacent parts should be between 120 μm and 150 μm to prevent fusing of parts, depending on part orientation [27]. The same minimum size should be used for holes or channels.
4. Wall thickness: The reported minimum thickness of a solid, thin wall is approximately 0.4 mm for SLM [15,28], although for the 3D printer used in this study the minimum wall thickness that could be obtained was 0.55 mm.
5. Volume gradients: The high thermal gradient of the metal powder can cause parts

to warp or distort. Therefore, sudden increases in part volume should be avoided, to prevent small features from experiencing warpage or a modification in mechanical properties due to the radiant heat of the large volume.

9.2.3 Low friction joint design

Some studies have successfully 3D printed non-assembly rigid body joints using SLM [27,29–31], however they require a relatively large clearance between the parts when printed in a pre-assembled position to prevent them from fusing [29]. This can hinder design scalability and miniaturization, and can result in excessive play when applied in a steerable mechanism. In addition, the functioning of rigid body joints can be hindered by friction from the rough surface finish of SLM. Therefore, the use of rigid body joints was excluded in our design, because these rely on sliding surfaces.

Rolling joints are examples of joints with low sliding friction, which do not require smooth polished surfaces. They consist of two bodies that are constrained by two or more flexures in a cross-linked configuration and roll over each other (Figure 9.1a-b) [32–35]. The flexures allow the bodies of the joint to rotate with respect to each other without slipping, and as such, a low stiffness of the flexures is desired. Advantages of rolling joints are strongly reduced friction and wear on parts, large displacements, and no need for lubrication [32,33].

A number of steerable surgical instrument designs have incorporated rolling joints [34,36–38]. Jeanneau et al. [32] and Zhang et al. [36] 3D printed rolling joints using material extrusion and selective laser sintering, respectively. In both cases the joint was printed with the flexures in a curved configuration, as shown in Figure 9.1a, which means there is no stress in the flexures in the straight position [32]. However, in order to prevent fusing of the flexures to the joint body during printing, a gap had to be established between the flexures and the body, leading to backlash in the design [32]. Alternatively, the flexures can be printed in a straight configuration (Figure 9.1c), as proposed by Halverson et al. [33]. This reduces the need for a gap, although the joint then needs to be placed in its curved position by means of an extra production step.

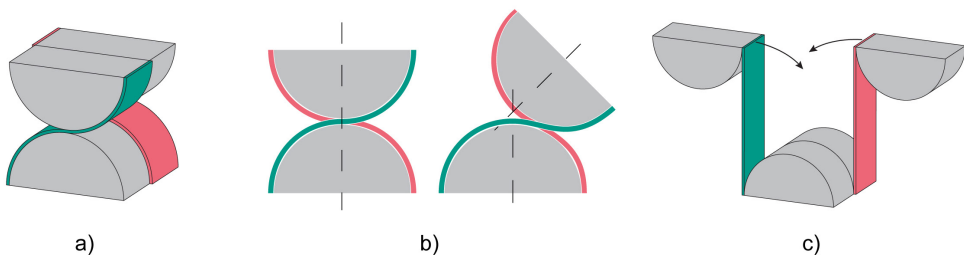


Figure 9.1: Rolling joint with the two different flexures indicated in green and red. a) 3-dimensional view of a rolling joint. b) Side view of the rolling joint in neutral position and in bent configuration. c) Unfolded rolling joint with flexures in a straight position, the arrows indicate the folding direction.

9.2.4 3D printing of flexures

A rolling joint requires compliant flexures with a low stiffness. The stiffness of the flexures is limited by the minimum wall thickness that can be printed, which in our case is approximately 0.55 mm, resulting in rigid walls unsuitable for flexures. The wall thickness is affected by the underlying laser scan modes performed by the printer [39]. Different laser scan modes are used for different parts of the layer, i.e. the outer contour and the interior region, and settings can be adjusted accordingly. In Figure 9.2a-b, the different laser scan modes for thick and thin walls are illustrated. For a thick wall (Figure 9.2a), the laser first fills the interior region of the layer with a parallel hatch pattern, after which the outer contour is scanned with a single line. Since the melt pool of the laser is larger than the laser spot itself, the laser moves with an offset from the designed wall. For a thin wall (Figure 9.2b), the laser only follows the contour of the wall, however, since there is not enough space to have the required offset, the melt pool of the laser spot will increase the wall thickness [40]. The influence of the melt pool can be controlled to a certain amount by parameters such as the scanning speed and laser wattage [39], however these settings also affect the print quality. As such, reducing the wall thickness is in practice not feasible due to the internal printer settings.

Another way to decrease the wall stiffness is by using lattice structures, as recent studies have shown [41–44]. Advantages of lattice flexures are a reduced bending stiffness, a significantly lower mass, and good off-axis stiffness [41]. The SLM printer used in this study has a special slicing mode in the software for lattice structures. Using the lattice

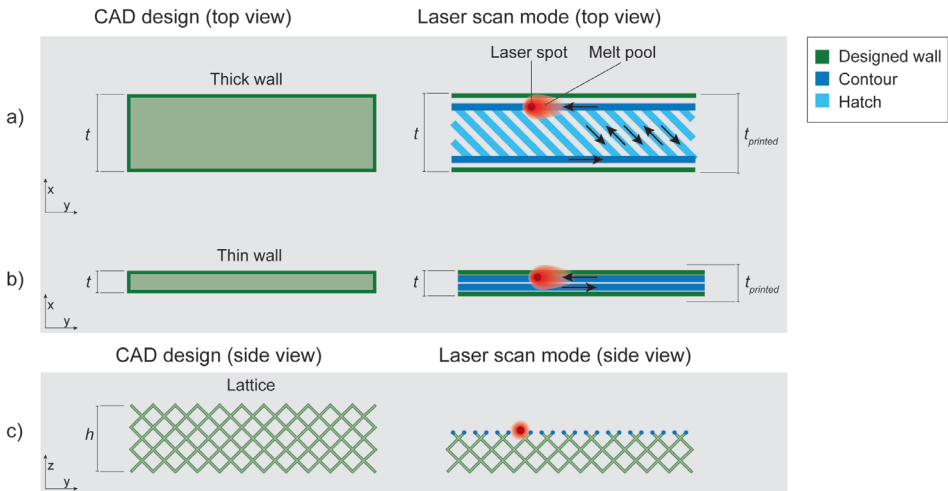


Figure 9.2: Schematic overview of the different laser scan modes available for the 3D printer used in this study, in which t is the designed thickness of the wall and t_{printed} the actual thickness of the printed wall. a) For a thick wall, the laser fills the interior region with a pattern called hatch, after which it follows the outer contour with an offset, resulting in a wall thickness similar to the designed wall. b) For a thin wall, only the contour is followed by the laser, which results in a wall thickness larger than designed due to the size of the laser melt pool. c) For a lattice wall, the laser only prints one point at a time.

mode, the laser prints one voxel at a time, as illustrated in Figure 9.2c, and only passes over the wall once. In this mode, the design of the lattice is completely 2-dimensional, therefore the thickness of the structure is purely determined by the laser spot size and printer settings. To develop the instrument, we further explored the possibility of using rolling joints in combination with lattice flexures.

9.2.5 Test parts

Lattice flexures

First, we explored the potential of 3D printed lattice flexures with different structures and lengths. The limitations of lattice mode are that the lattices can only be printed straight and perpendicular to the build plate, along the z-axis. We designed test parts as shown in Figure 9.3a, consisting of a solid wall of 10 mm z-height and 1 mm thickness, interrupted by lattices with lengths of 10 mm and 25 mm. The lattices consist of a 2-dimensional grid, with cell sizes of 1 x 1 mm (L-1), 0.75 x 0.75 mm (L-0.75), 0.5 x 0.5 mm (L-0.5), 0.25 x 0.25 mm (L-0.25), and 0.05 x 0.05 mm (L-0.05) (not pictured). The lattices are constructed within the software of the SLM printer as dimensionless vectors based on an elementary cell. To define the cell, first, a cube is defined with x, y, and z values corresponding to the desired lattice grid size. For the first line a start point is defined at X0-Y0.5-Z0 and an end point at X1-Y0.5-Z1 (AB in Figure 9.3b), for the second line the start point is defined as X0-Y0.5-Z0 and the end point as X1-Y0.5-Z1 (CD in Figure 9.3b), together defining one cell of the grid. The software divides the vectors from start to finish in voxels, corresponding to one voxel per layer height. As such, the lattices are theoretically designed with no thickness, while in practice the thickness of the lattice will approach the size of the laser spot, including its melt pool, and be circular in shape. Since all the struts of the grid have an overhang angle of 45°, they can be printed without requiring support structures. Each of the grid sizes was printed five times, resulting in a total of 25 test parts.

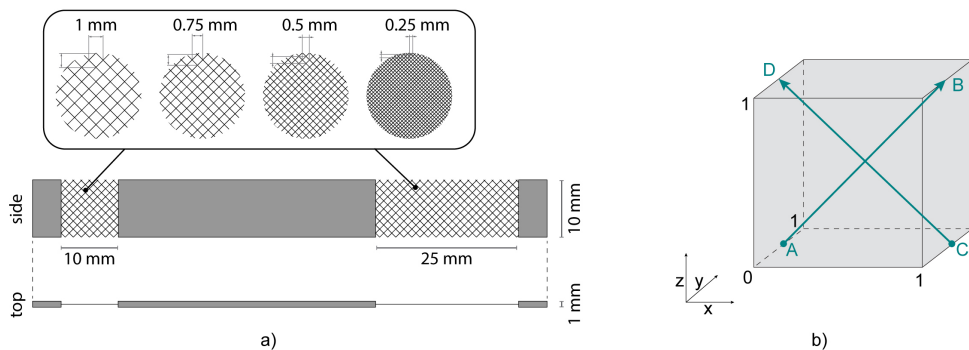


Figure 9.3: Design of lattice test parts. a) Full test part, with lattice grid sizes of 1 x 1, 0.75 x 0.75, 0.5 x 0.5, 0.25 x 0.25 and 0.05 x 0.05 mm (not pictured). b) One lattice cell as designed in the software of the SLM printer, consisting of two dimensionless vectors AB and CD.

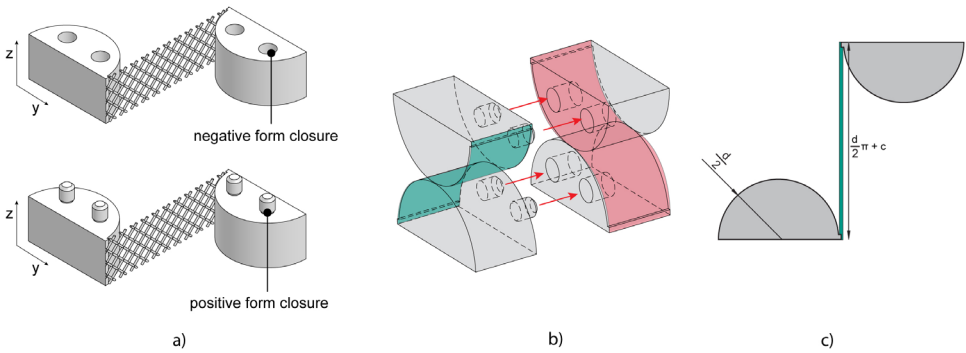


Figure 9.4: Design of the rolling contact joint in its unfolded configuration. a) CAD model of the two joints showing the positive and negative form closure. b) Assembly of the positive and negative part. c) Side view of the joint with parameters, in which d is the diameter of the joint, t is the thickness of the lattice, and c is a clearance.

Rolling joint

We explored the feasibility of printing rolling joints with lattice flexures, by testing two design variables: the size of the joint and the structure of the lattice. The joints were printed in two halves with straight flexures, according to Figure 9.1c. We introduced positive and negative form closures on the joint body to connect the bodies, as shown in Figure 9.4a-b. The joints were designed with a diameter d of 10 mm, 7.5 mm, and 5 mm, with a z -height of 5 mm, 3.75 mm, and 2.5 mm respectively. The length of the flexure is directly related to the joint size by $\frac{d}{2}\pi + c$, in which c is a clearance of 0.15 mm. All three sizes of the joints were printed with four lattice structures: L-1, L-0.75, L-0.5, and L-0.25 (12 full joints). In total three batches of joints were printed, resulting in a total of 36 full joints. In between the batches, the results were analyzed and revised where necessary.

9.2.6 Production

The used parameters of the SLM process are summarized in Table 9.1. All test parts were positioned with the lattices perpendicular to the movement of the wiper, and in parallel with the argon flow.

Supports were removed using wire electrical discharge machining (wire EDM) (Fanuc, Oshino, Yamanashi, Japan) with 0.25 mm brass wire. Wire EDM can efficiently remove

Table 9.1: Process parameters used in this study.

Layer height	50 μ m			
	Scanning speed (mm/s)	Laser Power (Watt)	Hatch distance (mm)	Offset distance (mm)
Hatch	742	219	0.11	0.1
Contour	408	120	-	0.05
Lattice	1000	140	-	0

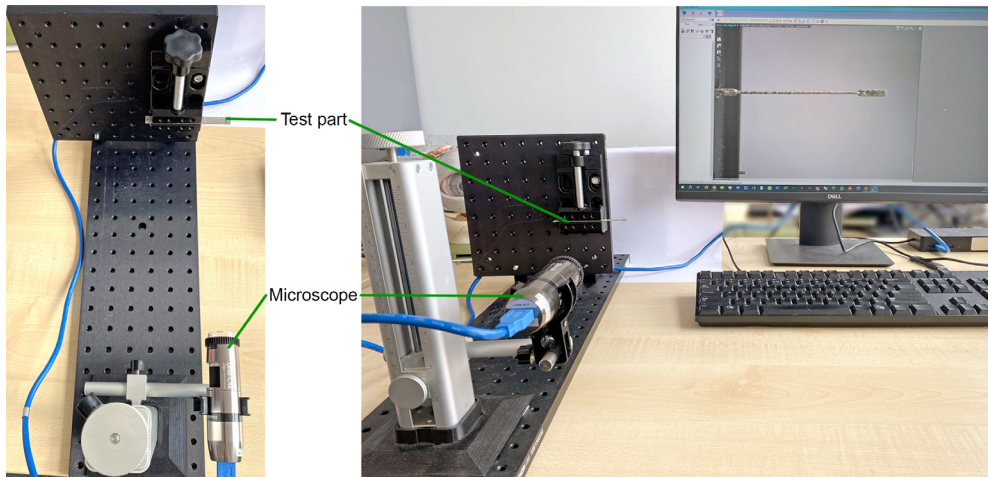


Figure 9.5: Set-up used to test the deflection of the flexures. The set-up shows one of the 25 mm lattices without weights. Only one side of the test part was tested at a time, to test the 10 mm flexure, the test part was reversed in the clamp.

support structures in a straight line parallel to the build plate on the underside of the part in a single step, as long as all features are at the same distance from the build plate. The joints were positioned on the build plate with the form closures on top, so that supports on the bottom could easily be removed in a straight line. The joints were assembled by pushing the two joint bodies towards each other, thereby forcing the lattice to follow the radius of the body, and connecting the two halves by means of the form closure, as shown in Figure 9.4b. Only one batch of the joints received a stress relief heat treatment at 850°C for 2 hours, after which the parts were cooled at room temperature.

9.2.7 Characterization

Dimensional accuracy

The wall thickness of the printed lattice flexures was measured using digital calipers, based on three measurements along the length of the flexure. The geometry and the strut sizes of the lattices were examined under a digital microscope (Dino-Lite 3.0, AnMo Electronics Corporation, Taiwan). We determined the theoretical and actual porosity of the lattices by isolating the 25 mm long lattice from the test parts after performing the other tests. Three lattices of each grid size were weighted on a calibrated scale, which was then divided by three to obtain their individual mass. For the theoretical porosity of the lattices, CAD-models of the structures were drawn in Solidworks (Dassault Systèmes, Paris, France), using a uniform strut diameter of 0.20 mm, and the mass of the structures was determined using the *Mass Properties* feature.

Bending performance

The lattice test parts were used to examine the bending stiffness of the different lattice structures, by measuring the deflection as a result of a calibrated force. Weights of 5 g,

10 g, 15 g, 20 g, 30 g, 40 g, 50 g, 60 g, 80 g, and 100 g were attached to both ends of the test parts subsequently while securing the middle part. The slope of the deflection of the lattice flexures was then measured using the digital microscope. The test setup is shown in Figure 9.5. The test was repeated three times, using new test parts for each measurement.

When applied in the rolling joint, the lattice flexures should have a bending radius that corresponds to the diameter of the joint, i.e. 5 mm, 7.5 mm, or 10 mm. The bending radius of the lattices was evaluated by curving them over the joint body, if they were able to lay flat across the surface the bending radius suffices. After assembling the joint halves, the bending angle of the joints was evaluated. According to Requirement 5 in Section 9.2.1, the instrument should have a steering angle of at least 45°, however the design of the rolling joints allows a 90° bending angle in both directions. Therefore, we tested the rolling joints by manually bending them up to a 90° angle in both directions. We considered the joints successful if they were able to be assembled and bent without breaking and withstood bending at least 100 times.

9.3 RESULTS

9.3.1 Flexures

All 25 lattice test parts printed successfully, however some broke during the removal with wire EDM. From observations we found that the lattices started to vibrate as a result of the wire EDM process, which led to a fracture originating from a small print defect. Therefore, only three test parts were tested per lattice structure. The 3D printed test parts are shown in Figure 9.6a, along with microscope images of the different lattice structures (Figure 9.6b-f). The microscope images show that L-1, L-0.75 and L-0.5 have a fairly regular pattern, whereas the more dense L-0.25 and L-0.05 have no discernible print pattern, with only a few small gaps visible between the struts (light blue ‘flecks’ in Figure 9.6e-f).

The wall thickness, strut size and weight of the lattices is given in Table 9.2. The wall thickness of all lattices up to L-0.25 is 0.26 mm on average, while the wall thickness of L-0.05 is 0.54 mm, similar to the thickness of a solid wall (0.55 mm). It is noticeable that although the pattern, as well as the ‘openness’, of L-0.25 and L-0.05 seems similar under the microscope, the wall thickness of L-0.05 is approximately twice as large. The average

Table 9.2: Results of the dimensional measurements of the different lattice types.

	L-1	L-0.75	L-0.5	L-0.25	L-0.05
Lattice size	1 x 1	0.75 x 0.75	0.5 x 0.5	0.25 x 0.25	0.05 x 0.05
Wall thickness (mm)	0.26	0.26	0.26	0.26	0.54
Strut size (mm) (n = 4)	0.20 ± 0.01	0.23 ± 0.01	0.19 ± 0.01	-	-
Theoretical porosity (g)*	0.087	0.110	0.150	0.207	0.444
Actual porosity (g)*	0.067	0.073	0.130	0.170	0.360

*For the 25 mm lattice

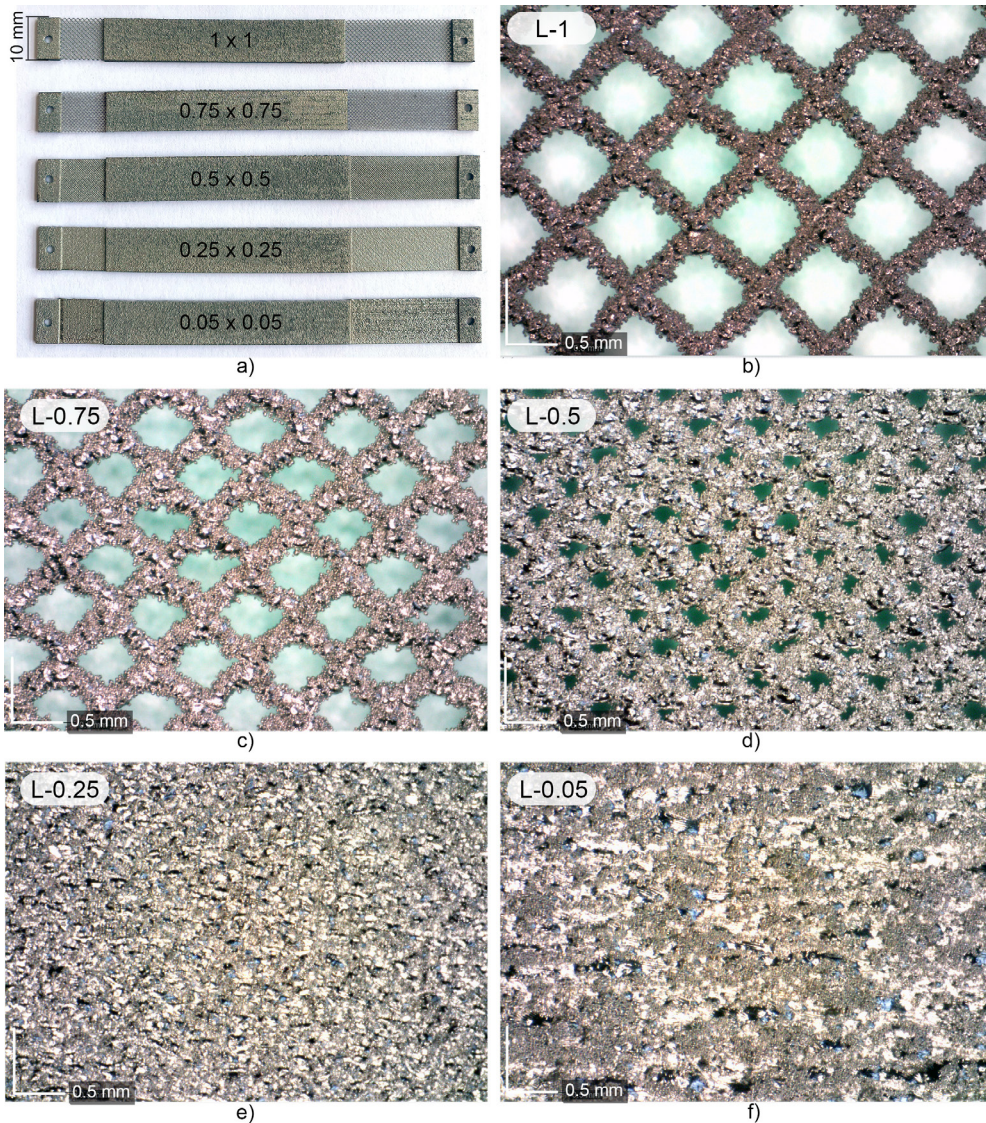


Figure 9.6: Results of the printed lattice flexures. a) Printed test strips. b) Close up of L-1 lattice. c) Close up of L-0.75 lattice. d) Close up of L-0.5 lattice. e) Close up of L-0.25 lattice. f) Close up of L-0.05 lattice.

strut sizes of L-1, L-0.75, and L-0.5 are approximately 0.20 mm. For the other lattice sizes, no separate struts could be discerned.

The results of the deflection test are shown in Figure 9.7a-b. As was expected, the L-1 lattices show the lowest bending stiffness and deflect the most under the applied force. The 10 mm and 25 mm L-1 showed a maximum slope under a 100 g load of 74.1° and 87.6° , respectively. One of the 25 mm L-1 mm strips broke off at the connection points when applying the mass of 100 g. The L-0.75 lattices were more fragile than the L-1 lattices: all

9. A NON-ASSEMBLY STEERABLE SURGICAL INSTRUMENT

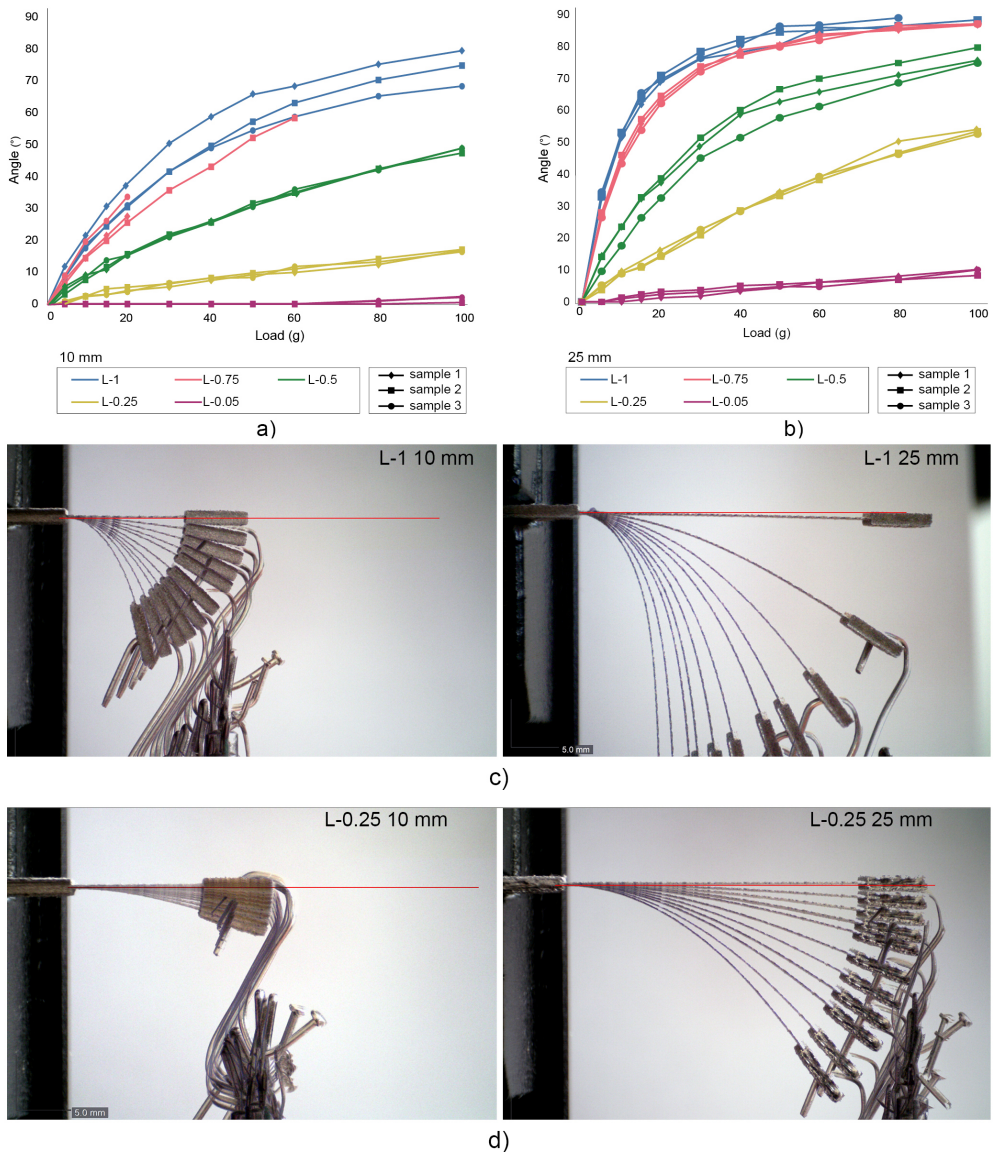


Figure 9.7: Results from the deflection tests for the 10 mm flexures and 25 mm flexures. a) Slopes of the 10 mm lattices (n=3). b) Slopes of the 25 mm lattices (n=3). c) Combined images of the deflection tests for the L-1 lattice 10 mm (left) and 25 mm (right). d) Combined images of the deflection tests for the L-0.25 lattice 10 mm (left) and 25 mm (right).

three of the 10 mm L-0.75 lattices broke; two at a load of 30 g and one at a load of 80 g. It is likely that this is due to geometrical imperfections or print defects [40], although none could be detected before the test.

In Figure 9.7a-b it can be seen that the slope of the L-0.75 lattices is closer to the L-1

lattices than the L-0.5 lattices. There appears to be little difference in flexibility for the L-1 versus the L-0.75 lattices. The L-0.05 lattices show hardly any deflection, with slope angles of 1.6° for the 10 mm lattice and 9.5° for the 25 mm lattice. The 10 mm L-0.05 did not show any deflection until 80 g of load was applied. In Figure 9.7c-d the deflection of one L-1 and one L-0.25 is shown for both flexure lengths and all loads. L-0.25 showed 77% less deflection for the 10 mm and 39% less deflection for the 25 mm length as compared to L-1. It was noticeable that for all lattices, with the exception of L-0.05, the lattices had plastically deformed after removal of the 100 g load, with as much as a 9° residual bending angle for the 25 mm L-1.

This test showed that the larger, less dense lattice sizes resulted in more flexibility, but were also more fragile and more difficult to print in a consistent manner. We observed no difference in lattice structure between L-0.25 and L-0.05 concerning openness or print quality. Nonetheless, the wall thickness of the L-0.05 lattice is twice as much as the L-0.25 lattice, resulting in a high stiffness flexure. Therefore, lattice sizes larger than L-0.25 are to be recommended for our purpose. Although the lattices are somewhat fragile, most can withstand at least 1 N of transverse force.

9.3.2 Rolling joints

The lattices of the joints in the batch that received the heat treatment became too brittle and broke off when bending. Therefore, the heat treatment was omitted for the following batches. In the subsequent batch, it was found that the lattices had fused to the joint body over a distance of approximately 1.5 mm, causing them to break at this location (Figure 9.8a-b). Therefore, for the third batch, we altered the design to incorporate the thickness of the lattice into the joint, as well as a clearance, as shown in Figure 9.8c, in which d is the joint diameter of 5 mm, 7.5 mm, or 10 mm, t the lattice thickness of 0.26 mm, and c the clearance value of 0.15 mm. This design ensured that the flexure was able to lay flat across the surface of the body without fusing.

During removal with wire EDM, most of the L-1 lattices broke at the attachment point, except for one 10 mm joint. For the remaining joints, of which a few examples are illustrated in Figure 9.9a, it was possible to curve the lattice over the joint body, indicating that the bending radius of the lattices corresponded to the joint size. However, when connecting the two joint parts the majority of the lattices broke at different places along the length of the lattice (Figure 9.9b).

The joints that were assembled successfully were the 10 mm diameter joints with L-0.5 and L-0.25 lattice; the 7.5 mm diameter joint with L-0.5 and L-0.25 lattice; and the 5 mm diameter joint with L-0.25 lattice (Figure 9.9c). All of them show a slight deformation in the form of twisting of the joint. All five assembled joints were able to bend up to 90° in both directions (Figure 9.9d-e). Once assembled, the joints were stable and did not show signs of breakage for at least 100 times bending. A difference in stiffness was clearly noticeable between the joints, the 5 mm diameter joint required more force to move than the larger joints, and the L-0.25 lattice required more force than the L-0.5 lattice.

For the rolling joint, we explored two variable design parameters: the joint size and

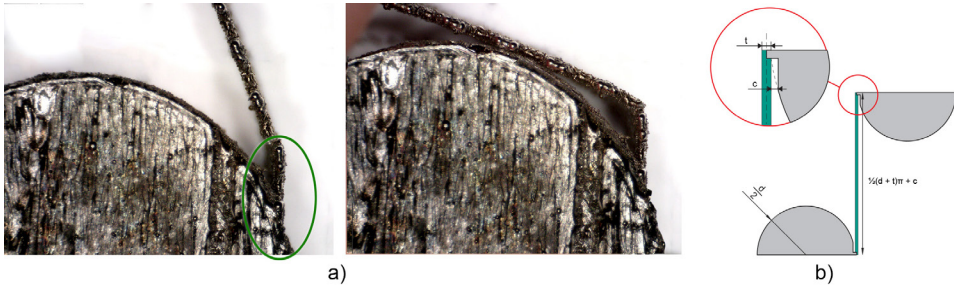


Figure 9.8: One of the failed joint batches and the redesign. a) A microscope close up of one of the joints, showing that the lattice is partially fused to the joint body, indicated by the green circle. b) The lattice breaks when attempting to bend it over the joint body. c) Redesign to prevent fusing of the lattice to the joint body, in which the lattice with thickness t is placed more to the side of the joint and a clearance c is added.

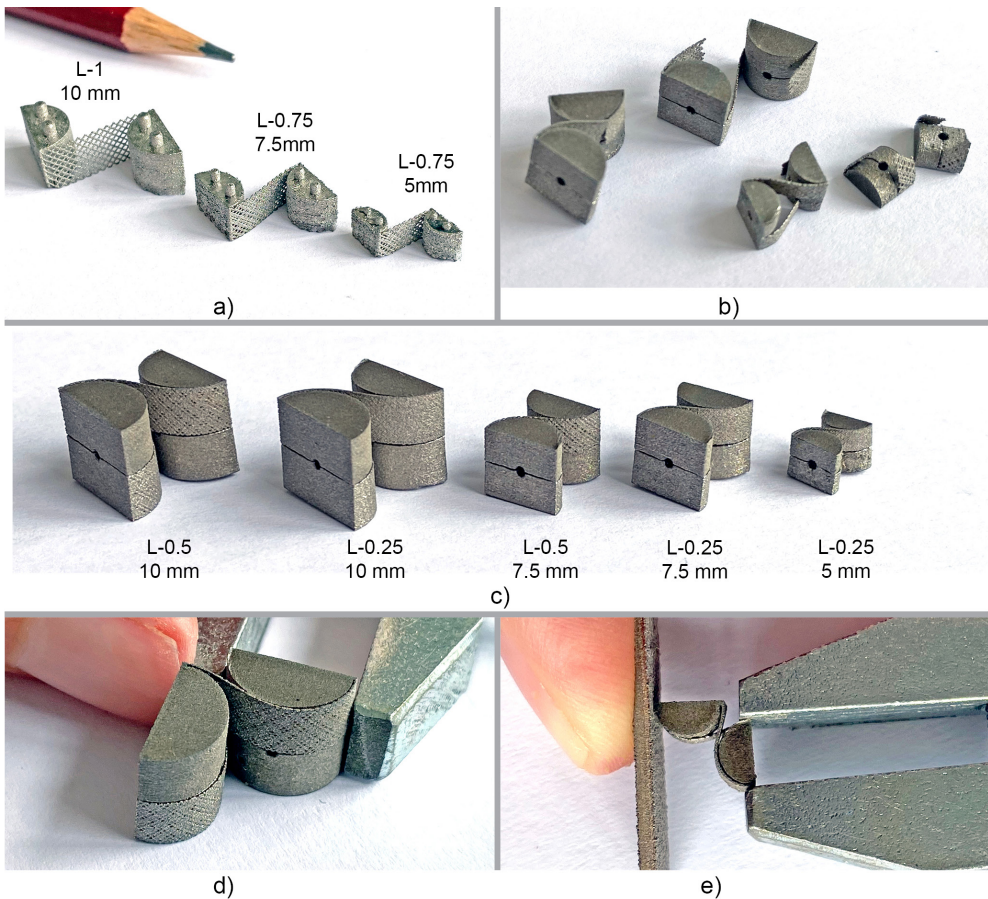


Figure 9.9: 3D printed rolling contact joints. a) Single 3D printed joint halves. b) Some of the broken assembled joints. c) The successfully assembled joints. d) The 10 mm L-0.5 joint illustrating a bending angle of 90° . e) The 5 mm L-0.25 joint illustrating a bending angle of 90° .

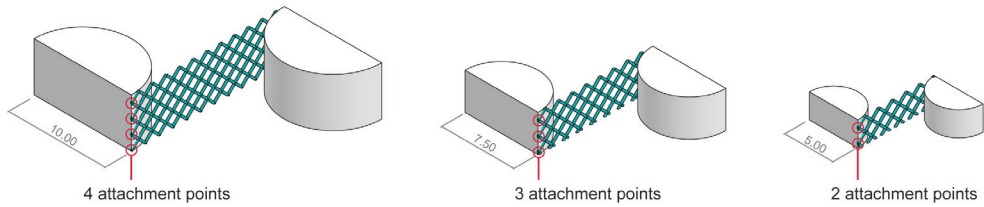


Figure 9.10: Effects of decreasing the joint size. When decreasing the size of the joint with a constant lattice size, the number of attachment points from the lattice to the joint also decreases, which can lead to a fragile connection.

the lattice structure. Reducing the joint size reduces the length of the flexure, increases the stiffness of the flexure, and reduces the height of the joint, which reduces the number of attachment points of the lattice to the joint. The latter is illustrated in Figure 9.10. A lower number of attachment points increases the fragility of the connection. This effect was especially noticeable in the joints printed with the L-1 lattices, which fractured at the attachment of the lattice to the joint. Increasing the lattice grid size decreases the stiffness of the flexure, but reduces the number of attachment points. A balance between joint size and lattice structure must be found to produce the smallest joints with the lowest stiffness while maintaining a sufficiently strong connection.

Bending radii of 10 mm, 7.5 mm, and 5 mm were feasible for all lattice grid sizes. However, only the stiffer lattices, L-0.5 and L-0.25, remained intact when assembling the joint halves. The 5 mm diameter joint was only functional with the stiffest L-0.25 lattice, although the resulting joint had a high bending stiffness and was therefore found unsuitable to apply in a steerable instrument. Since the working of the lattices seems to be optimal when the joints are not assembled, i.e. the lattice is not forced into a pre-tensioned position, in the next section for the instrument design we explore the use of single-layer rolling joints with a different lattice configuration that does not require assembly or pre-tensioning of the flexures.

9.4 INSTRUMENT DESIGN AND MANUFACTURE

9

9.4.1 Joint configuration and actuation

Actuation of the instrument without relying on cables can be implemented by for instance making use of ribbons [12], thin rigid rods [45,46], or multi-linkage systems with rigid body joints [47,48]. As both ribbon actuation and multi-linkage systems are prone to sliding friction during actuation, we settled on using rigid rods to actuate the steering and the grasper. The schematic design and working principle of the instrument are shown in Figure 9.11. In this design, two pairs of rolling joints are placed next to each other with the flexures in a straight configuration. By applying an inwards force to the handle, the flex-

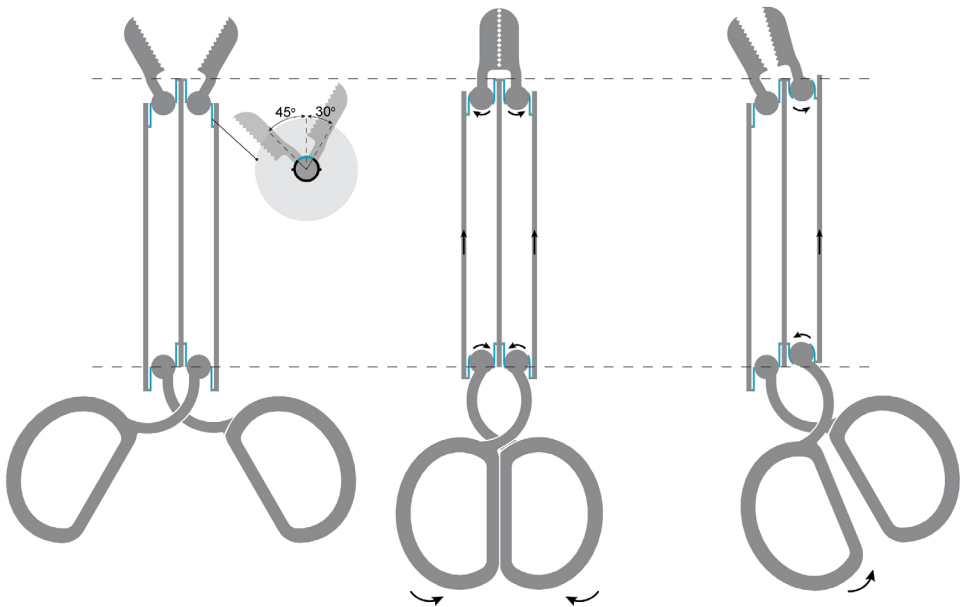


Figure 9.11: Working principle of the non-assembly steerable instrument, in which the flexures are indicated in blue, showing the neutral position (left), closing of the grasper (middle), and steering of the grasper from the neutral position (right). The grey dashed lines show the position of the middle rod.

ures roll over the circular joint and transfer the motion through the rigid rods to the grasper. The joints have been given a diameter of 5 mm, with rods of 1 mm thickness, resulting in a total width of 15.5 mm. The height of the entire instrument is 5 mm, which gives the lattices sufficient attachment points to the joint and the shaft. The grasper is printed in its open position with jaws in a 30° angle. To obtain a 45° steering angle, the largest rotation for each grasper jaw results in a 75° rotation (Figure 9.11). The length of the flexure is calculated based on the arc length on the surface of the joint diameter for this angle, given by $\pi(d + \frac{t}{2}) \cdot \frac{75}{360}$, which equals 3.4 mm. To ensure sufficient flexibility of the flexures, we increased this length to 5 mm.

9

9.4.2 3D printed prototypes

The initial prototype of the design, employing L-1 lattices (Figure 9.12a), revealed two issues. First, upon rotation, the stiffness of the flexures caused an outward displacement of the outer rods (Figure 9.12a). Second, despite the intended 1:1 motion transfer, the prototype's grasper was unable to fully close. To address this, we enlarged the joints at the handle from 5 mm to 7.5 mm, amplifying handle movement and ensuring complete grasper closure during actuation (Figure 9.12b).

To prevent the outward movement of the rods, we considered reducing the flexure stiffness or mechanically securing the rods. We opted for the latter, which requires a mechanical connection allowing the outer rods to move relative to each other and the inner rod.

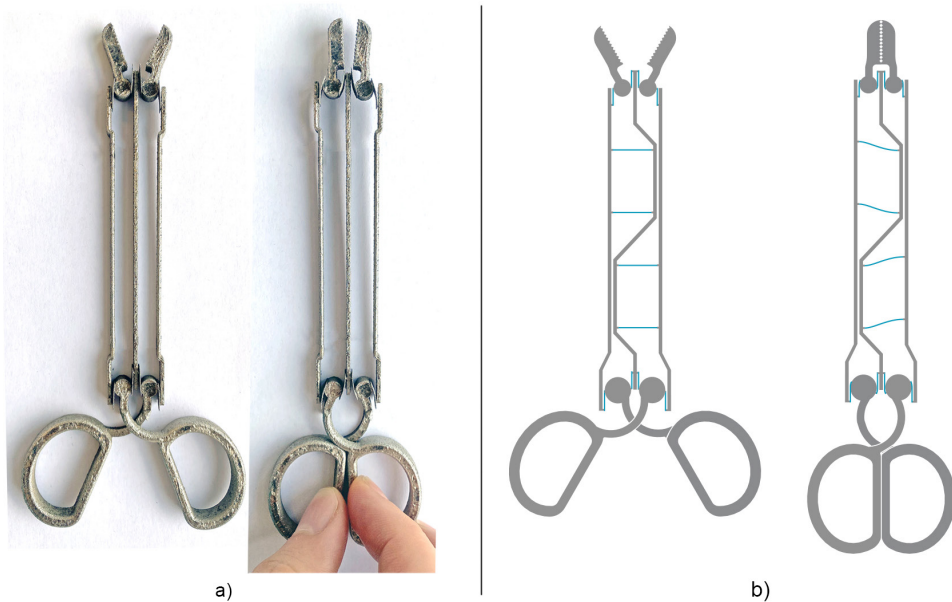


Figure 9.12: First 3D printed prototype and design iteration. a) The 3D printed prototype in open (left) and closed (right) position. In the closed position it can be seen that the outer rods are pushed outwards, and that the grasper does not fully close. b) Adjusted design of the non-assembly instrument, in which a linear compliant mechanism was added to prevent the rods from moving outwards, and the joints near the handle have been increased in size. The top shows the grasper in neutral position, and the bottom shows the closing of the grasper and deformation of the compliant flexures.

This connection is longitudinally flexible yet laterally rigid. To achieve this, while fulfilling our requirements regarding assembly and post-processing, we implemented a linear compliant mechanism using lattice flexures connecting the outer rods to the inner rod. For small displacements, as is the case in our design, this compliant mechanism facilitates unidirectional motion. In addition, to reduce the stiffness of the flexures, we enhanced their slenderness by utilizing the instrument's full width, which involved changing the rod shape from straight to 'meandering' (Figure 9.12b).

The adjusted design was printed two times, again with lattices of L-1 (Figure 9.13a). The total printing time was approximately 6 hours. When removing the prototype from the build plate using wire EDM, stresses within the material caused significant deformation of the grasper and handles, as shown in Figure 9.13b. This deformation caused torsion of the flexures. Both prototypes functioned for a short time, as can be seen in the video linked by the QR code at the end of this Chapter, but after a few manipulations, the lattices at the grasper side failed. This time, the grasper was able to fully close (Figure 9.13c). However, the outer rods show clear deformation towards the distal end, indicating they are still being forced outwards when actuating the grasper. The desired steering angle of 45° of the grasper could not be obtained, no more than 20° was possible before the lattices started to fail.

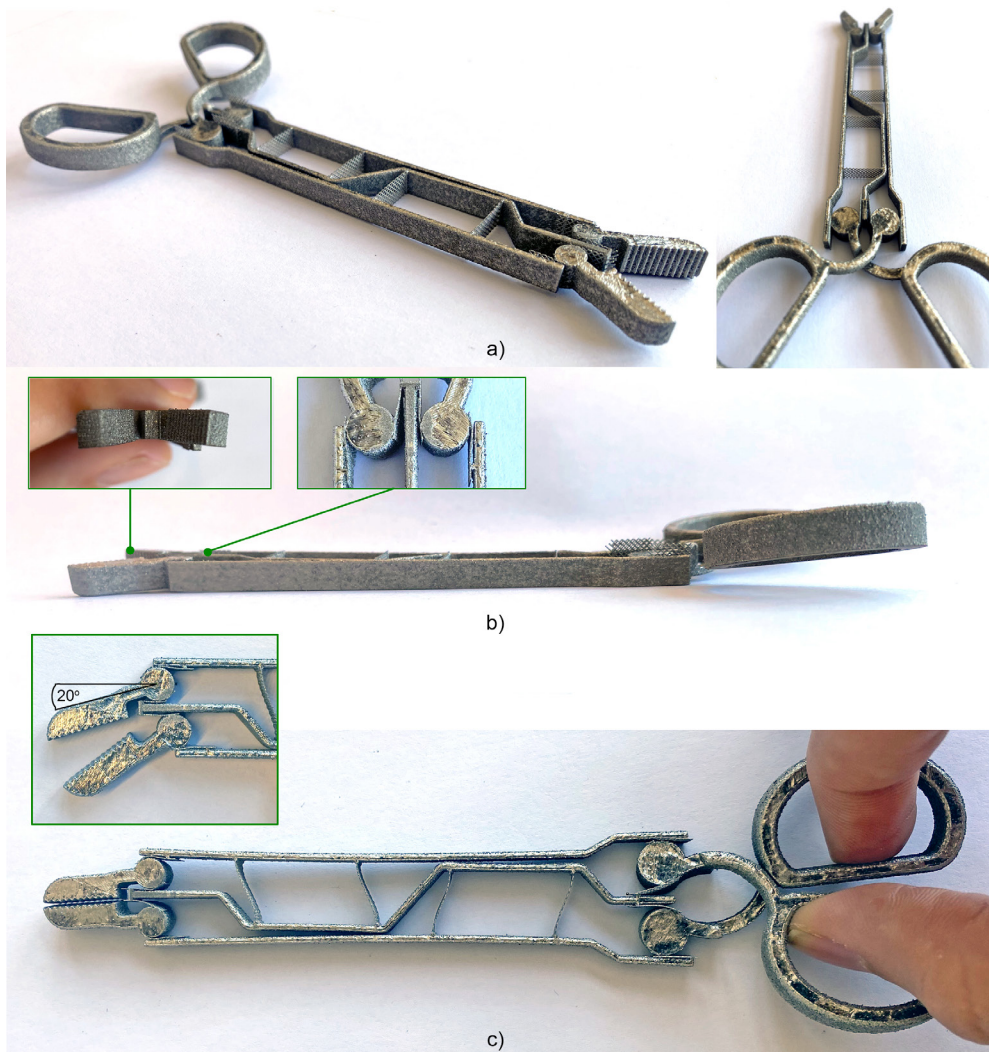


Figure 9.13: Second iteration of the 3D printed prototype. a) 3D printed prototype. b) Side view of the prototype, showing clear warpage in the handle, and close ups of the warpage in the grasper as well as the torsion in the flexures. c) Closing of the grasper was possible with this prototype, although deformation of the outer rods is visible. The grasper was able to bend 20°.

9

9.5 EVALUATION AND DISCUSSION

9.5.1 Flexures and joints

This chapter explores the possibility of designing a completely non-assembly steerable surgical instrument using SLM printing with titanium. Due to the rough surface finish of SLM printed parts, which can interfere with the motion of mechanical parts, negating the advantages of non-assembly instruments by requiring extensive surface treatments

to function, we attempted to design a low friction instrument that is not hindered by the rough surface finish. To do so, we explored the possibility of 3D printing compliant flexures with a lattice structure, to reduce the stiffness and miniaturize the instrument. We succeeded in printing various lattice designs with differences in stiffness, by which we reduced the minimum printed wall thickness to 0.26 mm (approximately 50% of the regular minimum wall thickness), in order to achieve low stiffness flexures. We found there is a fine line between printability and functionality; the lattices are very sensitive to print parameters, factors such as the location on the build plate and total volume of the parts can affect the results.

The difference in wall thickness between L-0.05 and the other lattice sizes likely stems from the fact that the cell size of this lattice is smaller than the laser spot size (0.05 x 0.05 versus 0.073 mm, excluding melt pool). Since one voxel is printed for each layer height, which is also 0.05 mm, there is significant overlap between the printed voxels and we hypothesize that this increases the melt pool surrounding the voxels, resulting in an increased wall thickness. We have not specifically investigated the behavior of lattices with grid sizes between 0.25 x 0.25 mm and 0.05 x 0.05 mm in this study, however, future studies to investigate the minimum grid size that results in a wall thickness of approximately 0.25 mm could contribute to the knowledge and understanding of lattice flexures.

Miniaturization of the flexures results in contradictory requirements. Since the minimum wall thickness remains a fixed value, reducing the grid size of the lattice leads to an increase in stiffness. This can be solved by a reduction in material in the form of a larger lattice size, although this makes for an increasingly fragile flexure. This, in turn, can be somewhat mitigated by increasing the height of the lattice. Alternatively, the design of lattices with variable grid sizes, in which a denser grid is applied towards the edges to maximize the number of attachment points, can be explored [49].

A rolling joint is advantageous considering the fragility of the lattice structures, since the bending angle of the lattice is confined by the solid portion of the joint, limiting sharp bending angles and preventing breakage. Although we have demonstrated that it is possible to 3D print functional rolling joints in different sizes, there are some downsides making it less feasible to apply in a non-assembly instrument. Since it is only possible to print the lattices in a straight configuration, they cannot be produced completely non-assembly, and bending of the lattices results in significant stress. Ideally, for torsion-stiffness and joint stability, the joint should consist out of at least three layers of crossed flexures in alternating directions instead of two, making it more complicated to produce non-assembly. However, for applications where size and assemblability are not of concern, the rolling joint can be a suitable solution for a low friction SLM joint that can be 3D printed in different scales.

9.5.2 Instrument design improvements

We incorporated an alternative design of a traditional rolling joint in the steerable instrument, which increased compatibility with the drawn-up requirements. Although the instrument was functional, the lattices only lasted for a short time before breaking. The

main reason for this were the significant stresses present in the material that caused substantial deformation of the grasper and handle, leading to warping of the flexures. Usually, these stresses are mitigated by applying a heat treatment immediately after printing, however this resulted in brittle lattices. Subsequent studies could explore the parameters of heat treatments to reduce stresses while maintaining lattice flexibility, as it has been shown that heat treatments provide the possibility of tuning the mechanical properties, although the relationship between different settings is not yet well understood [41].

The instrument design can further be improved by elongating the flexures of the rolling joints, further increasing the flexibility. This might also prevent the deformation in the outer rods caused by the inherent bending stiffness of the flexures. At the handle side, the height of the joints can be raised to increase the attachment points for the lattice. In the prototypes in Figures 9.12-13, the length of the shaft was adjusted to the size of the build plate, however with a larger build plate the length can be increased. In that case, we suggest adding more meanders and flexures to the middle rod to retain the position of the outer rods. In order to miniaturize the width of the total instrument, the radius of the rolling joints would need to decrease, which is in practice limited by the minimum bending radius of the flexures. More research is necessary to determine this minimum radius. With the current lattice structure and SLM printer used in this study, we speculate that it is not possible to decrease the diameter more than 5 mm, unless the wall thickness of the lattices can be reduced further. Alternatively, the design can be adjusted so that only one half of the grasper is steerable, and the other half is stationary.

It should be noted that although titanium can withstand the temperature required for sterilization, in practice the rough porous surface is very challenging to sterilize, can potentially damage tissue, and risks leaving particles behind during the surgery. A solution for clinical implementation could be adding a flexible sleeve of a biocompatible material around the instrument.

9.5.3 Design process

Usually in a standard design process, first a design is drawn up, after which a specific production process is chosen and the design is adjusted to its specifications. However, in the case of AM, an incredible amount of design freedom can be obtained which can be difficult to comprehend for designers. In this study, we demonstrated a different approach towards designing for AM. We started with an analysis of the production method, in this case SLM, and attempted to expand its boundaries to generate a completely new design. Without a thorough analysis of the printer parameters, the non-assembly design that we have presented would not have been contrived, which is why this can be considered a 3D printer-driven design process. There are some caveats to this method, as the current design is adjusted to the conditions of one specific printer. The type of SLM printer that we used is in general suitable for large parts, but less suited for miniature work such as in this study. With a printer suitable for small parts, better results can be obtained, and more design directions can be explored. Nonetheless, the design process presented here shows the potential of designing at the limits of the production boundaries.

9.6 CONCLUSION

This study explored the feasibility of designing a non-assembly steerable surgical instrument using SLM printing. The rough surface finish of SLM printed parts poses challenges in creating functional non-assembly instruments, requiring extensive surface treatments. Therefore, we attempted to design a low-friction instrument that is not hindered by the rough surface finish of SLM. We explored the possibility of 3D printing compliant flexures with a lattice structure, to reduce the stiffness of the flexures and miniaturize the instrument. Various lattices with grid sizes ranging from 1 mm to 0.05 mm were successfully printed, and we succeeded in reducing the thickness of the flexures from 0.55 mm with regular print settings, to 0.26 mm with lattice design. The lattices were applied in the design of rolling joints with crossed, curved flexures in 10 mm, 7.5 mm, and 5 mm diameters. We showed that all lattice grid sizes were able to obtain a bending radius of at least 5 mm and that the larger grid sizes have lower bending stiffness than the smaller lattice sizes. The number of attachment points of the lattice to the joint body was found to be important, since this determines the fragility of the connection. For the 5 mm joints, this means that using a large lattice size to reduce the flexure stiffness often results in joint failure, due to the low number of attachment points. The pre-tensioning of the lattices in the rolling joints led to breakage of the lattices, therefore in the instrument design we explored the use of rolling joints with straight flexures that did not require pre-tensioning, and as such do not require assembly. The resulting steerable instrument is completely non-assembly, and specifically adjusted to the parameters of the SLM process. We showed the potential of the design through several prototypes, although the fragility of the lattices limited their longevity. Further research and development are needed to enhance the durability of lattice-based instruments for clinical applications.

9.7 REFERENCES

- [1] C. Culmone, G. Smit, P. Breedveld, Additive manufacturing of medical instruments: A state-of-the-art review, *Additive Manufacturing*. 27 (2019) 461–473. <https://doi.org/10.1016/j.addma.2019.03.015>.
- [2] P. Tack, J. Victor, P. Gemmel, L. Annemans, 3D-printing techniques in a medical setting: a systematic literature review, *BioMedical Engineering OnLine*. 15 (2016) 115. <https://doi.org/10.1186/s12938-016-0236-4>.
- [3] K. Lussenburg, A. Sakes, P. Breedveld, Design of non-assembly mechanisms: A state-of-the-art review, *Additive Manufacturing*. 39 (2021) 101846. <https://doi.org/10.1016/j.addma.2021.101846>.
- [4] L.F. Velásquez-García, Y. Kornbluth, Biomedical Applications of Metal 3D Printing, *Annual Review of Biomedical Engineering*. 23 (2021) 307–338. <https://doi.org/10.1146/annurev-bioeng-082020-032402>.
- [5] C.A. Seneci, Jianzhong Shang, A. Darzi, Guang-Zhong Yang, Rapid manufacturing with selective laser melting for robotic surgical tools: Design and process considerations, in: *2015 IEEE/RSJ International Conference on Intelligent Robots and Systems (IROS)*, IEEE, 2015: pp. 824–830. <https://doi.org/10.1109/IROS.2015.7353467>.
- [6] F.S.L. Bobbert, K. Lietaert, A.A. Eftekhari, B. Pouran, S.M. Ahmadi, H. Weinans, A.A. Zadpoor, Addi-

- tively manufactured metallic porous biomaterials based on minimal surfaces: A unique combination of topological, mechanical, and mass transport properties, *Acta Biomaterialia*. 53 (2017) 572-584. <https://doi.org/10.1016/j.actbio.2017.02.024>.
- [7] S.L. Sing, J. An, W.Y. Yeong, F.E. Wiria, Laser and electron-beam powder-bed additive manufacturing of metallic implants: A review on processes, materials and designs, *Journal of Orthopaedic Research*. 34 (2016) 369-385. <https://doi.org/10.1002/jor.23075>.
- [8] S. Nahata, O.B. Ozdoganlar, Feasibility of Metal Additive Manufacturing for Fabricating Custom Surgical Instrumentation for Hip and Knee Implants, *Procedia Manufacturing*. 34 (2019) 772-779. <https://doi.org/10.1016/j.promfg.2019.06.207>.
- [9] R. Singh, A. Suri, Three-Dimensional Printed Ergonomically Improved Microforceps for Microneurosurgery, *World Neurosurgery*. 141 (2020) e271-e277. <https://doi.org/10.1016/j.wneu.2020.05.105>.
- [10] R. Kontio, Designing and Additive Manufacturing A Prototype for A Novel Instrument for Mandible Fracture Reduction, *Surgery: Current Research*. 03 (2013) 2-4. <https://doi.org/10.4172/2161-1076.S1-002>.
- [11] S.M. Fuller, D.R. Butz, C.B. Vevang, M. V. Makhlof, Application of 3-Dimensional Printing in Hand Surgery for Production of a Novel Bone Reduction Clamp, *The Journal of Hand Surgery*. 39 (2014) 1840-1845. <https://doi.org/10.1016/j.jhsa.2014.06.009>.
- [12] A. Sakes, K. Hovland, G. Smit, J. Geraedts, P. Breedveld, Design of a Novel Three-Dimensional-Printed Two Degrees-of-Freedom Steerable Electrosurgical Grasper for Minimally Invasive Surgery, *Journal of Medical Devices*. 12 (2018) 011007. <https://doi.org/10.1115/1.4038561>.
- [13] C.A. Seneci, G. Gras, P. Wisanuvej, J. Shang, G.-Z. Yang, 3D printing of improved needle grasping instrument for flexible robotic surgery, in: 2017 IEEE/RSJ International Conference on Intelligent Robots and Systems (IROS), IEEE, 2017: pp. 2524-2530. <https://doi.org/10.1109/IROS.2017.8206072>.
- [14] Y. Hu, L. Zhang, W. Li, G.-Z. Yang, Design and Fabrication of a 3-D Printed Metallic Flexible Joint for Snake-Like Surgical Robot, *IEEE Robotics and Automation Letters*. 4 (2019) 1557-1563. <https://doi.org/10.1109/LRA.2019.2896475>.
- [15] S. Coemert, M.F. Traeger, E.C. Graf, T.C. Lueth, Suitability Evaluation of various Manufacturing Technologies for the Development of Surgical Snake-like Manipulators from Metals Based on Flexure Hinges, *Procedia CIRP*. 65 (2017) 1-6. <https://doi.org/10.1016/j.procir.2017.03.108>.
- [16] M. Hanief, M.F. Wani, Effect of surface roughness on wear rate during running-in of En31-steel: Model and experimental validation, *Materials Letters*. 176 (2016) 91-93. <https://doi.org/10.1016/j.matlet.2016.04.087>.
- [17] L. Löber, C. Flache, R. Petters, U. Kühn, J. Eckert, Comparison of different post processing technologies for SLM generated 316l steel parts, *Rapid Prototyp J*. 19 (2013) 173-179. <https://doi.org/10.1108/13552541311312166>.
- [18] K. Lussenburg, R. van Starckenburg, M. Bruins, A. Sakes, P. Breedveld, Polishing of metal 3D printed parts with complex geometry: Visualizing the influence on geometrical features using centrifugal disk finishing, *PLoS One*. 18 (2023) e0289730. <https://doi.org/10.1371/journal.pone.0289730>.
- [19] S. Bagehorn, J. Wehr, H.J. Maier, Application of mechanical surface finishing processes for roughness reduction and fatigue improvement of additively manufactured Ti-6Al-4V parts, *International Journal of Fatigue*. 102 (2017) 135-142. <https://doi.org/10.1016/j.ijfatigue.2017.05.008>.
- [20] C. Culmone, P.W.J. Henselmans, R.I.B. van Starckenburg, P. Breedveld, Exploring non-assembly

REFERENCES

- 3D printing for novel compliant surgical devices, *PLOS ONE*. 15 (2020) e0232952. <https://doi.org/10.1371/journal.pone.0232952>.
- [21] C. Culmone, K. Lussenburg, J. Alkemade, G. Smit, A. Sakes, P. Breedveld, A Fully 3D-Printed Steerable Instrument for Minimally Invasive Surgery, *Materials*. 14 (2021) 7910. <https://doi.org/10.3390/ma14247910>.
- [22] N.P. Castledine, J.H. Boyle, J. Kim, Design of a Modular Continuum Robot Segment for use in a General Purpose Manipulator, in: 2019 International Conference on Robotics and Automation (ICRA), IEEE, 2019: pp. 4430–4435. <https://doi.org/10.1109/ICRA.2019.8794249>.
- [23] B. V. Johnson, Z. Gong, B.A. Cole, D.J. Cappelleri, Design of Disposable 3D Printed Surgical End-Effectors for Robotic Lumbar Discectomy Procedures, in: Volume 5A: 42nd Mechanisms and Robotics Conference, American Society of Mechanical Engineers, 2018: p. V05AT07A055. <https://doi.org/10.1115/DETC2018-85257>.
- [24] D.B. Roppenecker, A. Pfaff, J.A. Coy, T.C. Lueth, Multi arm snake-like robot kinematics, in: 2013 IEEE/RSJ International Conference on Intelligent Robots and Systems, IEEE, 2013: pp. 5040–5045. <https://doi.org/10.1109/IROS.2013.6697085>.
- [25] S.N. Economidou, M.J. Uddin, M.J. Marques, D. Douroumis, W.T. Sow, H. Li, A. Reid, J.F.C. Windmill, A. Podoleanu, A novel 3D printed hollow microneedle microelectromechanical system for controlled, personalized transdermal drug delivery, *Additive Manufacturing*. 38 (2021) 101815. <https://doi.org/10.1016/j.addma.2020.101815>.
- [26] J. Jiang, X. Xu, J. Stringer, Support Structures for Additive Manufacturing: A Review, *Journal of Manufacturing and Materials Processing*. 2 (2018) 64. <https://doi.org/10.3390/jmmp2040064>.
- [27] F. Gutmann, M. Stilz, S. Patil, F. Fischer, K. Hoschke, G. Ganzenmüller, S. Hiermaier, Miniaturization of Non-Assembly Metallic Pin-Joints by LPBF-Based Additive Manufacturing as Perfect Pivots for Pantographic Metamaterials, *Materials*. 16 (2023) 1797. <https://doi.org/10.3390/ma16051797>.
- [28] J. Kranz, D. Herzog, C. Emmelmann, Design guidelines for laser additive manufacturing of light-weight structures in TiAl6V4, *Journal of Laser Applications*. 27 (2015) S14001. <https://doi.org/10.2351/1.4885235>.
- [29] Y. Liu, J. Zhang, Y. Yang, J. Li, J. Chen, Study on the influence of process parameters on the clearance feature in non-assembly mechanism manufactured by selective laser melting, *Journal of Manufacturing Processes*. 27 (2017) 98–107. <https://doi.org/10.1016/j.jmapro.2017.04.005>.
- [30] F. Calignano, D. Manfredi, E.P. Ambrosio, S. Biamino, M. Pavese, P. Fino, Direct Fabrication of Joints based on Direct Metal Laser Sintering in Aluminum and Titanium Alloys, *Procedia CIRP*. 21 (2014) 129–132. <https://doi.org/10.1016/j.procir.2014.03.155>.
- [31] M.A.A. Leeflang, F.S.L.S.L. Bobbert, A.A.A. Zadpoor, Additive manufacturing of non-assembly deployable mechanisms for the treatment of large bony defects, *Additive Manufacturing*. 46 (2021) 102194. <https://doi.org/10.1016/j.addma.2021.102194>.
- [32] A. Jeanneau, J. Herder, T. Laliberté, C. Gosselin, A Compliant Rolling Contact Joint and Its Application in a 3-DOF Planar Parallel Mechanism With Kinematic Analysis, in: Volume 2: 28th Biennial Mechanisms and Robotics Conference, Parts A and B, ASMEDC, 2004: pp. 689–698. <https://doi.org/10.1115/DETC2004-57264>.
- [33] P.A. Halverson, L.L. Howell, S.P. Magleby, Tension-based multi-stable compliant rolling-contact elements, *Mechanism and Machine Theory*. 45 (2010) 147–156. <https://doi.org/10.1016/j.mechmach>

- theory.2008.11.013.
- [34] J.W. Suh, K.Y. Kim, J.W. Jeong, J.J. Lee, Design Considerations for a Hyper-Redundant Pulleyless Rolling Joint with Elastic Fixtures, *IEEE/ASME Transactions on Mechatronics*. 20 (2015) 2841–2852. <https://doi.org/10.1109/TMECH.2015.2389228>.
 - [35] J.P. Kuntz, *Rolling Link Mechanisms*, 1995.
 - [36] D. Zhang, Y. Sun, T.C. Lueth, Design of a novel tendon-driven manipulator structure based on monolithic compliant rolling-contact joint for minimally invasive surgery, *International Journal of Computer Assisted Radiology and Surgery*. 16 (2021) 1615–1625. <https://doi.org/10.1007/s11548-021-02442-w>.
 - [37] Y. Sun, T.C. Lueth, Cruciate-Ligament-Inspired Compliant Joints: Application to 3D-Printed Continuum Surgical Robots, in: *2021 43rd Annual International Conference of the IEEE Engineering in Medicine & Biology Society (EMBC)*, IEEE, 2021: pp. 4645–4648. <https://doi.org/10.1109/EMBC46164.2021.9630239>.
 - [38] P. Berthet-Rayne, K. Leibrandt, K. Kim, C.A. Seneci, J. Shang, G.-Z. Yang, Rolling-Joint Design Optimization for Tendon Driven Snake-Like Surgical Robots, in: *2018 IEEE/RSJ International Conference on Intelligent Robots and Systems (IROS)*, IEEE, 2018: pp. 4964–4971. <https://doi.org/10.1109/IROS.2018.8593517>.
 - [39] Z. Wu, S.P. Narra, A. Rollett, Exploring the fabrication limits of thin-wall structures in a laser powder bed fusion process, *The International Journal of Advanced Manufacturing Technology*. 110 (2020) 191–207. <https://doi.org/10.1007/s00170-020-05827-4>.
 - [40] T. Maconachie, M. Leary, B. Lozanovski, X. Zhang, M. Qian, O. Faruque, M. Brandt, SLM lattice structures: Properties, performance, applications and challenges, *Materials and Design*. 183 (2019) 108137. <https://doi.org/10.1016/j.matdes.2019.108137>.
 - [41] E.G. Merriam, L.L. Howell, Lattice flexures: Geometries for stiffness reduction of blade flexures, *Precision Engineering*. 45 (2016) 160–167. <https://doi.org/10.1016/j.precisioneng.2016.02.007>.
 - [42] A. Jiansheng Pan, B. Jianwei Wu, C. Yin Zhang, D. Hui Wang, E. Jiubin Tan, Design and analyze of flexure hinges based on triply periodic minimal surface lattice, *Precision Engineering*. 68 (2021) 338–350. <https://doi.org/10.1016/j.precisioneng.2020.12.019>.
 - [43] J. Kruis, F. Cosandier, G. Perruchoud, L. Kiener, H. Saudan, 6 Design principles for SLM-based compliant mechanisms, in: *Joint Special Interest Group Meeting between Euspen and ASPE Advancing Precision in Additive Manufacturing*, European Society for Precision Engineering and Nanotechnology, 2019.
 - [44] Y. Zhang, J. Wu, J. Tan, Compliance Model and Structure Optimization Method Based on Genetic Algorithm for Flexure Hinge Based on X-Lattice Structure, *Complexity*. 2021 (2021) 1–14. <https://doi.org/10.1155/2021/8819422>.
 - [45] S.F. Hardon, F. Schilder, J. Bonjer, J. Dankelman, T. Horeman, A new modular mechanism that allows full detachability and cleaning of steerable laparoscopic instruments, *Surgical Endoscopy*. 33 (2019) 3484–3493. <https://doi.org/10.1007/s00464-019-06849-0>.
 - [46] G.J.M. Tuijthof, T. Horeman, Surgical Device, in *Particular for Minimally Invasive Surgery*, WO2014148898A1, 2014.
 - [47] H. Yamashita, A. Iimura, E. Aoki, T. Suzuki, T. Nakazawa, E. Kobayashi, M. Hashizume, I. Sakuma, T. Dohi, Development of endoscopic forceps manipulator using multi-slider linkage mechanisms, in:

REFERENCES

- The 1st Asian Symposium on Computer Aided Surgery, 2005: pp. 201-204. <https://doi.org/10.5759/jscas1999.7.127>.
- [48] J. Mueglitz, G. Kunad, P. Dautzenberg, B. Neisius, R. Trapp, Kinematic problems of manipulators for minimal invasive surgery, *Endoscopic Surgery and Allied Technologies*. 1 (1993) 160-4.
- [49] R. Wauthle, B. Vrancken, B. Beynaerts, K. Jorissen, J. Schrooten, J.-P. Kruth, J. Van Humbeeck, Effects of build orientation and heat treatment on the microstructure and mechanical properties of selective laser melted Ti6Al4V lattice structures, *Additive Manufacturing*. 5 (2015) 77-84. <https://doi.org/10.1016/j.addma.2014.12.008>.



Video of the steerability and opening and closing of the prototype (download).

10

DISCUSSION

10.1 MAIN FINDINGS

The goal of this thesis was to explore the contributions of non-assembly AM for the production of complex medical devices, by demonstrating that AM technology can be used to simplify the production chain. We developed a series of 3D printed prototypes for various medical applications that examine the implementation of non-assembly AM and its consequences for the design and production process. Here we summarize the main findings pertaining to the major research objectives that we identified in the introduction.

Part 1: To investigate the state-of-the-art and to identify the main challenges for implementation of non-assembly AM.

In Chapter 2 we investigated the state-of-the-art of non-assembly mechanisms and the design solutions used to 3D print them. A classification was proposed that divides current non-assembly mechanisms into those in which movement is based on geometrical design and those in which movement is based on material design. We identified a gap in research for non-assembly mechanisms consisting of geometry-based mechanisms and multiple materials. Inspiration for these kinds of mechanisms can be found in nature: for instance, joints in the human body combine rigid, separate bones with flexible tendons.

One of the challenges that was identified for non-assembly AM is that standard components, which ordinarily can be bought off-the-shelf, need to be redesigned to work with the constraints of the AM technology and materials. This can be a difficult and time-consuming endeavour. In Chapter 3, we investigated the state-of-the-art of 3D printed springs. Although AM offers new opportunities for the design of springs, the lack of knowledge on exact properties of AM materials makes it difficult to theoretically model spring designs. AM springs currently rely on trial-and-error practical experiments, which makes it fairly time-consuming to obtain the required properties. To apply AM springs in non-assembly mechanisms, a separate spring design process with respect to the print settings is often required.

Another challenge identified in Chapter 2, is that non-assembly mechanisms, due to their interconnected structure, offer little room for post-processing operations such as surface finishing techniques. This is especially relevant for metal AM technologies, which suffer from a rough surface quality. In Chapter 4, we explored a method of visualizing polishing patterns on AM metal parts with complex features, where a visual pattern on the surface of the part was used to indicate which surfaces were targeted by the process. This visualization method gave insight into whether a polishing method was effective on all surfaces, to help establish design guidelines for common post-processing techniques to design more effective non-assembly mechanisms.

Part 2: To develop 3D printed prototypes of novel medical devices that demonstrate that the free complexity offered by AM can be used to simplify the production chain, while at the same time advancing design opportunities for medical devices.

One of the challenges of AM is the limited manufacturing accuracy and resolution. In Chapter 5, we attempted to 3D print a miniature trocar for eye surgery, with sub-millim-

eter scale features, which is on the limits of the resolution of SLA technology. We found it was not possible to 3D print the existing design of the trocar, due to the difficulty of creating a hollow tube in that size range. Based on an analysis of the working principle of SLA, we changed the design of the trocar cannula from a straight tube to a helical structure and printed the valve in opened - rather than closed - position. With this solution, we showed that it was possible to create a functional trocar by optimizing the design and production process for the chosen AM technology.

Chapter 6 presented the design of a minimum assembly AM steerable, laparoscopic instrument, called 3D-GriP. The instrument has a pistol-grip handle with a compliant end-effector actuated by cables allowing omnidirectional steering and consists of only five separate 3D printed parts. Further integration of parts was not possible, since the control mechanism of the joystick for steering required pre-tensioning of a spring, which had to be produced from a different material to obtain the required properties. Compliant joints and snap-fit connectors were used to simplify the assembly process, thereby increasing part complexity to simplify production. This instrument was designed to exploit the advantages of AM by enabling rapid assembly for the production of small-scale manufacturing of patient-, surgeon- or procedure specific instrumentation. Further exploring non-assembly steerable instruments, Chapter 7 presented the design of a miniature steerable light pipe, which was printed in a single production step. Only one cable was required for its actuation, for which the optical fiber was used, bringing the effective part count of this complex instrument to two. The design of Acci is an example of how exploring the boundaries of AM can lead towards a new innovative design for a specific application.

In Chapter 8, the design of a non-assembly vitrectome handle mechanism was explored. A vitrectome is used in eye surgery to remove vitreous from the body of the eye, and has to adhere to high-precision requirements. The new design, consisting of a dual diaphragm mechanism, was produced using multimaterial 3D printing and tested for its mechanical properties, such as the force provided by the diaphragms, and the frequency of the mechanism. Rather than relying on standard components, such as O-rings, each part of the multimaterial mechanism had to be specifically designed and tested for its function. The simplicity of the non-assembly design was complicated by the need for support material, which cannot be removed from an enclosed chamber. Therefore, the chamber was divided into two parts to facilitate the removal of the support material. A screw connection was introduced to simplify assembly afterwards and ensure correct positioning of the parts. The design process of the vitrectome illustrates that support can form a challenge when designing non-assembly mechanisms, which can be solved by designing smart assembly solutions to still minimize assembly time and effort.

Whereas the 3D-GriP in Chapter 6 still required actuation cables to be inserted after printing, Chapter 9 presented a completely non-assembly laparoscopic instrument, including its actuation system, 3D printed in titanium. In contrast to the resin used to print the 3D-GriP, titanium is a medically approved and biocompatible material. The instrument has a scissor-handle and is actuated by means of rigid rods, enabling planar steering in two directions. In order to circumvent the problems with surface finishing techniques

for metal non-assembly mechanisms, the design was made without sliding surfaces, which increase friction and can hinder the working of the mechanism, to prevent the need for post-processing. As such, the design relies on rolling joints with compliant flexures, which were 3D printed using a lattice structure to provide them with the necessary flexibility and the ability to produce them on a sub-millimeter-scale. This instrument showed a novel approach towards the design process, in which the instrument design was created specifically for the chosen AM process by thoroughly exploring its production limits.

General contribution

This thesis shows that non-assembly additive manufacturing can contribute to a new generation of medical devices, where the design freedom of AM can be leveraged to enhance the functionalities without being limited by assembly requirements. The use of AM paves the way for surgeon- and patient specific devices, which can be produced on-demand without requiring extensive production and assembly facilities and can therefore contribute to localized manufacturing.

10.2 LIMITATIONS OF THE RESEARCH

For some of the designs presented in this thesis, such as the metal grasper (Chapter 9) and the trocars (Chapter 4), it was not possible to produce them on a scale that is realistic for their surgical application area. The possibility of using non-assembly design comes with an increased complexity for the components of the design, which, given fixed dimensions for the instrument, means that features should be increasingly small and produced with a high resolution. Unfortunately, most currently available 3D printers are not capable of 3D printing on such a small scale with a high resolution. Although for some AM technologies, such as SLA and SLM, the reported resolution for feature sizes should theoretically be sufficient to produce surgical instruments on an appropriate scale, in practice there are many limitations that hinder functional implementation. For instance, the resolution is not valid for all types of geometrical features, such as ‘negative features’ like holes and channels, and material properties play a role as well, such as a lack of stiffness in the case of polymers or a too high stiffness in the case of titanium.

Although one of the advantages of non-assembly is a reduced assembly time, this does not automatically lead to a decrease in total production time. In some cases, non-assembly designs require additional post-processing steps, depending on the used AM technology, such as removal of support material (Chapter 8), surface finishing techniques (Chapter 3), or cleaning of uncured resin out of cable channels (Chapter 6). Currently there are no studies that offer a direct comparison of non-assembly with traditional assembly methods in terms of total production time. One of the problems with such a study is that often non-assembly designs, such as the ones presented here, are radically different from their traditional-assembly counterparts and, therefore, cannot be used for a direct comparison. In addition, these designs are one-off prototypes, of which the manufacturing process has not been optimized, therefore it is unfeasible to compare them to mass-man-

ufactured products. Therefore, an interesting direction would be to study the difference in production time for a 3D printed medical device which requires traditional assembly, as compared to a non-assembly design. Such a study could give more insight into whether the advantages of non-assembly outweigh any complications in the additional post-processing steps.

10.3 DESIGN FOR NON-ASSEMBLY

This thesis covered a broad range of AM-related explorations, ranging from polishing tests to designs for miniature surgical instruments. Their common ground is their relevance to the design of non-assembly devices, which is still a relatively unexplored area of AM. We can summarize the explorations of this thesis towards design for non-assembly in two themes: smart assembly and 3D printer-driven design.

10.3.1 Smart assembly

One of the practical limitations of non-assembly design is that the more components a device has, the more challenging it becomes to make it non-assembly. Each component has certain (functional) requirements and connections to other components, but also has to conform to the choice of AM process, build direction, support placement, etc. Therefore, not all components can be printed with optimum settings for their functionality. In addition, in the absence of assembly, the space for unavoidable post-processing, such as removing of support structures, cleaning of unprocessed material, or polishing of rough surfaces, is limited, and the difficulty of performing the post-processing steps can inadvertently lead to an increase in total production time. In those cases the advantage of non-assembly is offset by the drawback of post-processing.

Strictly speaking, a non-assembly device is one that requires no assembly step whatsoever, no matter the number of components and its technical capabilities. This is easy for relatively simple devices, such as a forceps, but becomes much more challenging with complex devices, especially when for instance force sensors or electrical circuits are included. This requires 3D printers with the capability to combine a huge amount of materials and production techniques. More realistic is the use of embedded 3D printing, in which separately produced components are embedded into the part during 3D printing [1]. This requires devices to be designed in such a way that there is space for the components, and that they can be placed into the part during production.

The above points illustrate that for complex devices, rather than eliminating assembly altogether, the focus should be on creating ‘smart’ assembly solutions, with the goal of reducing the overall production time and simplifying the production process, including printing, assembly and post-processing, as compared to conventional manufacturing [2]. We have given several examples of smart assembly in this thesis, such as the inclusion of the screw thread in the vitrectome mechanism (Chapter 8) to facilitate removing of support material, and the snap fit connectors in the joystick of the 3D-GriP (Chapter 6) to facilitate tensioning of the spring and the inclusion of an embedded part.

10.3.2 3D printer-driven design

Designing non-assembly devices requires re-thinking the way products are traditionally designed and manufactured, to fully utilize the geometrical complexity enabled by AM. As such, the choice for the AM process has to be taken into account early on in design process, since this determines the available material and geometrical options. To utilize the opportunities of AM to their full extent, a thorough understanding of the AM process is necessary, to navigate its boundaries. In this thesis we have demonstrated a specific way of designing in which the boundaries of the 3D printer determine the final design and, to a certain extent, function. The free geometrical complexity of AM is leveraged to overcome some of the limitations of AM technology. For example, the lattice structures designed in Chapter 9 can be used to create thinner features than what can be created with regular print settings. Similarly, the helical structures in Chapter 5 allowed us to create tiny hollow tubes that could not be produced in a different way (Figure 10.1). Additionally, the design of the steerable light pipe presented in Chapter 7 arose because of the ability to 3D print a helical structure of that size. This can be considered 3D printer-driven design: the output of the printer determines the final shape, hence the design has to be adapted to the printer that will be used. With the immense design space provided by 3D printing, it can be impossible to fully utilize or consider all design possibilities. Without ways to limit the design space, it is all too easy to revert back to traditional designs. 3D printer-driven design is a way to decrease the design space in order to make it manageable for the designer and printable for the printer. Once the absolute limits of the printer are known, it is possible to start advancing the boundaries of the design. The design steps that were followed for the designs in this thesis can be globally formulated in the following design guidelines (Figure 10.2):

1. Choosing the AM process, and gaining a thorough understanding of its specifications [3]. This includes theoretical knowledge about the working principle of the AM process, as well as practical knowledge about design guidelines, and test prints to find a baseline for the printer's capabilities.
2. Exploring available material, geometry, and process parameters. For materials, this includes their mechanical properties, such as stiffness, hardness, tendency to

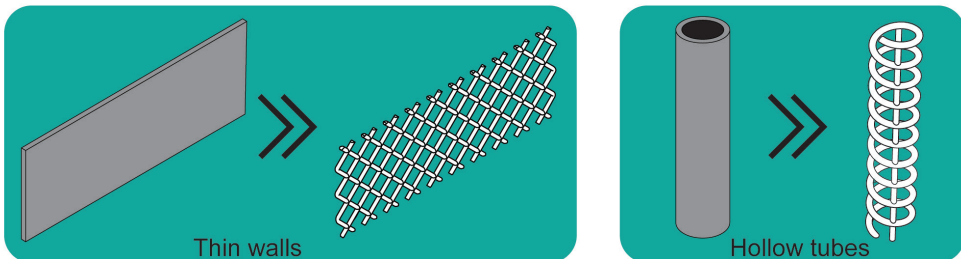


Figure 10.1: Examples of design solutions used in this thesis to overcome AM production limitations for thin walls and hollow tubes by increasing the geometrical complexity.

warp. For geometry, this includes accuracy, dimensional tolerances, and minimum feature size. For process parameters, this includes build orientation, layer thickness, support structures. This can be done systematically by printing specific test parts relevant to the design.

3. Applying AM specific solutions to the design. For instance, by utilizing the geometrical complexity offered by AM for small features, such as thin walls, and to consolidate components wherever possible, into one complex rigid part or by using flexures to connect moving parts. The design guidelines of the AM process should be used to choose the optimum build direction and to redesign components in such a way that they do not require support, or only the minimum amount of support that can easily be removed.
4. Evaluating which parts or features of the design pose challenges, for instance with regards to the build direction or support removal. Applying smart assembly solutions to reduce production time or circumvent production problems when appropriate, and adjusting accordingly. This is an iterative process repeated as often as necessary.

10.4 FUTURE OUTLOOK

10.4.1 Technological developments and materials

In recent years there has been an exponential increase in new and innovative AM technologies, including technologies capable of producing micro- or nanoscale parts. However, the production of medical devices requires the ability to both produce macro-scale parts, such as the handle of instruments, as well as micro-scale parts, such as the tip of forceps used in eye surgery. So far, there are little AM processes that are able to produce micro-scale features on a macroscale part [4]. One of the challenges for this is the printing speed for micro-parts: in order to obtain a high-accuracy part, the layer height and voxel-size need to be incredibly small [4,5], resulting in long printing times, even for small objects [6]. For larger objects with miniature details, the printing time may become unacceptably long. One solution is to improve slicing algorithms, making it possible to indicate a ‘low accuracy’ section, such as in the internal part of the object, and a ‘high accuracy’ section, such as at the outer edges or at the location of high-accuracy details [7]. Hybrid processes are another solution, in which for instance AM processes on a macro-scale are combined

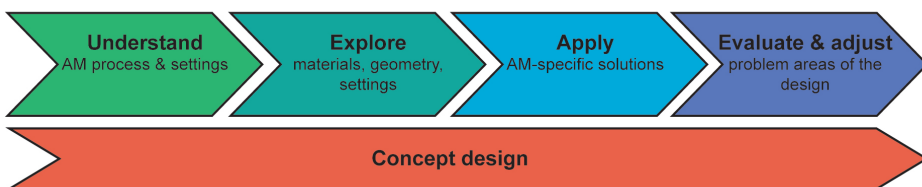


Figure 10.2: Global steps of a 3D printer-driven design process.

with micro-scale processes to obtain the desired geometry and accuracy [8,9], or in which 3D printing is combined with a shrinkage technique to miniaturize the parts [10]. Further developments in the technology of both hybrid AM technologies as well as software improvements are expected to make strides for the production of macro-scale parts with micro-scale features and high accuracy.

Medical devices can contain a large number of different parts, among which standardized mechanical components, such as springs, bearings, and sliders. Producing these mechanical components as non-assembly mechanisms requires redesigning for AM and thoroughly testing in order to know their exact mechanical properties. The freedom of complexity of AM complicates this, since there are a large number of AM parameters that can influence the 3D printed part. In some cases, it may not be possible to produce entire medical devices using one AM process, due to limitations in material or build manner that require compromises in functionality. AM technologies capable of 3D printing multiple materials are being developed, for instance in order to 3D print composite materials [11,12]. One example of this that is currently on the market is the 3D printer released by Markforged, capable of 3D printing a polymer using material extrusion, and depositing fibres cut to size to reinforce the part. Such technology could also be used to integrate cables for actuation in steerable surgical instruments in one single printing step. Multiple material printing with two or more AM materials is currently limited to Polyjet and material extrusion, however these techniques only allow for combining polymers. True multi-material printing with a combination of metals and polymers could benefit non-assembly mechanisms, for instance the ability to integrate springs with certain spring constant or elastomeric grippers for soft tissue [13]. Besides from developing AM machines able to handle these radically different materials, one area that still requires attention is the interface between the different materials to ensure proper attachment [14].

Biocompatibility of polymer materials used in AM is also a huge concern. In Chapters 5 and 6, we utilized stereolithography, which uses liquid resins, for the production of trocars and an omnidirectional gripper. For the trocars, we made use of a biocompatible resin, which has been approved by the FDA for use in dental applications. However, even for approved biocompatible resins, there are still concerns of toxicity due to leaching of compounds [15]. Although the used biocompatible resin has a very good dimensional accuracy, it is too brittle for use in compliant applications. Therefore, for the 3D-GriP prototype in Chapter 6 we used a non-biocompatible resin, which has a high-elongation at break, making it suitable for compliant applications. The recent interest to use AM for functional medical devices has pushed the development of biocompatible resins with advanced engineering properties, and therefore a larger range of non-toxic polymer materials is expected in the near future.

10.4.2 Towards clinical use

Crucial for the use of AM in medical scenarios is the ability to sterilize the devices. Common sterilization methods for medical instruments are for instance autoclave, gamma radiation, UV sterilization, and ethylene oxide gas [16]. Not all of these techniques are

suitable for 3D printed instruments, due to possible changes in material properties under certain temperatures or conditions [17]. So far, only few studies have investigated the effect of common sterilization methods on AM materials, specifically polymers, and more research is required to gain a full understanding of the risks and possibilities [17]. There is less concern for the influence of sterilization on AM metals, since they can withstand high temperatures. However, for 3D printed metals the rough and porous surface finish hinders sterilization, since dirt and particles can accumulate there. Polishing the surface can improve the sterilizability, although as we have seen in Chapter 4, for geometrically complex parts or non-assembly mechanisms, not all surfaces are within reach of polishing methods.

A possible solution is to consider disposable use, so that the device only needs to be used once, and only requires one sterilization cycle. In that case, sterilization could be integrated into the production process itself, since many AM processes already make use of high temperature, as is the case for FDM technology, or UV light, as is the case for vat photopolymerization [18]. The process could then be considered ‘self-sterilizing’, when care is taken that fabrication occurs in a closed, sterilized environment. This will help facilitate local production of medical devices, for instance in a specialized department in the hospital itself, or for low-income countries, provided the equipment is low cost. The use of non-assembly mechanisms can contribute to simple and quick manufacturing, as it does not require specialists or additional production facilities for assembly.

One of the benefits of using AM for the production of medical devices is the ability to create one-off personalized products. For instance, the handle of the 3D-GriP presented in Chapter 6 was designed to be personalized for the surgeon by means of the parametric CAD model. An interesting step forward would be to further develop the parametric CAD model, so that it can be personalized by means of hand measurements. Other designs presented in this thesis, such as the vitrectome (Chapter 8) and the metal grasper (Chapter 9), could benefit from the same approach, as they also have the potential of customisation for hand sizes or preferences of the surgeon. In some cases personalization for the patient can be achieved as well, for instance the trocars in Chapter 5 can be adjusted in length depending on the thickness of the sclera to ensure a safe operation.

10.4.3 Future of non-assembly medical devices

In Chapter 2, we proposed a classification of non-assembly mechanisms divided into multi-body, mono-body, mono-material, multi-material, and pattern-based mechanisms. Multi-body mechanisms closest resemble conventional assemblies, in which mechanisms consist of separate parts. Multi-material mechanisms, such as the vitrectome in Chapter 8, are capable of leveraging most advantages of AM as compared to traditional manufacturing, and as a consequence require a completely different design approach. Pattern-based mechanisms have been developed the least, and show the most innovative approach towards mechanisms. Their design is comparable to the design of metamaterials, in which geometrical structure and material are closely integrated. Technological advances in AM processes in terms of resolution and multi-material options offer many possibilities to

create pattern-based mechanisms on a smaller scale with ever-increasing functionality. This can lead to a fusion between designed mechanisms and metamaterials, where we envision mechanisms so intertwined with the materials they are made of that they become indistinguishable from each other. For medical devices, this would mean an unprecedented amount of functionality that can be added to simple materials. The best use for this type of mechanism was already described by Richard Feynman in 1959:

“A friend of mine (Albert R. Hibbs) suggests a very interesting possibility for relatively small machines. He says that, although it is a very wild idea, it would be interesting in surgery if you could swallow the surgeon. You put the mechanical surgeon inside the blood vessel and it goes into the heart and “looks” around. (Of course the information has to be fed out.) It finds out which valve is the faulty one and takes a little knife and slices it out.” [19]

This picture was painted more than 60 years ago, yet this still remains a futuristic prospect. However, we are slowly getting closer to making this a reality. Examples are a capsule that can be swallowed to take a biopsy in the intestinal tract [20], microrobots that can manoeuvre in the eye in the presence of a magnetic field [21], or drug-delivering microrobots that travel in the vascular network [22]. These ‘microsurgeons’ are mostly still limited to performing one single task, so there are still steps to be taken to integrate multiple tasks into one single robot, or alternatively, to have a whole clinical ‘team’ of robots that can all perform one of the necessary tasks. Non-assembly AM can play an important role here for the development of such highly integrated, multi-functional devices.

REFERENCES

- [1] K. De Laurentis, C. Mavroidis, F.F. Kong, Rapid Robot Reproduction, IEEE Robotics & Automation Magazine. (2004) 86–92.
- [2] E.H. Childs, A. V. Latchman, A.C. Lamont, J.D. Hubbard, R.D. Sochol, Additive Assembly for Poly-Jet-Based Multi-Material 3D Printed Microfluidics, Journal of Microelectromechanical Systems. 29 (2020) 1094–1096. <https://doi.org/10.1109/JMEMS.2020.3003858>.
- [3] C.A. Seneci, Jianzhong Shang, A. Darzi, Guang-Zhong Yang, Rapid manufacturing with selective laser melting for robotic surgical tools: Design and process considerations, in: 2015 IEEE/RSJ International Conference on Intelligent Robots and Systems (IROS), IEEE, 2015: pp. 824–830. <https://doi.org/10.1109/IROS.2015.7353467>.
- [4] R. He, J. Landowne, J. Currie, J. Amoah, W. Shi, D. Yunus, Y. Liu, Three-dimensional printing of large objects with high resolution by scanning lithography, The International Journal of Advanced Manufacturing Technology. (2019). <https://doi.org/10.1007/s00170-019-03862-4>.
- [5] E. Dely, N. Liverman, T. Fregin, L. Haugabrook, C. Moore, 3D micro-mirror lithography for mass production, in: E.M. Panning, M.I. Sanchez (Eds.), Novel Patterning Technologies 2018, SPIE, 2018: p. 32. <https://doi.org/10.1117/12.2300951>.
- [6] S. Hengsbach, A.D. Lantada, Rapid prototyping of multi-scale biomedical microdevices by combining additive manufacturing technologies, Biomedical Microdevices. 16 (2014) 617–627. <https://doi.org/10.1186/1547-2615-16-617>.

REFERENCES

- org/10.1007/s10544-014-9864-2.
- [7] Y. Li, H. Mao, P. Hu, M. Hermes, H. Lim, J. Yoon, M. Luhan, Y. Chen, W. Wu, Bioinspired Functional Surfaces Enabled by Multiscale Stereolithography, *Advanced Materials Technologies*. 4 (2019) 1800638. <https://doi.org/10.1002/admt.201800638>.
- [8] M. Malinauskas, L. Lukoševičius, D. Mackevičit, E. Balčinas, S. Rekštyt, D. Paipulas, Multiscale 3D manufacturing: combining thermal extrusion printing with additive and subtractive direct laser writing, in: J.I. Mackenzie, H. Jelínková, T. Taira, M. Abdou Ahmed (Eds.), *Laser Sources and Applications II*, SPIE, 2014: p. 91350T. <https://doi.org/10.1117/12.2051520>.
- [9] S. Dehaeck, M. Cavaiani, A. Chafai, Y. Tourtit, Y. Vitry, P. Lambert, Hybrid Two-Scale Fabrication of Sub-Millimetric Capillary Grippers, *Micromachines*. 10 (2019) 224. <https://doi.org/10.3390/mi10040224>.
- [10] M. Ochoa, J. Zhou, R. Rahimi, V. Badwaik, D. Thompson, B. Ziaie, Rapid 3D-print-and-shrink fabrication of biodegradable microneedles with complex geometries, in: 2015 Transducers - 2015 18th International Conference on Solid-State Sensors, Actuators and Microsystems (TRANSDUCERS), IEEE, 2015: pp. 1251-1254. <https://doi.org/10.1109/TRANSDUCERS.2015.7181157>.
- [11] Y. Pan, A. Patil, P. Guo, C. Zhou, A novel projection based electro-stereolithography (PES) process for production of 3D polymer-particle composite objects, *Rapid Prototyping Journal*. 23 (2017) 236-245. <https://doi.org/10.1108/RPJ-02-2016-0030>.
- [12] C.C. Spackman, K.C. Picha, G.J. Gross, J.F. Nowak, P.J. Smith, J. Zheng, J. Samuel, S. Mishra, A Novel Multi-material Additive Manufacturing Technique for Fabricating Laminated Polymer Nanocomposite Structures, *Journal of Micro and Nano-Manufacturing*. 3 (2015). <https://doi.org/10.1115/1.4029263>.
- [13] P. van Assenbergh, C. Culmone, P. Breedveld, D. Dodou, Implementation of anisotropic soft pads in a surgical gripper for secure and gentle grip on vulnerable tissues, *Proceedings of the Institution of Mechanical Engineers, Part H: Journal of Engineering in Medicine*. 235 (2021) 255-263. <https://doi.org/10.1177/0954411920971400>.
- [14] M.J. Mirzaali, M. Cruz Saldivar, A. Herranz de la Nava, D. Gunashekar, M. Nouri-Goushki, E.L. Doubrovski, A.A. Zadpoor, Multi-Material 3D Printing of Functionally Graded Hierarchical Soft-Hard Composites, *Advanced Engineering Materials*. 22 (2020) 1901142. <https://doi.org/10.1002/adem.201901142>.
- [15] M. Carve, D. Wlodkowic, 3D-Printed Chips: Compatibility of Additive Manufacturing Photopolymeric Substrata with Biological Applications, *Micromachines*. 9 (2018) 91. <https://doi.org/10.3390/mi9020091>.
- [16] W.A. Rutala, D.J. Weber, *Guideline for Disinfection and Sterilization in Healthcare Facilities*, 2008, 2008.
- [17] R. Told, Z. Ujfalusi, A. Pentek, M. Kerenyi, K. Banfai, A. Vizi, P. Szabo, S. Melegh, J. Bovari-Biri, J.E. Pongracz, P. Maroti, A state-of-the-art guide to the sterilization of thermoplastic polymers and resin materials used in the additive manufacturing of medical devices, *Materials & Design*. 223 (2022) 111119. <https://doi.org/10.1016/j.matdes.2022.111119>.
- [18] T.M. Rankin, N.A. Giovinco, D.J. Cucher, G. Watts, B. Hurwitz, D.G. Armstrong, Three-dimensional printing surgical instruments: are we there yet?, *Journal of Surgical Research*. 189 (2014) 193-197. <https://doi.org/10.1016/j.jss.2014.02.020>.
- [19] R.P. Feynman, Plenty of Room at the Bottom, *Engineering and Science*. 23 (1960) 22-36.

- [20] M. Ben Salem, G. Aiche, L. Rubbert, P. Renaud, Y. Haddab, Design of a Microbiota Sampling Capsule using 3D-Printed Bistable Mechanism, in: 2018 40th Annual International Conference of the IEEE Engineering in Medicine and Biology Society (EMBC), IEEE, 2018: pp. 4868-4871. <https://doi.org/10.1109/EMBC.2018.8513141>.
- [21] O. Ergeneman, C. Bergeles, M.P. Kummer, J.J. Abbott, B.J. Nelson, Wireless Intraocular Microrobots: Opportunities and Challenges, in: Surgical Robotics, Springer US, Boston, MA, 2011: pp. 271-311. https://doi.org/10.1007/978-1-4419-1126-1_13.
- [22] C. Xin, D. Jin, Y. Hu, L. Yang, R. Li, L. Wang, Z. Ren, D. Wang, S. Ji, K. Hu, D. Pan, H. Wu, W. Zhu, Z. Shen, Y. Wang, J. Li, L. Zhang, D. Wu, J. Chu, Environmentally Adaptive Shape-Morphing Microrobots for Localized Cancer Cell Treatment, ACS Nano. 15 (2021) 18048-18059. <https://doi.org/10.1021/acsnano.1c06651>.

ACKNOWLEDGEMENTS

At the end of this thesis, I would like to thank all the people without whom this work would not have existed. I want to start by thanking my supervisors, Paul and Aimée, for their mentorship and guidance. Paul, thank you for convincing me to work on this PhD project, even though that wasn't my plan when I first stepped into your office. I've had a great time working in the BITE group and in such an inspiring environment as the BME department. I'm grateful that you and Aimée were available when I needed you, but also allowed me to find my own path in this project.

I want to thank everyone from the 3D MED consortium, for the nice collaborations and the inspiring talks. Thanks to Marta and Mart for working with me on part of this project, I really enjoyed our collaboration. I'm grateful for all our brainstorming and your help setting up tests, without which some of the projects in this thesis would never have succeeded.

A big thanks to my colleagues at DEMO, Remi and David. Remi, without you many of my prototypes would never have succeeded, thanks for your tireless work and your willingness to always push 3D printers to their limits, even if they explode. David, I've enjoyed all our chats about whatever tiny project you were working on, and of course your tips for our home renovations. It's been a pleasure working with you both!

I am very lucky that I had the possibility of performing my work in such a great department as BME. Thanks to all the staff in this department for making everything run smoothly. Thanks to Angélique, Marjolein, Sabrina, and Amanda of the secretary for always being there for support and for the fun chats.

It is almost impossible to walk around the first or third floor corridor without having a nice conversation with someone. I want to thank all colleagues, past and present, who made this department feel so welcoming: Helda, Mahdiyeh, Mahya, Pedro, Shahram, Michelle, Sander, Mohammed, Nazli, Eline, Khashayar, Monika, Dirk, Maria, Ebrahim, Lenart, Edwin, Gerwin, Nazli, Ingmar, Sebastien, Jelle, Nianlei, Bob, Jinlai, Sara, Vahid, Marit, Martijn, Suzanne, Teddy, Ludovica, Sara, Federica, Christoph, and everyone I may be forgetting. Françoise, thanks for making me feel included from the very start of my PhD. Jiahui, you are hilarious, I thoroughly enjoyed all our funny conversations and teaching you English words that should never be repeated. Thanks for all the laughs and orange juices. Costanza, I remember laughing with you from the day I started my PhD, I have so many fond memories of working with you. You truly gave colour to this department: I still listen for running footsteps along the corridor and seeing a yellow rain jacket will always remind me of you.

Special thanks to a special place: the Fish tank. Pier, Mauricio, Katerina, Judith, Jon, Anneke, and Chunfeng, thanks for always providing a place where work is optional and

ACKNOWLEDGEMENTS

fun is obligatory. Your office truly was a safe haven during Covid times, and I cherish all the dinners, drinks, and birthdays we celebrated. Thanks for always being there when a distraction is needed.

To my office mates, Merle, Jette, Vera, Esther, Mostafa, Fabian, and Karin, thank you for creating such a great place to work in, without you it would have been much less enticing to come in to the office. I have really enjoyed our work discussions, brainstorming, lunches, and coffee breaks. Merle, it's always a pleasure to hang out with you, and you certainly are no joke to me. Jette, thanks for always looking out for everyone in our office, you are a force of nature. Fabian, I've really enjoyed our bonding experiences over 3D printer failures and discussing nerdy slicer tips. Esther, thanks for always offering a listening ear when it's needed. Mostafa, you are a great supporter and always reminding us to be proud of our work. Vera, you make every conversation fun and it's always great to laugh about silly things with you.

Good friends make everything better and I am lucky to have been able to share this experience with some of my best friends. Niko, thanks for all the coffee, talks, lunches, and dinners. I would never have enjoyed my time here as much without you. I'm sure you will amount to great things, you are a true paper writing-machine, and I look forward to the day I can call you Professor Niko. Janna, thank you for always being just a phone call away, and always being my biggest supporter. I am so proud of you for pursuing your own PhD dream, even if it is parttime. No one deserves it more than you! Kim and Linda, we have been friends since the very start of our TU journey and even being partly in different countries hasn't changed that. I cherish our real life and digital hang outs, and I hope we'll have that for many years to come. Even if the times are hard, I know I can count on you. Truus and Janine, some things never change and one of them is our friendship. Thanks for all the unforgettable moments, I can't wait until we are old and grey and still ending up in strange adventures together.

Last but not least I would like to thank my family, pap, mam, Steven, and Sigrid, thank you for your support, for listening and understanding, and always having my back. Finally, I want to thank the two most important people in my life. Kleine muis, er is niets wat mijn dag beter maakt dan het zien van jouw glimlach. Iedere dag met jou is een avontuur. Jaap, jouw invloed op mijn leven valt niet in woorden uit te drukken. Bedankt dat je mijn partner bent, dat je me hebt gepusht om deze PhD aan te nemen, voor het zijn van mijn sparringpartner, voor de technische bijlessen, voor het altijd luisteren en advies geven, voor altijd aan mijn kant staan, en voor alle dingen die je doet die ik ben vergeten. Ik weet niet hoe ik het zonder jou had kunnen doen.

CURRICULUM VITAE

Kirsten Marie-Anne Lussenburg, born 31-05-1989 in Utrecht, The Netherlands.

Employment

- Sep. 2023 - Present **Postdoctoral researcher**
Biomechanical Engineering & Cognitive Robotics, TU Delft, Delft
- Jan. 2019 - Sep. 2023 **PhD researcher**
Biomechanical Engineering, TU Delft, Delft
- May 2015 - Jan. 2019 **Industrial design engineer / project leader**
Pharmafilter B.V., Amsterdam
- Apr. 2012 - Feb. 2014 **Curator**
Material Library 'Made Of..', TU Delft, Delft
- Sep. 2013 - Nov. 2013 Design intern
Sustainable Design Agency Ideal&Co, Amsterdam

Education

- Sep. 2011 - Sep. 2014 **Master Integrated Product Design,**
Faculty of Industrial Design Engineering, TU Delft, Delft
- Sep. 2007 - Jun. 2011 **Bachelor Industrial Design Engineering**
TU Delft, Delft
- Sep. 2001 - Aug. 2007 **Gymnasium Bèta**
CSG Vincent van Gogh, Assen

LIST OF PUBLICATIONS

Publications part of this thesis

- K. Lussenburg, P. Breedveld, A. Sakes, Development of a Novel 3D-Printed Steerable Light Pipe for Eye Surgery, submitted (2023).
- K. Lussenburg, R. van Starckenburg, A. Sakes, P. Breedveld, 3D printer-driven design of a non-assembly titanium surgical instrument using compliant lattice flexures, *Materials & Design* 240 (2024). <https://doi.org/10.1016/j.matdes.2024.112845>.
- K. Lussenburg, R. van Starckenburg, M. Bruins, A. Sakes, P. Breedveld, Polishing of metal 3D printed parts with complex geometry: Visualizing the influence on geometrical features using centrifugal disk finishing, *PLoS One*. 18 (2023) e0289730. <https://doi.org/10.1371/journal.pone.0289730>.
- K. Lussenburg, M. Scali, M. Stolk, D. Robijns, A. Sakes, P. Breedveld, Exploring High-Precision Non-Assembly Mechanisms: Design of a Vitrectome Mechanism for Eye Surgery, *Materials*. 16 (2023) 1772. <https://doi.org/10.3390/ma16051772>.
- K. Lussenburg, M. Scali, A. Sakes, P. Breedveld, Additive Manufacturing of a Miniature Functional Trocar for Eye Surgery, *Front Med Technol*. 4 (2022). <https://doi.org/10.3389/fmedt.2022.842958>.
- C. Culmone, K. Lussenburg, J. Alkemade, G. Smit, A. Sakes, P. Breedveld, A Fully 3D-Printed Steerable Instrument for Minimally Invasive Surgery, *Materials*. 14 (2021) 7910. <https://doi.org/10.3390/ma14247910>.
- K. Lussenburg, A. Sakes, P. Breedveld, Design of non-assembly mechanisms: A state-of-the-art review, *Addit Manuf*. 39 (2021) 101846. <https://doi.org/10.1016/j.addma.2021.101846>.

Other publications

- K. Lussenburg, N. van der Velden, Z. Doubrovski, J. Geraedts, E. Karana, Designing with 3D Printed Textiles: A case study of Material Driven Design, 5th International Conference on Additive Technologies - ICAT 2014 Vienna, Austria, (2014). ISBN: 978-961-281-579-0

